THE POST-LGM EVOLUTION OF MILFORD SOUND, FIORDLAND, NEW ZEALAND

TIMING OF ICE RETREAT, THE ROLE OF MASS WASTING & IMPLICATIONS FOR HAZARDS

Jesse Leif Dykstra

Department of Geological Sciences

University of Canterbury

A thesis submitted in partial fulfilment
of the requirements for the degree of

Doctor of Philosophy (PhD)
in Geological Sciences/
Hazard & Disaster Management

2012

Abstract

The plate-boundary Alpine Fault runs immediately offshore of the popular tourist destination of Milford Sound, which is visited by more than half a million tourists each year. Glaciers retreated from the fiord between ~24-16 ka, leaving behind a legacy of extreme topography, including some of the world's highest sea cliffs, which tower nearly 2 km above the fiord. Visitors come to view the spectacularly steep and rugged landscape, with many cruising the fiord by boat.

This project utilizes ^{10}Be surface exposure dating of glacially modified surfaces, to gain further insight into the glacier retreat history of Milford Sound. Exposure dates from strategic locations near the entrance to the fiord indicate that the main trunk glacier had retreated about 9 km from its peak LGM position by ~18 ka. Additional ^{10}Be and calibrated Schmidt Hammer data from a range of positions within the Milford catchment provide strong evidence that the main trunk glacier receded rapidly after about 18 ka, retreating a further 16 km to a position near the present-day confluence of the Tutoko and Cleddau rivers, by ~16 ka.

Available seismic reflection data suggest that post-glacial sediment infill has been strongly influenced by massive deposits of rock avalanche debris. New high-resolution bathymetric and seismic reflection data reveals the presence of at least 18 very large (10^6 - 10^7 m^3) post-glacial rock avalanche deposits which blanket ~40% of the fiord bottom. Geomorphic mapping and field investigation reveal the presence of at least ten additional very large to giant (10^6 - 10^8 m^3) terrestrial landslide deposits in the lower Milford catchment; radiocarbon and surface exposure dating indicate that these events occurred during the Holocene, between ~9-1 ka. Ages of six of these deposits are in agreement with published rupture dates on the southern on-shore portion of the Alpine Fault.

Abstract (cont.)

Coseismic landslides are common in New Zealand; seismic shaking serves as the primary trigger for failures that are preconditioned by progressive degradation of rock mass strength. At Milford Sound, most large landslides are probably earthquake-initiated, given the close proximity of the Alpine Fault and the high seismicity of the Fiordland region. Most landslide source areas are on slopes of 50-70°, and extend to ridgelines; landslides commonly fall from heights of 500-1,500 m directly into the fiord. Possible impacts of a future Alpine Fault or Fiordland subduction-zone earthquake may include landslide-generated tsunami, such as those that caused 174 deaths in the fiords of western Norway between 1905 and 1936.

Results indicate that landslides of $\sim$3 x 10^6 m^3 have fallen off the slopes surrounding Milford Sound about once every thousand years; such landslides would have generated waves with amplitudes of $\sim$4 m and maximum local runup of up to 17 m. Landslide-generated displacement waves will travel the length of the fiord in less than 5 minutes.

Several hundreds to thousands of people could be exposed to future co-seismic landslide-induced displacement waves at Milford Sound, depending upon the the season, and time of day. Based on the most recent available visitor numbers, and estimated resident/worker populations, the long-term risk due to landslide-generated tsunami at Milford Sound is estimated to be 0.38 deaths/year (assuming no prior warning). This risk is slightly higher than recent risk assessments for Norwegian fiords, which host less visitors than Milford Sound, and do not experience large earthquakes.

Acknowledgements

I owe much to all of those special and dedicated people who have helped bring this challenging project to fruition.

Firstly, a gigantic cheers to my principal supervisor, Professor Tim Davies, who saw the potential value of this project in the first place, and showed unwavering support for me throughout, despite many challenges and disruptions. Tim managed to give me space when I was working through tough times, while providing me with the encouragement and support that I needed to get to the end. Thanks Tim, I can't thank you enough!!

I am also very thankful for the expertise, advice and support of Dr. Philip Barnes, my co-supervisor at NIWA. I always ended up seeing things much more clearly after our meetings. The value of Dr. Barnes' input, especially near the the beginning of the project and over the last 12 months, cannot be overstated. Much appreciated Phil!

Thanks also to Professor Jarg Pettinga, Head of the Geological Sciences Department, whose patience and support throughout this project has been greatly appreciated. Dr. Stefan Winkler convinced me that Schmidt Hammer exposure dating could be a useful tool for this project. Thank you for pointing me in that direction Stefan, and for your regular advice and support along the way. Professor Jim Cole was instrumental in my decision to pursue a PhD at Canterbury, and his never-ending enthusiasm for natural hazards research has been an inspiration. Dr. Mark Quigley has also been an inspiration, both in terms of helping me out with the nuances of TCND sampling, and in the relaxed, approachable and genuine manner that he has communicated with the public and the media in the aftermath of the Canterbury earthquakes.

Allison (Pat) Roberts, what a gem within the department! Thanks for always considering the challenges of my project (and figuring out how to conjure up an extra few dollars to cover fieldwork expenses). Your patience and organization are great assets. Many others in the Geological Sciences Department have also contributed to the project along the way, including John Southward, Janet Warburton, Rob Spiers, Sacha Baldwin-Cunningham, Kerry Swanson, Cathy Higgens, Dr. Vanessa Tappenden, Dr. Anekant Wandres, and James Oram, who persevered with teaching me how to process the TCND samples, despite plenty of difficulties. Thanks to Kurt Joy for being a well of knowledge when it comes to TCND, and for finding out the right value for the ^{9}Be concentration!

I would also like to thank Albert Zondervan and Graham Hancox at GNS, for their valuable input with respect to the TCND data and landslide distribution. Several people helped out with field work at various stages; special thanks to Andrea Dykstra, Steve Hutchinson and Dr. Volker Nock, who were all amazingly enthusiastic, despite the daunting terrain and sand flies.

Lastly, I would like to thank my lovely partner, Suzanne Furkert. Your tireless love and support is an integral part of this project, and largely because of your patience and enthusiasm, several months worth of fieldwork went pretty much like clockwork. Your mountaineering skills and general outdoor savviness were comforting; you were the best field assistant that any geologist could ask for! Thank you for your understanding and patience, especially through the writing up period.

The project could not have proceeded without financial support. Academic study was supported by a Rotary International Ambassadorial Scholarship and a New Zealand International Doctoral Research Scholarship. Fieldwork, laboratory processing and sample analysis were supported by external funding from the Mason Trust Fund, and Tim Davies' GNS subcontract. Further financial support was provided by GNS, in the form of a reduced rate for AMS analysis of TCND samples. In-kind support was provided by NIWA, who generously shared their submarine data for Milford Sound.

Contents

List of Figures

LIST OF FIGURES

List of Tables

Glossary

~ approximately

2-D two-dimensional

3-D three-dimensional

AABW Antarctic Bottom Water

ACR Antarctic Cold Reversal

AK Alaska, U.S.A.

ANOVA Analysis of variance

ANSTO Australian Nuclear Science and Technology Organisation

B.C. British Columbia, Canada

DEM Digital elevation model

DOC Department of Conservation

ENSO El Niño-Southern Oscillation

Fjord Fiord (New Zealand spelling)

GNS GNS Science (formerly the Institute of Geological and Nuclear Sciences)

LGIT Last Glacial/Interglacial Transition

LGM Last Glacial Maximum

MM Modified Mercalli intensity scale

MRE Marine reservoir effect

MS Milford Sound

MWP-1A Meltwater pulse 1A

NIWA National Institute of Water and Atmospheric Research (formerly the New Zealand Oceanographic Institute)

NZ New Zealand

RA Rock Avalanche

GLOSSARY

SED Surface exposure dating

SH Schmidt Hammer

SHD Schmidt Hammer dating, or Schmidt Hammer exposure dating

SST Sea surface temperature

SWW Southern Hemisphere westerly winds

TCN Terrestrial cosmogenic nuclides

TCND Terrestrial cosmogenic nuclide dating

UC University of Canterbury

WAIS West Antarctic Ice Sheet

YD Younger Dryas chronozone

Chapter 1

Introduction & project background

"For thousands of feet upwards the eye looks upon straight cut rocky frontages, not worn smooth by time, or by wind or water, but as sharply defined and as fresh looking in all respects as if riven asunder but yesterday by the stupendous wedges of Titanic Masons" James Hingston describing Milford Sound, 1883.

1.1 Project background

Milford Sound is the northern-most fiord of Fiordland National Park, a seismically active region in the south-western corner of New Zealand's South Island. Accessible by public road, and surrounded by natural beauty, Milford Sound is one of the world's premier natural attractions. Over 500,000 visitors arrive each year to experience what poet Rudyard Kipling described as the "eighth wonder of the world". Glaciers last retreated from the area starting approximately 17 ka, leaving behind a legacy of extreme topography, including some of the world's highest sea cliffs. Each year, increasing numbers of visitors come to view the spectacularly steep and rugged landscape, with the vast majority cruising the fiord by boat.

The Milford Sound region also hosts the remains of many large post-glacial landslides. One of the world's most active plate-boundary faults, the Alpine Fault, crosses the narrow continental shelf just offshore of Milford Sound. In such steep mountainous regions, catastrophic seismically-induced landslides can have a major influence on landscape development, and where these powerful geomorphic events conflict with human activity, they can pose a significant risk to life and infrastructure. A particularly devastating hazard can arise when large landslides fall into water bodies such as fiords, generating catastrophic displacement waves that can affect many kilometres of coastline, causing destruction up to 10s of metres above sea level. In western Norway (a region that does not experience large earthquakes), catastrophic landslides fall into the fiords about every 100 years. During the last century 174 people have been killed by landslide-generated tsunami in Norway.

Milford Sound is an iconic natural attraction and high-profile tourist destination, located in an exceptionally steep and seismically active area with a high concentration of large post-glacial landslides. Despite these factors, the potential risk from landslides and landslide-generated tsunami has not been previously investigated.

1.1.1 Regional setting

Te Wāhipounamu (the "place of greenstone" to the original Māori inhabitants), or the South West New Zealand World Heritage Area, encompasses an area of 2.6 million hectares in the south west of New Zealand's South Island (see Figure 3.1), including four national parks; Aoraki/Mt. Cook, Westland, Mt. Aspiring and Fiordland. Te Wāhipounamu, which includes approximately 10 % of New Zealand's total land area, was designated a World Heritage Area in 1986, in recognition of its superlative natural environment, and as an outstanding example of the Earth's evolutionary history.

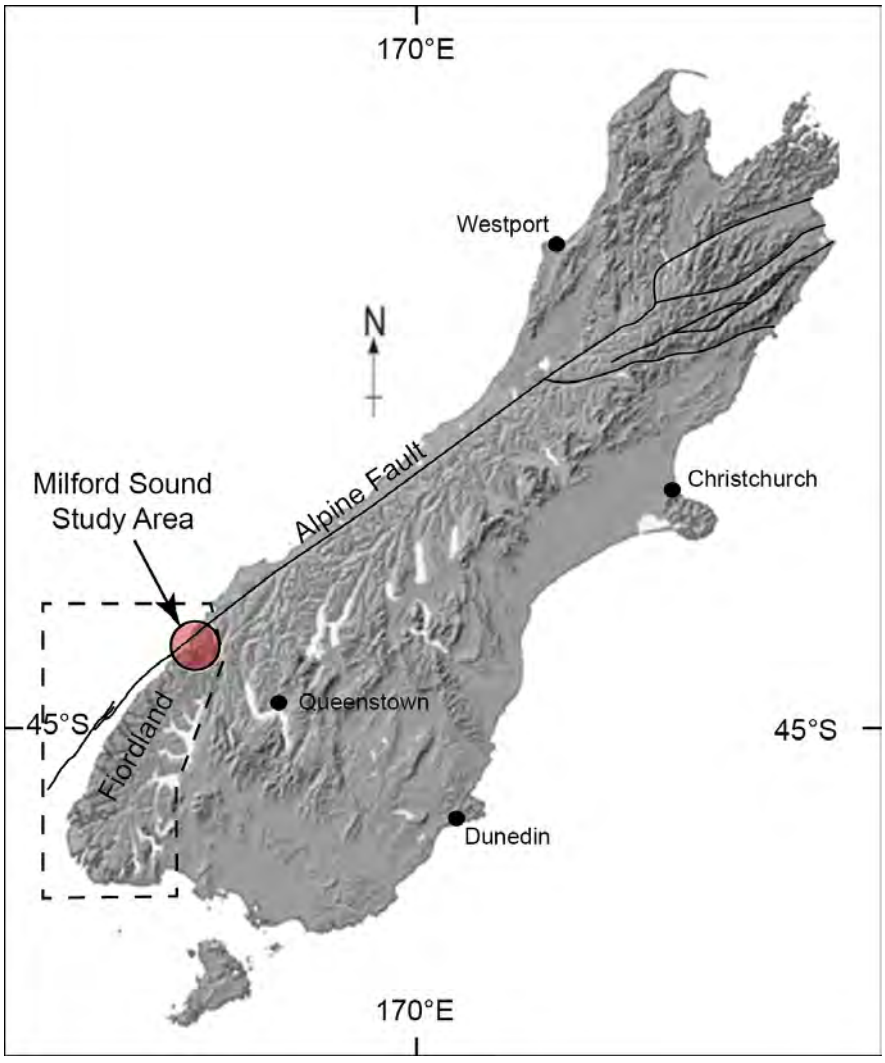

Figure 1.1: Topographic relief map of the South Island of New Zealand. Study area within red circle. Dashed line around Fiordland indicates the extent of Figure 1.5

Approximately 2 million hectares of temperate rainforest encompass the world's most extensive suite of Gondwanaland flora and fauna, including podocarp and beech species, and flightless birds such as the Kiwi and Takahe.

Fiordland National Park covers ∼1.25 millions hectares (nearly half) of the Te Wāhipounamu World Heritage Area. In addition to unique flora and fauna, Fiordland also hosts spectacularly well-preserved glacial geomorphology, including many classic examples of glacial landforms such as fiords, hanging valleys, and cirque lakes. Very high rock mass strength has limited the erosion of glacial features, preserving a legacy of geomorphology from the Last Glacial Maximum (LGM). Numerous fiords, cirques, glacial staircases and hanging tributary valleys have been preserved since deglaciation, although mass-wasting processes continue to modify the landscape and transport hill-slope material to valley bottoms in the forms of colluvium and alluvium (Augustinus, 1995; Korup, 2005b).

Milford Sound is a glacially-carved fiord, surrounded by sheer rock walls which tower over a kilometre above the sea. While the natural attractions draw many visitors, the fiord is also a potentially dangerous place. Across the narrow entrance to the fiord lies an active transform plate boundary, where the Indo-Australian Plate collides obliquely with the Pacific Plate. The new Milford Sound visitors centre is situated less than 15km from the strike-slip Alpine Fault, which last ruptured around 1717 A.D., producing an earthquake of about M_w 8.1 (De Pascale and Langridge, 2012). The probability of an earthquake of similar magnitude occurring along the southern portion of the Alpine Fault within the next 50 years is estimated at ∼30% (Berryman et al., 2012b).

Fordland's active tectonic setting also gives rise to a very wet climate. The extreme topography of the Fiordland mountains forces up the prevailing westerly winds, resulting in mean annual precipitation of nearly 7 m at Milford Sound. During the Last Glacial Maximum (LGM), these climatic and tectonic conditions were favourable for the advance of tide-water glaciers, which deposited material in large fans at the edge of the narrow continental shelf (Barnes, 2009; Barnes et al., 2001, 2005).

1.1.2 Potential rockfall/tsunami hazard

Most large rock avalanches occur in the relatively resilient, massive, and coherent bedrock walls of steep, young valleys, such as those found in glaciated (or recently glaciated) mountainsides and fiords (Allen et al., 2011; Hewitt et al., 2008; Korup, 2005b). Glacial steepening and changing permafrost conditions can precondition these bedrock slopes for catastrophic failure. In valleys which contain lakes or fiords, sub-aerial or submarine landslides can generate large displacement waves, sometimes with

Figure 1.2: Milford Sound, mid-fiord view looking northwest towards the Tasman Sea. Mitre Peak (1,683 m) on the left skyline, the Lion (1,302 m) on the right skyline. Harrison Cove is just visible in the bottom right of the frame. The width of the main fiord in the foreground is approximately 2 km. Author photo.

devastating consequences.

1.1.2.1 Examples from western Norway

In the fjords of western Norway, historical records and preserved rock avalanche deposits indicate that catastrophic rockslides occur approximately every 100 years. During the last 100 years, 174 people have been killed by landslide-generated tsunami in the Norwegian fjords, including the 1934 Tafjord rockslide which generated a wave that ran up 62 m, killing 41 people (Eidsvig et al., 2011, and references therein) (see Chapter 4, Table 4.1).

Presently, hazard evaluation and risk assessment for the Norwegian fjords is based on high-resolution sonar imagery of landslide deposits, seismic reflection data, and event chronology developed from radiocarbon dating and surface exposure dating. The ongoing risk in Norway is currently managed by identifying and monitoring potential failure areas, calculating slide paths and estimating slide properties at the points of impact (e.g. Blikra et al., 2002). High-risk locations are monitored more intensively, and include the Aknes slide area above Storfjorden, and the Akernes crevasse on Tafjord. A landslide of 50 million cubic metres is estimated at Akernes, which could generate a tsunami of up to 30 m in height (Eidsvig et al., 2011). The current system of hazard evaluation and mitigation is thought to be effective in reducing the risk in western Norway, because large landslides are normally preceded by smaller events and by accelerating movements of the rock bodies (Blikra et al., 2002; Jorstad, 1968).

1.1.2.2 Lituya Bay

The potential for a co-seismic landslide to generate an extremely large displacement wave is clearly illustrated by the 1958 event in Lituya Bay, Alaska. On the evening of 9 July, an M_w7.7 earthquake along the Fairweather Fault (crossing the the head of Lituya Bay) triggered a rockslide of $\sim$30 x 10^6 m^3on an adjacent hillslope. The rockslide swept into the bay and generating a 150 m high displacement wave which travelled at speeds of up to 160 km/hr, and devastated forests around Lituya Bay up to a maximum height of 524 m above sea level (Miller, 1960).

1.1.2.3 Milford Sound

Like Alaska (and in contrast to western Norway), landslides in Fiordland are most likely earthquake-initiated, and therefore precursory minor rockfalls are unlikely. In Fiordland, it is likely that seismic activity serves as the primary trigger for failures

that ultimately result from progressive degradation of rock mass strength, beginning with deglaciation.

In the highly seismic terrain of Fiordland, large landslides are common, and many post-glacial rock avalanche deposits are documented, with the highest concentration of large events near Milford Sound (Hancox and Perrin, 2009; Korup, 2005b). Most of these recognized events initiated on subaerial slopes, and ended up in valley bottoms where they have been preserved in the landscape. However, there are also steep slopes above (and within) Milford Sound, and as documented in Capter 4, this study shows that many large rock avalanches and rockslides have fallen into the fiord since the last glaciation (see Chapter 4). In addition to potential rock slope failures from the steep walls of Milford Sound, several rivers have built significant deltas which are actively prograding into the fiord. Delta slopes could be susceptible to failure, which could be triggered by seismic shaking or heavy sedimentation (e.g. due to flooding). Despite the potential hazards associated with landslides and landslide-generated tsunami at Milford Sound, the perception of risk is slight, perhaps because humans have only frequented the area within the last century, and historical records are sparse.

Establishing an accurate spatial and temporal record of past landslide activity near the popular tourist destination of Milford Sound (see Figure 1.3) is an important aspect of understanding and preparing for the possible impacts of a future Alpine Fault or Fiordland subduction-zone earthquake. These impacts may include landslide-generated tsunami, such as those that have killed 174 people in similar environments (see Figure 1.4) in the fiords of western Norway.

1.1.2.4 Assessing the hazard and establishing risk

In order to quantitatively establish the risk associated with future landslides and landslide-generated tsunami at Milford Sound, several additional pieces of information are required:

- establish the spatial distribution of submarine and subaerial landslide deposits,
- determine the absolute or maximum ages of the deposits - based on radiometric dating and/or glacial retreat timing,
- establish the rockfall Magnitude-Frequency (M-F) relationship - based on approximate sizes/maximum ages of events,
- establish expected tsunami size range - impulse wave heights and maximum run-up (in this case, based on simple analytical models),

Figure 1.3: Milford Sound, head of fiord with Cleddau delta at centre frame and Deepwater Basin to the right. View looking southeast up the Cleddau Valley. From left to right are the Milford Visitors Centre and harbour, Milford Sound Village, the airport, and the docks at Deepwater Basin. Barren Peak (1,561 m) in the left foreground (above the Milford Visitors Centre), Sheerdown Peak (1,878 m) on the right skyline. The width of the main fiord in the foreground is approximately 1.2 km. GNS photo.

Figure 1.4: Similar fiord landscapes. **A**. Tafjorden, Norway. **B**. Milford Sound, New Zealand

- generate an inundation M-F relationship, based on calculated wave runup,
- determine the number of people at risk,
- calculate their vulnerability, depending on where they are exposed to the hazard

The information noted above is required to make a first-order quantitative estimate of the risk due to landslide-generated tsunami, based on maximum expected impulse wave heights and estimated run-up.

1.1.3 Thesis organization

The main body of this work is divided into 5 chapters:

- Chapter 1: Introduction & project background - project setting, background material and literature review.
- Chapter 2: Fiord evolution in New Zealand: temperate southern hemisphere fiords on a transform plate boundary - Post-LGM climate change and fiord evolution styles.
- Chapter 3: The post-LGM evolution of Milford Sound, reconstructed from geomorphic, sedimentary and seismic reflection records, constrained with new terrestrial cosmogenic nuclide dating (TCND) and calibrated Schmidt Hammer (SH) surface exposure ages. Includes data types and sources, field and laboratory methods and results.
- Chapter 4: Landslide distribution at Milford Sound & implications for natural hazards and risk management - spatial and temporal distribution of 30 large terrestrial and submarine landslide deposits, tsunami wave height modelling and risk assessment for future events.
- Chapter 5: General discussion, summary and recommendations for future work.

Chapters 3 and 4 each begin with brief preamble that is intended to summarize crucial elements of previous chapters; while some of this material is slightly repetitive, it is included with the intention of making each individual chapter more accessible as a stand-alone document.

1.2 Field area description

The study area for this project encompassed the majority of the Milford Sound catchment, including all hillslopes that could potentially contribute rock avalanche material directly into the fiord or lower tributary valleys; a total area of ∼500 km^2. Within the study area there are ∼35 km^2 of steep rock slopes that could potentially contribute rock avalanche material directly into Milford Sound, as well as ∼10 km^2 of submarine rock slopes and delta slopes that could generate submarine landslides. As discussed in detail in subsequent chapters, the close proximity of the active Alpine Fault and Fiordland subduction zone may play a major role in spatial and temporal landslide distribution in the region.

1.2.1 Contemporary climate, sediment yield and vegetation

The Southern Hemisphere Westerly winds (SWW) are largely responsible for regulating precipitation, ocean circulation and heat flow within temperate latitudes of the Southern Hemisphere, and are generally found between 35° and 60° south latitude, although their position varies depending on seasonal to orbital timescales Knudson et al. (2011, and references therein). The SWW are also influenced by interannual-decadal scale coupled ocean-atmosphere climate phenomena, including the El Niño-Southern Oscillation (ENSO), the Inter-decadal Pacific Oscillation (IPO), and the Southern Annular Mode (SAM) and Pacific-South American Mode (PSA) (e.g. Lee et al., 2010). The mean position and variability of the SWW belt are also sensitive to global climate change, increasing in intensity and migrating poleward in response to interglacial warming (Toggweiler et al., 2006). For example, recent results from Knudson et al. (2011), based on proxies for the relative contributions of marine and terrestrial organic matter to marine sediments in several New Zealand fiords, confirm that westerly flow was stronger (weaker) during periods of warmer (cooler) climate in southern New Zealand.

Located within the SWW belt between 42° and 39° south latitude, the Southern Alps and Fiordland Mountains form the ∼800 km-long northeast-southwest trending main divide of the South Island, presenting a prominent barrier to the prevailing westerly winds from the Tasman Sea. Orographic uplift of the maritime winds from the Tasman sea generates a steep precipitation gradient along the West Coast (see Figure 1.6), with the maximum precipitation peaking at around 12,000 mm per year a few kilometres west of the main divide. Just 10 km east of the main divide, annual rainfall falls off to as little as 300 mm, due to the rainshadow effect (Griffiths and McSaveney, 1983). Fiordland also experiences extremely high precipitation, with as much as 14,000

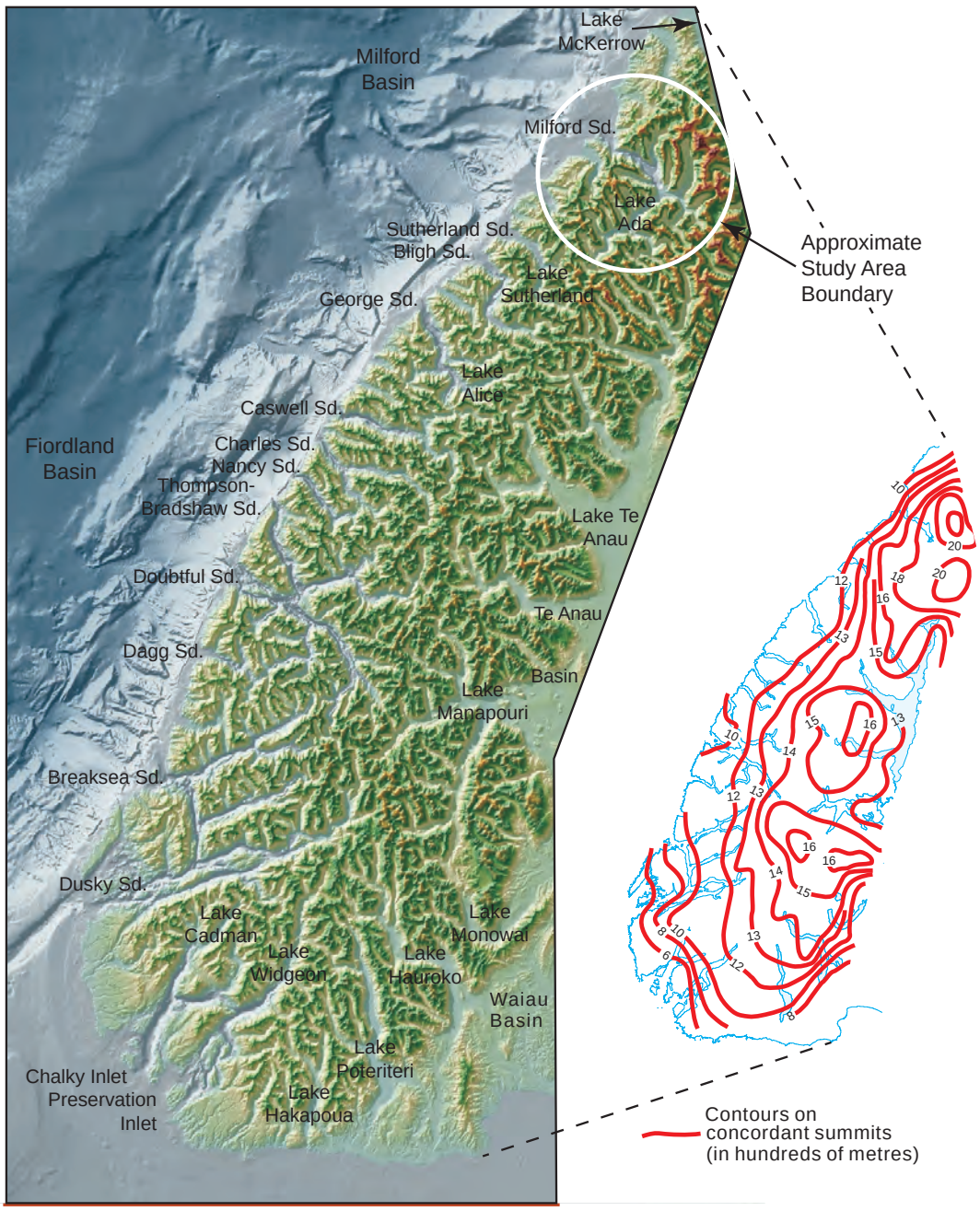

Figure 1.5: Shaded relief map of Fiordland, illuminated from the northwest. Digital elevation data from LINZ (on land) and NIWA (offshore). Inset shows Fiordland summit accordance, 200 m contour interval. Based on Turnbull et al. (2010), figures 5 and 6.

mm per year recorded near Milford Sound (N.I.W.A., accessed 27 April, 2012). Average recorded annual rainfall at Milford Sound exceeds 6,500 mm, compared to just 900 mm only 70 km away at Queenstown (N.I.W.A., accessed 27 April, 2012).

Contemporary erosion processes are highly variable in New Zealand; sediment yields vary over 4 orders of magnitude (from <20 t/km^2/y, to nearly <30,000 t/km^2/y). Catchment-specific sediment yields depend upon several location-dependent factors, including annual precipitation, resistance of basement rocks to weathering (i.e. basin lithology and structure), tectonic activity and the Quaternary history of the catchment (e.g. supply of glacial sediment, vegetation changes, human activity) (Hicks et al., 1996).

In the Southern Alps, a combination of rapid uplift, high orographic precipitation and basement rocks of easily weathered, foliated schists north of Fiordland have resulted in extremely high erosion rates up to 10 mm per year, approximately equal to the tectonic uplift rate (Augustinus, 1992; Fitzsimons and Veit, 2001). Other processes that have contributed to the unusually high erosion rates in the Southern Alps include earthquake activity, glacial erosion and paraglacial processes such as post-glacial fluvial dissection and landsliding of over-steepened slopes(Allen et al., 2011; Korup et al., 2004).

Erosion rates in Fiordland are much lower than in the Southern Alps (Hicks et al., 2003; Korup, 2005a; Pickrill, 1993), despite similarly high precipitation and seismicity. Pickrill (1993) examined several core samples of post-glacial sediments from New Zealand fiords (including Milford Sound), and found that long-term average sediment yields vary from 28 to 109 t/km^2/y. This low range of values is in marked contrast to a figure of 13,300 t/km^2/y obtained earlier by Griffiths, based on measurements of sediment load in the Cleddau River, which flows into Milford Sound (Fitzsimons and Veit, 2001; Knudson et al., 2011). The relatively low denudation rates in Fiordland are thought to be due to weathering-resistant crystalline plutonic rocks that dominate Fiordland geology, and a relatively low rate of uplift (in the range of 0.5-1 mm/year, Kim and Sutherland (2004)) due to the predominantly strike-slip motion of the plate boundary Alpine Fault south of Haast. Although catchments in the Southern Alps are more frequently affected by landslides, Korup (2005a) noted that long-term disruptive effects such as those due to landslide damming and subsequent perturbations in sediment flux, are more persistent in Fiordland.

Like most of Westland, Fiordland vegetation is dominated by thick indigenous rainforest of southern beech or mixed conifer/broadleaf species (Mark, 1998). North of Fiordland, in the west-central zone of the Southern Alps, is the conspicuous “beech-

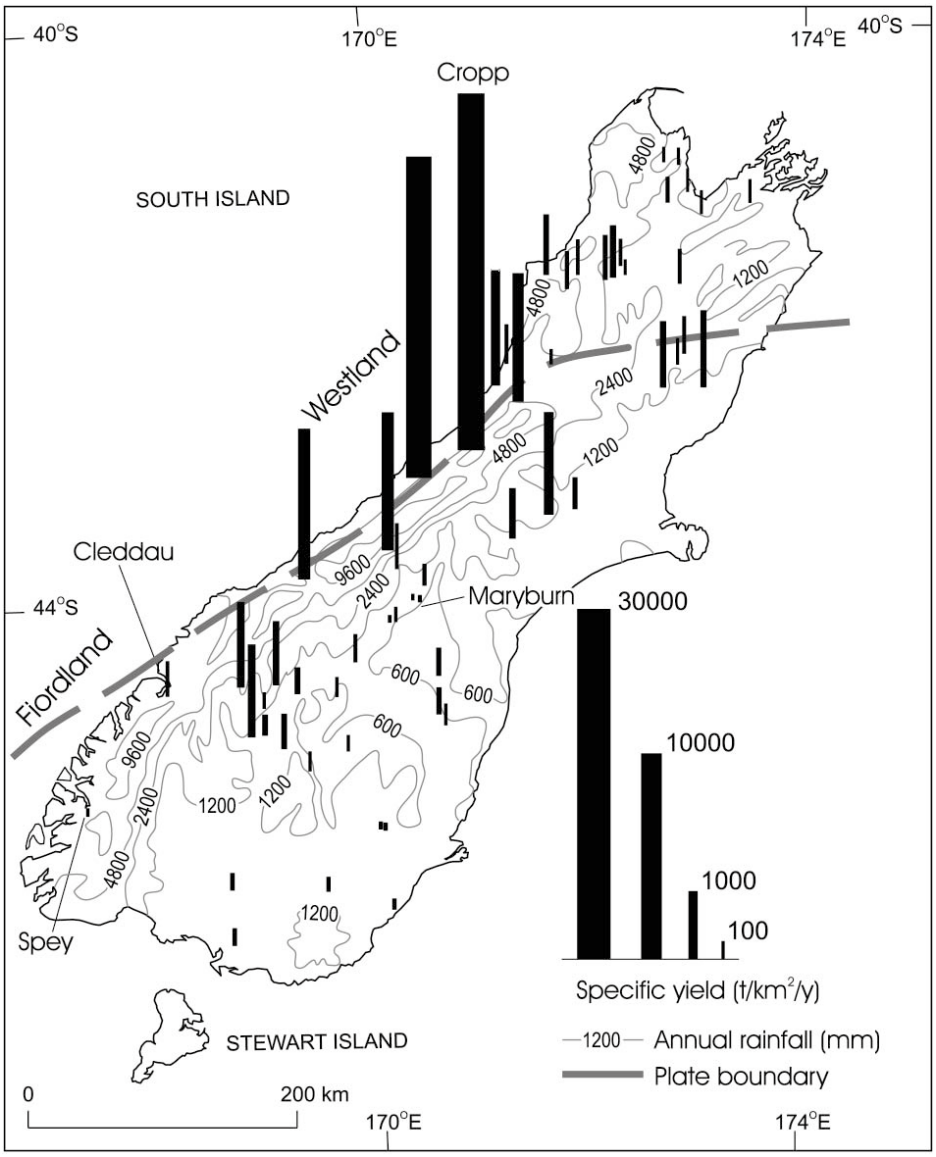

Figure 1.6: Contemporary precipitation isohyets and sediment yields for selected South Island catchments, based on Fitzsimons and Veit (2001), figure 4b. The Cleddau data point is located near the head of Milford Sound. Data based on Hicks et al. (1996)

gap"; a 150 km long zone between the tree line of the western Southern Alps and the west coast where the beech (*Nothofagus*) forest is absent. Although hotly debated, the favoured explanation for the striking absence of beech forest in central Westland is a slow reinvasion of *Nothofagus*, following exclusion during the LGM due to the glaciers extending beyond the present coastline. The beech-gap region is typified by lowland conditions favourable for rapid recolonisation by Podocarp forests, including fertile soils and abundant transport of seeds by birds; in addition many beech species (with the exception of Mountain Beech) benefit from an association with nitrogen fixing bacteria, therefore beech forests tend to recolonise following large-scale disturbance relatively slowly (Leschen et al., 2008).

Recently, investigation of the population genetics of two species of fungus beetles led Leschen et al. (2008) to conclude that beetle populations were divided into northern and southern populations by glacial ice advance some 64-105 ka, suggesting a pre-LGM glacial control for the beech gap. This explanation has raised some questions about the presence of extensive beech forests in Fiordland (e.g. McGlone, 1985), and led some early researchers to conclude that growth of Fiordland glaciers during the LGM was minor compared to that in south Westland (Holloway, 1954). The results of the current study provide clear evidence that the fiord valleys of northern Fiordland contained substantial glaciers as recently as 17-16 ka; the glacier that occupied Milford Sound was grounded on the narrow continental shelf during the LGM (see Chapter 3).

1.2.2 Geological setting

1.2.2.1 Regional geological history

The South Island of New Zealand has a complex geological history, including three major tectonic regimes in the Phanerozoic; the Tuhua Orogeny (Devonian and Carboniferous), Rangitata Orogeny (Cretaceous), and the Kaikoura Orogeny, during the Cenozoic. The oldest rocks dated so far in New Zealand are some 680 millions years old (when New Zealand formed part of the Gondwana margin); these rocks were deformed and uplifted during the Tuhua Orogeny, and reflect severe folding and plutonic intrusions. Following the Tuhua Orogeny, the New Zealand Geosyncline developed over 200 million years, with deposition of a vast thickness of sandstone along an island arc system. Deposition in the New Zealand Geosyncline ceased with a period of uplift during the Rangitata Orogeny, which peaked approximately 130 millions years BP, and produced the late Cretaceous Peneplain. The New Zealand crustal region broke away from Gondwanaland some 80 millions years ago, after which much of New Zealand

sunk below sea level, resulting in the accumulation of a series of Paleogene and early Neogene marine sediments. Most of those sediments have since been removed from the South Island by uplift and erosion during the present mountain-building episode, the Kaikoura Orogeny, which began some 26 million years BP (Fitzsimons and Veit, 2001).

Oblique convergence and strong interplate coupling between the Pacific and Indo-Australian Plates during the last 6.4 million years has resulted in a transpressional regime and large-scale deformation, including uplift and erosion of sandstones and siltstones from the Tuhua Orogeny (Claypool et al., 2002; Walcott, 1998). These greywacke and argillite sequences comprise the Torlesse Supergroup of the northern and eastern Southern Alps, and the metamorphosed equivalent, the Haast Schist Group, in the southwest ranges. Together the Torlesse and Haast group rocks form the spine of the Southern Alps. Immediately east of the Alpine Fault, the schists are very high grade, but metamorphic grade decreases progressively to the east (Korup et al., 2004). Rapid uplift of up to 10 mm per year in the Southern Alps has resulted in total topographic uplift in the range of 15-20 km (Claypool et al., 2002; Kamp et al., 1989; Norris and Turnbull, 1993). The relatively modest topographic expression (< 3000 m) that typifies the Southern Alps today is an indication that denudation rates have been extremely high, keeping pace with uplift (Korup et al., 2004).

1.2.2.2 Contemporary geology of Milford Sound

Milford Sound is deeply incised into the extreme northeastern corner of the Fiordland Block, which is bounded to the west by the Alpine Fault, and a disjointed network of lesser faults. Much of the geology of Milford Sound itself is part of the Arthur River Complex (ARC); a composite body of gabbroic to dioritic gneiss that has been interpreted as a Mesozoic batholith emplaced at mid-crustal levels and subsequently buried to deep crustal levels Claypool et al. (2002); Hollis et al. (2003)). The ARC includes the garnet-hornblende-bearing homogeneous Milford Gneiss, the banded dioritic Harrison Gneiss, the gabbroic/dioritic gneisses of the Pembroke Granulite, and lesser migmatite and ultramafic rocks (see Figure 1.9). The ARC separates metamorphosed gabbroic to dioritic plutonic rocks of the 138-162 Ma old Darran Complex (part of the Median Tectonic Zone; a Mesozoic island arc complex) from granulitic rocks of the Western Fiordland Orthogneiss (Paleozoic rocks of the Gondwana margin)(Hollis et al., 2003; Wandres et al., 1998). Together the ARC and Darran Complex form most of the extreme topography that borders Milford Sound. To the west, the ARC is bounded by mylonites and cataclasites of the Anita Shear Zone, which was formed during mid-Cretaceous rifting of the Gondwana margin and the opening of the Tasman sea (Klepeis

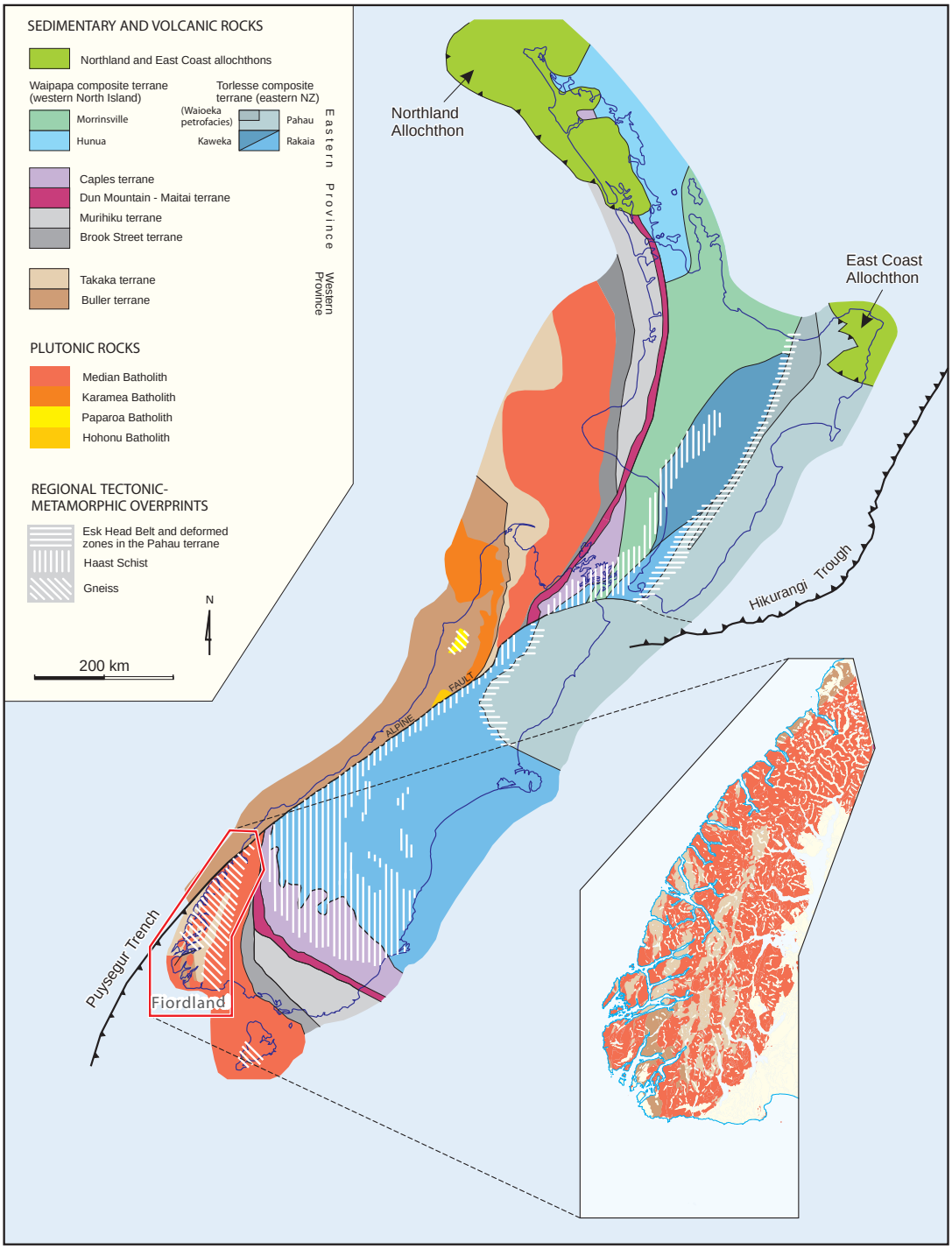

Figure 1.7: Basement geology of New Zealand, subdivided into terranes, batholiths and allochthons, with regional tectonic-metamorphic overprints. Inset map higlights Fiordland area. Based on Turnbull et al. (2010), figure 3.

et al., 1999).

1.2.2.3 Tectonics: Plate boundary

Currently, the tectonic geomorphology of Fiordland and the Southern Alps is dominated by the northeast-southwest trending Alpine Fault, which is the result of oblique (∼68°) convergence of the Pacific and Indo-Australian plates for some 800 km along most of the length of the South Island, including the off-shore portion of the fault west of Fiordland (Barnes et al., 2005), and the Marlborough fault system in the north (Berryman et al., 1992; Norris and Turnbull, 1993). The Alpine Fault extends offshore to the south of Milford Sound, where the southern 230 km of the fault traverses the continental margin off Fiordland, gradually making the transition from a transpressive regime to oblique subduction of the Australian plate beneath the Pacific plate at the Fiordland subduction zone (Barnes et al., 2005). The subducted Australian plate dips more steeply to the north beneath northern Fiordland, becoming sub-vertical from about 75-150 km depth (Reyners et al., 2002; Sutherland et al., 2006a; Turnbull et al., 2010. The offshore extensions of the plate boundary are marked by the Hikurangi Trench to the northeast and the Puysegur Trench southwest of Fiordland.

In contrast to the Southern Alps, the Fiordland Mountains are characterized by relatively low rates of uplift (∼0.5-0.6 mm per year, Kim and Sutherland (2004); Shuster et al. (2011)), due to the predominantly strike-slip motion of the Alpine Fault in northern Fiordland. The geology of the Fiordland Block, which forms the Fiordland Mountains, is dominated by crystalline Paleozoic-Mesozoic basement rocks of high rock-mass strength, with lithologies of granitic to gabbroic composition, including granites, diorites, gabbros, and orthogneisses (Claypool et al., 2002). As the Alpine Fault strikes to the southwest, it crosses part of the narrow continental shelf just offshore of Milford Sound at the Anita Shear Zone, which bisects the outer basin of the fiord (Hollis et al., 2003). The Fiordland Block is bounded by the Alpine, Hollyford, and Fiordland Boundary faults, as well as the Moonlight Fault, which extends to the northeast where it crosses Lake Wakatipu (Norris and Turnbull, 1993).

Seismicity in the region is high due to transpressive deformation along the northeast boundary of Fiordland, and active subduction of the Australian Plate at the Puysegur Trench, which lies along the southeast boundary of Fiordland. A steeply dipping zone of earthquake activity underlies the Fiordland coast, and is thought to be related to the east-dipping subduction zone (Claypool et al., 2002; Kim and Sutherland, 2004; Turnbull et al., 2010). Seismic activity is associated with the subducted Australian plate, and is predominantly manifested by normal faulting above ∼16km, and by in-

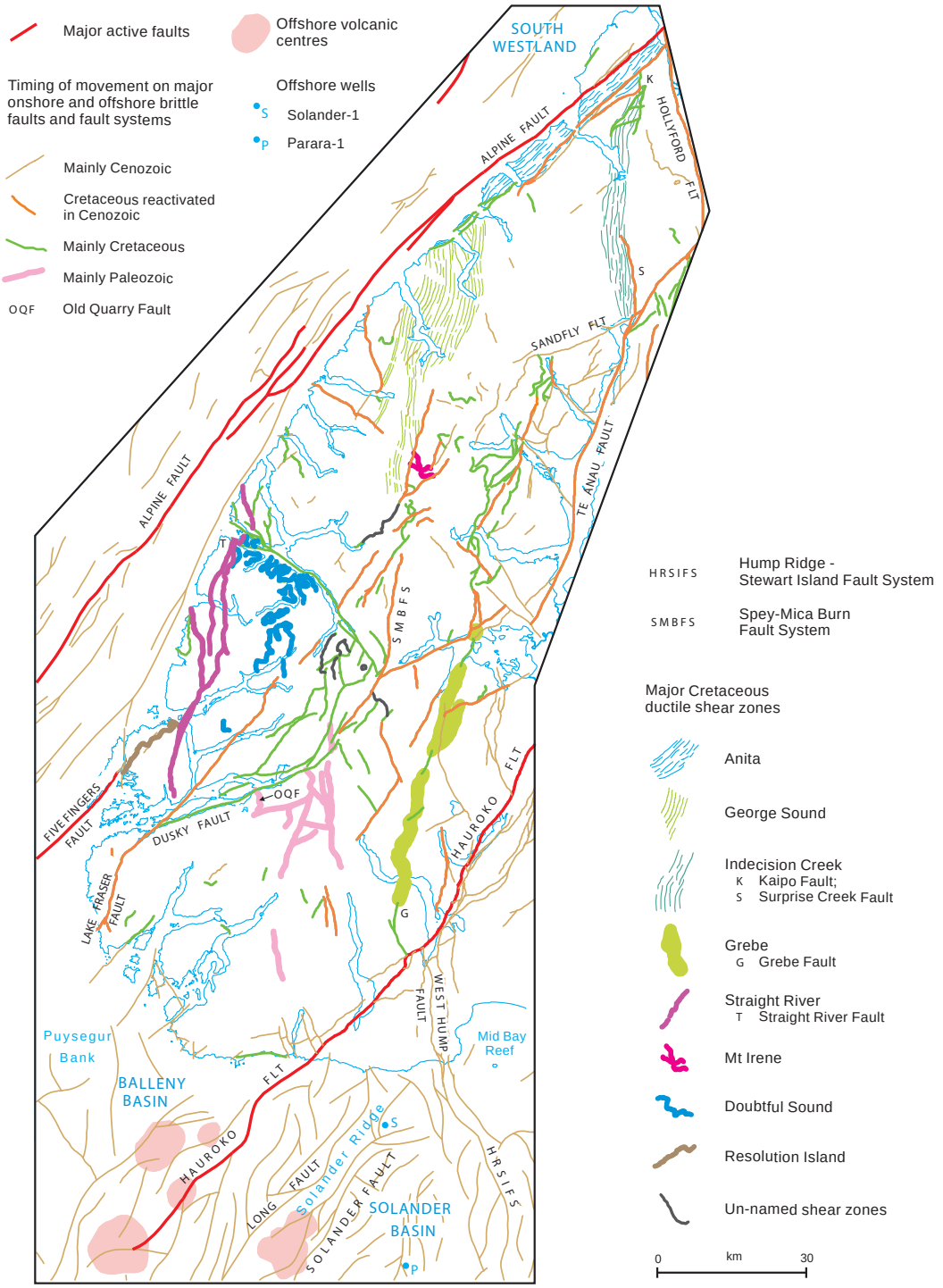

Figure 1.8: Major faults and ductile shear zones in Fiordland. Milford Sound at upper right of figure, between the Alpine and Hollyford faults. After Turnbull et al. (2010), figure 67.

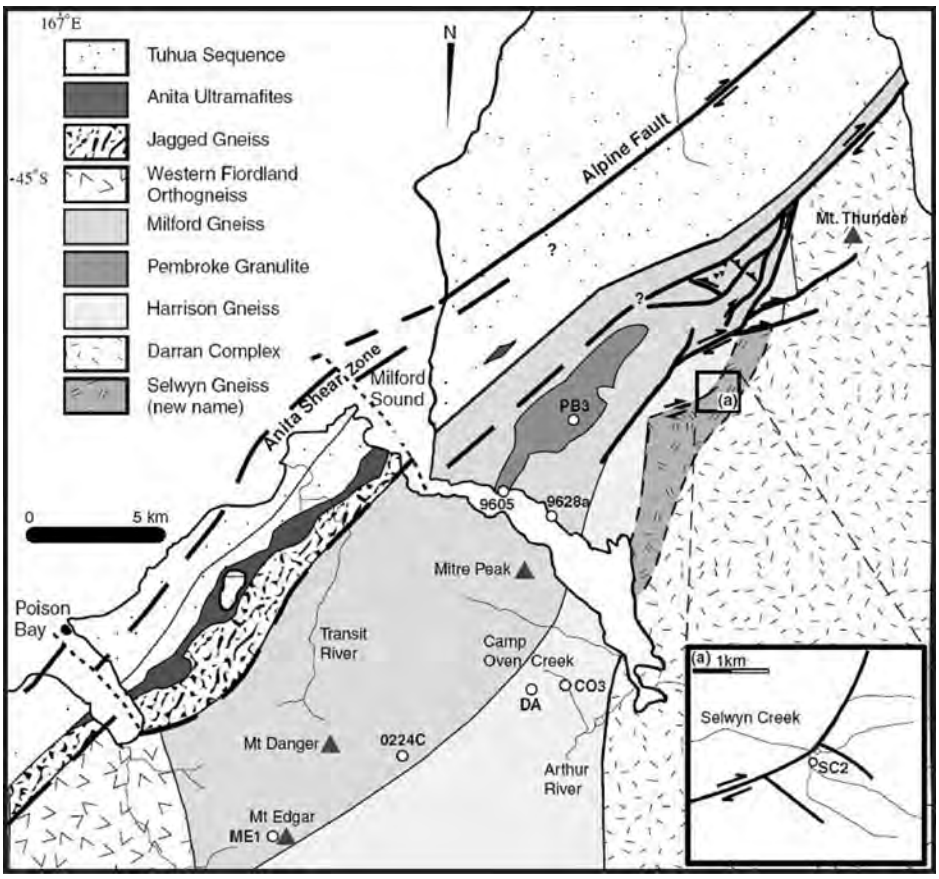

Figure 1.9: Geology of Milford Sound and the Arthur River Complex. After Hollis et al. (2003).

terplate thrust faulting at greater depths (Reyners et al., 2002). Immediately offshore of Fiordland, wedges of Holocene sediment are being deformed by shortening west of the Alpine fault; a process which accommodates up to 20% of modern plate motion (Barnes et al., 2005). The majority of the plate boundary motion is accommodated by the Alpine Fault and nearby inland subsidiary faults (Turnbull et al., 2010).

Fiordland has experienced three earthquakes greater than M_w 7, and seven greater than M_w 6 over the last 150 years (Hancox et al., 2002). The M_w 7.2 Fiordland earthquake of August 22, 2003 was the largest shallow earthquake in New Zealand for over 35 years (Hancox et al., 2003), and the 2009 Fiordland subduction zone earthquake is the largest thrust fault event recorded in New Zealand (G.N.S.). Historical earthquakes in and around Fiordland are shown in Figures 1.10 and 1.11.

1.2.2.4 Slip rates and recent earthquake activity on the Alpine Fault

Late Quaternary dextral slip rates have been estimated at 27 ± 5 mm/yr for the central section of the Alpine Fault (Norris and Turnbull, 1993), and 23 ± 2 mm/yr for south Westland (Sutherland et al., 2006b). Berryman et al. (2012a) estimated a significantly slower slip rate of ∼17-18 mm/yr at Haast. Barnes (2009) investigated the dextral displacements of well-preserved relict offshore glacial outwash fans and moraines that straddled the Alpine Fault, and calculated that the offshore slip rate for the segmented section of the fault between Milford and George Sounds is 27.2 (-3.0/+1.8) mm/yr.

A chronology of recent Alpine Fault ruptures has been generated based on off-fault paleoseismic records of landscape change events, including landsliding and forest disturbance, channel aggradation and coastal dune formation (e.g. Wells and Goff, 2007; Wells et al., 1999), as well as from on-fault evidence (e.g. Wells et al., 1999; Yetton, 1998). Based on these records, the Alpine Fault has ruptured somewhere along its length at least four times in the past 1000 years, producing earthquakes of about M_w 8. The latest Alpine Fault rupture occurred around 1717 A.D. on the southern onshore portion of the fault, extending from near Milford Sound to near the Haupiri River, a distance of at least 380 km (Berryman et al., 2012a; De Pascale and Langridge, 2012; Wells et al., 1999; Yetton, 1998) .

Recent work along the southern onshore part of the Alpine Fault has included 5 trenches excavated across the fault trace at the Haast, Okuru and Turnbull Rivers (Berryman et al., 2012a). That study found that the last three ruptures have likely been in A.D 1717, A.D. 1230 ± 50 and A.D. 750 ± 50, or an average recurrence interval of 480 years, with an average dextral displacement of 17-18 mm/yr. This displacement rate is somewhat lower than that calculated by other workers (e.g. Barnes, 2009;

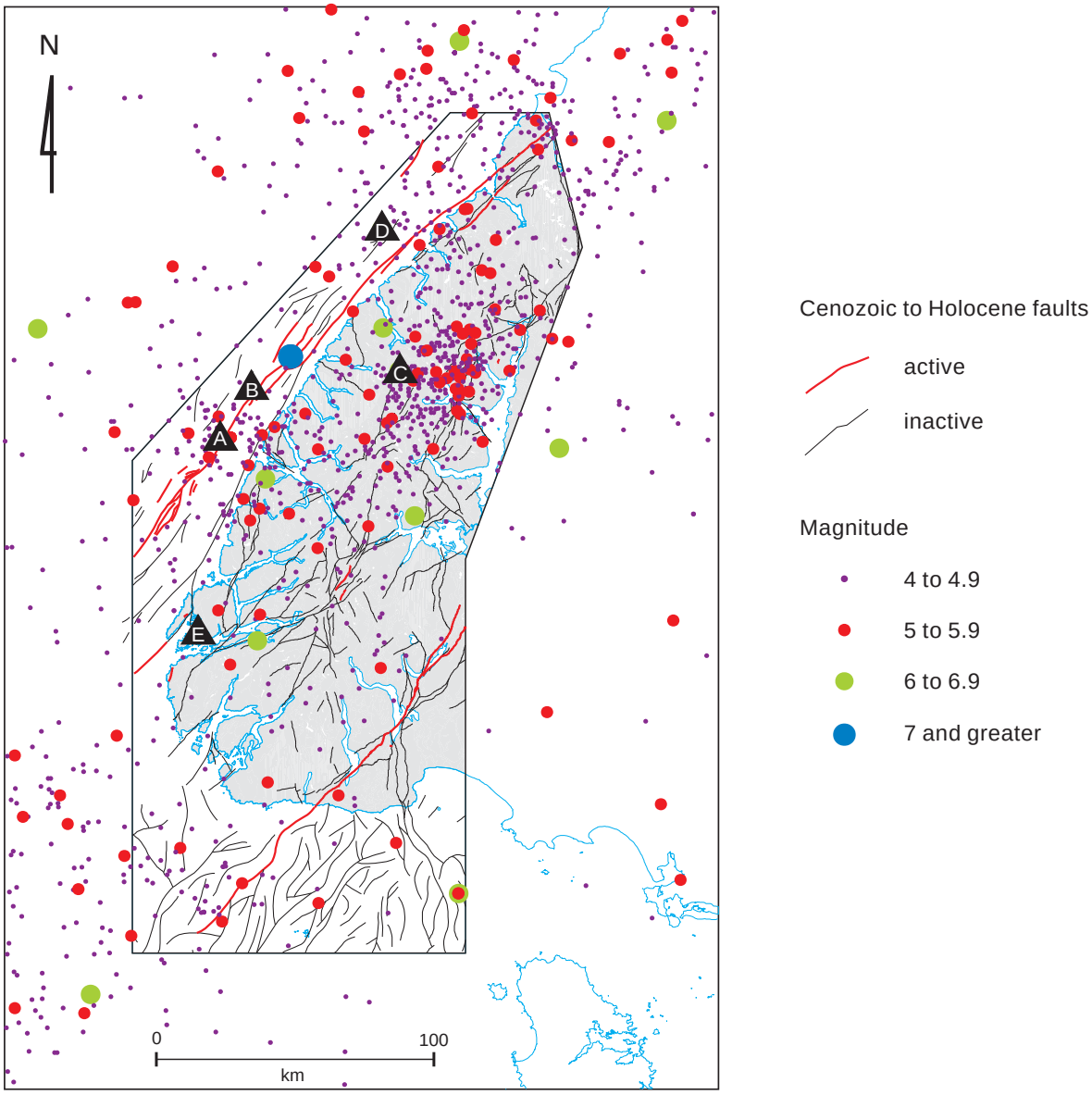

Figure 1.10: Earthquakes since 1900 in and around Fiordland, plotted by magnitude, with known major Cenozoic faults shown. Major earthquake epicentres, marked by black triangles, are: A. Secretary 1993, M_w 6.8; B. Fiordland 2003, M_w 7.2; C. Te Anau 1988, M_w 6.7; D. Milford 1976, M_w 6.5; E. Dusky Sound 2009, M_w 7.8. The blue circle marks the 1938, M_w 7 earthquake off Charles Sound. Most large earthquakes in Fiordland are relatively deep and not obviously associated with major fault surface traces, as they are related to the subduction interface. After Turnbull et al. (2010), figure 73.

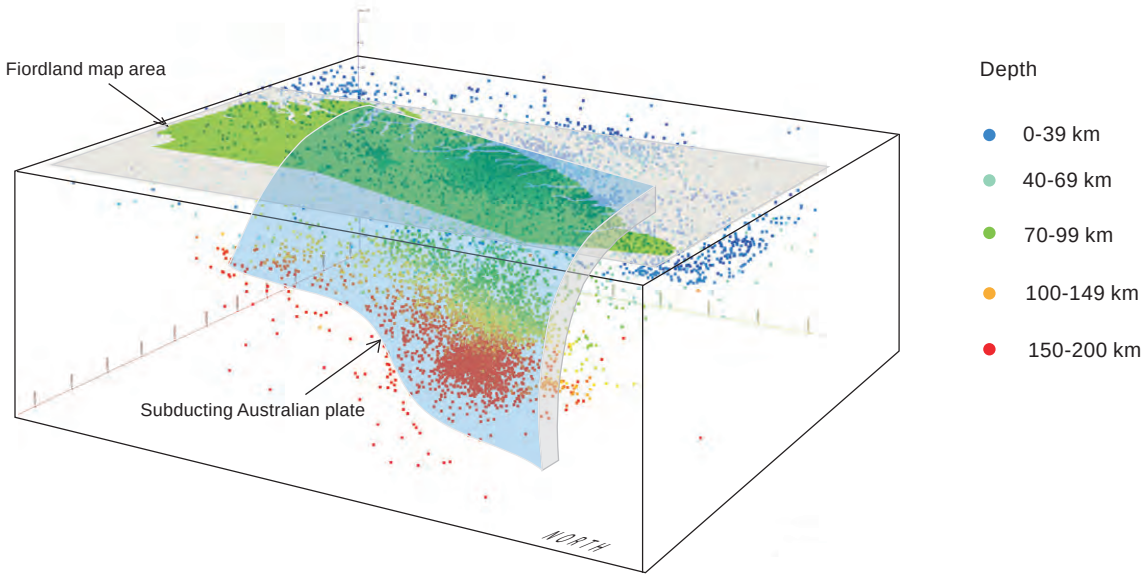

Figure 1.11: Major and minor Fiordland earthquakes since 1900, plotted according to depth. Perspective view from the northeast. Deeper earthquakes are concentrated in the northeast, with increasing depth and dip angle of the subducting Australian plate, which is sub-vertical below about 75 km beneath Fiordland. After Turnbull et al. (2010), figure 73.

Sutherland et al., 2006b), and would require that there is distributed faulting or off-fault deformation that is not reflected in the visible fault trace.

De Pascale and Langridge (2012) examined a natural exposure across the Alpine Fault trace near Gaunt Creek, approximately half-way between previously existing paleoseismic records from the Haast and Toaroha Rivers (which are ∼200 km apart). Their work constrained the most recent rupture to A.D. 1710-1930, validating earlier off-fault records of a 1717 event, and confirming that the most recent event encompassed the middle part of the central section of the Alpine Fault.

Berryman et al. (2012b) investigated an ∼8,000 year record of at least 24 Alpine Fault earthquakes from river terrace sediments at Hokuri Creek, near where the fault crosses Lake McKerrow. Berryman et al. (2012b) constrained the timing of the earthquake record using radiocarbon dating of pollen and leaves that were deposited with silty sediments during ponding periods immediately following vertical displacement of existing drainage channels which crossed the fault. Based on this proxy evidence, they estimated that over the last ∼8,000 years, the mean rupture interval on the southern portion of the Alpine Fault has been ∼330 years. Based on the observed distribution of fault rupture intervals, Berryman et al. (2012b) estimated that the probability of the next rupture occurring within the next 50 years is ∼30%.

1.2.2.5 Topographic expression

Topographic relief in the central Southern Alps extends from sea level up to a maximum of over 3700 m, at Aoraki/Mount Cook. Local relief (i.e. valley floor to mountain peaks) near the Main Divide is in the range of 1,000-2,700 m, with a modal slope gradient of 33-34°between 1,000 and 2,000 m elevation above sea level(Allen et al., 2011). The Fiordland Mountains have a maximum height of 2,000-2,700 m in northern Fiordland, but typically rise to 1,400-1,800 m further south. Based on dating of raised marine terraces, subduction-related uplift in Fiordland appears to be in the order of 0.5 mm per year (Kim and Sutherland, 2004; Shuster et al., 2011), although uplift rates may be slightly higher in central and northern Fiordland (Korup, 2005b), closer to the onshore Alpine Fault.

1.2.3 Regional late-glacial history

In the northern hemisphere mid-latitudes, the Last Glacial Maximum (LGM) and subsequent transition to interglacial conditions are relatively well-constrained. Most northern hemisphere ice sheets are thought to have reached their LGM positions around 24-26

ka, with climate amelioration beginning around 20 ka in North America, and slightly later in Europe (Clark et al., 2009). Although a synchronous interhemispheric LGM has been inferred by some workers (e.g. Schaefer et al., 2006), recent work is building up evidence that the southern hemisphere LGM may have started earlier (30-35 ka, Suggate and Almond, 2005; Vandergoes et al., 2005), and likely lasted longer than the northern hemisphere LGM.

The LGM in New Zealand is now also relatively well-constrained; previous work has suggested that the Last Glacial/Interglacial Transition (LGIT) began between 16 and 18 ka (Alloway et al., 2007; Barnes, 2009; Clark et al., 2009; Suggate and Almond, 2005; Sutherland et al., 2007; Turney et al., 2006; Vandergoes et al., 2005), although recent revisions of the ^{10}Be production rate for New Zealand by Putnam et al. (2010b) put the LGIT beginning no later than 19 ka. As a long (∼1500 km), relatively narrow (∼200-300 km) and mountainous archipelago spanning ∼37°-47°S, New Zealand presents a prominent barrier to the southern mid-latitude westerlies, and provides an important and significant contribution to the post-LGM glaciation record in the southern hemisphere. An exceptional record of Quaternary glaciations is preserved in New Zealand landforms and near-surface deposits (Barrell, 2011), although recent work (Alexander et al., 2011; Reznichenko et al., 2011) implies that the moraine age record may be contaminated by non-climatic rock-avalanche-generated moraines. A list of New Zealand glaciations and interglaciations over the past ∼400,000 years (correlated to MIS stages) is included in Table 1.1.

While gaps in late Pleistocene and Holocene glacial records in New Zealand are steadily being filled in, there remains much scope to add to the current understanding of past glacial/interglacial cycles in New Zealand. A significant objective of this study is to enhance the understanding of the glacial retreat history in Fiordland, specifically at Milford Sound. ^{10}Be surface exposure dating of strategically located glacially modified surfaces has been used to further constrain the glacial retreat history in the study area. A detailed discussion of the results and implications of this work is provided in Chapter 3.

1.2.4 Geomorphology of Milford Sound

Milford Sound is a 17 km long glacial fiord with extremely steep bedrock walls extending up to two thousand meters above sea level, and dropping to nearly 300 m below sea level. The fiord occupies a deep glacially-incised valley in northern Fiordland, and is flanked on the north by Mt. Pembroke (2,015 m) and Mt. Grave (2,225 m), and on the south by the peaks of the Mitre ridge-line (up to 1,720 m). The north face of the

Table 1.1: New Zealand glaciations and interglaciations [a]

MIS Stage	Glaciation	Interglaciation	Approximate Age (ka BP)
1		Aranui	0-18 (incl. LGIT)
2	LGIT[b]		11.5-18
	Late Otira		18-30
3	Mid Otira		30-50
4	Late Otira		∼65
5		Kaihinu	
6	Waimea		
7		Karoro	
8	Waimaunga		no specific NZ age-control
9		not named	
10	Nemona		
11		not named	
12	Kawhaka		

[a] based on Suggate (1990), after Barrell (2011).
[b] Last Glacial/Interglacial Transition (LGIT), including late glacial events such as the Antarctic Cold Reversal (ACR).

iconic Mitre Peak towers some 1,680 m above the south shoreline of Milford Sound, contending for the title of highest sea cliff in the world, as it falls directly to the fiord in a horizontal distance of approximately 1 km. Numerous other peaks and ridges surround Milford Sound, including the west peak of Mitre (1,720m), Rover Peak (1,524 m), the Elephant (1,508m), Mt. Philipps (1,446 m), the Lion (1,302 m), and Cascade Peak (1,209 m), all of which form steep (>45°) sea cliffs that plunge directly into the fiord. To the east, the Milford catchment is separated from the north-south trending Hollyford Valley by the Darran Mountain range, including the ice-covered bulk of Mt. Tutoko (2,723 m), the highest peak in Fiordland. The Hollyford River follows the north-south trending Livingstone Fault trace, which forms a natural boundary between the Fiordland Mountains to the west, and the Southern Alps to the east.

1.2.4.1 Quaternary deposits

In Fiordland, extensive Quaternary deposits are limited to the Waiau and Te Anau basins and southern Fiordland, with lesser Quaternary deposits blanketing valley floors elsewhere (Turnbull et al., 2010). Relatively young, post-glacial alluvium covers most valley floors and underlies modern floodplains, with units generally consisting of locally-

derived, unconsolidated, often angular, bouldery gravel and sand. These sediments often form alluvial fans, which grade downstream onto flatter alluvial terraces. Prograding river deltas are a feature of most fiords, and larger deltas represent the transport and accumulation of significant amounts of alluvial sand and gravels, which are commonly interbedded with thin units of organic-bearing mud. Milford Sound in particular has a large catchment which captures a number of large rivers, and several large deltas are actively building out into the 290 m deep inner fiord basin.

Post-glacial landslide deposits are common in Fiordland, with the highest concentration of large events located near Milford Sound (Korup, 2005b). Landslide debris is generally very angular, and ranges from 10+ m blocks of semi-intact bedrock to chaotic bouldery and gravelly material mixed with fine-grained powder from rock fragmentation. Scree and slopewash deposits are present in steep-sided valleys, while peat swamp deposits occur in valley bottoms behind temporary barriers created by moraines, landslide deposits or alluvial fans. Shoreline deposits of sand and/or gravel occur along the outer coast of Fiordland, as well as within some fiords and inland lakes (Turnbull et al., 2010).

Tills, moraines and outwash gravels associated with late Quaternary glacial advances are generally restricted to the drainages of lakes Monowai, Hauroko and Poteriteri, in southern Fiordland (Turnbull et al., 2010, and references therein). Elsewhere, there is little subaerial Quaternary glacial sediment preserved in the landscape, however there is evidence of LGM lateral moraines preserved at Yates Point and Saint Anne Point, on either side of the entrance to Milford Sound (Sutherland et al., 2006b; Turnbull et al., 2010, this study, Chapter 3). During the LGM, sea level was ∼120 m lower than it is today, and tidewater glaciers deposited extensive systems of moraines and outwash fans on the narrow continental shelf; these depositional systems were active until the onset of climate amelioration between ∼24 ka (Shulmeister et al., 2005, this study, Chapter 3) and 17 ka BP (Barnes, 2009) initiated glacier retreat. At Milford Sound, an extensive terminal moraine system is preserved in the submarine environment offshore (see Chapter 3 for details).

1.2.4.2 Erosional landforms

Despite extensive forest cover, many rock slopes around Milford Sound still clearly bear the signatures of glacial erosion. Small-to-medium scale erosional features are common, including rock polish, glacial grooves, striations and p-forms (plastically moulded forms, such as cavettos, flutes, channels and potholes, Bennett and Glasser, 1996). Larger-scale erosional forms are also well-preserved in the valleys of the Milford Sound catchment,

including cirques and hanging valleys.

The steep walls of Milford Sound clearly reflect the influence of glacial erosion, and may yet have capacity to adjust to the removal of the buttressing forces of glacier ice. Although glacial debuttressing has often been invoked as a potential mechanism for pre-conditioning rock slopes to failure (e.g. Evans and Clague, 1988; Geertsema et al., 2006; Hewitt et al., 2008), deglaciation may not be a primary cause of alpine slope failures in temperate regions. McColl et al. (2010) examined the mechanisms behind post-glacial alpine slope failures, and found that debuttressing of valley slopes as glaciers retreat is not likely to cause rock slope instability, as long-term slope angles are primarily controlled by the rock-mass properties. McColl et al. (2010) argue that temperate glacier ice does not provide significant slope support (due to bouyancy), ductile glacier ice allows rock deformation, stress-release joints result from erosion of rock (not glacier unloading), and slopes dewater as glaciers retreat. They conclude that while glaciers can play a major part in eroding and steepening rock slopes, debuttressing in temperate regions does not further destabilize formerly glaciated slopes.

1.3 Literature review

1.3.1 Landslide classification and terminology

The general term "landslide" is used to refer to a broad range of slope failures, including those that originate in bedrock, soil/regolith, or debris (a combination of rock, soil and vegetation). A landslide may consist of extremely gradual movement (i.e. "creep"), or it may initiate suddenly and travel at great speed. Various schemes have been devised in order to further classify landslides according to their specific type of movement (e.g. fall, topple, slide, spread or flow), the source material involved and the velocity of movement. The landslide classifications of Hutchinson (1968), Varnes (1978) and Cruden and Varnes (1996) are widely used in the literature.

Further classifications of landslide types have been suggested by various authors; for example, Hungr et al. (2001) suggest a systematic approach to the classification of landslides of the flow type, resulting in ten sub-classifications, including rock avalanches. Evans and DeGraff (2002) suggest the term "massive rock slope failure", which includes rock avalanches, as well as submarine landslides originating in bedrock, syn-eruptive flank collapses on volcanoes (eg. Mt. St. Helens, Glicken, 1990), and deep-seated, slow-moving bedrock landslides.

Table 1.2: Landslide Classification

Type of mass movement[a]			**Type of Material**		
				Engineering soils	
			Bedrock	Fine	Coarse
Falls			Rock fall	Earth fall	Debris fall
Topples			Rock topple	Earth topple	Debris topple
Slides	Rotational		Rock slump	Earth slump	Debris slump
	Translational	Few Units	Rock block slide	Earth block slide	Debris block slide
		Many Units	Rock slide	Earth slide	Debris slide
Lateral Spreads			Rock spread	Earth spread	Debris spread
Flows			Rock flow	Earth flow	Debris flow
			Rock avalanche	Debris avalanche	
			Deep creep	Soil creep	
Complex/compound			Combination of two or more principal types of movement		

[a] Based on Cruden and Varnes (1996) and Hungr et al. (2001). Fine soils are defined as those with granular size fraction less than 20%.

For simplicity and clarity, the present study refers to the landslide classification based on Cruden and Varnes (1996), with additions from Hungr et al. (2001). This classification is shown in Table 1.2.

1.3.1.1 Rock avalanches

Large bedrock landslides can evolve into fast-moving rock avalanches, which are among the most dangerous and destructive natural surface processes in mountainous regions (Cruden and Varnes, 1996; Densmore et al., 1997; Qi et al., 2011). The body of literature associated with catastrophic rock slope failures is large and diverse, and occasionally contains inconsistent terminology and definitions. The terminology used in this study with reference to these type of events is clarified in the following sections.

Hungr et al. (1999) define a rock avalanche as "an extremely rapid, massive, flow-like motion of fragmented rock from large rock slide or rock fall". This definition effectively describes the majority of the landslides referred to in this study. These events are typically initiated by catastrophic failure of bedrock slopes, and are characterized by extremely high energy, due to their large size ($>10^6$ m^3) and high speed (typically 100-250 km/hr, up to 320 km/hr). This high energy can result in rapid run-out over distances of five to ten times the total fall height (Davies et al., 2010; Davies and McSaveney, 2009; Dufresne et al., 2010; Hewitt et al., 2008; Shugar and Clague, 2011. Such events have variously been referred to in the literature as "rockslide-avalanches" (Mudge, 1965), "rockfall avalanches" (Schuster and Krizek, 1978), "Sturzstroms" (Heim, 1932; Hsu, 1978; Selby, 1993) and most commonly, "rock avalanches". The terms "avalanche" and "flow" are used interchangeably in the literature to refer to the fluid-like, or streaming motion of granular material, and therefore may refer to rock, debris or snow avalanches.

The commonly used term "*rock avalanche*" is adopted within this study to describe catastrophic failure of rock slopes, although the more general terms "landslide" and"rock slope failure" are also used, depending on context. Rock avalanches, as described here, require sudden, large-scale failure of rock slopes, with a fall height of hundreds of meters. The volume of rock required to generate the streaming, or flow behaviour of a rock avalanche is large, however a precise size at which the transition to rock avalanche occurs is obviously difficult to determine. While some authors have suggested that a minimum of 10 x 10^6 m^3 of material is required to generate a rock avalanche (Hsu, 1978), others have concluded that streaming behaviour can occur with as little as 0.05 x 10^6 m^3 (Davies and McSaveney, 2002).

1.3.2 Landslides & landscape evolution in mountain regions

Many very large (10^6 - 10^7 m^3) and huge ($\geq 10^8$ m^3) landslides are concentrated in the worlds' major Cenozoic mountain belts, including the Himalayas, the Tian Shan ranges of central Asia, the coast ranges of north-western North America, the Andes and the Southern Alps of New Zealand. In each of these mountainous regions, previously unrecognised rock avalanche and rockslide events have recently been documented (e.g. Weidinger and Korup, 2009), including many that were originally attributed to other processes (e.g. glacial moraines). Misinterpretation of non-glacial depositional landforms as glacial deposits is problematic when they are used as indicators of climate change (McColl and Davies, 2011; Shulmeister et al., 2009; Winkler et al., 2010).

Hewitt et al. (2011) investigated a series of landforms that characterize the upper Indus catchment in the Karakoram Himalaya, including flights of river terraces, lacustrine deposits, sediment fans and epigenetic gorges, and found that the landforms were the result of large landslides that had dammed tributary valleys between 3 and 8 ka ago, indicating that late Quaternary landslide events play a major role in Himalaya landscape evolution. Most of these landforms had been previously assumed to be tens to hundreds of thousands of years old, and were assigned to glacial processes such as moraines and glacier-dammed lakes, or tectonic processes.

Catastrophic rock slope failures have significantly influenced the development and geomorphology of Quaternary landscapes of mountainous regions throughout the world. Improved access to mountain regions, and availability of high-resolution data (satellite images, aerial DEMs, LIDAR, etc.) have greatly enhanced our ability to recognize and interpret geomorphic features and processes in mountainous terrain (Hewitt et al., 2008).

1.3.3 Hazards associated with rock avalanches

Research increasingly shows that catastrophic rock slope failures are a major natural hazard in regions of steep or mountainous topography. The hazards associated with large rock avalanches may extend far beyond any immediate local impact, and may have secondary effects that influence the hazardscape over large geographical areas, for many years:

Table 1.3: Summary of hazards associated with rock avalanche events[a]

	Primary hazard or effect	Risk or possible impact
Immediate	streaming rock debris	injury or death, property damage
	severing of lifelines	disrupted transport, communications
	associated debris flow	may travel 100s of km, highly destructive
	displacement wave	injury or death, property damage
Short term	landslide dam	inundation, catastrophic outburst flood
	river aggradation/avulsion	flooding, property or infrastructure damage
	ongoing lifeline disruption	delayed medical care, supplies/water/food
	secondary instability	subsequent landslides
Long term	river aggradation	flooding, loss of productive land
	increased sediment supply	debris flows, debris torrents
	large-scale property damage	high economic cost of repairs
	business disruption	economic hardship, possible emigration
	public perception of risk	loss of tourism

[a] this is not an exhaustive list of hazards associated with rock avalanche events, but rather a brief summary of a range of possible impacts that could expected.

1.3.3.1 Historical rock avalanches: devastating examples from Alaska and Peru

A spectacular and well-known historical example of a coseismic subaerial rock avalanche occurred in 1958 in Lituya Bay, Alaska. A M_w8 earthquake along the Fairweather Fault caused ~30 x 10^6 m^3 of rock to fall from a height of ~900 m into the bay, generating a 150 m high displacement wave that ran up to an elevation of 524 m, and devastated forests in a wide swath around the bay (Miller, 1960). Although the region was sparsely populated, 2 people died that were on a boat in the bay. Landslide-generated tsunami and associated risks are discussed in greater detail below.

Another well-known historical example of a large, complex rock avalanche with far-reaching effects occurred on 31 May, 1970 (Plafker and Ericksen, 1978). A M_w 7.75 earthquake occurred off the coast of Peru, causing thousands of landslides, including a cataclysmic collapse of part of the 6,300 m north peak of Nevados Huascaran, the highest mountain in the Peruvian Andes. Approximately 50 - 100 x 10^6 m^3 of granite, snow and ice fell nearly 4,000 m from the source, travelling 14.5 km at an average velocity of 280 - 335 km/hr, before coming to rest in the Rio Santa valley, where the deposit temporarily dammed the Rio Santa river. The initial failure occurred in ice-covered rock near the top of the peak, which then fell onto a steep glacier, entraining

water and debris, and eventually taking on the form of a huge debris avalanche. The streaming debris devastated a wide swath, destroying farmland and settlements along the way. The flow split around and climbed over a 230 m high ridge called Cerro de Aira, branching out towards the towns of Ranrahirca and Yungay. The Yungay lobe included large impact scars; the geometry of some of these crater-like depressions suggest that some boulders were projected up to 4 km, travelling at speeds of over 450 km/hr (perhaps due to acceleration caused by topographic constrictions). The largest boulder projectile was estimated to weigh 65 tonnes. Although early reports suggested that the avalanche killed at least 24,000 people (including 18,000 in Yungay, and some 600 people on terraces on the opposite side of the Rio Santa river, Plafker and Ericksen, 1978), a recent re-examination of the event indicates that the death toll was ∼6000 (Evans et al., 2009a). The Rio Santo river soon overtopped the debris dam, generating further debris flows that travelled 180 km to the sea, causing widespread damage to transportation routes, structures and communication infrastructure .

The events of 31 May, 1970 are made even more tragic by the knowledge that a similar, only slightly less destructive event had occurred in 1962, when a large piece of hanging glacier fell from the north peak of Nevados Huascaran (Evans et al., 2009a; Plafker and Ericksen, 1978). The rock and ice avalanche travelled much the same route that the larger 1970 event would just 8 years later, with similarly devastating results. However the 1962 debris avalanche was deflected by the ridge of Cerro de Aira, and the town of Yungay was spared, but nine small towns, including Ranrahirca were destroyed, with a death toll of 4,000-5,000. Unfortunately, the lessons of 1962 were not enough to save Yungay and it's inhabitants in 1970.

Less than one year later (18 March, 1971), another devastating rock avalanche struck the Peruvian Andes. The failure occurred in limestone, with 100,000 m^3 of rock falling approximately 400 m towards the shores of Lago (lake) Yanahuin, and generating a catastrophic displacement wave that ran up to a height of 30 m, destroying the Chungar Mining camp and killing an estimated 400-600 people (Evans and DeGraff, 2002).

1.3.4 Preconditioning and the role of climate change

The fundamental factors which can precondition a rock slope to failure include lithology, and tectonic, structural and erosional history. Although precursory associated minor rockfalls, gravitational creep and fracturing are common in rock avalanche terrain, significant prior weathering and loss of rock coherency seems to actually lessen the likelihood of catastrophic rock slope failure, instead favouring more numerous, smaller rock falls and slides (Hewitt et al., 2008). Most rock avalanches occur in the rela-

tively resilient, coherent, massive bedrock walls of steep, young valleys, such as are common in tectonically active regions, deeply incised valleys, volcano flanks, glaciated mountainsides, and fiord landscapes. Glacial steepening and changing permafrost conditions are especially important mechanisms which can precondition bedrock slopes for catastrophic failure triggered by earthquakes or extreme weather (Allen et al., 2011; Augustinus, 1995; Evans and Clague, 1988; Hewitt et al., 2008; Huggel et al., 2012.

In recent decades, a number of large rock slope failures have occurred in mountain regions of the world that have experienced conditions linked to climate change (e.g. the Alps, Caucasus, British Columbia/Alaska ranges, Andes and Southern Alps). Huggel et al. (2012) identify at least 15 large slope failures that have occurred in these mountain regions since 1991, and that were likely triggered or preconditioned by extreme weather or climate change. Some authors have concluded that increasing landslide activity in mountain regions may be an important consequence of rising mean, minimum and maximum temperatures and increasingly extreme weather (e.g. Allen et al., 2011; Huggel et al., 2012), but the validity of climate change as a mechanism for the postulated increase is unproven.

In high mountain regions, snow, glacial ice and permafrost sensitive to temperature and precipitation changes may compromise slope stability via increased thawing and meltwater production, conductive heat transfer to subsurfaces, and/or ice retreat and debuttressing effects (Evans and Clague, 1994; Huggel et al., 2012). Significant changes in precipitation magnitude or frequency can affect infiltration rates and pore water pressures, increasing stresses and potentially destabilizing hillslopes. Increased fluvial incision as a result of increased precipitation or meltwater can also destabilize slopes through channel downcutting and/or slope undercutting (debuttressing effects, Augustinus, 1995; Ballantyne et al., 1997). Climate change may also alter the resilience of slope materials through physical or chemical weathering, by destabilizing permafrost regimes in regions where the fractures in jointed rock are filled with ice (Davies et al., 2001; Harris et al., 2009). As noted by Evans and Clague (1994), even modest climate change can perturb natural processes in mountain ranges, with implications for natural hazards and risk assessment.

1.3.5 Initiation: the influence of seismic shaking and slope over-steepening

Many catastrophic rock slope failures in these seismically-active regions were triggered by earthquakes (e.g. Eberhart-Phillips et al., 2003; Evans et al., 2009b; Jibson et al., 2006; Keefer, 1984; Lee et al., 2009; Liu et al., 2012; McSaveney, 1978; Qi et al., 2011; Strom and Korup, 2006; Zhao et al., 2012), although it is also common for large rock

avalanches to occur without a seismic shaking trigger (e.g. Cruden, 1976; Evans and Clague, 1988; Evans et al., 1989; Geertsema et al., 2006; Hancox et al., 2005; McSaveney, 2002; Wilson, 2009). Glacially over-steepened rock slopes can be weakened by stress-release fracturing following glacier retreat (McColl et al., 2010), as are slopes that are gradually steepened by the processes of tectonic uplift and fluvial incision. Table 1.4 shows a summary of known large catastrophic landslides in mountain ranges around the world.

Although the recent discovery of large prehistoric landslide events in many of world's major mountain ranges has improved recognition of the various hazards associated with large rock slope failures, many more events have occurred that are no longer preserved in the landscape. In the Karakoram Himalaya, well-preserved prehistoric landslide deposits are concentrated in ice-free valleys, with only 10% of deposits found in glaciated valleys (Hewitt et al., 2008). In marked contrast, the majority of historic events occured in narrow glaciated valleys, where the deposits have been quickly modified or removed by glacier or fluvial processes (eg. Hancox et al., 2003; Shugar and Clague, 2011). This clearly indicates that the record of prehistoric events is biased towards events that occurred in ice-free valleys; a warning that we should expect many more large landslide events in glacierized regions than the prehistoric record would suggest (Hewitt et al., 2008).

Table 1.4: Partial inventory of mountain regions with at least 50 known large ($>10^6$ m^3) catastrophic rock avalanches[a]

Number of known events	Mountain Region
more than 100	European Alps; Switzerland and Austria Karakoram Himalaya Caucasus Ranges; Armenia Andes: Chile and Argentina **Southern Alps; New Zealand**
50-100	Alaska/Yukon Ranges China; Qin Ling and other ranges Pamir Ranges; Tajikistan Nanga Parbat and western Himalaya Norway

[a] Modified from Hewitt et al. (2008)

1.3.5.1 Coulomb theory and friction

The mechanisms of slope failure in granular material depend upon the relationships between the forces of gravity, and internal friction. Basic granular flow theory holds that if the slope of the surface of a granular material is less than the maximum angle of stability, gravity can not overcome the the inertia provided by internal friction, therefore the slope will remain stationary. Experimental measurements show that the internal friction, and therefore Euler's "*critical angle of repose*", depends upon the material density, grain shape and surface area, porosity and the ability of the grains to interlock with each other (Collins and MeLosh, 2003).

However, experiments also show that the factors contributing to internal friction for most naturally occurring "dry" rock slope failures vary only slightly, so the angle of repose differs by no more than a few degrees. Therefore, the frictional resistance to sliding of most dry rock granular material is approximately proportional to the overburden pressure. This relationship is commonly referred to as Coulomb's law, and is shown in equation 1.1 below:

$$f = \mu\rho \tag{1.1}$$

where f is the shear strength, which is proportional to the overburden pressure ρ, and the constant μ. The constant μ is termed the "*coefficient of friction*", and generally has a range of 0.5-0.7 for granular, rock-based materials (Collins and MeLosh, 2003). Consequently, for rock slope failures, both the *critical angle of repose* and the *coefficient of friction* may be considered to be approximately independent of material density, grain shape and surface area, porosity and overburden pressure. As a result, the ratio of vertical fall height H to horizontal runout distance L should be a proxy for the coefficient of friction. Many authors therefore refer to the slope of travel, H/L, as the *Fahrboschung* after Heim (1932), or "*apparent coefficient of friction*".

The *Fahrboschung* should therefore be approximately the same for any dry rock avalanche (regardless of size or setting), and Coloumb's Law becomes:

$$f = \rho\mu_{apparent} \tag{1.2}$$

where $\mu_{apparent}$ is the slope, H/L, defined by the angle β. The length of the avalanche deposit is shown as L^d.

However, in practice, large rock avalanches commonly show an exceptional mobility that is not explained by simple Coulomb friction. The *Fahrboschung* for large dry rock and debris avalanches is typically much lower than that for smaller events. Rock avalanches and some debris avalanches involving more than $\sim 10^6$ m^3 of material show

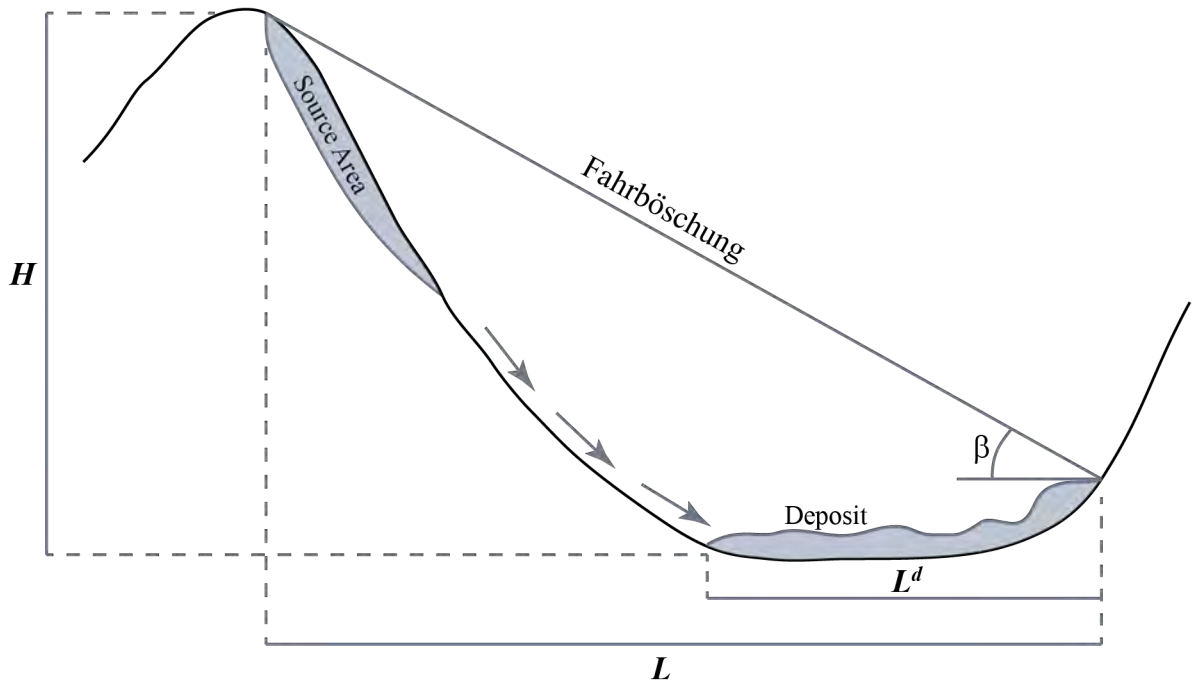

Figure 1.12: Schematic cross-sectional view of basic rock avalanche elements and geometry, in a confined valley environment.

a negative correlation between H/L and volume V (Collins and MeLosh, 2003; Davies and McSaveney, 2002). This strongly suggests that some mechanism exists in large rock avalanches which progressively lowers the effective internal friction with increasing avalanche volume. Possible explanations for this relationship are discussed in more detail in subsequent sections.

Large rock avalanches commonly demonstrate complicated behaviour, and it is only recently that modelling of the physics of the transport mechanisms involved has begun to realize the subtleties of motion. For example, 7,500 years ago, a 36 km^3 edifice collapse of Socompa volcano in Chile's Atacama desert generated a gigantic volcanic debris avalanche which involved $\sim$25 km^3 of debris, travelling up to 40 km from the source, and covering a total area of 500 km^2 (Kelfoun and Druitt, 2005; Van Wyk De Vries et al., 2001). The complex, but well-documented morphology of the Socompa deposit has now been successfully simulated using numerical models with a constant basal shear resistance of $\sim$50 kPa (Kelfoun and Druitt, 2005). The simulated deposit manages to re-create many of the features of the real deposit, including the reflection of the primary avalanche wave off of the western and northern margins of the basin, and

subsequent secondary flow that travelled 15 km at an oblique angle to the primary flow (Kelfoun et al., 2008). Intense basal comminution is evident in the Socompa deposit (Le Corvec, 2005), suggesting that overburden stresses could have been countered by internal forces from dynamic rock fragmentation (Davies and McSaveney, 2002), providing a mechanical explanation for such a low basal shear resistance (Davies et al., 2010).

1.3.6 Energy and transport

In a rock avalanche, large-scale catastrophic failure of a previously intact, generally coherent bedrock slope results in a rapidly moving stream of debris, accompanied by a very large cloud of dust. These events are characterized by rapid run-out of large volumes of pulverized rock debris, which "stream" over large areas (Collins and MeLosh, 2003; Davies and McSaveney, 2002; Davies et al., 2006; Hewitt et al., 2008). The German term "Fahrbahnböschung" was originally used by Heim (1932) to describe the slope of the path of debris travel. The abbreviated form, "Fahrböschung" is commonly used in modern literature to refer to the relationship between the vertical drop height (H) and the total run-out distance (L), as detailed in Figure 1.12.

1.3.6.1 Diagnostic features of rock avalanche deposits

Although rock avalanches tend to have relatively short transport times (generally less than 3 minutes) (Hewitt et al., 2008), the high energy associated with the rapid movement of debris ensures that the initial failed rock mass is largely converted to granule, sand and silt sized particles (Davies et al., 2007; Hewitt et al., 2008; McSaveney, 2002). The clay fraction in undisturbed rock avalanche deposits can be relatively minor (generally 1-5%) (e.g. Shugar and Clague, 2011); a fact which can help differentiate rock avalanche-derived diamictons from other diamictons (e.g. glacial tills) which may have a much larger clay fraction, but lack very fine (sub-micron) clasts.

According to Hewitt et al. (2008), rock avalanche deposits can be defined by a suite of 5 elements; three vertical and two horizontal. The vertical elements are (1) the subaerial surface and upper zone (carapace) of the deposit, which is generally dominated by large angular blocks, (2) the main body of the deposit, where coarser fragments are supported by a matrix of crushed and pulverized particles and (3), the basal zone where interactions with substrate materials can be important. The horizontal elements are (4) the main body of the deposit and (5) the distal rim.

In general, large rock avalanche and volcanic debris avalanche deposits tend to have several common morphological and structural characteristics (after Hewitt et al., 2008):

- long run-out
- high angularity of all clasts, regardless of clast size,
- increased comminution with travel distance,
- jigsaw fractured clasts,
- preservation of lithologies from source rock,
- remnant stratigraphy (lack of mixing between lithological units),
- reverse grading (presence of a coarse carapace,Dunning (2005))
- high level of compaction,
- longitudinal and transverse surface morphological features,
- hummocky topography

1.3.6.2 Emplacement forms

By nature rock avalanches have high kinetic energy, and low cohesion and tensile strength; characteristics that lend themselves to a complex and varied range of emplacement forms. The simple, or classic rock avalanche deposit is spread over a large area in sheets and/or lobes which can be up to 50 m or more thick (e.g. Socompa, however supraglacial deposits tend to be much thinner), with relatively minor surface relief. In practice, this classic form only arises where the run-out is unimpeded by major topographic features, such as ridges or valley walls that run perpendicular to the direction of movement. In contrast to the classic case, most rock avalanche events run in valleys, are some tens or hundreds of metres deep and include complex interactions with local topographic features, resulting in the debris stream being split, dispersed, concentrated, or redirected. These complex behaviours can result in three-dimensional variations in velocity and stress fields, which can in turn fundamentally alter deposit characteristics (e.g. Cruden and Varnes, 1996; Hewitt et al., 2011). In general, as a result of interactions with local topography, run-out characteristics and deposit morphology vary greatly between individual rock avalanche events (Hewitt et al., 2008).

Figure 1.13 is a USGS photo of a rock avalanche deposit on the surface of the Black Rapids Glacier (Alaska), which illustrates several elements of complex transport and emplacement behaviour. Although unimpeded by major topographic barriers, the rock avalanche travelled across a wide, glacier-filled valley, crossing a 25 m high

medial moraine before running into (and part way up) the lateral moraine at the toe of the opposite valley wall. Flowbands show clear evidence of deflection by both the medial and lateral moraines, and transverse compressional ridges on the proximal side of the medial moraine indicate the sudden deceleration of the debris due to the obstacle (Dufresne and Davies, 2009; Shugar and Clague, 2011).

Figure 1.13: Rock avalanche onto Black Rapids Glacier, Alaska, following the 2002 M_w7.9 Denali earthquake. The total fall height is approximately 800 m, with a total travel distance of approximately 5-6 km. The volume of the deposit in the foreground is approximately 8-12 x 10^6 m^3. Average debris thickness is 2-3 m (Shugar and Clague, 2011). USGS/Dennis Trabant photo, 2002.

Longitudinal ridges and/or longitudinal flowbands are characteristic of some rock avalanche deposits. The genesis of these features was investigated by Dufresne and Davies (2009), who argue that elongate ridges, flowbands and aligned hummocks are an intrinsic tendency of granular flows. Longitudinal ridges tend to be aligned radially from the source, are generally restricted to the proximal and medial parts of large ($>$ 10^6 m^3) debris sheets, and locally rise up to tens of meters above the surrounding debris surface. Longitudinal ridges are found in large rock avalanches emplaced on deformable substrates, as well as in some volcanic debris avalanches. Dufresne and Davies (2009) differentiate between longitudinal ridges, and flowbands, which may form in debris that spreads out on the surface of glaciers, as well as some volcanic debris avalanches, and pyroclastic flows.

Granular flow on glaciers results in the fragmenting rock melting ice and mixing with water at the debris-ice interface, which increases pore-water pressure and reduces friction. The mobile debris may then separate according to lithology and/or clast size, as it flows, producing distinct thin bands that may extend the length of the deposit.

At the previously mentioned Black Rapids Glacier deposit, the flowbands differentiate between alternating bands of coarse blocks and finer debris (Shugar and Clague, 2011).

Transverse compressional ridges are commonly expressed on the surface of rock avalanche debris sheets, where sudden deceleration due to topographic obstructions causes the debris sheet to buckle under compression (Dufresne and Davies, 2009; McSaveney, 1978).

1.3.6.3 Run-up and landslide dams

In some cases debris movement is partially or entirely blocked by major topographic features, preventing the full development of the rock avalanche, and resulting in deposits that are tens to hundreds of metres thick. Mobile rock avalanche debris may climb steep slopes on opposite valley walls (e.g. Evans et al., 1994, leaving a characteristic ridge of debris called a "brandung", which marks the maximum extent of moving debris (Heim, 1932). In the case of the Avalanche Lake rock avalanche in the Mackenzie Mountains of Canada's Northwest Territories, approximately 200 x 10^6 m^3 of rock fell a maximum vertical distance of 1,220 m at speeds up to 80 m/s, resulting in an unprecedented run-up of 640 m. This extraordinary mobility may have occurred in an ice-free environment (Evans et al., 1994).

Where rock avalanches travel across main valleys, their deposits can spread up to several kilometres up or down valley (eg. Dunning et al., 2006). Such deposits may be laterally extensive, and resistant to erosion due to the compaction and broad grain size distribution of the deposit (Hewitt et al., 2008). These deposits can impound mountain drainages, creating landslide dams that may catastrophically fail within months (eg. Dunning et al., 2006; Korup et al., 2006), or persist for hundreds to thousands of years (Clague and Evans, 1994; Costa and Daz, 2007). New Zealand examples include the 2,200 year old landslide-dammed Lake Waikaremoana (Davies et al., 2006; Korup, 2002), and the prehistoric Mount Wilberg rock avalanche that may have briefly dammed the Wanganui River (Chevalier et al., 2009). Another example of a long-lived landslide dammed lake in New Zealand is the ∼900 year-old Lake Ada, in Fiordland (described in this thesis, see Chapter 5).

Deposits in narrow valleys can be up to hundreds of metres thick, such as in the 1999 Mount Adams rock avalanche, in Westland, New Zealand. 10-15 x $10^6 m^3$ of fragmenting rock fell nearly 1,800 m into the Poerua valley, creating a 120 m high debris dam which temporarily impounded the Poerua River. In less than 48 hours a lake with an estimated volume of 5-7 x $10^6 m^3$ formed behind the deposit. The dam breached 6 days later, causing a dam-break flood which transported large amounts

of landslide debris downriver and inundated farmland in the valley below. Alluvium sourced from the rock avalanche deposit continues to be transported downriver during floods, causing ongoing aggradation and inundation of formerly productive farmland (Hancox et al., 2005; Korup, 2005a,c).

1.3.6.4 Blast damage

With some rock avalanches the accompanying dust-laden wind-blast can cause damage well beyond the extent of the main deposit, such as in the 1999 Mount Adams rock avalanche. In the Poerua valley a zone of flattened and de-barked trees extended up to 100 m above the main debris deposit (Hancox et al., 2005. A more recent example of blast damage occurred on 10 September 2003, in the Tsatichhu River valley in eastern Bhutan. An estimated 7-12 x 10^6 m^3 rock avalanche fell into the valley, blocking the Tsatichhu river and generating a wind blast that damaged the adjacent forested valley slopes. The resulting rock avalanche dam failed catastrophically on 10 July, 2004, releasing a flood surge with a peak discharge of 5,900 m^3/s (Dunning et al., 2006).

1.3.6.5 Influence of substrate materials

When rock avalanche debris impacts or travels across deformable sediments (e.g. fluvial/glaciofluvial or lacustrine/glaciolacustrine fills in valley bottoms) stress can be transferred from the moving debris to the deformable sediments. This interaction can result in complex deformation structures including folding and faulting in the underlying soft sediment, and may influence the morphology of the rock avalanche deposit, as ridges, folds, or lenses of bulldozed deformable material interact with the rock avalanche material. Soft sediment may become entrained within the moving rock avalanche debris, but in most cases the rock avalanche material does not mix with entrained sediment (a possible exception may occur when the entrained substrate material has a very high moisture content, which can further increase the mobility of at least part of the debris, Hewitt et al. (2008)). Consequently, rock avalanche deposits normally retain the lithology, and indeed some of the structure of the parent rock, even when they have travelled significant distances across deformable sediment of a completely different origin.

1.3.7 Mobility and potential mechanisms

Despite their high mobility and streaming behaviour, rock avalanches are generally "dry" events which occur without significant addition of moisture, and are commonly

accompanied by clouds of dust which rise over the moving debris (eg. Aa et al., 2007; Hancox et al., 2005).

Rock avalanches can travel large distances (up to tens of kilometres) that may belie the internal friction conditions of the pulverized rock mass. Some researchers argue that an intergranular medium (usually water) must be added to the debris to increase pore pressures and explain the long run-out distances that are common with rock avalanches. However, most studied rock avalanche deposits are characterized by a comminuted mass of densely compacted, fractured and pulverized diamicton, which maintains the lithology of the original bedrock, and leaves little void space to accommodate pore fluids (Hewitt et al., 2008).

Other researchers explain the unusual mobility of large rock avalanches by invoking a buoyant, low-friction layer of moist sediment (e.g. Legros, 2002), vaporized pore water (Goguel, 1978), or compressed, trapped air (Shreve, 1968) at the base of the moving debris.

Two hypothesis that do not rely on pore fluid or a low-friction basal layer to explain the high mobility of streaming pulverized rock debris are "dynamic fragmentation" (Davies and McSaveney, 2009, 2002) and "acoustic fluidization" (Collins and MeLosh, 2003).

1.3.7.1 Dynamic fragmentation

Davies and McSaveney (2009, 2002) explain the extremely low frictional resistance to motion demonstrated by large rock avalanches (as well as intact block slides and volcanic debris avalanches), by modelling the dispersive pressures caused by fragmentation within the moving rock/debris. Clasts moving within a translating mass of rock debris are subjected to direct stress from overburden, and rotational stress directed by the shear field. The combination of these stresses causes clasts to fracture explosively into smaller and smaller fragments as local stresses exceed rock strength. Davies and McSaveney (2009, 2002) postulate a transfer of energy in a shearing, fragmenting rock mass; kinetic energy (from rock mass motion) and potential energy (from overburden stress) combine to exceed rock strength, causing fragmentation, which releases more kinetic energy in the form of an isotropic dispersive stress. In effect, the resulting increased internal pressure (approximately triple the ambient pressure of previously intact grains) supports some of the pressure on the shear layer, reducing the overall frictional resistance to shear.

Davies and McSaveney (2009, 2002) further argue that dynamic fragmentation encourages dilation of the rock mass, increasing void space, and further lowering rock

strength, which helps to perpetuate the process at the front of the moving rock mass. Although fragmentation is a net energy sink (some energy is lost due to the breaking of bonds during creation of new surfaces), the stresses on a moving rock mass are redistributed by dynamic fragmentation. The net result is that motion at the rear of the mass may actually be retarded by fragmentation, while deceleration at the front of the mass is reduced, increasing run-out.

Davies and McSaveney (2009, 2002) demonstrate that exceptionally long run-outs can occur with normal friction coefficients (i.e. not requiring the presence of pore fluid), providing that high instantaneous internal pressures generated by rock fragmentation are considered. Their work suggests that dynamic fragmentation may explain the high mobility of large rock slope failures, including the Waikaremoana landslide and the Falling Mountain rock avalanche (both of New Zealand), as well as the Socompa volcanic debris avalanche in Chile.

1.3.7.2 Acoustic fluidization

Collins and Melosh (2003) argue that the extraordinary mobility of rock avalanches may be due to acoustic fluidization, where the initial collapse and high-energy transport of rock debris generates high-frequency pressure fluctuations, which counter local overburden stresses and reduce frictional resistance to shear. They conclude that acoustic fluidization can facilitate self-sustaining motion of a rock avalanche at much lower driving stresses than predicted by Coulomb's law (i.e. slopes less than the critical angle of repose), without invoking any pore fluid. However, Sornette and Sornette (2000) concluded that the phenomenon is insufficiently energetic to work in reality.

1.3.7.3 Addition of moisture

Regardless of the mechanism(s) for the mobility of dry rock avalanche debris, the addition of moisture from entrainment of snow, glacier ice, or saturated sediment can greatly increase the mobility and volume of rock avalanches, even resulting in a transition to debris flow, as at Huascaran. This transition is illustrated by the 1984 Mount Cayley rock avalanche and debris flow in British Columbia (Evans et al., 2001). The initial rock avalanche occurred in dissected pyroclastic rock on the western flank of Mount Cayley (an extinct Quaternary volcano), and travelled at speeds of 42-70 m/s, covering a horizontal distance of 3.46 km, while dropping 1.18 km (Fahrboschung 19°). The rock avalanche then transformed partially into a debris flow that travelled a further 2.6 km down the Turbid Creek valley, temporarily blocking the Squamish River. Saturation of the disintegrating rock mass by entrainment of wet sediment, snow and ice is believed

to have facilitated a transformation into debris flow due to the generation of increased pore pressure in the streaming debris (Evans et al., 2001).

1.3.8 Glacier ice

Glacier ice can have a major influence on the mobility, transport, emplacement, and longevity of rock avalanche deposits. In glacierized mountain regions, rock avalanches commonly fall onto glaciers, from where the debris is eventually transported away and incorporated into various forms of glacial transport (e.g. supraglacial, englacial or subglacial debris), and eventually deposited as subglacial till, or in lateral and/or terminal moraines. During this process a major portion of the finer fraction (i.e. silt-sized and smaller) may be entrained by meltwater and removed down valley. Rock avalanches that fall onto glaciers tend to be especially mobile, and may morph into debris flows as the streaming debris incorporates large amounts of moisture during travel across the glacier (Evans et al., 1989, 2001).

In turn, rock avalanche deposits have a major influence on glaciers, as the debris can form an insulating blanket that reduces ablation, perhaps causing an advance and terminal moraine formation (Reznichenko et al., 2011). Rock avalanche events are thought to have contributed much of the glacier debris in Alaska and the Karakoram, and are a major component of denudation and sediment flux in glaciated mountain ranges of the world (eg. Hewitt et al., 2008; Korup et al., 2010; Reznichenko et al., 2011).

1.4 Landslide hazards in New Zealand

Landslides are a frequent and potentially dangerous natural hazard in New Zealand, but have so far caused relatively few deaths because the population density is very low, especially in mountainous regions. Mass wasting processes play a major role in the high erosion rate of the Southern Alps, as tectonic uplift along the plate-boundary Alpine Fault is balanced by exhumation (Allen et al., 2011; Hovius et al., 1997; Korup, 2004). In northern Fiordland and the Southern Alps, seismicity induces stress-reducing fracturing and rock-mass dilation, gradually reducing rock strength. Landslides have accounted for over 360 deaths in New Zealand since 1840, including the 1846 Waihi disaster, where a landslide blocked a stream, causing an outburst flood three days later that overwhelmed the Maori village of Te Rapa, killing 60 people (Crozier, 2009).

1.4.1 Historical landslides and impacts

Earthquake shaking and extreme weather have triggered historic failures in New Zealand (e.g. Hancox et al., 2003; Whitehouse and Griffiths, 1983), however there are other historic events where such triggers are not implicated (e.g. see Aoraki/Mt. Cook rock avalanche below). More than twenty rock avalanches and large rockfalls are known to have occurred since 1950 in the central Southern Alps, many originating from the steep east-southeast facing hanging wall of the Main Divide Fault (Allen et al., 2011; McSaveney, 2002). The vast majority of these events initiated from within 300 vertical metres above or below glacier ice, suggesting that glacial recession and permafrost degradation plays a major role in preconditioning failure slopes in the region (Allen et al., 2011).

Hancox et al. (2002) studied 22 historical earthquakes in New Zealand, and found that the minimum Modified Mercalli (MM) shaking intensity) for earthquake-induced landsliding is about MM6, with widespread failures occurring at MM7-8. The 22 August 2003 M_w 7.2 earthquake near Thompson Sound in Fiordland produced shaking intensities up to MM9, and generated more than 400 landslides on steep slopes within 20-30 km of the rupture zone (Hancox et al., 2003). Although landslide effects were widespread, Hancox et al. (2003) found that slope failures were mostly superficial, involving regolith or shallow bedrock. The fact that the 2003 Fiordland earthquake did not result in any large-scale deep-seated bedrock failures, suggests that many of the older landslides were triggered by larger earthquakes, which may have involved rupture of the Alpine Fault (Hancox et al., 2003).

In contrast to the 2003 earthquake, the 15 July 2009 Dusky Sound earthquake

(M_w 7.8, with shaking intensities up to MM7) generated far fewer landslides, despite affecting similar steep topography in southern Fiordland. According to GNS science, the 2009 Fiordland subduction zone earthquake is the largest thrust fault event recorded in New Zealand, however it was accompanied by an unusually low level of landsliding, likely due to a relatively low frequency release of energy, which was focussed offshore (www.gns.nz, accessed 10 May, 2012).

1.4.1.1 The 14 December 1991 Aoraki/Mount Cook rock avalanche

One of the most spectacular historic landslides in New Zealand was the 14 December, 1991 collapse of Aoraki/Mount Cook, New Zealand's highest peak. Approximately 12 x 10^6 m^3 of rock fell up to 2,720 vertical metres from the summit ridge of the mountain (see Figure 1.14), travelling a total of 7.5 km in only 2 minutes (average speed 60 m/s) (McSaveney, 2002). During it's descent, the rock avalanche doubled in volume as it entrained additional rock, snow and ice on it's way over the Grand Plateau ice field, down the steep icefall of the Hochstetter Glacier, and finally onto the broad, gently-sloping Tasman Glacier, where debris rode 70m up onto the opposite moraine wall.

The Aoraki/Mount Cook rock avalanche included the former summit of High Peak, and the 700 m high rock buttress that supported it. As a result, the height of Aoraki was reduced by 10m, and the summit moved 14 m to the southwest. The event initiated without an obvious triggering mechanism (such as seismic shaking or prolonged precipitation), or prior warning, shortly after midnight on a clear moonlit night. There were no injuries or fatalities, but several climbing parties, who were preparing to climb High Peak, were at nearby Plateau Hut when the rock avalanche initiated. The moving debris came to within 300 m of Plateau Hut (McSaveney, 2002), which is situated on the Grand Plateau, below and to the northeast of High Peak.

1.4.1.2 Fatalities due to landslides in New Zealand

Historic landslides in New Zealand have often been triggered by earthquakes, such as in the 1929 Murchison earthquake, where 17 people died, most of whom were caught in landslides generated by seismic shaking. According to GNS science (www.gns.cri.nz, accessed 2 April, 2012), the total number of deaths attributed to earthquakes in New Zealand (including those cause by earthquake-related landslides) was less than 300 prior to the the 22 February 2011 Christchurch earthquake, which claimed an additional 182 lives (including at least 5 deaths due to rockfall around the Port Hills). Due to the low population density and rugged nature of New Zealand, most landslides occur in

Figure 1.14: High Peak of Aoraki/Mt. Cook following the 14 Dec. 1991 Rock Avalanche. View to the southwest, with Plateau Hut and the Grand Plateau in the foreground. Source area is clearly visible, starting from directly below the highest point. Travel distance included in photo $\tilde{3}.5$ km. The debris continued down the Hochstetter Glacier (out of frame to the left), travelling a further $\sim$4 km to the Tasman Glacier. Photo by T. Chinn, 17 Dec. 1991.

remote, sparsely populated mountain regions without causing fatalities. Nevertheless, occasionally landslide-related fatalities do occur in remote areas, such as the 2002 Ramsay Glacier rockfall which killed a tramper who was attempting to traverse around a glacial lake, beneath an unstable section of moraine wall (McSaveney et al., 2003). As future climate change affects seasonal and permanent ice and snow cover in the ranges of New Zealand, it may become increasingly important to assess and monitor the risks associated with landslide hazards in the mountains.

1.4.2 Prehistoric landslides

Although the historic record of landslides in New Zealand extends only as far back as 1840, there are also many prehistoric landslide deposits preserved in the geological record, with more than 100 events identified to date (Hewitt et al., 2008), and more discovered nearly every year (eg. Allen et al., 2011; McColl and Davies, 2011; the current study). It is likely that many more so-far undocumented prehistoric landslides have occurred in the Holocene in New Zealand. Among the documented prehistoric events preserved in New Zealand are the gigantic Green Lake Landslide (27 km^3) and the John O'groats rock avalanche (1 km^3), both in Fiordland (Hancox and Perrin, 2009, 1994), as well as numerous other large events such as the 0.5 km^3 Craigieburn rock avalanche in Canterbury (Orwin, 1998; Whitehouse and Griffiths, 1983).

1.4.2.1 Landslides in the Southern Alps and Fiordland Mountains

In the temperate Southern Alps, ice cover is relatively minor (11%, Korup, 2005b) compared to the Karakoram or ranges of north-western North America, so landslides that fall onto glaciers are not as common in New Zealand. Nevertheless, high rates of tectonic uplift and precipitation can combine to erode or otherwise modify large deposits within a few decades in the Southern Alps (Hewitt et al., 2008; Korup, 2005c; Korup and Clague, 2009; Korup et al., 2004). Consequently, the record of prehistoric landslide events in the Southern Alps is likely representative of only a fraction of the actual number of events. It is important to enhance that record, especially in light of recent research which has identified bedrock landsliding as the primary erosional process in the Southern Alps, and shown that the bulk of that erosional work is done by high-magnitude, low-frequency events (Hancox et al., 2003; Hovius et al., 1997; Korup, 2005b), which are more likely to be preserved in the landscape.

Approximately 2% of the total land area in the Southern Alps and Fiordland mountains show signs of landslide activity (Allen et al., 2011; Korup, 2005b). Most of these

events probably occured within the last 26 ka, as failures preserved within established Last Glacial Maximum (LGM) ice limits must post-date glacial recession. The first inventory-based study of preserved large (10^6 m^3) landslides in the Southern Alps identified 46 prehistoric events (Whitehouse and Griffiths, 1983), and estimated the long-term occurrence rate (i.e. over the past 1,700 years) at one event per 94 years. Whitehouse and Griffiths (1983) also determined that most large rock avalanches were likely triggered by large earthquakes.

Active dextral transpression along the onshore portion of the Alpine Fault causes rapid uplift of up to 10 mm per year in the Southern Alps (Claypool et al., 2002; Norris and Turnbull, 1993). McSaveney (2002) estimated an average rate of 1 large landslide event per 20 to 30 years for the steep east-southeast facing hanging wall of the Main Divide Fault zone of the Southern Alps; a 60 km long zone of nested oblique reverse faults and connecting strike-slip faults which is a backthrust of the plate-boundary Alpine Fault. Along the Main Divide, the upthrown blocks of the hanging wall are pervasively fractured, as uplift and erosion facilitate stress-relief fracturing and dilation of the generally low-grade metamorphosed greywacke bedrock (Cox and Findlay, 1995).

In contrast to the Southern Alps, the mountains of northern Fiordland are subjected to relatively low rates of uplift ($<$ 1mm per year, Claypool et al., 2002; Kim and Sutherland, 2004), as they lie adjacent to the offshore section of the Alpine Fault, where plate motion is predominantly strike-slip (Barnes, 2009). Despite the relatively low uplift in Fiordland compared to the Southern Alps, the Fiordland Mountains are extremely rugged, hosting local relief of up to 2,000 m, with some of the tallest and steepest bedrock slopes on earth. The lithology of the Fiordland Mountains tends to be resilient to erosion, preserving spectacular examples of relict LGM geomorphology in the form of steep-sided U-shaped valleys, hanging valleys, and ice-sculpted bedrock. With improved availability of high quality remote sensing data and digital mapping, additional landslide inventories have been developed for the Southern Alps and the Fiordland mountains, with the aim of informing landslide-related sediment flux and earthquake hazard studies (e.g. Allen et al., 2011; Hancox and Perrin, 2009; Hancox et al., 2003; Hovius et al., 1997; Korup, 2005b, the current study). A summary of these inventories is included in Table 1.5.

Table 1.5: Studies of landslide distribution in the Southern Alps and Fiordland

Author	Location	Number of landslides	Study area
Whitehouse & Griffiths (1983)	Central Southern Alps	46	10,000 km^2
Hovius et al. (1997)[a]	Western Southern Alps	4984	4,970 km^2
Hancox et al. (2003)[b]	Southern Fiordland	422	3000 km^2
Korup (2005b)	Western Southern Alps and Fiordland	778	18,670 km^2
Hancox & Perrin (2009)[c]	Fiordland	39	20,000 km^2
Allen et al. (2011)	Central Southern Alps	509	21,300 km^2
this study[d]	Milford Sound catchment, Fiordland	37	500 km^2

[a] 1940-1955 only; includes many small landslides.
[b] inventory of landslides caused by the 2003 M_w 7.2 Fiordland earthquake, includes many small and ephemeral landslide scars.
[c] inventory of very large ($> 10^7$ m^3) postglacial landslides in Fiordland.
[d] includes ∼31 landslides $> 10^6$ m^3 - see Chapter 4 for details.

The Fiordland region contains at least 70 very large ($> 10^6$ m^3) known prehistoric landslides (see Figure 1.15) of post-glacial age (Hancox and Perrin, 2009, the current study), including one of the largest landslides on earth, the Green Lake rockslide (27 x 10^9 m^3), near Lake Monowai. The spatial and temporal distribution of landslides in the Milford Sound area, and implications for associated hazards and risk management are discussed in detail in Chapter 4.

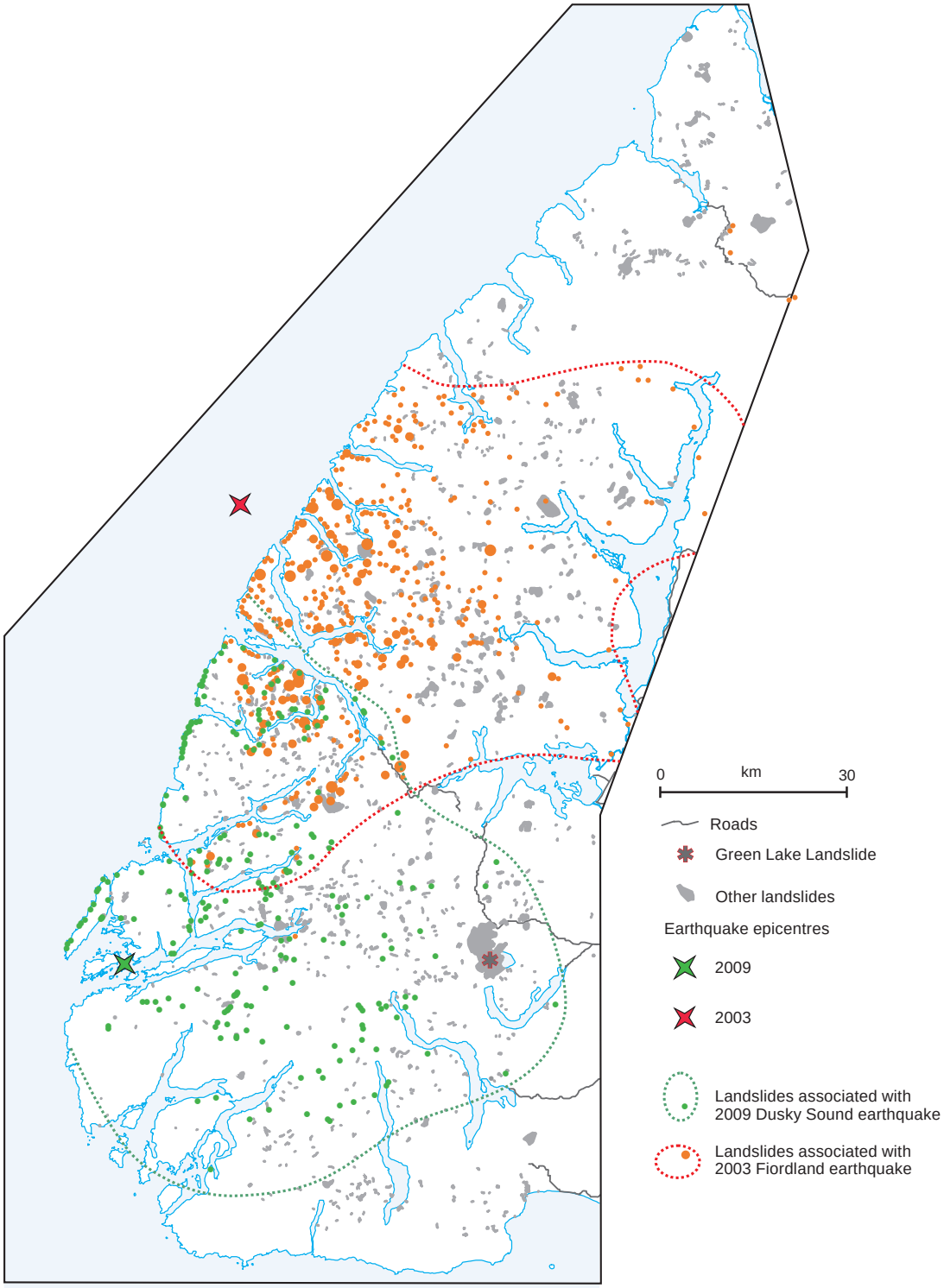

Figure 1.15: Large landslides in Fiordland, shaded in grey, ranging from complex rock slides to rock falls and rock avalanches. The Green Lake Landslide (marked) is one of the largest landslides on earth (27 x 10^9 m^3). The many landslides (mostly smaller debris flows and debris avalanches) that were triggered by the 2003 Fiordland and 2009 Dusky Sound earthquakes are shown in red and green, respectively, together with the earthquake epicentres. After Turnbull et al. (2010), figure 61 and Hancox and Perrin (2009).

1.5 Landslide-generated tsunami

The fiord landscapes of Norway, British Columbia/Alaska, Chile, and New Zealand contain some of the most extreme topography on Earth. In these mountainous regions, tectonic and glacial processes have sculpted landscapes that are heavily dissected by glacial valleys, including those that host glacial lakes, fiords, and landslide-dammed lakes. The interaction of large landslides with fiords and lakes creates another, secondary but potentially very dangerous hazard.

Subaerial or submarine landslides that interact with a body of water can generate large displacement waves, sometimes with devastating consequences, as with the 1971 Chungar, Peru disaster. Another tragic example occurred 0n 9 October, 1963, when filling of the Vajont reservoir in Italy triggered a large subaerial landslide that generated displacement waves that ran up to 235 m, overtopping the concrete arc dam and destroying the village of Longarone, killing over 1900 people (Panizzo et al., 2005a).

Tsunami generated by subaerial landslides are the most destructive natural hazard in Norway, where at least 170 people were killed by large displacement waves in the twentieth century alone. The most recent Norwegian disasters, and their relevance to Fiordland, are discussed in Chapter 4. Submarine failures can also generate displacement waves with devastating consequences; on 17 July, 1998, a M_w 7 earthquake offshore of Sandaun Province, Papua New Guinea triggered a submarine landslide that generated displacement waves with a maximum run-up of 15 m. The waves affected approximately 30 km of coastline, and killed over 2,100 people. A combination of eyewitness accounts, numerical modelling, submarine surveys and hydrophone records suggest that the displacement waves were generated by a submarine landslide that occurred approximately 10 minutes after the main earthquake shock, approximately 25-35 km offshore, and with a volume of 4-8 x 10^6 m^3 (Imamura and Hashi, 2003; Okal et al., 2002).

1.5.1 Tsunami hazards in Fiordland

Of the more than 40 tsunamis that have been recorded in New Zealand over the last 165 years, 14 were from distant earthquake sources, 18 were from regional or local earthquake sources, and 4 were the result of landslides generated by local earthquakes. Only one was from a spontaneous landslide not associated with an earthquake, and 8 were from unknown sources, likely including submarine landslides. At least three historic tsunami have occurred with run-up heights of more than 10 m, two of which were generated by strong local earthquakes in the Wairarapa and Gisborne (1855 and

1947 respectively). A large South American earthquake in 1868 caused a tsunami with run-up of 1-4 m around the main New Zealand coast, and up to 10 m in the Chatham Islands (based on GNS unpublished historical tsunami database, from Berryman, 2005).

Historical tsunami records for Fiordland are rare, at least partially due to the remote location and relatively short period of record keeping (<150 years) in the region, which is too short to reflect the range of tsunami events that could be expected (Berryman, 2005). However, there are some indications of recent tsunami activity related to landslides. The Southland Times reported on May 23, 1987, that a massive slip the previous day at Deep Cove (in Doubtful Sound) created a 2-3 m high wall of water that lifted a 17 m boat onto a wharf, destroying it. In addition, there is reference in Brodie (1964) to a surface disturbance in Milford Sound (possibly a displacement wave) generated by a submarine collapse of the Cleddau delta. Instability of deltaic and nearshore sediments is believed to be a major contributor to the high risk of tsunami along the Pacific Coast of North America (Bornhold et al., 2001), and has been identified as a potential risk for locally generated tsunami along the Kaikoura coast margin on the east of the South Island (Fauth et al., 2005; Walters et al., 2006).

There is also sparse evidence for historical tsunami in the deep fiord lakes of the region. The 1988 Fiordland earthquake (M_w 6.1) caused the collapse of some lake deltas, as well as a subaerial landslide into the North Fiord of Lake Te Anau, which generated a 1 m high displacement wave (Turnbull and Beanland, 1988). Brodie and Irwin (1970) noted eye-witness accounts from the summer of 1937-38, when earthquake movement at Lake Wakatipu caused surface waters off the Rees-Dart delta to become "violently turbulent and discoloured by sediment", possibly due to submarine delta slumping.

The 2003 Fiordland earthquake generated more than 400 landslides, with estimated volumes up to 700,000 m^3. A wedge-shaped failure in gneiss bedrock, with an estimated volume of 200,000 m^3 collapsed into Gold Arm of Charles Sound (see Figure 1.16), generating a displacement wave that travelled ∼800 m across the fiord, stripping vegetation up to 5 m above the high tide limit, and damaging a helipad and wharf (Hancox et al., 2003). Due to the remote, unpopulated nature of the area affected by the landslide and associated waves, there was no associated loss of life; the situation would likely have been much more dangerous if it had occurred at Milford Sound during peak tourist season.

It is likely that a significantly larger magnitude earthquake (> M_w 7.2) occurred in Fiordland some time around 1826. Descriptive accounts by sealers who were at Dusky Sound at the time, indicate that a much greater area of Fiordland was subjected to

Figure 1.16: Rockfall, Gold Arm, Charles Sound, and resulting displacement wave, following the 22 August 2003 M_w7.2 Fiordland Earthquake. After Hancox et al. (2003).

landsliding than in 2003, and that the 1826 earthquake was accompanied by significant uplift and deformation. In particular, the uplift suggests that slippage along the Fiordland subduction interface was the most likely source of the earthquake (Downes et al., 2005). It is possible that the 1826 Fiordland earthquake corresponds with Maori tradition of a large tsunami wave in Southland (thought to have occurred in the 1820s), that killed a large group of people. However, it is perhaps more likely that the two events are unrelated, as the tsunami was more likely to have been generated by a Puysegur subduction zone earthquake than a Fiordland subduction zone or Alpine Fault earthquake, based on fault-rupture tsunami propagation modelling (Downes et al., 2005).

There are numerous examples of prehistoric tsunami preserved in the geological record in New Zealand, with evidence of wave run-up to at least 32 m above mean sea level. Most of these paleotsunami deposits are probably from earthquake or landslide events with a local source, although the New Zealand tsunami record is far from complete (Walters and Goff, 2003).

1.5.2 Previous Milford Sound tsunami hazard assessments

There are three known documents which specifically address the hazard from tsunami waves (either seismogenic or landslide-generated) at the head of Milford Sound:

1) Downes et al. (2005) used a 2-D numerical propagation model to simulate waves

along the Fiordland coast from a range of local seismogenic tsunami sources and scenarios. Their results indicate potential wave heights at the Cleddau delta of 0.5 m and 1.0 m, from Alpine Fault and Fiordland Subduction Zone earthquakes respectively. The Downes et al. (2005) numerical model simulated wave amplitude, but approximated all fiord shorelines as vertical walls, and therefore did not attempt to simulate wave runup onto the relatively gently-sloping Cleddau Delta at the head of Milford Sound. The Downes et al. (2005) model was designed to cover the entire Fiordland coast, so relatively small high resolution bathymetric features (i.e. like the Cleddau delta) were not incorporated.

2) In a natural hazards assessment for the Cleddau Village (commissioned by the Department of Conservation), Grindley et al. (2007) reviewed general wave height predictions for the open Fiordland coast from Berryman (2005) and Downes et al. (2005), and calculated wave runup heights at the Cleddau Delta based on solitary wave runup theory (Li and Raichlen, 2001). Grindley et al. (2007) estimated a maximum wave runup height of 5.7 m at the Milford Village, based on the large Fiordland Subduction Zone earthquake scenario of Downes et al. (2005) (i.e. a 1 m wave at the Cleddau delta), but did not calculate runup based on the open-coast wave height of Berryman (2005) (i.e. 4-6 m, once every 500 years). Grindley et al. (2007) did not consider subaerial or submarine landslides as a potential source for local tsunami at Milford Sound. They did however state that "there is a large run out distance between where rockfall occurs, and where the site is located" as a primary reason for concluding that it was unlikely that the Milford Village will be affected by landslide hazards in the future. Grindley et al. (2007) did not provide any clarification or quantification of their assumption of large runout distance.

3) A specific tsunami hazard review (Mabin and Tipler, 2008) for the proposed Milford Village was also commissioned by DOC. Mabin and Tipler (2008) cited the modelled open-coast wave heights of Berryman (2005) in their review, and simulated a solitary wave running towards the Cleddau delta from near St. Anne Point, using a two-dimensional numerical wave propagation model that assumed a perfectly straight run through Milford Sound, without any wave reflection or refraction effects (although the fiord bottom profile was incorporated in the model). Their model results showed that small waves ($\sim$1 m high) would be attenuated by around 10% by the time that they reached the Cleddau Delta, while larger waves ($\sim$5 m high) were amplified, reaching 10 m by the time they reached the head of the fiord. However, Mabin and Tipler (2008) did not use the Berryman (2005) wave heights in their runup analysis, based on an assertion that offshore-generated tsunami waves would be refracted by the geometry of

Milford Sound; instead they adopted the fiord-head wave height of Downes et al. (2005) for their runup calculations. Mabin and Tipler (2008) calculated inundation of the Cleddau delta by assuming that wave runup would be roughly equivalent to maximum wave height at the shore (i.e. no higher than 1m), citing results of inundation modelling by Berryman (2005) for major coastal communities around New Zealand. Mabin and Tipler (2008) did not provide any justification for extending those results to a fiord-head environment, and did not note that their adopted wave height of Downes et al. (2005) was modelled based on the assumption that all shorelines around Milford Sound were vertical (i.e. complete absence of the Cleddau delta or foreslope).

Mabin and Tipler (2008) also considered landslide-generated impulse waves in their review, noting historical disasters from Lituya Bay and the Vajont reservoir in Italy. The Tutoko, Adelaide and Donne rock avalanche deposits were acknowledged by Mabin and Tipler (2008), who concluded that Darran Complex rocks were prone to failure, while the predominantly gneiss bedrock slopes surrounding Milford Sound were not likely to produce large landslides. Mabin and Tipler (2008) concluded that large landslides were unlikely to occur near Milford Sound in the future, although they did not provide any geological or geotechnical justification for why bedrock slopes in the Darrans would be more likely to fail than geologically and geomorphically similar, but possibly more tectonically active (given proximity to the Alpine Fault) slopes surrounding Milford Sound. Mabin and Tipler (2008) also investigated bathymetric maps of Milford Sound, and noted that there are anomalous topographic irregularities on the bottom of the fiord, and speculated that they could be deposits of landslide or glacial origin, or bedrock irregularities. From their analysis, Mabin and Tipler (2008) concluded that Milford Sound is "less likely to be subject to rock avalanche events than other parts of Fiordland". However, Mabin and Tipler (2008) did consider landslides into Milford Sound as a potential source of impulse waves, and also concluded that future, more detailed investigation of the potential hazard was desirable.

It is noted that the bulk of literature considering wave runup in fiord environments, including observational data, physical laboratory experiments (e.g. scaled 3-D physical models of fiord basins), and analytical and numerical methods, supports maximum wave runup heights that are 2-5 times wave amplitudes (e.g. Braathen et al., 2004; Di Risio and Sammarco, 2008; Fritz et al., 2009, 2004; Harbitz et al., 2006; Jorstad, 1968; Lynett and Liu, 2005; Miller, 1960; Pedersen and Gjevik, 1983; Slingerland and Voight, 1979).

1.6 Research motivation and objectives

This project was initiated by my academic supervisor, Dr. Timothy Davies, who questioned the potential hazards associated with landslides and landslide-generated tsunami in the extreme landscape of Fiordland, New Zealand. An initial review of the available landslide and tsunami literature from Fiordland, combined with a perusal of recent work related to landslide-generated tsunami in the fiords and lakes of western Norway suggested that a more detailed investigation of the risks related to landslide-generated tsunami in the steep fiords and glacially-carved lakes of New Zealand had substantial merit. The potential project was discussed with Dr. Philip Barnes of NIWA, who confirmed that high resolution sonar and seismic reflection data were available for Milford Sound. Dr. Barnes agreed to act as co-supervisor for the project, and a Ph.D project was born.

1.6.1 Project Scope: Milford Sound

The project focusses on Milford Sound and its catchment area. Milford Sound is the northern-most fiord of Fiordland National Park, a region of spectacular natural beauty and extreme topography in South Western New Zealand. As the most accessible, and arguably most spectacular of New Zealand's fiords, Milford Sound is one of the world's premier natural attractions, hosting nearly 600,000 visitors annually, of whom 450,000 cruise on the fiord by boat (D.O.C., 2006).

1.6.2 Research objectives

The research program was designed around five primary objectives:

1. improve the understanding of the post-LGM evolution of Milford Sound, including implications for paleoclimate reconstruction
2. improve the understanding of contemporary mass wasting processes and related hazards at Milford Sound
3. establish the distribution of post-glacial landslide deposits at Milford Sound, including both submarine and subaerial deposits
4. establish a first-order quantification of the risk of landslide-generated tsunami at Milford Sound
5. provide recommendations to help facilitate the management and/or mitigation of risks associated with landslide-generated tsunami at Milford Sound

1.6.3 Research Questions and Hypothesis

The primary research hypothesis was simply:

there are geomorphic and sedimentary records of large, potentially tsunami-generating Holocene landslides preserved at Milford Sound

In order to test this hypothesis, the research program was designed to address the following questions:

- what was the timing of glacial retreat at Milford Sound?
- Is there geomorphic evidence for incipient and past slope failure on the steep rock slopes of Milford Sound and nearby valleys?
- Is there a geomorphic record of Holocene landslide activity preserved in the submarine and subaerial geomorphology of the study area?
- What is the spatial distribution of submarine and subaerial landslide deposits within the study area?
- Can source areas for these deposits be identified?
- Is there evidence that landslides were co-seismic?
- Could any landslides have generated displacement waves large enough to threaten life and/or property?
- What is a reasonable estimate for the frequency of landslide-generated tsunami in the Holocene?
- what is a reasonable estimate of the risk of death due to landslide-generated tsunami at Milford Sound? Is that risk generally acceptable to society? Is the risk to individuals (visitors or workers) within generally acceptable limits?
- Given the importance of Milford Sound as an international tourist destination, what options are there to manage or mitigate future risk?

Specific methodologies and materials used to accomplish research objectives and answer the above questions are described in detail in the relevant chapters.

Chapter 2

Fiord evolution in New Zealand: temperate southern hemisphere fiords on a transform plate boundary

2.1 Introduction and background

Submarine sediments in the fiords and narrow continental shelf of Fiordland may contain some of the most complete southern hemisphere mid-latitude late-glacial paleoclimate records (Barnes and Pickrill, unpublished). Some records have been documented, (e.g. Barnes, 2009; Knudson et al., 2011; Pickrill et al., 1992), but there remains a wealth of yet-unexplored paleoclimate information to be investigated in Fiordland, perhaps due at least in part to the inherent logistical difficulties and economic costs associated with collecting material samples from remote submarine environments. However, these records are potentially globally important, given New Zealand's strategic position as a sensitive monitor of southern hemisphere climate change (e.g. Barrell, 2011; McGlone et al., 1993).

The present chapter is predominantly a background and literature review chapter which considers the unique geographic and tectonic setting of Fiordland, and synthesizes available data (both published and unpublished) to present a generalised fiord evolution model for New Zealand; this model was initially proposed by Barnes and Pickrill (2003), who examined the range of fiord architecture in Fiordland, and considered geomorphic and sedimentary evidence available at the time. Chapter 3 considers

the specific evolution of Milford Sound, and implications for future geomorphic processes and associated natural hazards.

2.1.1 Previously unpublished data and interpretations

The generalised fiord evolution model presented in the current chapter is based on earlier work undertaken by Barnes and Pickrill (unpublished), who examined the range of fiord architecture in Fiordland, based on geophysical, geomorphic and sedimentary evidence from a range of data collected by NIWA, including:

- 3.5 kHz and Uniboom seismic reflection profiles of fiord thalwegs and cross sections, collecting during NIWA research cruises in 1977, 1981 and 1983.
- sidescan sonar surveys and bottom sampling (piston coring, grab samples, underwater camera) during those NIWA cruises.
- multibeam swath bathymetry and backscatter sonar imagery collected during the NZ-France GeodyNZ-Sud cruise, 1993.
- single-beam sounding data from inner coastal zones and fiords, collected by the Royal NZ Navy.
- multi-channel seismic reflection data collected by NIWA in 1997.
- seismic reflection profiles collected by Mobil Oil Company (1972), and LINZ (2000).
- sediment cores and grab samples were analysed for texture, calcium carbonate and organic carbon concentrations.

2.1.2 The last ice age

Much of the established climatostratigraphy for the last glacial cycle is heavily reliant on records from northern hemisphere mid-latitudes, which generally indicate that growth of ice sheets to their maximum (LGM) positions occurred from 33-26.5 ka ago. Most northern hemisphere ice sheets were in their LGM positions between about 26 ka and 19-20 ka (Clark et al., 2009, and references therein). Climate amelioration began around 20 ka in North America, and slightly later in Europe (Alloway et al., 2007; Clark et al., 2009). Strong fluctuations accompanied overall climate amelioration from ∼20-13 ka, followed by strong cooling which returned much of the North Atlantic region to near-LGM conditions from ∼13-11.5 ka (the Younger Dryas (YD) chronozone, Alley, 2000).

The Younger Dryas cooling period was followed by rapid warming and glacial retreat in the northern hemisphere, with near present-day climatic conditions reached by ∼10 ka.

2.1.2.1 Inter-hemispheric climate synchronicity

The relative lack of published southern hemisphere paleoclimate records has left the important issue of climate synchronicity between the Northern and Southern Hemispheres open to debate. Schaefer et al. (2006) concluded that large-scale retreat of mid-latitude LGM glaciers began around 17 ka in both hemispheres, based on a wide-ranging suite of mid-latitude ^{10}Be moraine chronologies, including records from the Lake Pukaki moraine complex in New Zealand. The onset of deglaciation of the West Antarctic Ice Sheet (WAIS), and resulting meltwater pulse 1A (MWP-1A) between ∼15 and 14 ka, may have been partially responsible for a 20 m eustatic sea level rise (from ∼-100 m to ∼-80 m, relative to sea level today) (Clark et al., 2009; Gomez et al., 2010; Mitrovica et al., 2009), but not all researchers agree with the precise timing and extent of sea-level rise (eg. Bamber et al., 2009; Gomez et al., 2010).

In addition to its impact on eustatic sea level, MWP-1A is an extremely important analogue for a potential future collapse of the WAIS. MWP-1A may have resulted in a substantial cooling of the Southern Ocean, causing expansion of Antarctic sea ice and intensification of the Southern Hemisphere Westerly (SWW) winds (Menviel et al., 2010); factors which may help to explain southern hemisphere cooling during the Antarctic Cold Reversal (ACR), from ∼14.5-12.5 ka, (Blunier et al., 1997). Somewhat paradoxically, deglaciation of the WAIS may have caused climate amelioration in the northern hemisphere prior to the Younger Dryas cool period (∼13-11.5 ka), by perturbing global ocean circulation driven by temperature and salinity gradients. A stronger halocline around Antarctica (caused by an increased freshwater input from meltwater and increased precipitation) may have led to suppression of Antarctic Bottom Water (AABW) formation, slowing the transfer of cold, dense bottom water from the Southern Ocean to the northern hemisphere (Menviel et al., 2010; Mitrovica et al., 2009).

While climate models incorporating ice cover, sea level and ocean circulation continue to improve, the climatic influences that each hemisphere may have on the other are not yet fully understood, complicating attempts to understand inter-hemispheric climate change (Alloway et al., 2007). For example, some workers have cited southern hemisphere records of supposed YD cooling, arguing that the influence of global atmospheric circulation has over-riden oceanic circulation, therefore climatic cooling in the

YD may have been a world-wide phenomenon, rather than an anti-phase northern hemisphere cooling event driven by changes in oceanic thermohaline gradients (e.g. Denton and Hendy, 1994; Schaefer et al., 2006). Some authors have argued for an extraterrestrial impact-driven cooling period around ∼12.9 ka, which contributed to extinction of the Pleistocene megafauna (e.g. Bunch et al., 2012; Firestone et al., 2007); however contrary evidence has led others to reject the hypothesis (e.g. Pinter et al., 2011).

2.1.2.2 Southern Hemisphere LGM

Although a synchronous inter-hemispheric LGM has been inferred by some researchers (e.g. Schaefer et al., 2006), many mid-latitude southern hemisphere records suggest that LGM positions may have been reached by southern hemisphere ice sheets by ∼35-30 ka, with LGM conditions lasting longer than in the northern hemisphere (Suggate and Almond, 2005; Vandergoes et al., 2005). Recent evidence from terrestrial speleothem, pollen and glacial geomorphic records from Chile and New Zealand, as well as Sea Surface Temperature (SST) reconstructions based on isotope chemistry, carbonate and pollen records from Southern Ocean marine records (Vandergoes et al., 2005 and references therein) suggest that the Last Glacial/Interglacial Transition (LGIT) began between 18 and 17 ka (Alloway et al., 2007; Barnes, 2009; Clark et al., 2009; Suggate and Almond, 2005; Sutherland et al., 2007; Turney et al., 2006; Vandergoes et al., 2005), postdating the northern hemisphere LGIT by about two thousand years.

Most paleoclimate reconstructions based on Antarctic ice cores indicate a period of marked cooling from ∼14.5-12.5 ka BP; the ACR, which interrupted an otherwise constant warming trend during deglaciation in the southern hemisphere, and preceded the northern hemisphere Younger Dryas (YD) cool period by nearly 2 ka (Blunier et al., 1997). Southern hemisphere mid-latitude paleoclimate reconstructions from Australian and Chilean SSTs also suggest a period of marked cooling between ∼14.5 and 13 ka, coinciding with the ACR (see Figure 2.1). However, some southern hemisphere mid-latitude records suggest a late-glacial cooling period that lagged the ACR, or even coincided with the YD (e.g. Alloway et al., 2007). Southern hemisphere cooling during the YD has been interpreted from the Waiho Loop moraine (Denton and Hendy, 1994), however any re-advance of the Franz Josef glacier to the Waiho Loop during the YD may be related to decreased ablation due to a landslide which partially covered the glacier (Alexander et al., 2011; Tovar et al., 2008). The paleoclimatic significance of the Waiho Loop is controversial, and is discussed in greater detail below.

To date, inconsistent timing of late-glacial cooling inferred from mid-latitude southern hemisphere records has left the question of inter-hemispheric climate synchronicity

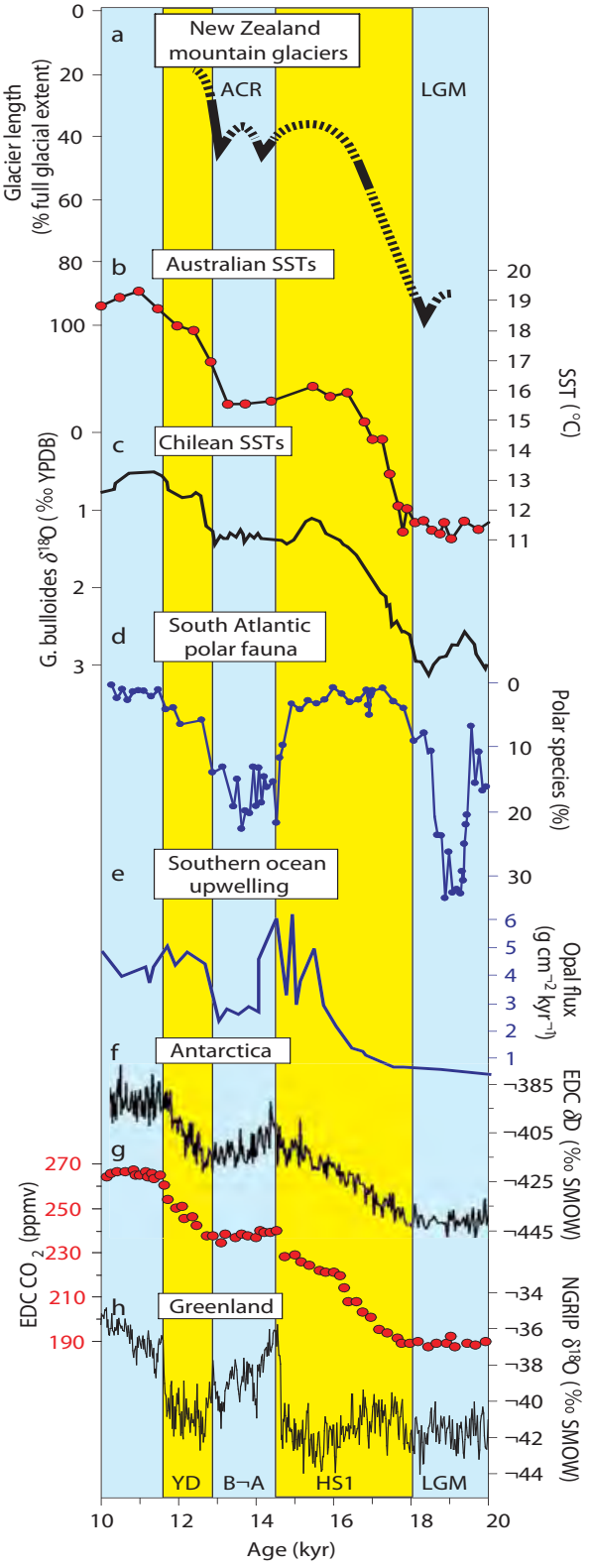

Figure 2.1: Southern hemisphere mid-latitude deglacial records, Putnam et al. (2010a)

open to debate. One thing is certain; further high-resolution paleoclimate records from mid-latitude sites in the southern hemisphere are essential to improving the understanding of inter-hemispheric climate change and response (Alloway et al., 2007; Vandergoes et al., 2005).

2.1.3 New Zealand's climate over the past 30,0000 years

Significant progress has been made by paleoclimate researchers towards reconstructing New Zealand's climate, especially for the period spanning the past 30 ka. Many New Zealand climate records (particularly those from the North Island) have benefited from tephra marker bed correlation based on an established chronology of over 20 tephras from eruptions spanning the last 30 ka (Alloway et al., 2007). To date, New Zealand climate proxy records generally agree that LGM conditions were reached around ∼30-28 ka, persisting until the beginning of rapid climate amelioration (the LGIT), around ∼20-16 ka, and that near Holocene climate conditions were reached by ∼15-11.6 ka (e.g. Alloway et al., 2007; Barnes, 2009; Shulmeister et al., 2010; Suggate and Almond, 2005; Sutherland et al., 2007; Turney et al., 2006; Vandergoes et al., 2005).

2.1.3.1 The LGM/LGIT in New Zealand

Despite broad, millennium-scale agreement on the boundaries of the LGM, LGIT and Holocene, millennium-century scale variability of these three most-recent climatic phases have not yet been fully constrained in New Zealand, particularly with respect to a late-glacial climate reversal (ACR or otherwise). Currently, available records highlight the complexity of post-LGM climate in New Zealand, but can not correlate specific regional climate trends. In fact, some data sets exclude any significant late-glacial climate reversal, suggesting that complex interactions between the strong westerly atmospheric circulation and the ENSO are a more likely source of climate variation in New Zealand than inter-hemispheric climate forcing (e.g. Shulmeister et al., 2010).

Various records from different locations and environments have lead to different interpretations of the LGIT in New Zealand; for example, some lowland terrestrial paleoclimate proxy records (including isotope chemistry, pollen, and organic carbon from three North Island wetlands and isotope chemistry from speleothems from the northwest South Island) have been interpreted as evidence for climatic cooling from ∼13.5-11.6 ka, a period which encompasses both the later half of the ACR and the Younger Dryas (Alloway et al., 2007). However, some similar climate proxy records from the South Island (e.g. Boundary Stream Tarn, Vandergoes et al., 2008) indicate a

climate reversal that coincides with the ACR. Other records exclude specific evidence for any late-glacial climate reversal (e.g. Shulmeister et al., 2010).

2.1.3.2 New Zealand glacial records

New Zealand's mountain ranges rise steeply from the sea, and generate significant orographic precipitation, particularly on the windward (west) side of the axial ranges of the South Island, where modern mountain glaciers are found near sea level at around 44°south latitude. An exceptional record of Quaternary glaciations is preserved in New Zealand landforms and near-surface deposits (Barrell, 2011), and the LGM-extent of glaciers is relatively well-constrained. Barrell (2011) recently updated the work of Suggate (1990), which delineated the LGM-extent of glaciers in the South Island based on a compilation of publications and interpretation of topographic maps. The Barrell (2011) update included revisions based on updated 1:250,000 geological maps (the QMAP project, completed by GNS science between 1993 and present) and additional research publications, and added North Island LGM ice limits.

Recently, Golledge et al. (2012) used a Parallel Ice Sheet Model (PISM; www.pism-docs.org) to simulate the LGM in the Southern Alps, and found that at least 6-6.5 °C of cooling, combined with a precipitation regime that was 25% drier than today, are required to reproduce the LGM ice-extent inferred from geological evidence and geomorphic mapping by Barrell (2011) (see Figure 3.34). However, their model did not reproduce glaciations in the Rakaia or Waimakariri valleys with precipitation set at -25%.

Traditionally, the strongest case for YD cooling in the southern hemisphere (and thus for synchronicity of inter-hemispheric climate change), has come from the Waiho Loop moraine on the west coast of the South Island. Twenty-five pieces of wood buried beneath glacial sediments at Canavan's Knob, some 1.6 km behind the moraine, have been ^{14}C dated to 13.4-12.8 Cal. ka (Denton and Hendy, 1994), suggesting that the Waiho loop moraine formed soon after this, during the YD chronozone. However, a YD origin for the Waiho loop has been a contentious issue, and a number of alternative chronologies have been argued:

- the dated wood may have been buried by a brief local glacial re-advance past Canavan's Knob during overall gradual glacial retreat from the Waiho loop following the ACR (e.g. Tovar et al., 2008).

- the Denton and Hendy (1994) wood samples may have originated from weathered, older wood that may have been contaminated with younger carbon; Turney et al.

2. FIORD EVOLUTION IN NEW ZEALAND: TEMPERATE SOUTHERN HEMISPHERE FIORDS ON A TRANSFORM PLATE BOUNDARY

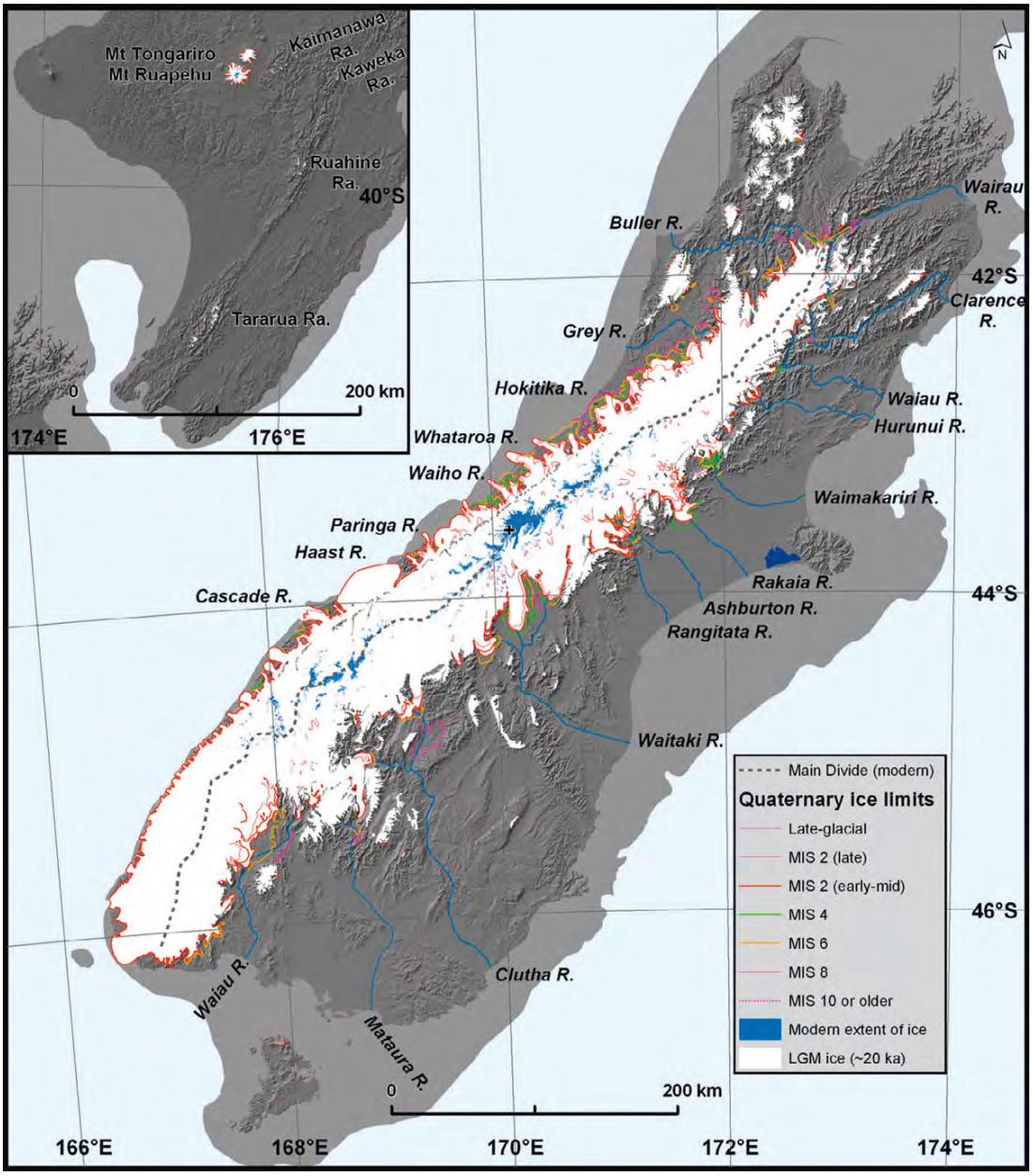

Figure 2.2: Approximate Quaternary ice limits in New Zealand. LGM ice shaded in white. Based on Barrell (2011), Figure 75.2.

(2007) concluded that the advance of the Franz Josef glacier to the Waiho loop moraine occurred ∼11 ka, based on what they considered to be more robust radiocarbon results.

- the Waiho loop moraine may not actually represent the termination of a climatic cooling event (either YD or ACR), as the ∼5°C of climatic cooling required to drive the advance to the Waiho Loop (Alexander et al., 2011) is not consistent with available climate proxy data, which indicate maximum late-glacial cooling of ∼2.5 °C (e.g. Vandergoes et al., 2008). Alternatively, a pronounced period of glacial advance during moderate cooling (∼2 °C) between ∼13-11 ka could have been driven by reduced ablation due to partial coverage of the Franz Josef glacier by rock avalanche debris (Alexander et al., 2011; Tovar et al., 2008).

- based on surface exposure dating of boulders from the Waiho loop moraine, Barrows et al. (2007) concluded that the moraine was deposited ∼10.5 ka ago, and was therefore not related to a YD advance. However, this age has also been disputed, by Applegate et al. (2008), on the basis that the moraine age cited by Barrows et al. (2007) may have been biased towards an unrealistically young age, if the dated boulders had been exhumed some time after they were deposited. The Barrows et al. (2007) exposure age calculations were based on the best available estimates of cosmogenic nuclide production rates at the time, which were calibrated with northern hemisphere sites; they did not have the benefit of a locally-derived production rate (e.g. Putnam et al., 2010b). Furthermore, if the oldest (non-outlier) moraine ages from Barrows et al. (2007) are calculated using the local production rate, the moraine ages then pre-date the ACR, as well as the YD.

There has been little published evidence for YD cooling beyond the Waiho Loop; in fact, pollen records of deglacial sequences from the Cobb Valley in the northwestern South Island showed no evidence for a YD temperature decline in New Zealand Singer et al. (1998). In addition, Barrows et al. (2007) examined SST reconstructions based on paleoclimate proxy records from marine sediment core SO136-GC11, retrieved from the Challenger Plateau in the Tasman Sea, and found that the ocean adjacent to southwestern New Zealand experienced rapid and uninterupted warming from ∼19-11 ka, a period which includes the YD.

Recently published records from New Zealand mountain glaciers may provide terrestrial evidence for an ACR-type signature. ^{10}Be surface-exposure dating (TCND) of 27 moraine ridges of the Birch Hill and mid-Macaulay moraine complexes in the

central South Island provide evidence (supported by locally derived ^{10}Be production rates) that late-glacial cooling in the Southern Alps culminated ∼13.6-12.7 ka (Putnam et al., 2010a,b). However, other records from mountain glaciers suggest relatively smooth and continuous glacial retreat from as early as 23 ka through to ∼15ka, and exclude any late-glacial climate reversal (e.g. Shulmeister et al., 2005, 2010; Sutherland et al., 2007). A mean ^{10}Be age of ∼12 ka on boulders from the Lake Misery moraines in Arthur's Pass has been interpreted to support a YD advance synchcronous with northern hemisphere records (e.g. Ivy-Ochs et al., 1999). However, it is worth noting that ^{10}Be chronologies for the Lake Misery moraines, as well as other late-glacial features in the Southern Alps (e.g. Shulmeister et al., 2005, 2010) were based on widely accepted global ^{10}Be production rates, which may be significantly higher than local production rates (Putnam et al., 2010a,b).

While a regional-scale picture of the LGIT in the Southern Alps is beginning to emerge, issues remain with constraining the pattern of deglaciation in specific areas; even when working in the same valleys, some authors infer rapid and/or episodic retreat (e.g. Schaefer et al., 2006, while others have found evidence for relatively smooth, uninterupted retreat (e.g. Shulmeister et al., 2010).

2.1.4 The LGIT in Fiordland

The LGIT in Fiordland is not particularly well constrained, as few records of late-glacial climate events have been published for the region. Tills, moraines and outwash gravels associated with late Quaternary glacial advances are generally restricted to the drainages of lakes Monowai, Hauroko and Poteriteri, in southern Fiordland, and the eastern drainages of lakes Te Anau and Manapouri, where glaciers drained onto a valley and basin foreland (Turnbull et al., 2010, and references therein). Little is known of late-glacial or Holocene ice limits elsewhere in Fiordland, as there is generally very little subaerial Quaternary glacigenic sediment preserved in the Fiordland landscape (Barrell, 2011).

The closest published terrestrial paleoclimate records to Milford Sound come from Cascade Plateau (some 75 km northeast), where an extensive sequence of lateral moraine ridges is preserved near the present-day coast at elevations from sea level (many moraines are truncated at the modern coastline) to 587 m.a.s.l. ^{10}Be TCND results from moraine boulders in the Cascade Valley reveal 3 major phases of glaciation over the past 100 ka, all of similar magnitudes. 8-10 lateral moraine ridges were deposited during the LGM from 22-19 ka, and multiple lateral and end moraines were deposited during retreat from the LGM position, suggesting rapid climate amelioration early in the LGIT

(Sutherland et al., 2007).

2.1.4.1 Marine records

There are also substantial marine records (both published and unpublished), which provide valuable insight into the post-LGM climate in Fiordland. During the LGM (between ~28-18 ka), sea level was ~120 m lower relative to today (see Figure 2.3, Fairbanks, 1989; Fleming et al., 1998; Milne et al., 2005), and tidewater glaciers delivered sediment to outwash fans on the narrow continental shelf; these depositional systems were active until glacial retreat began some time before 18-17 ka, leaving behind an extensive geomorphic and sedimentary record of post-LGM climate change in New Zealand (e.g. Barnes, 2009; Knudson et al., 2011; Pickrill et al., 1992). These records are largely unexplored, and may contain important information about past environmental change in New Zealand, as discussed in subsequent sections.

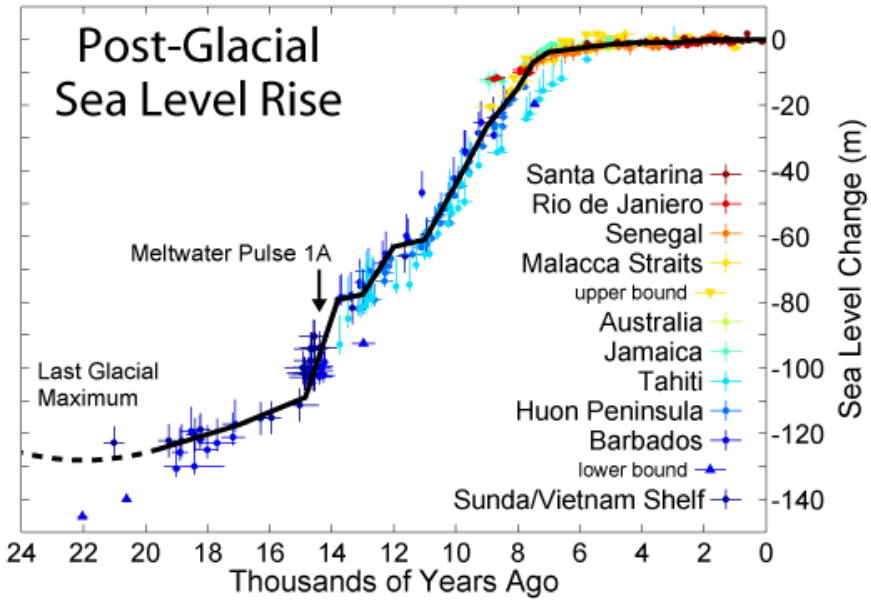

Figure 2.3: Global post-glacial eustatic sea level. Based on data in Fairbanks (1989); Fleming et al. (1998); Milne et al. (2005).

2.2 Fiord evolution: styles and diversity

Since the LGM, fiords in different regions of the world have evolved in different ways, resulting in the global diversity of fiord environments that exist today. A range of

factors, including climate, style and timing of ice retreat, changing sea level and sedimentation regimes, tectonic activity, and changing ecological conditions (e.g. marine transgression, catchment reforestation) combine to make the evolutionary history of each fiord unique. The largest concentrations of fiord landscapes occur in mountainous regions of:

- western Europe, from ∼55 to 80°N (e.g. Norway/Svalbard, Iceland)
- western North America (British Columbia, Alaska), from ∼48 to 60°N
- eastern North America (Newfoundland and Labrador, Baffin Island, Ellesmere Island, Greenland), from ∼47 to 83°N
- western South America (Patagonian Chile, including Tierra del Fuego), from ∼43 to 55°S, hosts the largest continuous fiord landscape on earth (Glasser and Ghiglione, 2009)
- west coast of New Zealand's South Island, from ∼44 to 46°S
- the Antarctic Peninsula, South Georgia, Kerguelen Islands and other Sub-Antarctic islands also contain fiord landscapes, many of which are still heavily glaciated

2.2.1 Evolutionary stages

Individual fiords may be at very different stages in their respective evolutionary development (see Figure 2.4). Some fiord basins are still completely or partially filled with ice, particularly those in polar regions (e.g. Greenland, Antarctic Peninsula), or in more temperate regions where valley glaciers are fed by heavy snow accumulation in very mountainous landscapes (e.g. Alaska, Chile). In other regions, fiord valleys are relatively ice-free, forming the deep, narrow marine channels that we tend to associate with classic fiords (e.g. Norway, B.C., New Zealand). Some fiords become blocked from the sea by sediment barriers, and eventually become freshwater lakes (e.g. Lake McKerrow, New Zealand), while fiords that are in the very late stages of fiord evolution may have been largely filled in with sediment (e.g. Big Bay; Barnes and Pickrill, unpublished).

2.2.2 Glacial isostatic adjustment

During the LGM (and previous Quaternary glacial periods), the large continental land masses of the northern hemisphere supported great ice sheets, which were up to 3 km

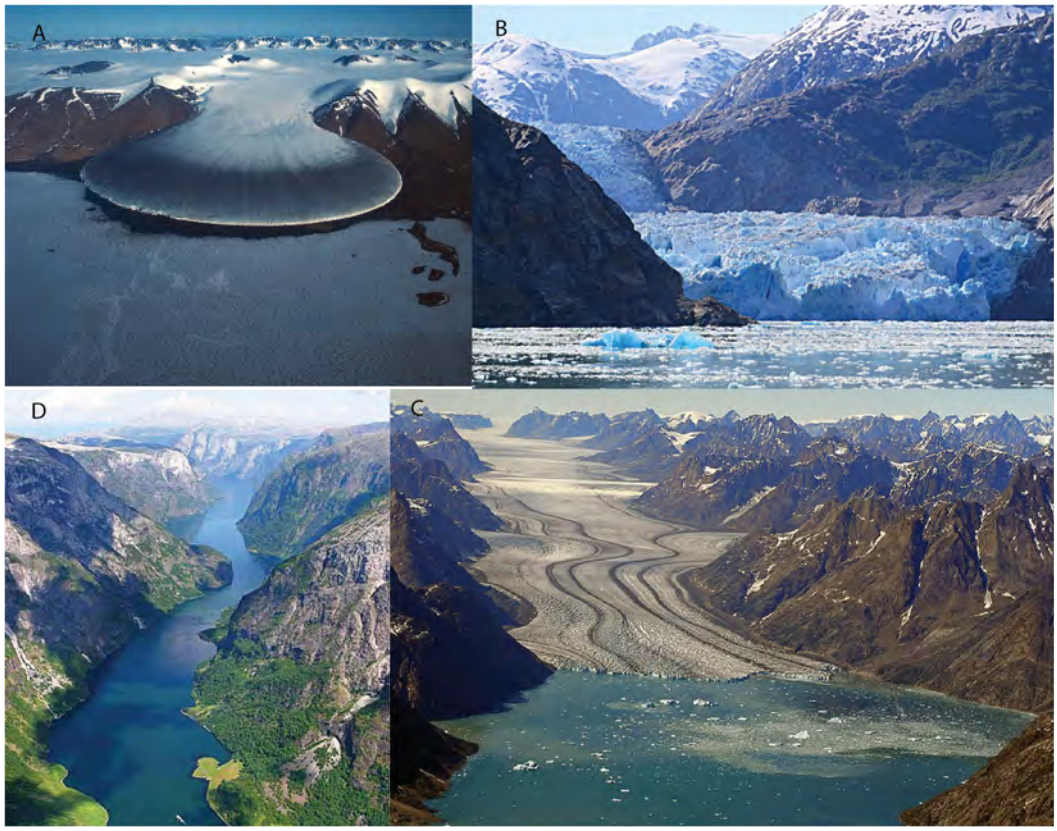

Figure 2.4: Fiords at various stages of evolution: A) Elephant Foot Glacier, Greenland. B) Grey Glacier, Chile. C) Unknown glacier, Greenland. D) Sognefjord, Norway.

thick. These ice sheets locked up enough water to cause a global (eustatic) sea level drop of around 120 m. The weight of the ice caused local isostatic depression of the earth's crust of up to 200 m (Clague, 1983; Fairbanks, 1989), which also had the effect of pushing up the land surrounding the ice sheets. As the ice sheets melted, isostatically depressed regions began to rise, while areas that were on the peripheral bulge began to settle (Fairbanks, 1989).

2.2.3 Northern Hemisphere fiord evolution

Continent-margin fiord landscapes in the northern hemisphere tend to have evolved within a complex framework of isostatic adjustment and eustatic sea level change, but in the Holocene, isostatic rebound has more than compensated for eustatic sea level rise, resulting in a period of rapid emergence (Clague, 1983; Fairbanks, 1989). For example, in southwestern British Columbia, relative sea level has fallen from as much as ∼200m above modern sea level, as the area rebounds from isostatic depression caused by the Cordilleran Ice Sheet. Marine transgression of glaciated fiords was driven by eustatic sea level rise during the early LGIT, but isostatic rebound eventually raised some fiord sills. This resulted in a transition from marine fiord, to saline lakes, which eventually became freshwater lakes as inflow gradually replaced saline water (Clague, 1983; James et al., 2009).

In the typically regressive post-glacial environment of the northern hemisphere, raised shorelines and fiord-head deltas can provide a record of relative post-glacial sea level. An example is Zeballos Inlet, a fiord on the western coast of British Columbia's Vancouver Island, where a dissected late Pleistocene fiord-head delta is preserved with a surface elevation ∼21 m above sea level, suggesting Holocene uplift of ∼20 m (Gutsell et al., 2004).

2.2.4 Southern Hemisphere fiord evolution

Other than the Antarctic continent, the southern latitudes of the southern hemisphere do not contain enough land mass to allow the nucleation of very large ices sheets, such as those that covered large parts of the continental northern hemisphere. An exception is Southern South America, which did support a substantial amount of ice during Quaternary glacial periods, with the expansion of the Patagonian Ice Sheets to both the Chilean and Argentinian coasts along over 1000 km of the Southern Andes. Rostami et al. (2000) investigated a series of raised marine terraces along ∼1000 km of coastline in Patogonian Argentina, and found that Holocene sea-level culminated

∼8-7 ka, at a relative level of 6-7 m.a.s.l. Corrected for regional tectonic uplift rates, the authors estimated an average isostatic uplift rate of ∼0.8 mm/yr over the past 7 ka, which is more than an order of magnitude lower than isostatic uplift rates seen in southwestern British Columbia during melting of the Cordilleran Ice Sheet (e.g. James et al., 2009). Raised shorelines and deltas are generally not preserved in Patagonian fiord landscapes, with fiords evolving in a mostly transgressive environment, due to the lower magnitude and slower rate of isostatic rebound compared to eustatic sea level rise.

2.2.4.1 New Zealand

Although New Zealand's South Island has been extensively glaciated during the Quaternary, the Southern Alps have not been covered by large enough ice-sheets to cause major isostatic adjustment. The exceptional LGM glacial record preserved in New Zealand landforms and near-surface deposits has allowed the LGM extent of glaciers to be relatively well-constrained (Barrell, 2011). Based on approximate LGM ice extent, Mathews (1967) concluded that a maximum post-glacial rebound of ∼30 m was possible in the Southern Alps. However, considerations of the isostatic implications of New Zealand's plate boundary setting suggest that isostasy is dominated by plate collision and subduction processes (e.g. Scherwath et al., 2006; Sutherland et al., 2006a). Several workers (e.g. Barnes and Pickrill, unpublished; Pickrill et al., 1992; Putnam et al., 2010b) have reached the conclusion that glacioisostatic rebound is a minor component of contemporary uplift, therefore it is nearly impossible to discern against a backdrop of tectonic activity.

Modest ice-related isostatic depression means that the New Zealand post-glacial sea level curve is dominated by eustatic sea level rise. During the LGM, sea level was ∼110 m lower relative to today (Fairbanks, 1989; Fleming et al., 1998; Milne et al., 2005), and tidewater glaciers terminated on the narrow continental shelf. Early in the LGIT, glaciers receded rapidly, and proglacial lakes formed behind fiord entrance sills. When eustatic sea-level rise inundated fiord entrance sills (which are typically 20 to 120 m deep), fiords became connected to the sea (Barnes and Pickrill, unpublished; Barnes, 2009; Pickrill et al., 1992). Thus, much like Patagonian fiords, New Zealand fiords have evolved in a mostly transgressive environment.

2.3 New Zealand fiords and environmental changes since the LGM

2.3.1 Sensitivity to environmental change

New Zealand is considered to be a sensitive monitor of climate change because it is one of very few sizeable land masses in the southern hemisphere westerly circulation zone. As a long (∼1500 km), relatively narrow (∼200-300 km) and mountainous archipelago spanning ∼37°-47° S latitude, New Zealand effectively intercepts the westerly circulation in the Antarctic-subtropical transition zone, amplifying climate signals and generating dramatic east-west environmental gradients that are very sensitive to changes in atmosphere and oceanic conditions (e.g. precipitation, temperature, glacial ice-cover) (Alloway et al., 2007; Barrell, 2011). As noted by McGlone et al. (1993), New Zealand's climate record holds global importance for three primary reasons:

1. New Zealand's remote position in the southwest Pacific means that it directly reflects changes in the ocean-atmospheric system without the complications associated with larger continental land masses.

2. a small number of well-dated terrestrial records of climatic perturbation can be used to effectively calibrate deep sea records from the adjacent oceans. New Zealand's relatively small size and maritime climate should ensure a high degree of correspondence between terrestrial and adjacent oceanic records.

3. New Zealand's small land mass and lack of a large ice sheet at the LGM meant that a definable range of terrestrial biotic environments persisted throughout the LGM (e.g. podocarp forests), and were able to respond rapidly to climate change.

2.3.1.1 Fiordland paleoclimate records

Sustantial southern hemisphere mid-latitude late-glacial paleoclimate records are preserved in submarine sediments from the fiords and narrow continental shelf of Fiordland (Barnes and Pickrill, unpublished). Some records have been documented, (e.g. Barnes, 2009; Knudson et al., 2011; Pickrill et al., 1992), but the Fiordland paleoclimate record is largely unexplored. The Fiordland coast extends ∼280 km from Lake Hakapoua at the far south of the South Island, to Lake Mckerrow, 25 km north of Milford Sound.

Fiordland includes a wide range of fiord morphologies and evolutionary histories (see Table 2.1 and Figure 2.9), including 13 major fiords that are open to the ocean (see Figure 1.5 for fiord locations). Some formerly open fiords evolved into proglacial

Table 2.1: Morphology of selected New Zealand Fiords[a]

Fiord	Length (km)	Sill depth (m)	Max. depth (m)	catchment area (km^2)	fiord/lake area (km^2)	ratio catchment/fiord area
Milford Sound	15.7	71	291	540	25	21.6
George Sound	21.2	76	224	305	33	9.2
Doubtful Snd.	40.4	111	421	627	84	7.5
Dusky Sound	43.9	99	317	861	181	4.8
Preservation-Inlet[b]	36.5	26	371	562	93	6.0

[a] data from Barnes and Pickrill (unpublished), Milford Sound data updated from current study.
[b] see Pickrill et al. (1992) for detailed description.

lakes that formed either behind barrier sills at fiord entrances, or behind bedrock sills or moraine deposits in formerly ice-filled valleys. Examples of open fiords include Milford and George Sounds and Preservation Inlet; saline lakes include Lakes Hakapoua and Sutherland, and freshwater lakes are impounded both at sea level (by barrier sills, such as at Lake McKerrow), and above sea level (behind bedrock or moraine sills, such as at Lakes Widgeon, Alice and Cadman).

2.3.2 Influence of tectonic setting and geology on fiord evolution and architecture

In addition to containing important paleoclimate records, New Zealand fiords exhibit a wide variety of evolutionary stages and fiord architecture, and therefore provide an important framework for understanding sedimentation processes that influence tectonically active, mid-latitude, temperate climate glacio-marine systems (Barnes and Pickrill, unpublished).

Geomorphic evidence supports this author's interpretation that the range of contemporary fiord architecture in Fiordland is largely due to the influence of the plate boundary Alpine Fault, which separates the relatively soft, erodible sedimentary basement rocks of the Buller terrane to the north, from the harder, more resilient rocks of the Median Batholith to the south. This transition is very evident near the entrance to Milford Sound; the landscape nearest to the coast is more denuded and deeply eroded than the remarkably steep topography that rises to nearly 2 km above the middle and inner basins of the fiord. Fiords incised into softer rocks to the north of Milford Sound have either been entirely infilled with sediment from fluvial deposition and longshore drift (e.g. Big Bay), or have been blocked from the sea by Holocene growth of barrier

spits (e.g. Lake McKerrow). In the hard basement rocks south of the Alpine Fault, fiords generally have had relatively low sediment input during the Holocene, and the maximum contemporary water depth of these open fiords ranges from ∼170-420 m.

2.4 Sedimentation processes

In most contemporary fiord environments that are open to the sea, relatively high precipitation rates in mountainous catchments means that abundant sediment is supplied to fiord-head deltas via seasonal river discharge (e.g. Norway, Alaska, British Columbia). Sediment deposition in fiord basins is largely controlled by the transport and redistribution of these deltaic sediments, either by suspended sediment circulation, or by delta slope failure and turbidity currents which transport sediments to the basin floor (Pickrill et al., 1992; Syvitski et al., 1985).

2.4.0.1 Low terrigenous input

Early studies of the sedimentology of New Zealand fiords (Glasby, 1978; Pantin, 1964) suggested that they follow similar sedimentation patterns to their northern hemisphere counterparts. However, later studies have shown that terrigenous sediment yields from fiord catchments in New Zealand are very low, regardless of season (e.g. Pickrill, 1993). Basin sedimentation rates are correspondingly low, averaging just 0.4-1.2 mm/yr for fiords south of Milford Sound (Pickrill, 1993; Pickrill et al., 1992). Milford Sound has a significantly higher basin sedimentation rate (an average of ∼1.3 mm/yr over the past 1,340 years, Knudson et al., 2011), probably due in part to its larger catchment/fiord area ratio. New evidence presented in this study suggests that the high sediment yield at Milford Sound is also due to the dominant influence of landslide processes on the catchment sediment budget (see Chapter 3 for details).

Basin sedimentation rates for all the mature fiords of Fiordland (including Milford Sound) are extremely low by global standards, even compared to the fiords of Norway, where sedimentation rates are in the order of 4-9 mm/year (e.g. Paetzel and Dale, 2010), despite similar resilient bedrock geology, and little contemporary glacier cover. Fiordland basin sedimentation rates are about double that for prodelta slopes (Pickrill, 1993), due to very low contributions from terrigenous sediment. This is in contrast to most contemporary fiord environments in other parts of the world; normally, relatively large catchment areas including headwater glaciers and high seasonal snow-cover, contribute abundant meltwater and sediment to river deltas. In these environments, prograding river deltas often dominate fiord sediment budgets (Barnes and Pickrill,

unpublished; Syvitski et al., 1985).

The extremely low modern sedimentation rates in most of the fiord basins of Fiordland cannot account for the thick deposits of laminated sediments which underlie relatively thin veneers of marine-derived sediment. Examples include George Sound, and Milford Sound, where seismic reflection data indicates that the underlying laminated units are in the order of 100s of meters thick (see Figures 2.7) and 3.28). A 100 m thick sediment fill would require an average sedimentation rate of ∼6 mm/year, over the past 17 ka. As this rate is much higher than the observed modern sedimentation rates of 0.4-1.3 mm/yr (see above), this provides clear evidence that the thick basin fills of laminated sediment must have been deposited in a pro-glacial lacustrine environment during a time of heightened sedimentation during glacier retreat, and prior to marine transgression. Lake Pukaki in the central Southern Alps is a modern analogue; it is fed by glacial runoff from several nearby valley glaciers (including the Tasman, Hooker and Mueller glaciers), and the modern sedimentation rate has been estimated at around 5-6 mm/year (Ditchburn and McCabe, 1977). Therefore, it appears reasonable to infer that the thick laminated sediments which underlie fiord basins are likely the result of heightened sedimentation in pro-glacial lakes during glacial retreat during the LGIT.

2.4.0.2 High in-situ biogenic sediment production

In contrast to delta-dominated sedimentation, and despite the extremely high precipitation and mountainous topography in Fiordland, most suspended particulate matter in New Zealand fiords is actually derived from in-situ biogenic sediment production from diatoms and plankton, with a smaller contribution provided by organic detritus from terrestrial sources (e.g. "tree slides": failures of thick mats of vegetation that cling to steep slopes) (Pickrill, 1987). New Zealand fiords have a typical estuarine circulation, with freshwater input at fiord heads flowing seaward at the surface; this seaward flow is replaced by landward circulation of oceanic water at depth. Within the seaward-flowing surface layer, suspended sediment is transported seaward in very low concentrations (generally <1 mg/l), more typical of coastal than estuarine environments (Pickrill, 1987). Except at modern deltas, the suspended load contains very little terrigenious mineral matter, and is mainly made up of organic and biogenic material.

New Zealand fiord heads are generally within a few km of the drainage divide, and catchment area/fiord area ratios tend to be relatively small south of Milford Sound. It is this author's interpretation that the overall paucity of suspended particulate mineral matter in open New Zealand fiords (i.e. those south of the Alpine Fault), is likely the result of a combination of factors:

- relatively small catchment area/fiord area ratios (see Table 2.1),
- extensive temperate forests or sub-alpine scrub cover the vast majority of steep, sub-alpine slopes in Fiordland; the vegetation reduces catchment sediment yield by stabilizing slopes and trapping sediment,
- consistently (rather than seasonally) high precipitation supports prolific vegetation growth,
- weathering resilience of the hard igneous (with metamorphic overprint) basement rocks south of the Alpine Fault,
- many fiord valleys contain lakes in their lower catchments, which serve to trap and store sediment

2.4.1 Sedimentology of fiord-head deltas

The largest rivers in Fiordland are marked by prograding fiord-head deltas, where topset sediment units of sand and gravel rapidly grade into a uniform blanket of marine mud (gyttja) on the forset slope (e.g. Pickrill et al., 1992). Lower delta foreset beds are characterized by a range of sedimentary environments; piston cores from the heads of Preservation Inlet and Thompson and George Sounds reveal massive organic-rich gyttja (Barnes and Pickrill, unpublished; Pickrill et al., 1992), similar to records from Nancy and Caswell Sounds (Glasby, 1978). These records contain no evidence of course sediments or graded beds that would indicate mass failures or turbidite deposits originating from post-depositional failure of delta forset slopes (Barnes and Pickrill, unpublished; Pickrill et al., 1992), and are likely slow-growing and stable.

A notable exception is Milford Sound; this study shows that the major contemporary deltas have continued significant progradation during the Holocene, due to ample sediment supply ($\sim$109 tonnes/km^2/yr, Pickrill, 1993) from the relatively large, mountainous catchment. Relatively heavy sediment accumulation at the main Milford Sound deltas has resulted in post-depositional deformation of forset slopes, as indicated by geomorphological and sedimentalogical evidence for recent delta slumps and turbidity currents (see Chapter 3).

South of Milford Sound, several modern fiord-head deltas overly relict deltas that were formed during lowstand periods, likely when proglacial lakes occupied inner fiord basins during periods of relatively high sedimentation, such as during glacial retreat. Such deltas have been reported by Pickrill et al. (1992) in Preservation Inlet, at -30 m and -34 m in Long Sound and Revolver Bay, respectively. Seismic profiles along

the relict Camelot delta in Thompson Sound suggest that relict deltas are underlain by progradational foreset sequences that extend well down-fiord (Barnes and Pickrill, unpublished). Holocene sediment cover over relict delta surfaces is generally very thin, indicating that even proximal sedimentation rates are in the order of 0.1-0.7 mm/yr at modern river deltas in Long Sound, Revolver Bay, and Thompson Sound (Barnes and Pickrill, unpublished).

2.4.2 Basin sedimentology

The basins of some New Zealand fiords (e.g. Preservation Inlet, Thompson Sound, Figure 2.5) are clearly sediment-starved; late-glacial sediments fill less than one third of those fiord cross sections (Barnes and Pickrill, unpublished; Pickrill et al., 1992). However, George (Figure 2.7) and Milford (Figure 3.28) Sounds, which have extremely mountainous drainages and the largest catchment/fiord area ratios, seem to have proportionally higher basin sediment infills. As supported by evidence presented in this study, Milford Sound appears to have experienced the highest Holocene sedimentation, with as much as two-thirds of the fiord cross section now filled in (see Chapter 3).

Typically, upper fiord basin sediments consist of brownish-black to olive-black organic-rich mud (gyttja), with an organic content of 12-18%, and calcium carbonate concentrations (predominantly marine shells) of 2-25%; the remainder is comprised of fine-grained clastic sediment. Organic content is dominated by fibrous remains from terrestrial vegetation (e.g. from tree slides into the fiords, or transport by rivers), and is highest on the prodelta slopes, decreasing downslope to the basin floor. Conversely, calcium carbonate concentrations are highest in seaward basins, and lowest in inner basins, especially on prodelta slopes where marine-derived sedimentation is diluted by inflowing rivers and associated terrestrial sediment. Gyttja units are generally massive, with burrow marks and other evidence of bioturbation common (Barnes and Pickrill, unpublished; Pickrill et al., 1992).

In seismic reflection profiles, the gyttjas appear as opaque, poorly-reflective units with occasional parallel reflectors; the base of these units tends to form an unconformity against an underlying opaque to parallel bedded unit. Cores from Preservation Inlet suggest that the underlying parallel bedded unit is a late glacial blue-grey clay, which was deposited into proglacial lakes that filled fiord basins during glacial retreat (Pickrill et al., 1992). Radiocarbon dates from Preservation Inlet put the transition from late-glacial clay to gyttja (and therefore to a forested catchment with limited headwater glaciers) at ∼14.25-18.45 years BP (Pickrill et al., 1992). A calibrated radiocarbon age of ∼14.3±0.9 ka BP has been obtained from peaty material overlying

the relict Whitewater Delta in George Sound (Barnes and Pickrill, 2003), indicating a transition from glaciated valleys to a predominantly-forested catchment around that time. This late-glacial seismic discontinuity has also been interpreted in seismic profiles from Thompson/Bradshaw (see horizon H1, Figure 2.5) and George Sounds (Barnes and Pickrill, unpublished).

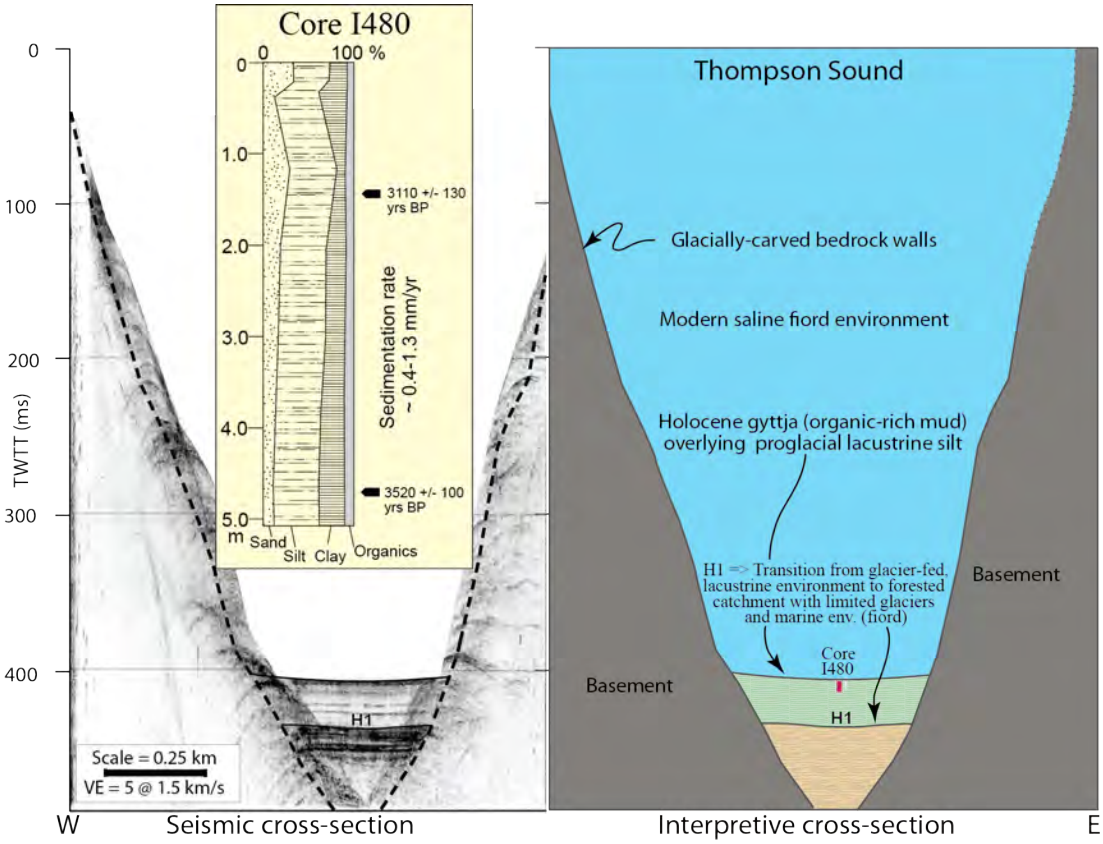

Figure 2.5: Thompson Sound: Uniboom seismic cross section and interpretation, located ∼15 km south of fiord entrance. Section from west to east. Note shallow basin fill and reflective discontinuity at H1. Core I480 from similar depth, ∼5km north of seismic cross section. Data provided by NIWA, interpretation, core log and radiocarbon ages after Barnes and Pickrill (unpublished).

2.4.2.1 Inner sills

Inner fiord basins are commonly separated from seaward basins by bedrock sills, which generally form near the junction of fiord arms; an example is the Narrows at Preservation Inlet, where a bedrock sill (-28 m) occurs just landward the arms formed by Revolver Bay and the outer basins. Shallow and constricting inner sills are scoured by

strong tidal flows, preventing deposition of fine sediment and leaving a thin lag surface of boulders, cobbles and calcareous sand overlying bedrock. Sediments are regularly swept off the sill crest, accumulating as prograding wedges of parallel-bedded sediment on the sill flanks (e.g. Pickrill et al., 1992.

2.4.2.2 Entrance sills

During the LGM, relative sea level was ∼110 m lower than today, and most Fiordland glaciers were grounded near fiord entrances, where they carved depressions in the bedrock of the narrow continental shelf (Barnes and Pickrill, unpublished). Following glacier retreat, marine transgression eventually drowned fiord entrance sills (see Figure 2.7 for George Sound seismic profile); today, sills differentiate outer fiord basins from the coastal marine environment, continental slope and deep marine basins beyond (see Figure 2.8). Shallower sills are subject to coastal wave energy, and display crested bedforms indicative of active sediment transport by waves, including symmetrical oscillatory ripples and megaripples. Deeper sills, (such as at Thompson Sound, ∼130 m deep), generally lack mobile sediment, with exposed bedrock or shallow lag surfaces of cobble and gravel overlying bedrock, as they are not subjected to major wave energy or associated transport of coastal sediment; these sediment-starved sills have not undergone significant Holocene growth (Barnes and Pickrill, unpublished; Barnes, 2009).

Evidence presented later in this study indicates that Milford Sound differs from the other fiords, as the entrance sill (see Figure 2.6) is well seaward of the fiord entrance, and extensive submarine terminal and lateral moraine deposits on the shelf mark the glacier extent (see Chapter 3, Figure 3.30).

Fiords with shallow entrance sills (e.g. Preservation Inlet) have thick accumulations of sandy sediment on landward slopes (see Figure 2.8; seismic reflection profiles clearly show prograding clinoform units overlying basin floor gyttjas. Cores and grab samples from shallow entrance sills show a transition from unstratified well sorted sand on sill crests, to interbedded units of mud and graded sand on landward sill slopes (Pickrill et al., 1992). Graded sandy units have been interpreted as episodic turbidite deposits from periodic overloading of sill crests by high sedimentation in a coastal environment (e.g. sediments transported during storms or by longshore drift), while the muddy units represent background sedimentation of predominantly fiord-derived pelagic muds (Barnes and Pickrill, unpublished). Progressive deposition of sandy sediments in such an active coastal environment eventually leads to barrier spit development and closure from the sea (e.g. Lake McKerrow).

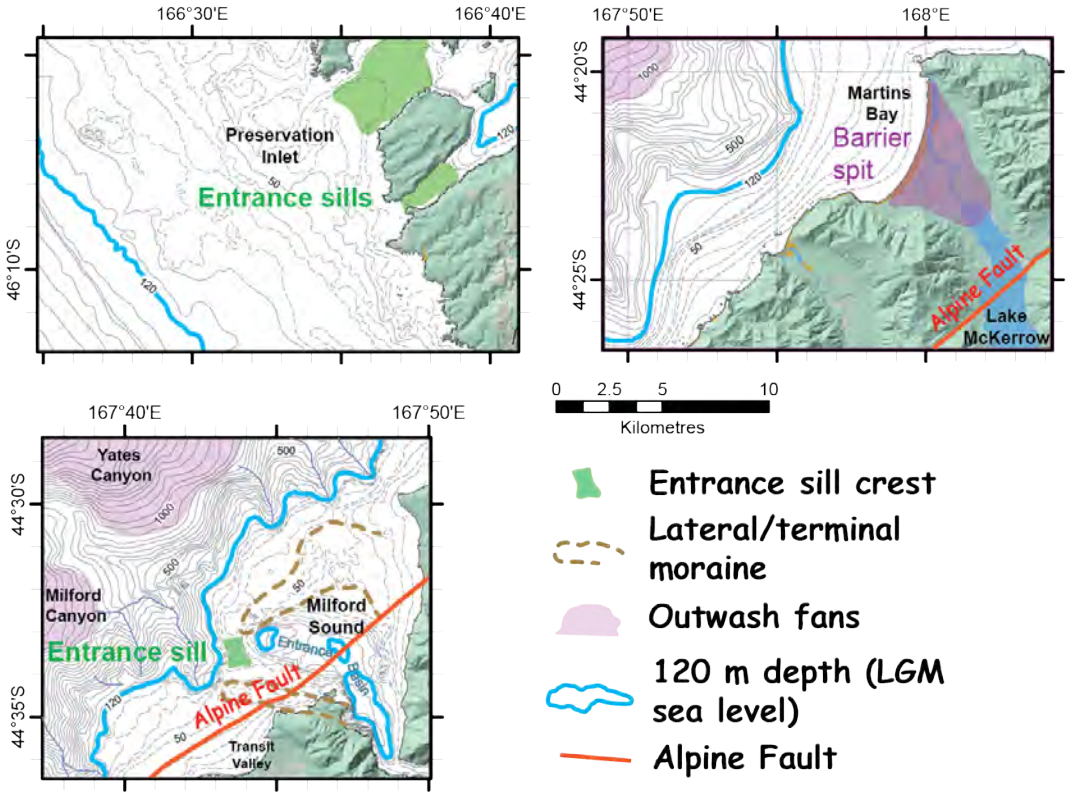

Figure 2.6: Fiord entrance sills; contemporary examples. Modified from Barnes and Pickrill (unpublished).

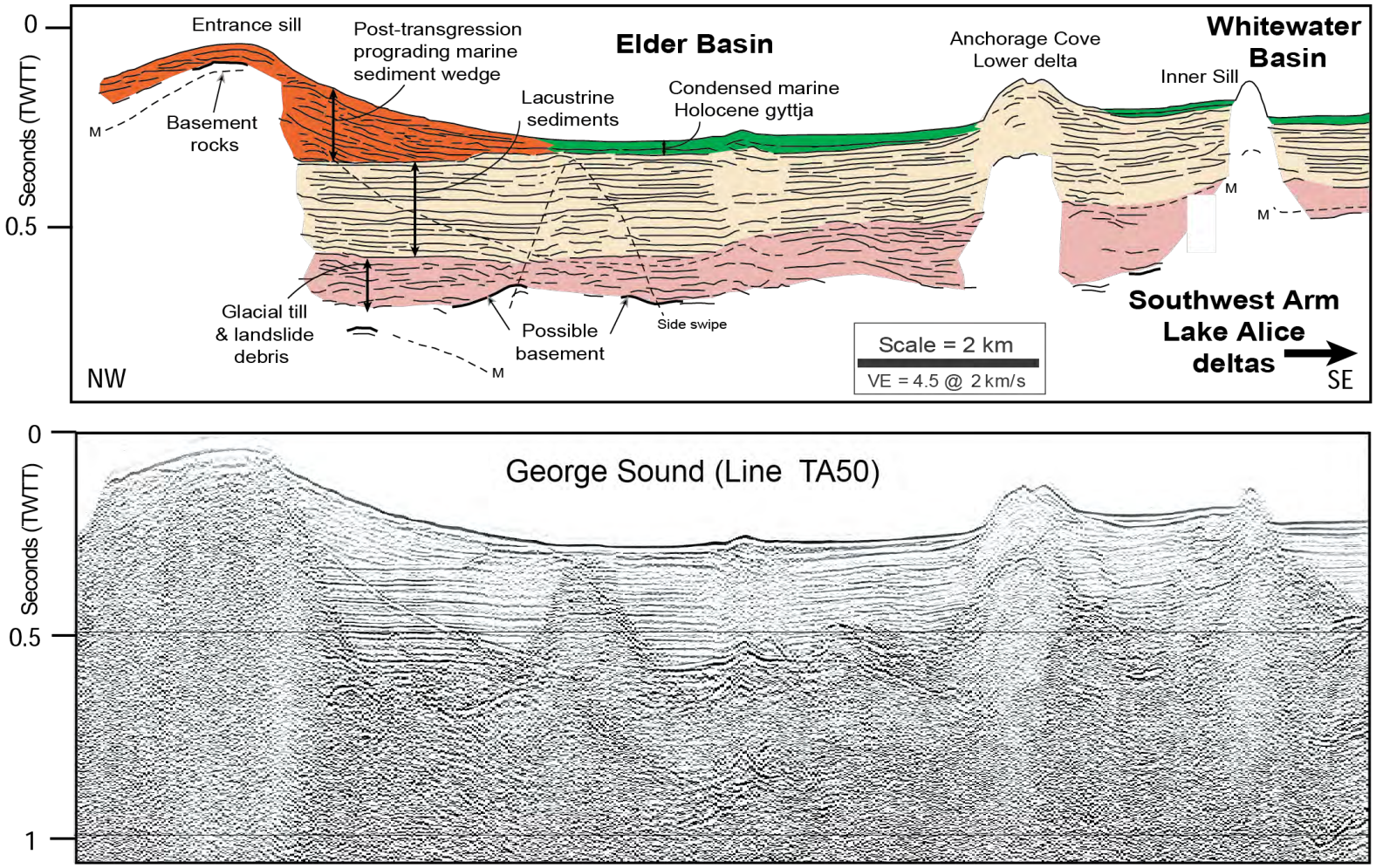

Figure 2.7: George Sound: Multibeam seismic profile and interpretation. Note thick prograding sediment wedge landward of entrance sill (orange unit), extensive parallel bedded lacustrine infill and thin overlying gyttja veneer (green unit). Data provided by NIWA, interpretation courtesy of Barnes and Pickrill (unpublished).

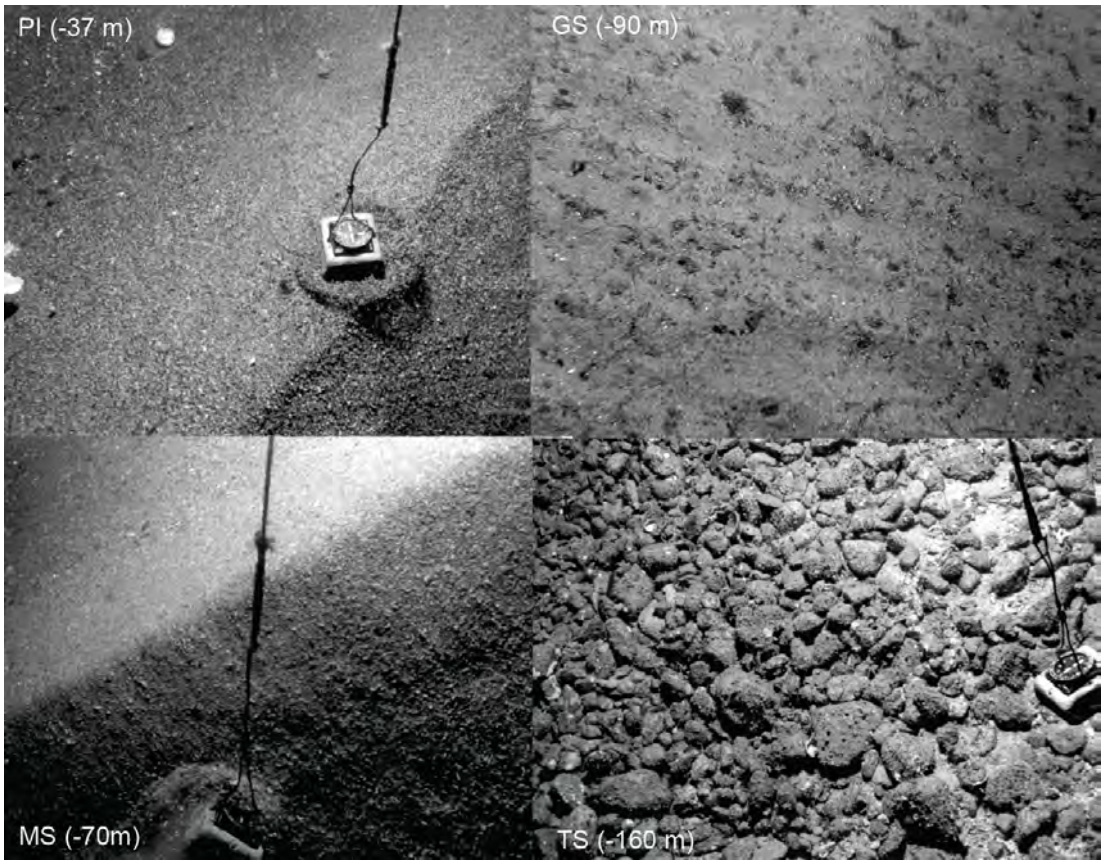

Figure 2.8: Fiord entrance sill sediments. From top left, clockwise: PI = Preservation Inlet, GS = George Sound, TS = Thompson Sound, MS = Milford Sound. Sample depth in parentheses. Photos provided by NIWA, depth data courtesy of Barnes and Pickrill (unpublished).

2.4.3 The influence of tree slides and landslides on fiord sedimentation

In the temperate and very wet contemporary climate of Fiordland, dense forests dominated by silver beech (*Nothofagus menziesii*) and local stands of rata (*Metrosideros spp.*) grow along very steep (up to near-vertical) fiord walls where little soil can persist. These forests apparently develop on a thick blanket of moss; as noted by Holloway (1954), "in the normal sense of the term, there is no soil at all". Holloway (1954) also noted that these forests are periodically devastated by "immense land-slides", resulting in various stages of stand redevelopment evident throughout Fiordland.

Field observations from the current study indicate that while some debris from tree slides may accumulate near shorelines (which tend to be very narrow, or non-existent) along steep-walled fiord margins, slides generally continue downslope to the fiord bottom. As the debris swath extends downslope, it completely denudes submarine slopes of benthic fauna, such as the black coral (*Antipathes fiordensis*, Grange and Singleton, 1988). Such events are recorded in fiord basin sediments; in most cores, gyttjas are interrupted by occasional thin beds (typically 0.2-2.5 cm thick, up to 8 cm thick) of granular sediment, commonly graded from gravel or sand at the bottom to sandy silt or silty sand at the top. The bottom of these units is generally a sharp or erosional contact, while the top of the units commonly grades into the gyttja above. Sandy laminae are generally too thin to be identified in seismic reflection profiles, but available core records suggest that they are widespread throughout fiord basins (Barnes and Pickrill, unpublished; Pickrill et al., 1992, Chapter 3, this study).

High resolution bathymetry from Thompson-Bradshaw Sounds indicate numerous talus debris fans on the fiord floor, at the base of subaerial gulleys (Barnes, personal communication, 2012), and similar features are common at Milford Sound (see Chapters 3 and 4). Sandy laminae often contain broken shell fragments and woody debris, and may be capped with coarse plant remains. Some of these units also contain remains of fauna from near-surface or mid-depth environments, suggesting that they represent episodic deposition from slope failures that originated subaerially, or near sea level (Barnes and Pickrill, unpublished).

2.4.3.1 Evidence for slope failure origin of sandy laminae

In a study of Nancy and Caswell Sounds, Glasby (1978) suggested that sandy laminae were bedload deposits from hyperpicnal flow during floods, however more recent data indicate that Fiordland rivers do not have high enough sediment concentrations for hyperpicnal flow (Pickrill, 1993). Glasby (1978) noted that the laminae could not be

correlated between individual cores, and that there was neither landward thickening of the units, or an increase in laminae frequency towards fiord-head deltas, as would be expected if the units were related to flood events. Other workers have interpreted the sandy laminae observed in cores samples as slope failure deposits; based on core samples and adjacent fiord morphology, the frequency and total thickness of sandy laminae appear to be related to fiord wall slope.

Results from the current study show that in cores from Milford Sound (which has the highest and steepest slopes in Fiordland), slide laminae make up ∼10% of the upper sediment collumn, compared to less than 2% at Preservation Inlet (Barnes and Pickrill, unpublished), which is typified by flatter slopes and relief below 1,000 m. Slopes flatter than ∼20% appear to contribute minimal slide laminae to the sediment column. Frequency of substantial slope failure deposits also appears to be greatest at Milford Sound, where slide return periods on the steepest slopes may be in the order of 1 in 150 years (Barnes and Pickrill, unpublished).

2.5 A conceptual fiord evolution model for New Zealand

Based on the data and analysis described above, and supported by a detailed paleoenvironmental reconstruction of Preservation Inlet by Pickrill et al. (1992) (see below for details), a conceptual fiord evolution model for New Zealand was developed by Barnes and Pickrill (unpublished); this is summarized in Figure 2.9, and described below. New EM300 30kHz multibeam bathymetry data collected in 2004 also supports these interpretations (e.g. Barnes, 2009, current study, Chapter 4)

2.5.0.2 LGM

As discussed earlier, LGM conditions were reached around ∼30-28 ka in New Zealand, with the onset of deglaciation and the LGIT around ∼20-16 ka, although some records suggest a slightly earlier LGIT, around ∼22-18 ka (e.g. Shulmeister et al., 2010; Sutherland et al., 2007 and this study, see Chapter 3). During the LGM, when sea level was ∼110 m lower relative to today, tidewater glaciers terminated on the narrow continental shelf. Most fiords have bedrock sills that have been incised into the continental shelf near the fiord entrance, and do not display significant moraine deposits (Barnes and Pickrill, unpublished; Pickrill et al., 1992). Exceptions include Milford Sound, where there is an extensive terminal moraine complex preserved on the continental shelf (see Chapter 3), and moraine deposits on the continental shelf off of Poison Bay and Sutherland Sound (Barnes, 2009).

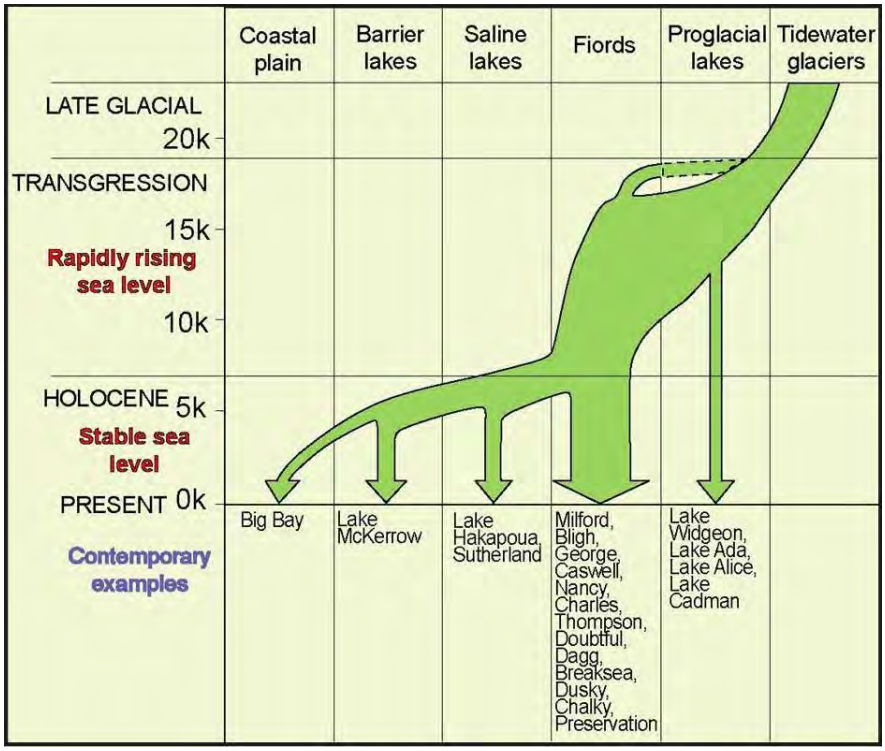

Figure 2.9: Conceptual fiord evolution model for New Zealand, and contemporary examples. Green arrows indicate present evolutionary phase of fiord (e.g. Milford Sound = open fiord; Lake McKerrow = barrier lake). Evolutionary progression from tidewater glacier indicated by following solid green path, y-axis is time before present. Time of marine transgression dependent upon sill depth. Courtesy of Barnes and Pickrill (unpublished). Dashed green path at the beginning of transgression shows that for fiords with very deep entrance sills (e.g. Thompson Sound), the first phase of eustatic sea level rise inundated the fiord in front of retreating ice, therefore no lake ponded behind the entrance sill.

During the LGM these glaciers transported sediment from their catchments to their terminuses, but apparently did not store significant amounts of sediment in their inner basins. Seismic reflection profiles from the deepest basins of Preservation Inlet and Thompson Sound provide evidence that glacier bases were at bedrock during peak glacial conditions (Barnes and Pickrill, unpublished; Pickrill et al., 1992); modern basin fills are dominated by massive mud (interpreted as Holocene marine-derived gyttja) overlying thick laminated late-glacial clay (interpreted as lacustrine sediments deposited in proglacial lakes during retreat). During the LGM, coalescing valley glaciers entrained and transported sediment from steep-sided valleys to the trunk glacier terminus, where the predominantly terrigenous sediment was deposited at the edge of the narrow shelf; ongoing slumps and debris flows fed a system of channels and outwash fans at the heads of deep submarine canyons, and on upper slope regions away from canyons (Barnes and Pickrill, unpublished; Barnes, 2009).

2.5.0.3 LGIT

Glacier retreat commenced around the beginning of the LGIT, when relative sea level was still ∼90-100 m lower, so freshwater proglacial lakes were impounded in basins behind terminal positions (entrance sills) that were above sea level, and some inner sills (e.g. Pickrill et al., 1992). Meltwater-fed rivers from receding glaciers built substantial deltas out into these lakes, with abundant glacially-derived sediment supply contributing to accumulation of thick lacustrine sediments between ∼17-10 ka. Glaciers were probably confined to valley headwaters, and catchments largely reforested by ∼12 ka; between ∼10-7 ka, eustatic sea-level rise led to marine transgression of most entrance sills, and transition to marine fiord environments (Barnes and Pickrill, unpublished; Pickrill et al., 1992).

2.5.0.4 Holocene

Holocene terrigenous sediment input has been extremely low, due to relatively small catchments, lush forest growth, sediment traps in upstream lakes and erosion-resistant bedrock (Barnes and Pickrill, unpublished). Background marine sedimentation, predominantly derived from in-situ biogenic sediment production from diatoms and plankton, interspersed with episodic inputs of terrigenous material from landslides, tree slides and flooding events, draped former lacustrine basins with a veneer of interbedded muddy gyttjas and sandy laminae (Barnes and Pickrill, unpublished; Pickrill et al., 1992).

Fiord head deltas have grown slowly during the Holocene; low terrigenous sediment input at river mouths (with the exception of Milford Sound) has allowed deltas to grow very slowly, without any evidence of past instability, such as slumping and turbidity currents that are characteristic of northern hemisphere fiord environments. Without significant fluvial sediment input to fiord basins, estuarine circulation of in-situ biogenic sediment is a dominant process, depositing sediment on the outside of bends and scouring narrows and fiord junctions where currents are strongest (Barnes and Pickrill, unpublished).

The Fiordland coast is subject to very high wave energy, which along with sediment supply from coastal wave erosion and terrestrial landslides, controls sedimentation at shallow entrance sills; wherever there is abundant sediment supply, thick sandy sequences have been deposited on landward sill slopes, generating unstable prograding clinoforms that gradually thin out and overly muddy fiord-bottom gyttjas. Sills which are deeper (or sediment starved), are characterized by scoured bedrock or thin lag surfaces of cobble and gravel, Barnes and Pickrill, unpublished; Pickrill et al., 1992).

2.5.1 An example: Preservation Inlet

Pickrill et al. (1992) examined seismic profile data, and sedimentological and micropaleontological data (including marine carbonate concentration, total organic carbon, diatoms and pollen) from three cores in Preservation inlet, in southern Fiordland. Age control was provided by ^{14}C dating of marine and freshwater fossils. Pickrill et al. (1992) found that towards the end of the LGIT, Preservation Inlet was occupied by a series of deep proglacial lakes that were impounded by shallow sills following glacier retreat.

With glaciers transporting sediment from headwater valleys and forests just beginning to re-establish, abundant meltwater transported sediment to these lakes, forming large sandy deltas and depositing finer laminated clay-rich sediments in distal basins. The rocky landscape was nearly barren, with sparse vegetation dominated by grass, scrub and shrubs. Pickrill et al. (1992) inferred a temperature ∼4 °C cooler than modern climate in Fiordland, based on diatom and pollen assemblages. With glaciated valley headwaters, the fiords would have been subject to significant cold air drainage, therefore a ∼4 °C cooling at the fiord could have been stronger than regional cooling at the time (Dr. J. Shulmeister, pers. comm.). With the onset of warming and the LGIT around ∼18 ka, the valley glaciers began to retreat, and lowland forests quickly developed. A rich freshwater fauna developed in the lakes, and deposition of organic mud accumulated over the laminated clays. Lake levels remained stable for several thousand

years, with relict delta surfaces indicating that paleo "Long Lake" impounded at ∼-30 m, paleo "Lake Preservation" at ∼-34 m, and a paleo lake in Revolver bay also at ∼-34 m. Eustatic sea level rise eventually caused successive overtopping of the sills, with marine transgression between 9.4 and 8.7 ka inundating the freshwater lakes and deltas, except Lake Widgeon, which remains above sea level today. Core stratigraphy and fossils from the inner basin of Preservation Inlet indicate that the transformation of Preservation Inlet into a marine fiord (very much as it exists today), was completed by 8 ka, around the time that global sea level stabilized.

2.5.2 Summary

New Zealand fiords exist at the geographic limit of temperate southern hemisphere fiord environments; they were glaciated during the LGM due to a unique suite of environmental conditions, including high precipitation and steep mountainous topography. Following the LGIT, the warm temperate climate and extreme rainfall has supported lush forest cover, and the resilient lithology has generated little terrigenous sediment input to the fiords. Eustatic sea level rise has dominated over minimal isostatic rebound, and most fiords have evolved in a trangressive environment. As a result, fiord infilling has been very slow by global standards, and some fiords have experienced little modification since deglaciation (Barnes and Pickrill, unpublished). The unique evolutionary processes that have shaped New Zealand fiords have left a legacy of geomorphic and sedimentary records of post-LGM environmental change in Fiordland (e.g. Barnes, 2009; Knudson et al., 2011; Pickrill et al., 1992), along with an equally valuable record of fiord evolution in this globally unique environment.

Chapter 3

The post-LGM evolution of Milford Sound

3.1 Introduction

Milford Sound hosts an exceptional legacy of glacial geomorphology; steep glacially-polished rock walls tower over a kilometre above what is surely one of the most spectacular fiord valleys on earth. Archetypal examples of hanging valleys, cirques and glacial staircases are ubiquitous, and smaller-scale glacial bedrock features (such as p-forms) can also be observed wherever the thick forest abates.

Despite outstanding preservation of bedrock glacial geomorphology at Milford Sound, the specific timing of glacial retreat during the LGIT has not previously been well constrained. While erosional (bedrock) features have been well-preserved in the Milford catchment, subaerial Quaternary glacial deposits are virtually non-existent, due to extremely high precipitation and low erodibility of the crystalline basement rocks.

An integral part of this project was to use terrestrial cosmogenic nuclide dating (TCND) and calibrated Schmidt Hammer dating (SHD) of glacially modified bedrock surfaces, combined with seismic reflection and core data from submarine sediments and submarine and subaerial geomorphic mapping, to better understand the glacial retreat history at Milford Sound. This chapter describes this work, which represents the first known attempt to constrain the timing of post-LGM glacial retreat and environmental change at Milford Sound. The results of this work have important implications for the distribution of large landslide deposits within, and near Milford Sound; constraining the ages of pre-historic landslide events and associated hazards facilitates assessment of risk related to future events (see Chapter 4).

3.1.1 Why study the evolution of Milford Sound?

As an easily accessible temperate-climate fiord in the mid-latitude southern hemisphere, Milford Sound was the natural choice for this project, which focuses on both the post-LGM evolution of the fiord, and the record of post-glacial landslides preserved in the catchment. In fact, these two evolutionary facets of the Milford catchment are inextricably linked; a substantial record of post-glacial landslides is constrained by LGIT timing, especially where chronological control for specific landslide events is not available (as is the case for most of the submarine deposits in Milford Sound). The maximum ages of these events, constrained by LGIT timing, directly influence estimates of risk associated with future landslides and landslide-generated tsunami (see Chapter 4).

The influence of a tectonically active plate boundary on fiord sedimentation is clearly evident in the Fiordland landslide record, particularly at Milford Sound, where extreme topography combines with seismic activity to cause mass wasting; at least 30 very large ($\geq 1 \times 10^6$ m^3) post-glacial landslides are preserved in the Milford catchment (Hancox and Perrin, 2009, and this study), and many smaller landslides have occurred in more recent times (Korup, 2005b). Sediment input from co-seismic landslides is likely a major contributing factor to Holocene terrestrial sediment input that appears to be significantly higher than other New Zealand fiords (Barnes and Pickrill, unpublished; Knudson et al., 2011; Pickrill, 1993). Data presented in this chapter document a fiord-bottom sediment package that is dominated by the products of mass wasting in the Milford catchment.

3.2 Methods

Although there is a wonderful legacy of glacial geomorphology (much of it LGM) preserved in the study area, extremely high precipitation and relatively low erodibility of basement rocks has resulted in a paucity of late-glacial sediment; there is very little Quaternary sediment preserved subaerially in the Milford catchment. Due to a lack of dateable glacial sediments preserved in the subaerial environment, the specific timing of glacial retreat during the LGIT was not previously well constrained for the glaciers that occupied Milford Sound and its tributary valleys.

3.2.1 Data types and sources

A multi-proxy approach was used to better understand the overall glacial retreat history at Milford Sound. To estimate the age of glacially-modified bedrock surfaces, Schmidt

Hammer (SH) relative hardness measurements were sampled for twenty-five exposed bedrock sites, calibrated with eight exposure ages from terrestrial (in-situ ^{10}Be) TCND analysis of glacially modified bedrock surfaces. The resulting exposure-age record was supplemented with seismic reflection and core data from submarine sediments, and geomorphic mapping of both submarine and subaerial environments; together these data allowed a millennial-scale reconstruction of the glacial retreat story at Milford Sound.

3.2.1.1 Surface exposure dating using terrestrial cosmogenic nuclides

Primary galactic radiation (predominantly composed of high-energy nucleons that originate outside of Earth's solar system) interacts with particles in the upper atmosphere, creating nuclear disintegration reactions that produce secondary cosmic radiation. Cosmic ray flux at the Earth's surface produces cosmogenic nuclides, some of which accumulate in rock and soil (Gosse and Phillips, 2001).

Cosmic ray flux varies both temporally and spatially; the amount of secondary cosmic radiation that reaches a specific point on the Earth's surface is dependent upon the intensity of Earth's magnetic field, which varies over time, and with geomagnetic position (altitude and latitude). Therefore, the accumulation of cosmogenic nuclides near the Earth's surface depends upon the exposure time of the surface relative to the half-life of the isotope, and the geomagnetic position of the site.

Over the past several decades, radiocarbon dating has been the most widely used numerical dating technique for Holocene and latest Quaternary environmental construction. Radiocarbon dating generally has a higher degree of precision than TCND, but depends upon the presence of suitable organic sediment, so age-control is commonly associated with depositional units that overlie, or underlie the unit that is being dated (e.g. a glacial moraine overlying a peat layer). Therefore, fully understanding the depositional environment and stratigraphic relationships is fundamental when interpreting radiocarbon results.

Surface exposure dating using TCND has developed rapidly in recent decades, and is now a widely used technique for understanding Earth surface processes, especially where direct age-control on bedrock or boulder surfaces is advantageous (e.g. the surface of a glacial moraine or landslide deposit, or glacially modified bedrock surface), or where there is a lack of organic material suitable for radiocarbon dating (e.g. polar regions). Although TCND is still not as precise as some other dating techniques available to geoscientists, Accelerator Mass Spectrometry (AMS) now allows accurate measurement of extremely low isotopic ratios, and improvements in geomagnetic models for the

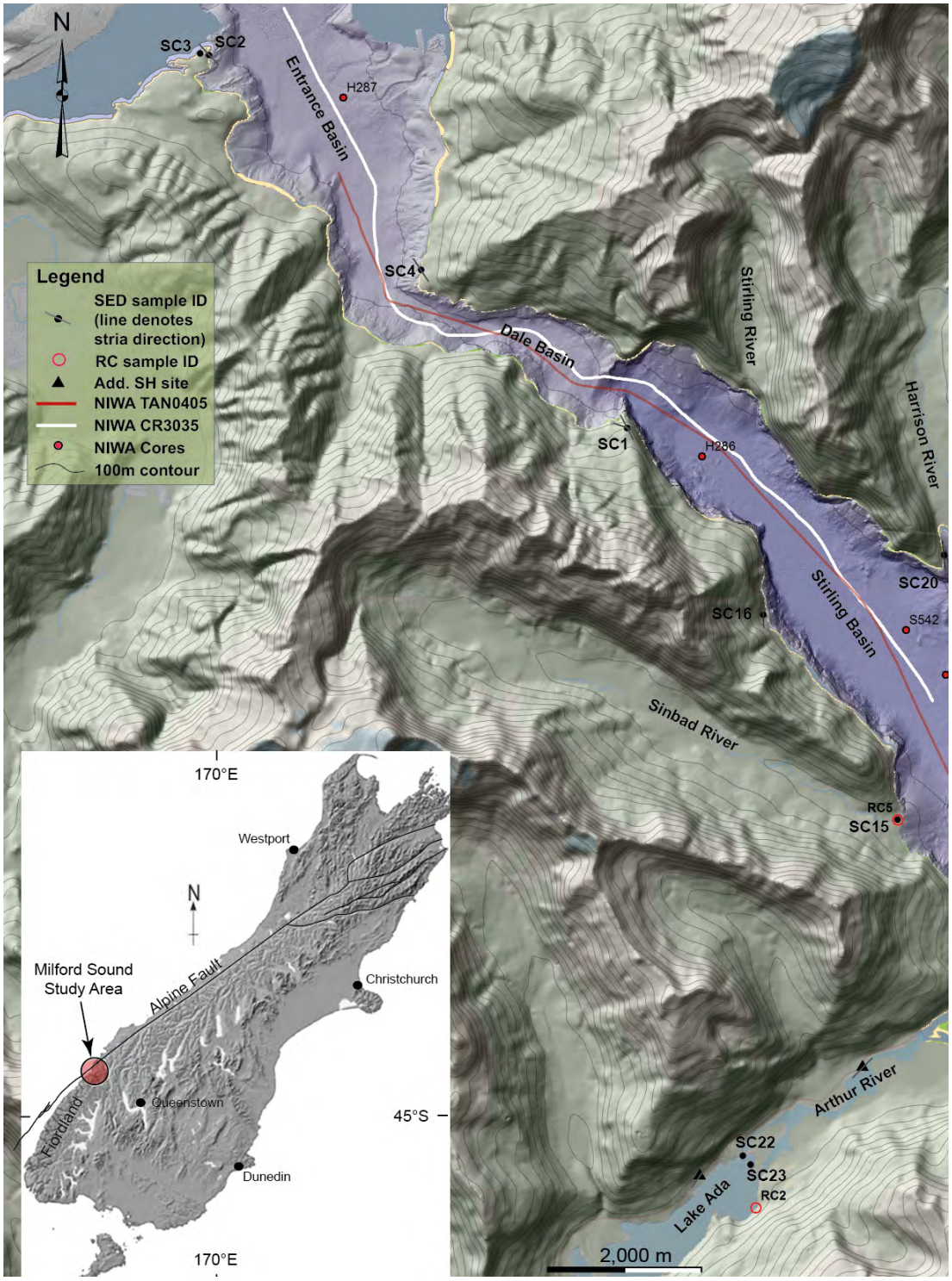

Figure 3.1: Hillshade map showing Milford Sound study area with sample locations (some samples were not analysed). Green shading = vegetation, contoured light blue shading = glacier ice cover, uncontoured light blue shading = rivers & lakes, yellow shading = shoreline, purple shading = marine (fiord). Part 1 of 2. Inset map shows study area relative to the South Island and Alpine Fault.

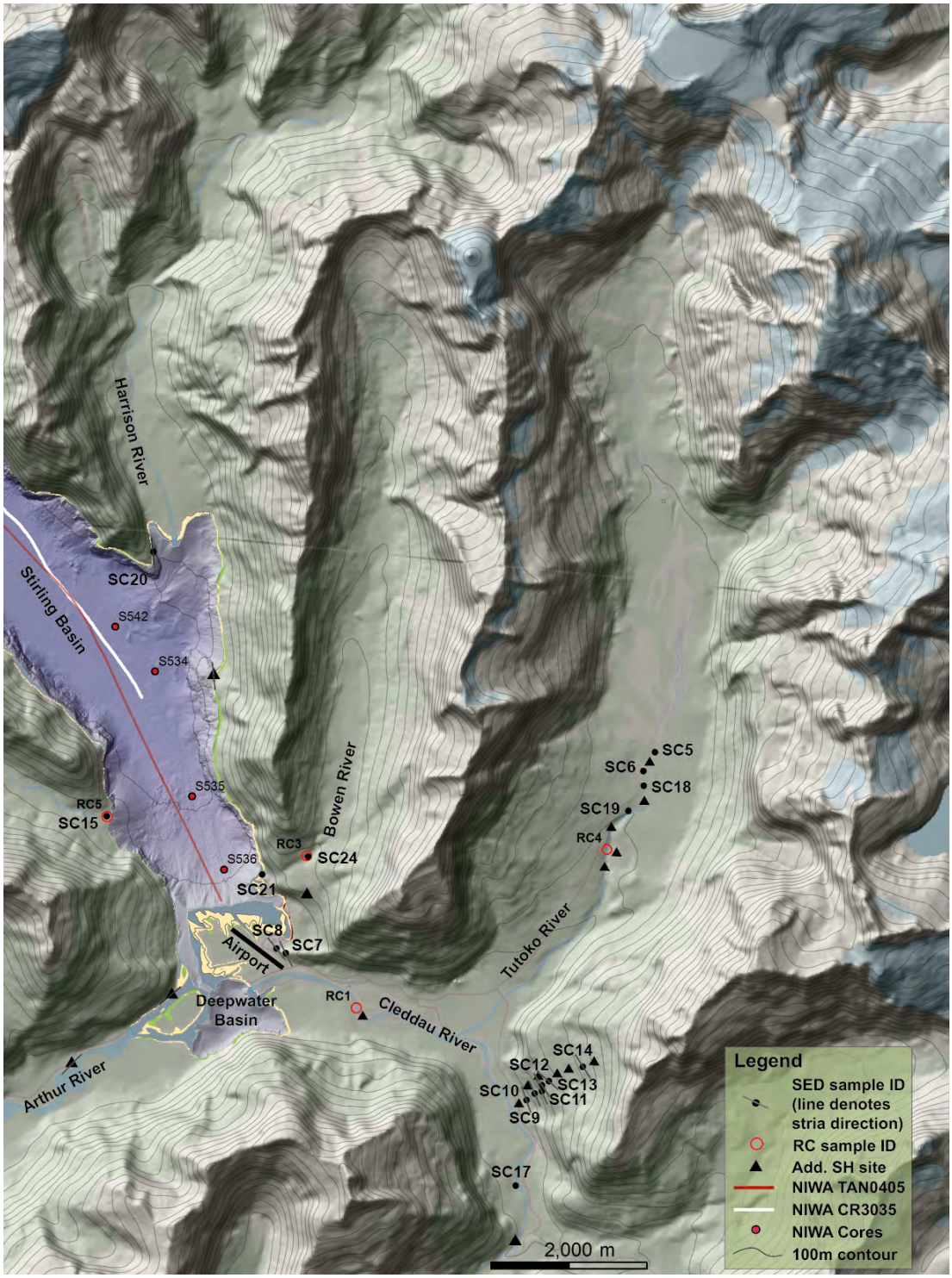

Figure 3.2: Hillshade map showing Milford Sound study area with sample locations. 100 m contours & bathymetry. Land contours & hillshade derived from LINZ/Univerisity of Otago 15 m DEM, fiord bathymetry & hillshade derived from NIWA data (see text). SED = surface exposure dating (^{10}Be) sample site. All SED sites include Schmidt Hammer (SH) testing. Line through SED symbols = direction of glacial stria. RC = radiocarbon sample site. Solid triangles are SH only test sites. Part 2 of 2.)

Earth's surface (e.g. see Balco et al., 2008) have facilitated the calculation of exposure ages with millennial-scale accuracy (e.g. Putnam et al., 2010a; Shulmeister et al., 2010). The precision of TCND continues to improve, but the accuracy of the technique is currently limited by uncertainty around terrestrial cosmogenic nuclide production rates, which are influenced by local variations in atmospheric pressure, magnetic field, and solar modulation (Gosse and Phillips, 2001; Putnam et al., 2010b).

3.2.1.2 TCN production rate variability and local calibration

Due largely to systematic uncertainty around local production rates, problems which require sub-millennial accuracy have traditionally not been well-suited to TCND. However, this situation may be improving, as locally-derived TCN production rates, calibrated with independent age-control data, are increasingly becoming available. Over the past two decades, a network of ^{10}Be production-rate calibration sites have been established, mostly concentrated in the northern hemisphere mid-latitudes (summarized in Balco et al., 2008), potentially allowing the application of local (rather than globally averaged) production rates to exposure-age calculations.

There are many southern hemisphere sites for which in-situ cosmogenic ^{10}Be measurements are available (e.g. Ackert Jr et al., 2008; Barrows et al., 2007; Schaefer et al., 2006; Shulmeister et al., 2010; Sutherland et al., 2007). However, until recently, exposure-age calculations have had to rely on available northern hemisphere production rates, in the absence of any calibrated mid-latitude ^{10}Be production sites from the southern hemisphere. Recently, Putnam et al. (2010b) derived a ^{10}Be production rate from boulders on the surface of a "debris flow" deposit in the Macaulay valley, in the central Southern Alps of New Zealand. This locally-derived production rate was calibrated with ten radiocarbon ages from a buried soil horizon beneath the deposit, which constrained the maximum age of the deposit to $9,690 \pm 50$ years before AD 2008. The calibrated local production rate was independently confirmed by measurements of ^{10}Be concentrations from the Boundary Stream Tarn (BST) moraines, which lie ∼60 km southwest of the Macaulay valley, and had been independently radiocarbon dated to $\sim 18,060 \pm 200$ years before AD 2008 (Vandergoes et al., 2008).

Further supporting evidence for the Macaulay production rate has come from the Lago Argentino area of Patagonia, where moraines have minimum-limiting ^{14}C age control; Kaplan et al. (2011) found that ^{10}Be exposure ages of surface boulders on the Lago Argentino moraines were younger than calibrated ^{14}C ages for the same moraine ridges, when calculated with the commonly accepted global average production rate (e.g. that used in the standard Cronus Earth calculator, Balco et al., 2008), but were consistent

with the radiocarbon ages when calculated using the Macaulay production rate. Although further testing of the Macaulay production rate on other mid-latitude southern hemisphere sites is desirable, current evidence suggests that the locally-calibrated production rate may be more applicable to New Zealand sites than the commonly accepted global calibration rates.

While a detailed discussion of the theory and application of surface exposure dating using in-situ cosmogenic nuclides is beyond the scope of this thesis, the subject has been well-covered by other authors. For example, the reader is directed to Gosse and Phillips (2001) and Dunai (2010) for in-depth reviews of the theory and application of TCND.

3.2.1.3 Aerial photography

Prior to field work, available black and white aerial photography was examined for evidence of landslide deposits and potential source areas, and bedrock features that may be indicative of deep-seated or incipient failure (e.g. cracking, slumping, detached, toppled or rotated blocks, or gravitational spreading). A stereoscope was used to view stereo pairs; photographs were provided by New Zealand Aerial Mapping Ltd., and were obtained from an altitude of 8,840 m, on 15 December, 1988.

3.2.1.4 Bathymetry: multibeam sonar (NIWA)

A high-resolution multi-beam sonar system was used by NIWA to acquire bathymetry of the Fiordland continental shelf and fiords, including the Milford Sound area. The data were obtained in 2004, using a Simrad EM300, 30 kHz multi-beam echo sounder aboard the *R. V. Tangaroa*. Additional EM300 multi-beam data were collected by LINZ during hydrographic surveys in 2008; these data were provided to NIWA. The DEM data provided by NIWA for the current project is a merged data set derived from both the 2004 NIWA survey and the 2008 LINZ data. Use of all NIWA data cited in this project was provided for by a data-sharing agreement with the University of Canterbury. The DEM data were provided by NIWA in ESRI grid format, with a 4 m grid size. This high-quality bathymetric data allowed the submarine geomorphology of Milford Sound to be investigated with a high level of detail.

3.2.1.5 Seismic reflection data (NIWA)

Multi-channel seismic reflection profiles of fiord thalwegs were collected by NIWA during research cruise CR3035 in 1997; the airgun source consisted of a single 105/45 GI gun

operated in GI mode at 2,000 psi pressure. These data were processed at NIWA. In 2004, boomer seismic reflection profiles were acquired during NIWA cruise TAN0405, using an Applied Acoustics CSP300J system. Hard copies of these seismic reflection data were investigated during a 2009 visit to NIWA's Greta Point facility in Wellington, and selected analogue profile sections from Milford Sound were later digitized. Images were professionally scanned, before processing using Adobe Photoshop. Processing included cropping of scanned images, converting to greyscale to reduce file size, and in some cases, applying a filter to remove some signal noise. Adobe Illustrator was used to draft and annotate seismic interpretation figures.

3.2.1.6 NIWA core samples

Six piston-core samples were recovered from Milford Sound bottom sediments by the former New Zealand Oceanographic Institute (presently NIWA); cores H285 and H287 were collected in 1971, and cores S534, S535, S536 and S542 in 1983. The sedimentary structure and features of all six cores were investigated during a 2011 trip to Greta Point. Core depth ranged from 1.5 m to over 4 m. Cores H285 and H287 were not logged in detail as they had dried and broken up, and were no longer coherent, so it was difficult to ascertain their true structure. Core S534 was considered to be the most representative of the four Stirling Basin cores; a detailed core log and discussion for core S534 are provided in subsequent sections. Some age control has recently been published for core S534 (Knudson et al., 2011), allowing comparison of the sedimentation record in Stirling Basin with other records. The remaining three cores from Stirling Basin (S535, S536 and S542) were also logged in detail, and full descriptions and core logs can be found in the appendices.

In addition to logging the cores, the following data were recorded from NIWA's data repository, and entered into an Excel spreadsheet:

- core stations and depth
- grain size distribution: mean grain size (Phi), standard deviations, skewness and kurtosis
- relative percentages of gravel, sand, silt and clay
- calcium carbonate and organic concentrations

These data are also provided in the appendices.

3.2.1.7 GIS mapping

In order to facilitate the management and geospatial referencing of large amounts of data from a wide range of sources (e.g. Land information New Zealand (LINZ) topographic mapping and DEM, NIWA submarine survey data, GNS geological data (QMAP), field sample sites and GPS data, aerial survey routes from GPS, landslide deposit areas, etc.), a Geographic Information System (GIS) was developed for this project. It is hoped that future work will yield additional data that can be easily added to the GIS, which was primarily developed using the ArcGIS software package from ESRI.

At present the GIS includes the following geospatial data (see Figures 3.1 and 3.2 for representative GIS mapping and data locations):

- Topography: 15 metre digital elevation model (DEM), based on LINZ aerial photogrammetry (same as that used for the national Topo50 map series), compiled by the National School of Surveying, University of Otago (Columbus et al., 2011),
- LINZ topographic mapping, covering the subaerial part of the study area (www.linz.govt.nz, accessed 30 September, 2010),
  - landcover: vegetation, hydrography (lakes, rivers, swamps, glacier ice), coastal features (rocks, shingle, sand), roads, structures, etc.
  - 20 metre contours
  - hillshade models
  - spot heights
- GNS Science geological data (QMAP, Turnbull et al., 2010),
  - structural geology: faults, folds, dikes, horizons, etc.
  - geological units: bedrock geology, Quaternary sediment, etc.
- NIWA submarine survey data,
  - bathymetry: 4 m DEM based on high-resolution multi-beam sonar data (cruise TAN0405, 2004, and LINZ hydrographic survey, 2008)
  - DEM-derived 5 metre contours, hillshade models
  - navigation and sounding data for seismic refection surveys: Uniboom (cruise TAN0405, 2004) and multi-channel (cruise CR3035, 1997)
  - locations for piston core samples (1971, 1983)

- field sample sites (TCND, Schmidt Hammer, radiocarbon, etc.),
- GPS tracking data and waypoints from field sites and aerial reconnaissance surveys,
- submarine and subaerial landslide deposits.

3.2.1.8 Vulcan 3-D model

The GIS facilitated the integration of subaerial geospatial data with submarine data from NIWA, enabling the production of a relatively seamless three-dimensional geomorphic model (see Figure 3.3) of the entire study area, using the Vulcan geological modelling software (by Maptek). The 3-D Vulcan model was generated by applying the following procedures:

1. ArcGIS (3D Analyst extension) was used for hillshade analysis of both sets of DEM data (LINZ DEM and NIWA bathymetric DEM). Resulting hillshade models were saved as high-resolution raster images.
2. ArcGIS was used to "smooth" out the DEM data, to minimize minor variations and irregularities. Due to the extremely high topographic relief of the study area, and in order to keep the amount of data in the 3-D Vulcan model manageable with a desktop computer, DEM smoothing was performed prior to contour production. Smoothing was accomplished by applying the "focal statistics" tool (ArcGIS Spatial Analysist extension) to the original DEMs; parameters used were "circle" neighborhood, with a radius of 3 cell units, and a statistics type of "mean". Original DEM data was saved as well.
3. the resulting smoothed DEMs were analysed with the ArcGIS 3D Analyst contour utility; 20 m contours were generated from the LINZ DEM, and 5 m contours from the NIWA bathymetric DEM.
4. The spatial extent of each of the two smoothed DEMS (LINZ topographic and NIWA bathymetric) was calculated as an edge polygon, using ArcGIS.
5. ArcGIS contours and DEM extents were exported as ESRI shapefiles, which were then available to import into Vulcan.
6. After importing into Vulcan, contours were used to create triangulated surfaces.

7. Triangulations were then visually checked for consistency with the imported DEM extents; any overlap in coverage was removed by adjusting the appropriate extent polygon. Any gaps in coverage were left unmodified.

8. Triangulations were trimmed to their revised extents using Vulcan's "relimit" utility. As the NIWA bathymetric DEM was derived from multi-beam sonar data, which does not normally extend as far as the shoreline, some data gaps are present between the submarine data and the LINZ subaerial DEM.

9. The LINZ and NIWA bathymetric triangulations were merged using Vulcan's "merge" utility. Individual triangulations were also retained.

10. ArcGIS hillshade images were imported into Vulcan, and registered to the triangulations (DEMs) using a minimum of 10 registration points each.

11. Registered hillshade images were then "draped" over Vulcan triangulations by applying them as texture mapping.

12. Vulcan was used to generate new contours at 20 m intervals, from the merged DEM triangulation.

The resulting integrated, georeferenced hillshade model was used for three-dimensional landscape visualization and geomorphic interpretation, including measurement of slope aspect and gradient, and estimation of landslide characteristics (see Chapter 4 for details).

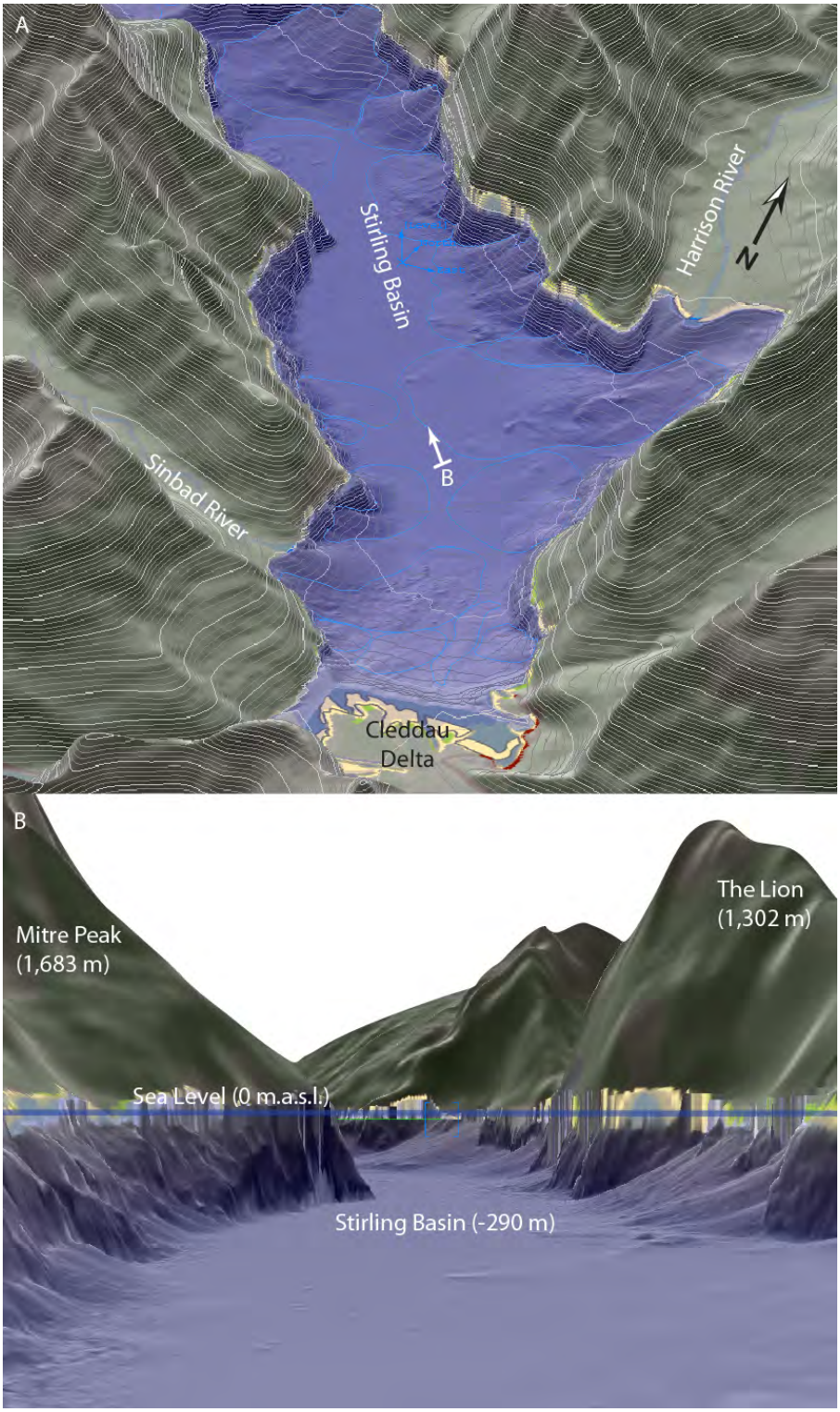

Figure 3.3: Vulcan 3-D model: A) Stirling Basin, oblique view, submarine shaded in purple. Contour interval 100 m. Submarine landslide deposits outlined in blue. B) Perspective view from point "B", indicated by arrow in A). Viewpoint looking northwest from sea level. Mottled shading near shoreline indicates data gap between subaerial DEM (LINZ) and bathymetric DEM (NIWA).

3.2.2 Timing of field work

Initial reconnaissance and preliminary field work (ground-truthing) for the Milford Sound study area were completed prior to November, 2009. Sample collection (material for TCND and radiocarbon analysis), SH hardness testing and helicopter aerial survey were primarily completed between November 2009 and April 2010, plus a trip in February 2011 to collect additional sample from several sites for TCND analysis. Despite challenging access to some sites as a result of steep and heavily forested slopes, and the typical Fiordland bouts of wild weather, field work progressed remarkably smoothly, with a total of approximately 85 days of field work required to access the sites and collect the field-based data described in subsequent sections.

3.2.2.1 DOC approval and permits

The field study area is located entirely within Fiordland National Park, which is managed by the Department of Conservation (DOC). Part of the study area was also within the Pembroke Wilderness area, northwest of, and adjacent to, Milford Sound. Wilderness areas are intended to be preserved in a pristine state; there are no tracks or huts, and all vehicular access (including aircraft overhead) is prohibited. As a result of the special wilderness, conservation and recreational values of the study area, research and access permits were required from the Minister of Conservation before field work could proceed.

Low Impact, Research and Collection Permit (No. SO-26550-RES) was applied for and granted by the Minister of Conservation, for field work within Fiordland National Park, including collection of rock, soil and organic samples, and Schmidt Hammer hardness testing. In addition, a Concession Permit for aircraft landing, and transportation support to non-concession areas (e.g. flying above Pembroke Wilderness Area) was applied for and granted by the Minister of Conservation for this project. Special conditions of the permits included thorough cleaning of all sampling equipment and footwear prior to fieldwork (to prevent spread of any noxious organisms), and research findings to be made available to DOC upon completion of the project.

3.2.3 Preliminary field investigations

Reconnaissance and preliminary field investigations within the study area were primarily focused on ground-truthing reasonably accessible sites for sampling of exposed bedrock, as well as landslide deposits and landslide source areas that had been identified from aerial photographs (see Figures 3.4 and 3.5). Ground-based investigation

Figure 3.4: Field reconnaissance photos: A) Milford airport and visitors centre from Mitre Peak. B) Tutoko valley. C) Fiordland bog. D) Camp at the base of Mitre Peak. E) Lake Adelaide, central Darrans reflected in tarn. F) Crossing the Tutoko River. G) Kayaking across Milford Sound, The Lion (1,302 m) in the background. Photos by S. Furkert.

included five large landslide deposits near the head of Milford Sound; one in the Tutoko valley, two in the Cleddau valley, one in the Arthur valley (Lake Ada), and one in the lower Sinbad valley (see Chapter 4, Figure 4.2 for locations and detailed discussion of these deposits).

3.2.3.1 Tsunami deposits

Several flat sites near sea level were also investigated that had been identified as having potential to store tsunami deposits. These sites were primarily located in the lower Cleddau River valley and on the Cleddau/Arthur delta. Several small test pits were excavated with hand tools, and bank exposures along the lower Cleddau River were cleared of loose material and investigated. None of the sites showed any obvious evidence of past tsunami, and field observations suggest that fluvial and mass movement processes dominate sedimentation on the active Cleddau/Arthur delta. Although few and far between, occasional flat sites around the shoreline of Milford Sound were able to be accessed by kayak, and were also investigated for potential tsunami deposits. None of these sites showed any evidence of tsunami deposits (such as sandy shell beds well above high tide level, or forest trimlines). The deep fiord basins, rocky shorelines and thick vegetation suggest that preservation of tsunami deposits within Milford Sound is fleeting at best.

Figure 3.5: Preliminary field work photos: A) Lower Cleddau valley river bank exposure. B) Cleddau delta test pit. C) Looking for shoreline tsunami deposits. Photos A & B by A. Dykstra, photo C by author.

3.2.3.2 Lake Adelaide landslide deposit

A huge rock avalanche deposit which dams Lake Adelaide was also investigated during a reconnaissance trip in February 2009 (see Figure 3.6), with access by foot up the rugged Moraine Creek valley. Although geographically close to Milford Sound (∼10 km southeast of Milford airport, off the bottom right of Figure 3.2), the Adelaide deposit lies on the east side of the drainage divide created by the Darran mountains, and drains into the Hollyford Valley. We re-visited the deposit in March 2010, this time accessing Lake Adelaide with a mountaineering-flavoured route from Homer Hut, via Gertrude valley to Gertrude Saddle, over Barrier Knob to Adelaide Saddle and down Gifford's Crack. Several ridges or lobes of the gigantic (∼2 km across) deposit were sampled over two days, including collecting 6 samples for TCND analysis. Fortunately, with a lot of extra weight in rock samples and gear, we were able to catch a helicopter ride back to Homer Hut! Although not reported here, the Adelaide TCND samples await future processing and analysis.

Figure 3.6: Lake Adelaide, field work photos: A) Tent Flat, Moraine Creek valley. B) Lake Adelaide, central Darran Mountains. C) Camp at Phil's biv. D) Typical angular boulders on surface of deposit. E) Lake Adelaide, rock avalanche deposit and source area to right (dashed red polygon), mid-left is Adelaide Saddle above Lake South America, and Mitre peak just visible in the background. F) Adelaide Saddle, about to descend to Lake South America via Gifford's Crack. G) Milford Sound from Adelaide Saddle. H) Crossing Barrier Knob. I) Lake Adelaide deposit, view north towards Moraine Creek valley. Photos by author, except B,D,E,F,H by S. Furkert.

3.2.4 Aerial reconnaissance survey

A helicopter reconnaissance survey of the Milford catchment, including collection of oblique aerial photographs and some video, was completed during field work in November 2009 and February 2010. The primary objectives of the aerial survey were:

- to confirm sampling sites suitable for SED of glacially-modified bedrock (either by TCND or Schmidt Hammer),
- to identify and photograph large landslide deposits,
- to identify and photograph potential landslide source areas,
- to identify and photograph bedrock features that may be indicative of deep-seated or incipient failure (e.g. tension cracks, slumping, detached, toppled or rotated blocks, or gravitational spreading (*Sackung*),
- to develop a general regional feel for potential risks related to landslides and landslide-generated tsunami, informed by close visual investigation of the extreme and inaccessible terrain.

The aerial survey proved extremely valuable, allowing a quick assessment of the viability of sites that were being considered for sampling. For example, the tree slide in the lower Cleddau valley was initially investigated from the air, and confirmed as a likely sampling location; likewise, the top of a bedrock spur (site SC1) across Milford Sound from Stirling Falls (and not obvious from water level), was established as a potential site for TCND sampling. In addition, previously unidentified landslide deposits were located during the aerial survey, including the Bowen valley deposit, and several deposits in the Arthur River catchment.

The helicopter survey also allowed the investigation of bedrock features that had been previously identified on aerial photographs as potential indicators of recent, or incipient failure. Flights concentrated on priority areas close to Milford Sound, including the east and north faces of Mount Philipps, the east, south and north faces of Barren Peak, the ridges above Sinbad valley, the north-facing aspects of Mitre Peak (and adjacent peak, 1141 m), the precipitous slopes of the Lion, the southwest face of the Elephant, and the south and west slopes of Mount Pembroke and Rover Peak.

Some slopes were deeply incised (up to ~40 m) where drainage had exploited obvious near-vertical or oblique structural weaknesses (see Chapter 4, Figure 4.9), however no obvious indicators of incipient failure were noted. Evidence for progressive weakening of certain slopes was noted; details are discussed in Chapter 4. Likely source areas for

Figure 3.7: Helicopter aerial survey. Photo by S. Furkert

several existing landslide deposits were investigated, including deposits in the Tutoko, lower Cleddau, Arthur and Bowen valleys, and slopes that could have contributed landslides directly into the fiord. Many source areas are readily observed (including above some of the larger submarine deposits) from geomorphic evidence, and are generally characterized by what appear to be deep-seated failures (based on observed headwall heights of up to several tens of metres) along steeply dipping failure planes, which are parallel or sub-parallel to face aspect. See Chapter 4 for a detailed discussion of these features.

3.2.5 Sample collection for surface exposure dating (TCND and/or Schmidt Hammer)

3.2.5.1 Glacially modified bedrock near sea level

There are many locations where excellent evidence of glacial modification (striations, glacial polish, p-forms) is preserved on the bedrock walls around Milford Sound. However, most of these locations are not practical for sampling, due to the extremely high and steep-walled cliffs that surround the fiord, and the almost complete lack of accessible shoreline. In river valleys upstream of the major deltas, thick vegetation covers

most slopes up to the treeline, and there are very few accessible bedrock exposures with evidence of glacial modification (see Figures 3.8 and 3.9).

Despite these challenges, twelve sites were identified where excellent examples of accessible glacially-modified bedrock were exposed at relatively low elevations (4 to 240 m.a.s.l.) around the fiord. SH testing was performed on all bedrock sites, and samples were collected for TCND analysis from eight of the twelve sites (see Figures 3.1 and 3.2). An additional fourteen sites were sampled for TCND or Schmidt Hammer analysis (including six TCND samples) along a vertical transect, where a recent tree slide had exposed glacially-modified bedrock in the lower Cleddau valley (details below). All sample sites were selected based on the following criteria:

- preference for sites with preserved surface features diagnostic of glacial activity (e.g. striations, polish, p-forms), or other evidence for negligible erosion since exposure,
- preference for sites with similar lithology and grain size, so that SH values could be meaningfully compared,
- surface areas with visible fracturing or evidence of spalling were avoided,
- adequate horizontal (or near-horizontal) flat surface for sampling, while staying a minimum of 30 cm away from corners or edges that could affect exposure,
- minimal potential for self-shielding by local topographic highs,
- relatively low elevation, well below tree line, so minimal seasonal snow cover,
- minimal coverage by lichens or mosses,
- sampled the highest points of bedrock outcrops which were not likely to have been covered by forest, therefore minimal potential for shielding by thick forest, or soil/regolith cover (some exceptions apply for the tree slide sample sites, see below).

For boulder test sites, the potential effects of post-depositional movement, exhumation and/or burial were minimized by only testing the largest exposed boulders (these were typically at least 4 m diameter) on the highest accessible, unmodified parts of the deposits. The following information was recorded at each sample site:

1. date/time of sampling,
2. GPS data (latitude, longitude, elevation, GPS waypoint reference),

Figure 3.8: Glacially modified bedrock face, near Stirling Falls. Surface features include glacial polish, stria, sichelwannen and cavettos. Ice direction is from right to left. Near-vertical cliff face extends ∼400 m above sea level, as well as ∼290 m below the water surface. Inset photo of lower cliff face from water level. Author photos, 2011.

Figure 3.9: Examples of exposed, glacially modified bedrock near sea level at Milford Sound. Photos by S. Furkert.

3. whether the sample was from exposed bedrock or a boulder,
4. general geology (see laboratory work for discussion),
5. strike and dip of primary bedrock structure, where applicable,
6. average bearing of observed directional glacial features (e.g. striations),
7. topographic shielding data (bearing and inclination for each horizon break point),
8. surface dip angle and direction for non-horizontal surfaces,
9. average TCND sample depth, where applicable,
10. average surface pitting depth,
11. moss cover depth, where applicable,
12. boulder dimensions, where applicable,
13. SH hardness measurements,
14. notes about general weathering, moss and lichen cover, geomorphic significance of site, etc.

A Garmin handheld GPS unit (model GPSMAP 62) was used in the field to record latitude, longitude and elevation data, and to store tracks and waypoints, which were later downloaded to the GIS database. Sample site elevations were checked by plotting GPS waypoint locations on the GIS digital elevation model; where significant discrepancies existed, the DEM elevation was used.

Access to many sampling sites was time consuming, involving kayak trips of up to 40 km (total distance), or walking routes of up to 10 km through mostly untracked bush (and occasionally a combination of both). Additional site access challenges included steep topography, river crossings, torrential rain, and hordes of hungry sand flies.

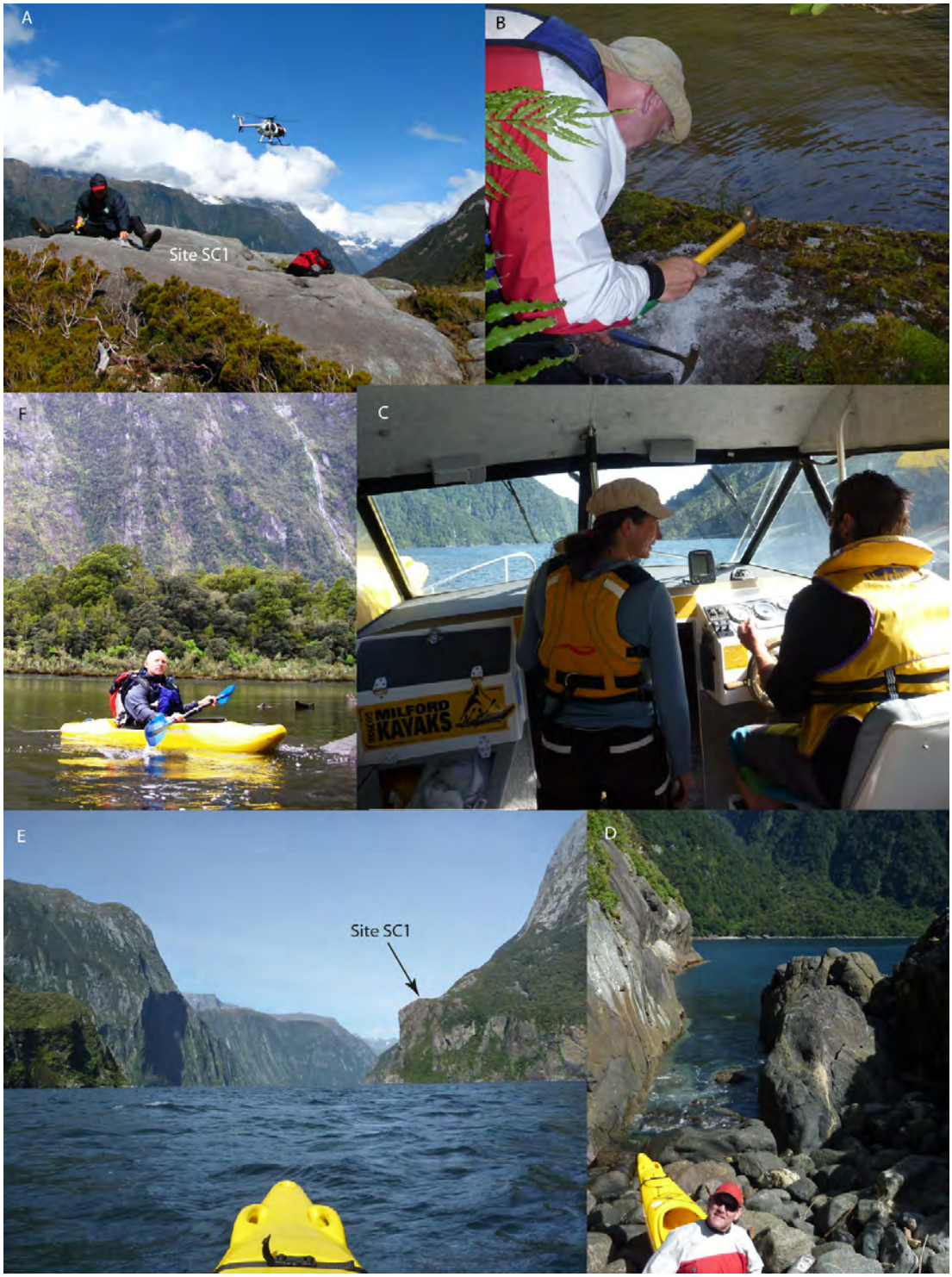

Figure 3.10: Selected field work photos: A) Helicopter access to an otherwise inaccessible site - SC1. B) Shoreline sampling, Harrison Cove. C) Boat transport of gear and kayak to St. Anne Point. D) Kayak access, site SC4. E) Dale basin, looking southeast. F) Shoreline investigation in Deepwater basin. Photos by S. Furkert, except C by author.

3.2.5.2 TCND sample collection

Bedrock samples for TCND analysis were collected using a 2 kg sledge hammer and chisel; the extremely hard, massive, crystalline bedrock of the study area was generally very resistant to the best efforts using hand tools, but the challenges of getting around the rugged terrain meant that carrying bulky power tools was not a valid option. For most TCND sites, the top 1-3 cm of rock was gradually chipped away, although some sites yielded slightly thicker samples (5-7 cm). Samples generally took about 1-3 hours to collect, with an average sample mass of around 1 kg (ranging from ∼700 grams to over 2 kg). Samples were stored in plastic bags, which were labelled with the sample site, sample number and collection date.

A pair of Suunto MC-2 field compasses (with clinometers) were used to measure bearing and inclination for horizon break points, strike and dip of bedrock structures, dip angle and direction for non-horizontal sampling surfaces, and bearing of glacial features. Compasses were set to correct for magnetic declination by 20° east.

3.2.5.3 Schmidt hammer hardness testing

The Schmidt hammer (SH) is a relatively inexpensive, portable and robust instrument that was originally designed for mechanical in-situ testing of concrete hardness. The utility of SH testing has expanded to include applications for rock mechanics (e.g. estimating the uniaxial compressive strength (UCS) and modulus of elasticity (E) of intact rock (Aydin, 2009), and geomorphology (e.g. dating bedrock surfaces, Shakesby et al., 2006). A simple classic Schmidt Hammer measures the percentage rebound distance ("R"-value) of a spring-loaded steel impact plunger that is released when it is pushed against a test surface. The extent to which the impact energy is recovered depends on the hardness (or resistance to impact damage) of the material (Aydin, 2009). There are currently several types of SH available:

1. L-type: mechanical, impact energy 0.735 N m (more sensitive to surface irregularities and measurement of weak, porous or highly weathered rock)

2. N-type: mechanical, impact energy 2.207 N m (less sensitive to surface irregularities, preferred for measurement of harder materials, such as crystalline rock)

3. BL-type (SilverSchmidt): electronic readout and data storage, measures Q-value, impact energy 0.735 N m

4. BN-type (SilverSchmidt): electronic readout and data storage, measures Q-value, impact energy 2.207 N m

SilverSchmidt hammers (BL and BN type) measure "Q"-value, which is the quotient of rebound velocity and inbound velocity; therefore, unlike R-value, Q-value is theoretically independent of the influences of friction and gravity, and SilverSchmidt hammers can be used in any orientation (www.proceq.com, accessed 9 September, 2012). Measurements from different instruments (even of the same type) are generally not directly comparable (as measurements of rebound energy vary depending on hammer condition, age, humidity, etc.), therefore data sets from more than one instrument must be calibrated using common test sites or test anvils. SilverSchmidt hammers compute R-value as well as Q-value, to allow comparison of data sets from standard, fully mechanical L and N type hammers.

Although calibrated radiocarbon ages generally have greater precision than most other absolute-age dating methods (e.g. TCND), the inherent reliance of radiocarbon dating on the presence of organic material can be limiting when attempting to determine the age of bedrock or boulder surfaces, as dating of organic-bearing sediments that overly (or underlie, in the case of boulders) the surface of interest can only provide minimum or maximum age control. In such cases, TCND may be a preferred dating method, as it theoretically allows the absolute exposure age of an inorganic rock surface to be directly measured. However, despite recent improvements in precision, TCND remains a laboratory-intensive, time-consuming and expensive technique (Shakesby et al., 2006; Winkler, 2009).

Using R-values as relative measure of surface exposure age is a technique that assumes that as a rock weathers, the formation of micro-fractures and chemical changes near the rocks surface combine to reduce surface hardness (McCarroll, 1989. The relative degree of weathering of near-surface rock is a function of the amount of time that it has been exposed to both structural weakening and chemical weathering processes, as well as the degree of surface roughness due to differential resistance of surface minerals to weathering. Therefore, factors like lithology, moss or lichen cover, and surface roughness prior to weathering must be considered. Lithology influences rock-surface hardness, resistance to weathering, and surface roughness, so only sites of similar lithological characteristics can be meaningfully compared. In general, R-values are most useful as an indicator of relative age when lithology is consistent, and it can be reasonably inferred that test surfaces had similar textures prior to weathering (McCarroll, 1991); examples include glacially polished bedrock surfaces, boulders on isostatically raised shorelines (e.g. Shakesby et al., 2011) and the surfaces of moraines (e.g. Winkler, 2005).

SH testing of most rock surfaces is non-destructive, leaving only a very slight mark on the surface of the rock, and large amounts of data can be collected relatively quickly; these can be advantages over destructive and time-consuming sampling required for dating techniques which require removal of large samples for laboratory work (e.g. TCND, weathering rind thickness) or excavation of sediment (e.g. radiocarbon dating).

In recent years, Schmidt Hammer Dating (SHD) has been developed as an absolute age-dating technique, by calibrating relative SH hardness measurements with independent age-control, such as TCND exposure ages or radiocarbon ages. This technique has primarily been applied in the context of dating glacially-scoured bedrock and boulder moraine surfaces of post-LGM age (e.g. Matthews and Owen, 2010; Owen et al., 2007; Shakesby et al., 2006, 2011; Winkler, 2009), but has also been successfully applied to other Holocene landforms, including rock avalanche deposits (e.g. Aa et al., 2007). Some workers have suggested that this technique, when applied within the limitations described above, can produced results with precision comparable to, or higher than TCND (Matthews and Owen, 2010; Matthews and Winkler, 2011; Shakesby et al., 2006; Winkler, 2009). However, other workers believe that the relatively high level of confidence that is commonly attributed to the accuracy of SH calibrated age-dating is not necessarily a true reflection of the reliability of the technique. This is due largely to the reporting of mean R-values (and corresponding small standard errors), without accounting for the measurement uncertainty associated with the independent age-control points (Dr. J. Shulmeister, pers. comm., 2013). The potential issues associated with assigning uncertainty to SH calibrated age-dating relationships are discussed in more detail below.

3.2.5.4 Schmidt hammer sampling strategy

All glacially-modified bedrock exposure sites (with the exception of Saint Anne Point sites SC2 and SC3, which were characterized by a markedly different lithology compared to other sites) were hardness tested with a BN-type hammer (SilverSchmidt). Q-values were also recorded for the top horizontal surfaces of some of the largest boulders on the surfaces of several landslide deposits. To eliminate as many non-age-related variables as possible, and to ensure measurement consistency, SH sample sites were chosen with the same criteria as those for TCND samples (see above), with the following additional criteria:

- similar lithology and grain size (all samples were from medium-grained crystalline hornblende-bearing gneiss of generally dioritic composition),

- areas with obviously different surface textures or roughness (e.g. stream scoured, or impacted by rockfall) were measured and recorded independently,
- visible fractures or rock flakes were avoided,
- adjacent measurements had a minimum spacing of 2 cm,
- measurements were not made in wet weather.

For all Schmidt hammer test sites, a minimum of 25 values per site (as recommended by Matthews and Owen (2010) and Shakesby et al. (2006)) were used to derive representative means, with the exception of site "Treeslide3" (n=20) and "SC17 (n=16). The majority of test sites contributed between 40 and 80 values (see Table 3.3). Shakesby et al. (2006) found that mean R-values remained fairly stable, and statistically indistinguishable, for sample sizes between 25 and 150. For some smaller test sites, a lack of suitable area constrained the number of test blows. Sites were generally clean, dry, and free of any lichen or mosses, and no preparation of the weathered bedrock surface was carried out.

For boulder test sites, the largest boulders on the top surfaces of landslide deposits were sampled. The smallest of these boulders measured ∼4 m long x 3 m wide x 4m high (∼48 m^3), and would have weighed around 140 tonnes. Exhumed landslide boulders from the Tutoko and Bowen river channels, and a recent exposure in the Tutoko rock avalanche deposit were also tested, for comparison with landslide surface boulders. Most boulder sites yielded a minimum of 40 Q-values.

Representative mean Q-values were based on combined measurements from multiple boulders from the same test site, where possible. The flat top surfaces of six test boulders had moss cover of up to 5 cm thick; for these sites moss was removed to clear an area large enough for at least 20 blows (∼10 cm x 10 cm), and the surface cleaned of any loose material before testing. SilverSchmidt measurements were always taken perpendicular to test surfaces, most of which were horizontal or near-horizontal (although the SilverSchmidt is designed so that measurements are independent of impact direction). Occasionally, small flakes of the rock surface were chipped off during a hammer blow, resulting in a much lower measurement than other measurements on the same surface. These values were clearly outliers, and were not reflective of other (non-chipping) blows on the same weathering surface. Recommended procedures (Dr. Stefan Winkler, personal communication, 2009) indicate to "not use the value if small fractures were chipped off during testing", therefore these values were not used in the data analysis. Occasionally, blows felt hollow, or did not produce the same rebound

sound as nearby blows on the same surface; this was nearly always the result of thin fractures in the rock, which also produced low measurements that were not used in data analysis.

3.2.6 Treeslide vertical transect, TCND and SH sampling

On the west flank of Mount Underwood in the lower Cleddau valley, an additional fourteen sites were sampled in a vertical transect from ∼35 to 685 m.a.s.l., on a swath of glacially-modified bedrock that was exposed by a tree slide in 2008 (Figure 3.11). The tree slide swath is normally blanketed with forest cover, but at the time of sampling, all sites were stripped to bare, clean bedrock. All fourteen sites were SH tested, and surface samples were collected from six of those sites (SC9-SC14) for TCND analysis; TCND sample sites were limited to rock surfaces that displayed clear evidence of glacial erosion, and were therefore not considered to have been significantly affected by erosion.

Tree slide sampling sites ranged from relatively broad, gently sloping benches (e.g. SC9,SC10,SC12), to much narrower (<2m wide) benches that break up the steep middle section (e.g. SC11,SC13), and the steep upper reach (SC14) (see Figure 3.12). The tree slide was accessed by foot, utilizing standard safety techniques from alpine climbing (i.e. ropes, harnesses and temporary anchors) for the steeper sections. The ∼400 m ascent to the middle-bench area included about five pitches of protected climbing, and took around 9-12 hours (including sampling) on each of two ascents. The first ascent was followed by a 300 m night abseil in the rain, using the abundant trees along the side of the tree slide scar for abseil anchors. The second ascent included sampling up to ∼700 m.a.s.l., and was (fortunately) followed by a helicopter pickup and descent to a waiting car at the bottom of the tree slide.

A return visit in February, 2011, facilitated collection of additional sample material for TCND analysis from the lower section of the tree slide. Due to inherently low quartz content in the local bedrock, approximately 1.5 kg of additional sample material was collected for each of sites SC9, SC10 and SC11 (see laboratory work, below). During this trip, additional sample material was also collected from site SC4, which was accessed by kayak.

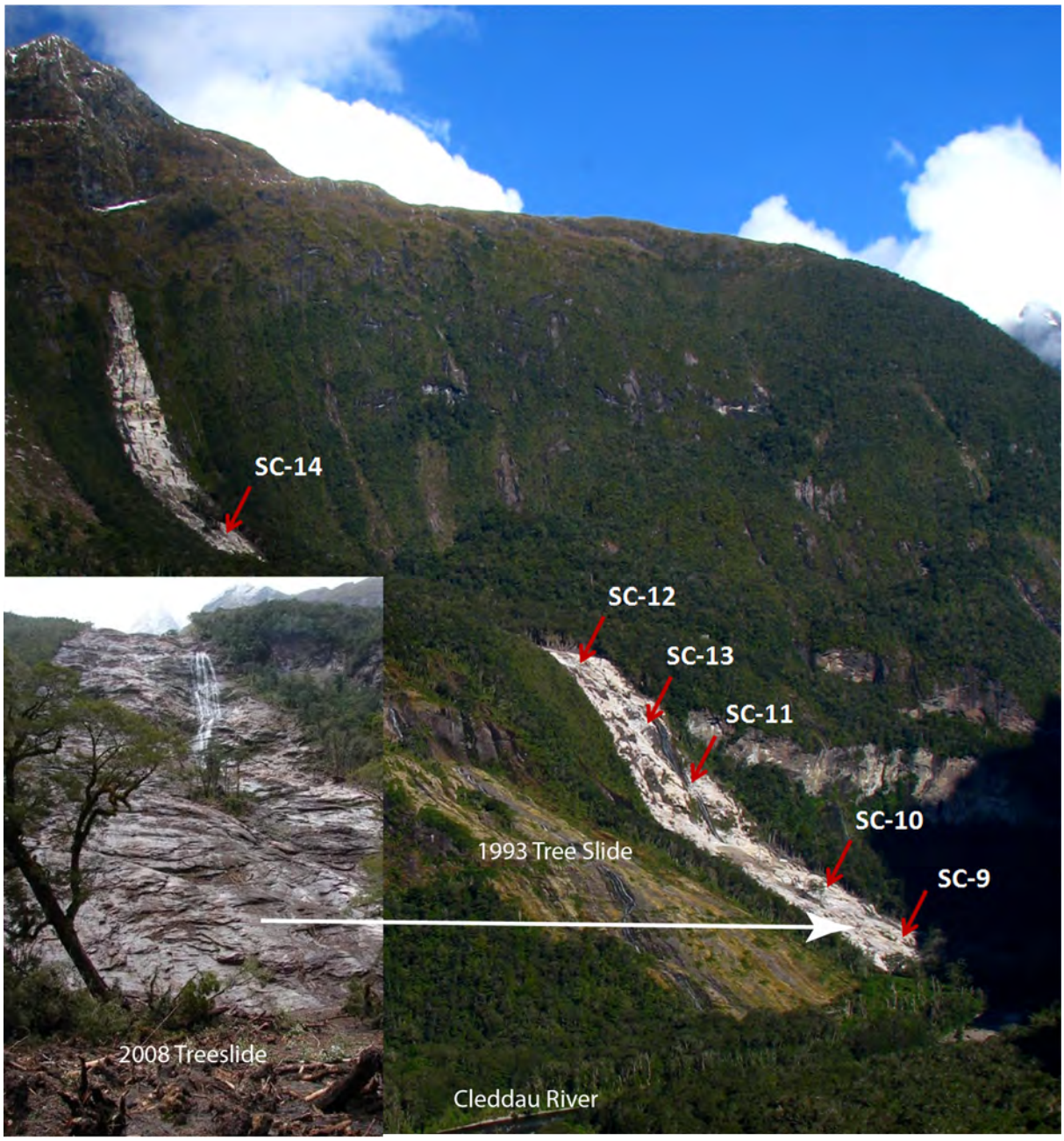

Figure 3.11: September 2008 tree slide, west face of Mount Underwood. Slide scar extends from treeline at ∼1000 m.a.s.l., to the Cleddau valley bottom at 35 m.a.s.l. Arrows and text indicate sample locations. Note partial regrowth of 1993 slide scar, immediately left of 2008 slide. Inset photo shows the lower part of the 2008 slide, photo by N. Oliver, Sept. 2008. Main photo: author photo, 2010.

Figure 3.12: Tree slide, selected field work photos: A) Lower tree slide, striated bedrock near site SC9. B) Near SC10, access route to right of waterfall. C) Preparing to sample at site SC11. D) SH measurements, near site SC13. E) Ascending between SC13 and SC12. F) Glacial grooves, site SC12. Photos by author, except B,C by S. Furkert.

3.2.7 Radiocarbon samples

Six large landslide deposits were investigated near the head of Milford Sound; one in the Tutoko valley, two in the Cleddau valley, one in the Bowen valley, one in the Arthur valley (Lake Ada), and one in the lower Sinbad valley. Field investigation included confirming the spatial extent of the deposits against available aerial photographs and geomorphic mapping, as well as attempting to assess the sedimentary and stratigraphic characteristics of the deposits (see Chapter 4 for deposit details). As noted previously, an additional large landslide deposit was also investigated, at Lake Adelaide, in the Hollyford catchment.

River-bank exposures, caused by recent re-activation of three of the deposits (Tutoko, lower Cleddau, and Bowen) were investigated; these exposures provided an excellent opportunity to independently date the corresponding landslide events using radiocarbon analysis of tree branches and twigs entrained within the landslide material. Three independent samples were collected for radiocarbon analysis from each of the three deposits (see Table 3.5).

The Lake Ada deposit was also independently dated using radiocarbon analysis of outer wood from drowned, standing tree trunks, which would have died shortly after the landslide dam formed the lake. Numerous drowned, standing trees are present in Lake Ada, ranging in diameter from ∼10 cm to over 40 cm. The outermost wood was removed from three of the trees that were in the best condition; hand tools were used from a kayak, to sample wood from ∼50cm above lake level.

Figure 3.13: Drowned standing tree in Lake Ada (not sampled). Author photo.

3.3 Laboratory methods and calculations

3.3.1 Schmidt hammer data

A total of ~4,300 SH measurements were recorded, including calibration tests before, during and near the completion of field work. All recorded Q-value measurements were entered into Excel spreadsheets, and organized by sample site and rock type (e.g. glacially-modified bedrock, eroded bedrock, boulder, etc.), resulting in 45 sample distributions that are presented here (see Tables 3.3 and 3.4, plus field calibration data sets, Figure 3.16). Basic statistics were calculated and histograms produced for each set of measurements, using Grapher8 software (a typical example is included in Figure 3.14).

3.3.1.1 Test for normal distributions

The Kolmogorov-Smirnov (K-S) test compares a sample distribution to a continuous reference distribution, and is sensitive to differences in both the shape and location of the distributions. The K-S test can be used to test if a SH sample distribution comes from a normally distributed population; for example, the computed K-S statistic will be less than the critical value (for $\alpha = 0.05$) 95% of the time, if the underlying population is normally distributed.

Because the means from site-specific Q-value measurement distributions are compared (and ideally used to generate a relative exposure-age chronology), the shape of the distributions must first be considered. If sample data are not normally distributed (e.g. bimodal or skewed), then comparison of the means may not be particularly informative. Grapher8 software was used to produce graphical representations of all Q-value sample distributions, and to calculate their K-S statistic (see Table 3.3). All Q-value sample distributions have K-S statistics that are smaller than the critical values ($\alpha = 0.05$), therefore their underlying populations can be considered to be normally distributed.

3.3.1.2 Test for equivalence of sample distributions

The means of Q-value measurements for bedrock sites follow a clear reverse linear trend when plotted against known exposure ages; as expected, mean SH values decrease with increasing exposure age. A wide range of mean Q-values (~48 to 62) was observed for exposure ages that differed by only ~4 ka (based on TCND analysis). Given the relatively large uncertainties associated with some of the constraining TCND data, compared to SH uncertainty, the statistical independence of SH hardness measurements

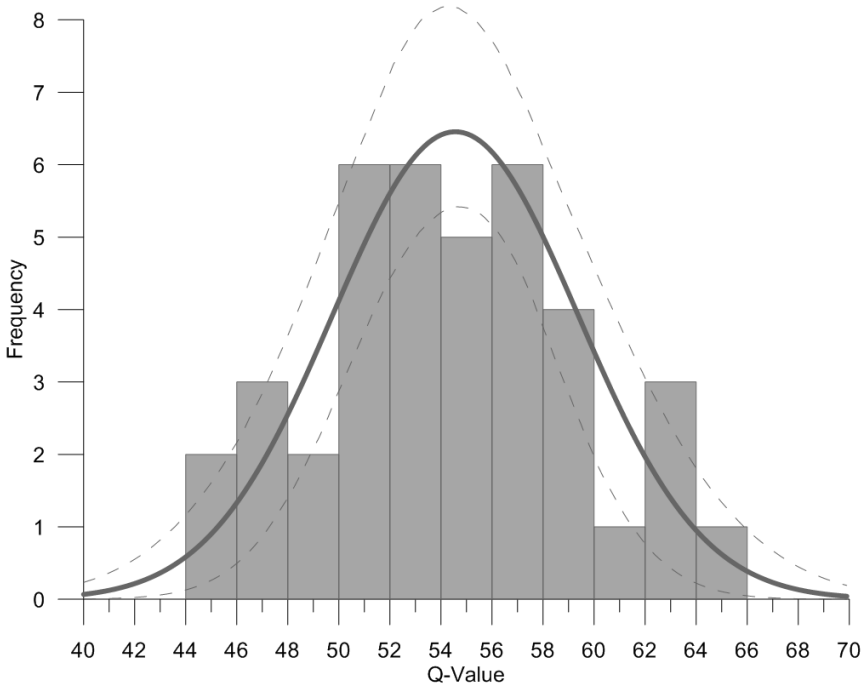

Figure 3.14: Typical Q-value distribution, for Pater Pt./SC16 (see Table 3.3). Reference normal curve has the same mean as the sample (54.56) and a standard deviation of 4.82 (4.88 for sample). Dashed curves bracket 95% confidence limits. For Kolmogorov-Smirnov test of normality, K-S statistic is 0.12, compared to a critical value of 0.21 (for $\alpha = 0.05$), so there is 95% confidence that the sample came from a normally distributed population.

from bedrock sites of differing exposure age is critical to establishing a realistic Q-value-age relationship.

Analysis of variance (ANOVA) provides a statistical test of equivalence of Q-value means; single factor ANOVA was computed for mean Q-value pairs, for bedrock sites where exposure age was constrained with TCND. In particular, tree slide TCND sites were compared, as variation in Q-values over the vertical transect should primarily reflect the ~3 ka of glacial down-wasting indicated by ^{10}Be exposure ages. Site SC11 was not included in ANOVA tests, due to an anomalously low ^{10}Be exposure age, which was not used in the Q-value-age calibration curve (see below for discussion).

ANOVA results ($\alpha = 0.01$, or 99% confidence level) show that Q-value means from tree slide sites SC9 and SC10 are statistically independent, while means from sites SC12 and SC14 are statistically equivalent (although they are statistically independent at $\alpha = 0.08$). ANOVA tests of pairs of sites where similar exposure ages are expected generally indicated that the sample distributions came from the same population; examples include sites near shoreline around Stirling Basin (SC7,SC16,SC20), compared with mid-level tree slide sites (SC12,SC14).

TCND Sample	Mean Q-value	SC4	SC1	SC16	SC20	SC7	SC9	SC10	SC12	SC14
SC4	52.10									
SC1	47.80	×								
SC16	54.56	×	×							
SC20	54.32	×	×	✓						
SC7	53.40	×	×	✓	✓					
SC9	62.17	×	×	×	×	×				
SC10	59.35	×	×	×	×	×	×			
SC12	55.51	×	×	✓	✓	✓	×	×		
SC14	53.13	✓	×	✓	✓	✓	×	×	✓	

Figure 3.15: Single-factor ANOVA tests for equivalence of Q-value means, for sites with TCND age control. Ascending order by distance from Milford glacier terminus (i.e. SC4 is closest). **x** indicates statistical independence of pair, at the $\alpha = 0.01$ significance level. Check marks indicate statistical equivalence of pairs.

3.3.1.3 Field calibration

The SilverSchmidt BN-type hammer was checked for consistency by taking calibration-test measurements on the top of a steel manhole rim, which was located at the Milford Visitors Centre. The manhole rim was easily accessible in an open location, protected by the building to the north, and under the cover of an overhanging roof, so it was

sheltered from wind, sun and rain. Several test blows were performed on the steel rim, in order to ensure consistency, and that any loose material was removed prior to measurement. Subsequent measurements were taken in exactly the same spot (marked by the impact of the plunger). Three separate sets of calibration measurements were performed; one at the beginning of sampling, one after ∼1,000 blows, and one near the end of sampling, after ∼3,600 blows. All three sets of measurements produced the same mean, within 95% confidence limits, so measurement consistency was deemed not to be an issue.

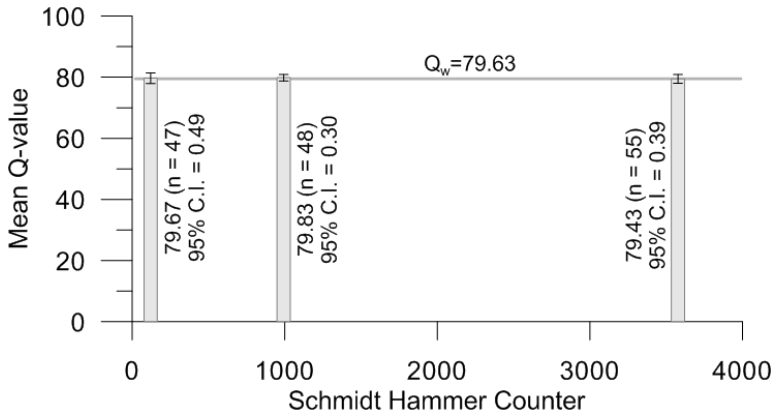

Figure 3.16: Schmidt hammer field calibration measurements: Q-value means from steel manhole rim at Milford Visitors Centre. Error bars are ± one standard deviation. Horizontal line represents weighted mean (Q_w). Field measurements completed at ∼4,300 on counter.

3.3.2 TCND sample preparation

Sample preparation was carried out at the University of Canterbury Cosmogenic Isotope Laboratory (see Figure 3.17), following their recommended procedures, with some additional steps required for extraction of quartz from the feldspar-rich samples (see below). The processes of ^{10}Be extraction from the quartz grains, and preparing AMS targets and procedural blanks were performed according to standard procedures by University of Canterbury Technicians, and are therefore not described in detail here.

Quartz predominantly occurs interstitially with feldspar in the generally dioritic, crystalline bedrock of the sample sites. Quartz and feldspar are hard, resilient silicate minerals with similar chemical properties, so they can be difficult to separate, particularly when they occur interstitially, as is common in fine-grained greywackes (e.g. Shulmeister et al., 2010), and the dioritic samples described here. Concentrated phosphoric acid breaks down feldspars at temperatures over ∼250°C, but does not attack

quartz until temperatures get above ∼300°C, therefore a phosphoric acid leaching process was used here to separate quartz from feldspar. An additional challenge is that most samples contain high concentrations of ferrous minerals (primarily hornblende, biotite and garnet, resulting in a mafic colour index of ∼30 to 50%). As a result, magnetic separation of mafic minerals had to be completed on all samples prior to phoshoric acid leaching. Due to these complicating factors, quartz extraction from samples was challenging and time-consuming.

Quartz extraction was carried out by the author; the basic steps in this process are as follows:

1. raw sample material from each sample was processed with a jaw crusher, before being run through a Bico disk pulverizer (disk spacing was previously adjusted to maximize the fraction at 75 to 500 microns),

2. pulverized material was sieved into four fractions (under 75 micron, 75-212 micron, 212-500 micron, and over 500 micron). Sieved fractions were stored in sample bags, each labelled with sample number and sieve size range,

3. fractions weights were recorded, then the 75-212 micron and 212-500 micron fractions were combined (this combined fraction was used for all subsequent processing),

4. combined 75-500 micron fractions were agitated and rinsed with warm water, until the rinse water ran clear, then set in a drying oven overnight,

5. initial rough magnetic separation was achieved by running the sample under a "lifting" magnet (this removed enough of the magnetic material to prevent the Franz Isodynamic magnetic separator from clogging during the next step),

6. samples were then run through a Franz Isodynamic magnetic separator. Ideal values for amperage, slide angle and tilt were determined by trial and error, based on multiple runs of small representative samples. Once separator settings were optimized, samples were each run through 3-5 times, until nearly all magnetic material had been removed. Magnetic and non-magnetic fractions were stored in labelled sample bags (the non-magnetic fraction was used for all subsequent processing).

7. non-magnetic fractions were then subjected to an "Aqua Regia" process, in order to dissolve metallic and organic compounds; samples were placed in labelled,

sealed plastic jars containing a freshly mixed concentrate of nitric and hydrochloric acid, and then immersed in an ultrasonic bath, which was set to operate for two 8 hour cycles over a 24 hour period,

8. following Aqua Regia, samples were thoroughly agitated and rinsed with warm water, and set in a drying oven overnight,

9. samples were then subjected to progressive phosphoric acid dissolution treatments to remove feldspars; ∼100 g fractions from each sample were weighed and mixed in 1 litre Pyrex flasks with ∼300 ml of concentrated (85%) phosphoric acid, and heated to ∼250°C. Samples were monitored as they heated up, and were "boiled" for a period of ∼20 to 60 minutes, until they showed signs of feldspar dissolution (i.e. gelling or milky colour). Samples were then cooled, prior to decanting and rinsing with warm water to remove the residual solution of siliceous gel and acid. Some samples had formed into a thick gel or solid during cooling, and required re-heating followed by mechanical breakdown with an acrylic rod,

10. once samples were clean and gel-free, they were dried, and ∼80 ml of 50% sodium hydroxide (NaOH) was added. Samples were then boiled for at least 15 minutes, to allow the NaOH to dissolve the silicate coating left on quartz grains following each phosphoric acid leach,

11. the previous two steps (phosphoric acid leaching and NaOH etching) were repeated until phosphoric acid treatment at temperatures of at least 280°C was applied for a minimum of 30 minutes without any resulting cloudiness of the solution. This took anywhere from 5-10 phosphoric acid-NaOH cycles for each 100 g fraction,

12. once all fractions from each individual sample were deemed "clean", they were combined and sent to the University of Canterbury Chemistry Department for analysis of aluminium concentration; for cases where the resulting concentration was still above the aluminium threshold (for AMS analysis) of 400 ppm, additional phosphoric acid leaching cycles were completed,

13. once confirmed below the aluminium threshold, samples were forwarded to James Oram at the University of Canterbury Cosmogenic Isotope Laboratory for final preparations prior to AMS measurement.

For most samples, kilogram initial sample mass resulted in final quartz masses of 8 to 50 g, although three samples that were collected from sites with quartz veins pro-

Figure 3.17: TCND sample preparation. A) Typical raw rock sample, prior to processing. B = biotite, H = interstitial quartz/feldspar, H = hornblende, G = garnet. B) Left mound is sample prior to magnetic separation, middle and right mounds are sample fractions following magnetic separation (right fraction is predominantly grains of interstitial quartz and feldspar). C) Franz Isodynamic magnetic separator at work. D) Phosphoric acid dissolution treatment. E) The final product: isolated, nearly pure quartz grains. Author photos.

duced more than 50 g of quartz each. In order to effectively isolate quartz grains from background feldspar minerals, samples were split into ∼100 g fractions, each of which required 5-10 cycles of phosphoric acid leaching. For some individual quartz-poor samples, this meant as many as 40 total successive cycles of phosphoric acid leaching. Even relatively quartz-rich samples required a minimum of ∼20 cycles to isolate sufficient quartz for AMS analysis.

3.3.3 TCND exposure age calculations

Terrestrial cosmogenic nuclide dating is based on the principle that cosmic rays interact with exposed rock surfaces, producing isotopes such as ^{10}Be at a predictable rate; the ^{10}Be production rate is predominantly controlled by neutron spallation, which decreases exponentially with depth. The vast majority of neutron spallation occurs within 3-4 m of the rock surface, and ^{10}Be production at ∼42 cm depth is half that at the surface (Gosse and Phillips, 2001). Exposure age dating of surfaces using ^{10}Be concentration necessarily assumes that there was zero concentration to begin with; therefore "inherited" ^{10}Be could be a problem if the surface had a prior exposure history. For example, inheritance of ^{10}Be may occur in a glacially-scoured bedrock surface which was not eroded deeply enough to sufficiently erase the pre-existing concentration of ^{10}Be, or a boulder that was previously exposed on the surface of an older deposit (e.g. moraine or landslide) could be entrained and transported by glacier ice to a new location.

All of the TCND samples for this project were inferred to be of post-LGM age, therefore erosion was considered to have been negligible over this time period (Gosse and Phillips, 2001), and samples were analysed for ^{10}Be only. While other workers who have similarly assumed negligible erosion in New Zealand (e.g. Putnam et al., 2010b; Schaefer et al., 2006; Shulmeister et al., 2010 have worked on the eastern side of the main divide, where precipitation is much lower than Fiordland, the presence of well-preserved glacial striae at many sample sites indicates a very low level of post-glacial erosion of bedrock surfaces. AMS analyses were carried out at GNS Science's Cosmogenic Isotope and Radiochemistry Laboratory, at the Gracefield National Isotope Centre, in Wellington, New Zealand. All measured sample ^{10}Be/^{9}Be ratios were corrected by full chemistry procedural blanks prepared by the University of Canterbury Cosmogenic Isotope Laboratory, from a commercially purchased ^{9}Be calibration solution; the measured ^{10}Be/^{9}Be ratio of the procedural blank was 4.9 x 10^{-5}. The Melbourne carrier solution used for preparation of procedural blanks had a ^{9}Be concentration of 1414 ± 2 ppm; this was density corrected to 1380 ppm (per Dr. David Fink),

Table 3.1: TCND sample details and ^{10}Be data

Sample ID	**Latitude (DD)**	**Longitude (DD)**	**Elevation (m.a.s.l.)**	**Sample thickness (cm)**[b]	**Shielding correction**[c]	$^{10}Be \pm 1\sigma$ **(10^4 atoms/g quartz)**[d]
SC1	-44.6145	167.8520	238	5	0.9439	8.32 ± 0.96
SC3	-44.5730	167.7809	14	1	0.9982	9.43 ± 0.73
SC4	-44.5971	167.8178	8	5	0.9333	6.31 ± 0.30
SC5[a]	-44.6490	167.9863	218	5	0.9201	1.49 ± 0.20
SC7	-44.6738	167.9278	76	2	0.9376	6.75 ± 0.35
SC9	-44.6897	167.9676	84	2	0.9001	6.19 ± 0.93
SC10	-44.6889	167.9689	145	2[e]	0.8309	2.74 ± 0.18
SC11	-44.6886	167.9701	235	2	0.7683	2.08 ± 0.33
SC12	-44.6874	167.9711	361	2[e]	0.8597	6.78 ± 0.66
SC14	-44.6856	167.9765	531	2	0.8746	9.72 ± 0.46
SC16	-44.6355	167.8751	34	2	0.9299	6.47 ± 0.43
SC17[a]	-44.6996	167.9664	60	3	0.9351	7.87 ± 0.24
SC20	-44.6279	167.9040	5	2	0.8633	3.79 ± 0.24
SC21[a]	-44.6647	167.9235	4	7	0.8891	2.57 ± 0.62

[a] boulder TCND sample, see Chapter 4 for discussion.
[b] assumed rock density 2.9 g/cm^3, except sample SC3, 2.6 g/cm^3.
[c] shielding correction due to topographic shielding, plus forest attenuation correction for SC10 through SC14 (see text).
[d] blank corrected ^{10}Be concentrations, referenced to the NIST SRM4325 standard (2.79 x 10^{-12}).
[e] sample thickness, before overburden correction (see text).

to compensate for atmospheric conditions at the University of Canterbury laboratory. AMS measurements were referenced to NIST SRM4325 standard reference material, with an assumed standardized $^{10}Be/^{9}Be$ ratio of 2.79 x 10^{-12} (Dr. Albert Zondervan, GNS Science, pers. comm.). Total analytical error for ^{10}Be concentrations ranged from ∼5 to 16% for bedrock sites, and from ∼13 to 30% for the (younger) boulder sites. The larger errors are the result of low AMS counts for ^{10}Be; this is directly related to the extremely low quartz extraction from some samples, as discussed above.

^{10}Be exposure ages were calculated from measured $^{10}Be/^{9}Be$ ratios using the methods incorporated in the CRONUS-Earth online exposure age calculator, Version 2.2 (Balco et al., 2008), which includes a sample thickness correction derived from the rock density and an assumed neutron attenuation length of 177 g/cm^2 (Farber et al., 2008). CRONUS-Earth uses the NCAR World Monthly Surface Station Climatology dataset to estimate mean sea level air pressure and temperature, and computes exposure ages based on four published global, time-varying geomagnetic field intensity (i.e. time-varying production rate) models, plus one constant production rate model. The constant production rate model tends to overestimate the true exposure-age for samples of ∼10 to 25 ka (Shulmeister et al., 2010), and was therefore not considered for this study. The four time-varying production rate models all produced results that were within about 2% of each other (i.e. well within measurement uncertainty). The CRONUS-Earth results presented here (Table 3.2) are based on the high-resolution geomagnetic framework of Lifton et al. (2005), as modified by Balco et al. (2008).

Corrections for seasonal snow cover or time-dependent changes in air pressure were not considered in exposure age calculations. All samples sites were below tree line, and only two (SC12 and SC14) were above 300 m.a.s.l., so snow cover was considered to be ephemeral, with insignificant shielding effect; similar assumptions have been applied at relatively higher-altitude TCND sample sites in the Southern Alps (e.g. Putnam et al., 2010a,b; Shulmeister et al., 2010).

^{10}Be exposure ages for this study were calculated using both the Macaulay and global production rates; both sets of ages are presented in the results section below (Figure 3.2). Four independent ^{14}C ages from wood entrained within two large landslide deposits agree with two ^{10}Be exposure ages (within measurement error) from large boulders on the surface of the deposits, when calculated using the Macaulay production rate. In contrast, the ^{14}C ages do not agree with exposure ages calculated using the global ^{10}Be production rate; these ages are ∼16% younger than the ages calculated with the Macaulay production rate. While it is possible that the wood samples came from trees that were already dead when they were entrained in the landslide deposits,

this scenario is considered to be unlikely for the following reasons:

1. duplicate ^{14}C ages (two for each deposit) are in agreement with each other; it seems highly unlikely that two pieces of entrained dead wood, collected from different locations in the deposit, would have ages which agree so closely (see Figure 3.2),

2. the wood samples were of intact branches or twigs (not badly damaged by transport), suggesting that they came from relatively young wood, which had not had time to decay prior to transport,

3. dead trees are unlikely to be preserved for long on the forest floor in Fiordland. In such a humid climate, it is very unlikely that all four pieces of sampled wood could have been preserved for hundreds of years (i.e. prior to entrainment and transport).

As there is no evidence to support significantly younger ages for the deposits than the maximum-limiting ^{14}C ages, the older ^{10}Be exposure ages, calculated using the local (Macaulay) production rate, are considered to be more indicative of the actual age of the deposits. The agreement with independent ^{14}C results also provides confidence that the methods described earlier for collecting, processing and analysing samples for calculation of ^{10}Be exposure ages (see methods section) can produce valid results. However,this confidence should be tempered by acknowledging that both sets of independent ^{14}C ages are from the Holocene (i.e. $\sim$4 ka and 9 ka); there are no independent age data for bedrock samples (which likely have exposure ages around 16-20 ka), therefore there is no way to independently validate the ^{10}Be exposure age calculations for glacially-modified bedrock surfaces. There are also relatively large uncertainties associated with the calculated ^{10}Be exposure ages for bedrock surfaces, which generate corresponding uncertainty about the specific timing of glacial retreat. However, despite the measurement uncertainties associated with the ^{10}Be samples, the overall glacial retreat story (see results) clearly emerges, in a similar way to deglacial chronologies presented recently by other authors (e.g. Shulmeister et al., 2010; Winkler, 2009).

3.3.3.1 Landscape uplift

Tectonic or glacioisostatic uplift can influence ^{10}Be production rates, if sample sites have had significantly altered altitudes during their exposure history, because cosmic ray flux varies with atmospheric pressure. Based on raised shorelines that were cut into bedrock by coastal erosion during the last interglacial, Fiordland has experienced

a relatively low rate of uplift (∼0.5 mm/year) over the past 130 ka (Kim and Sutherland, 2004); this is likely due to the predominantly strike-slip motion of the adjacent plate boundary Alpine Fault.

Berryman et al. (2012b) noted that in the last Alpine Fault earthquake, ∼1 m of vertical displacement occurred at Hokuri Creek, and estimated a rupture recurrence interval of ∼330 years; this suggests a vertical displacement of ∼3 mm/year. However, this displacement represents a single event, is directly on the fault trace, and may not be indicative of long-term average uplift rates some distance away from the Alpine Fault.

On the offshore portion of the Alpine Fault between Milford and George Sounds, Barnes (2009) investigated the displacements of well-preserved relict glacial outwash fans and moraines, and noted no significant ovservable vertical displacement. There are similar displaced submarine glacial features near Saint Anne Point, which also show very little indication of vertical displacement (see discussion below), further suggesting that post-LGM vertical displacement on the immediate offshore portion of the Alpine Fault near Milford Sound has has been relatively minor.

Putnam et al. (2010b) inferred an average uplift rate of 0.5 mm/year based on relative heights of the LGM shoreline at Lake Pukaki, and calculated that a nominal average 2 mm/year uplift rate would result in exposure age corrections that were within the range of time-varying production rate uncertainties for samples that were ∼9 ka old. They attributed uplift to tectonic (rather than glacioisostatic) processes, based on evidence that the shoreline has been tilted by 14 m vertically as it gets closer to the Alpine Fault, and assumed that uplift over the past 16 ka has had negligible effect on ^{10}Be production, as most isostatic recovery would have occurred soon after retreat of LGM glaciers.

At Milford Sound, glacial ice up to several hundred metres thick would have occupied the valley bottoms during the LGM, which would presumably have caused some glacioisostatic depression of the region; however, there is no obvious evidence that would allow the effects of isostacy to be quantified; any relict LGM shorelines are now well beneath the sea, due to eustatic sea level rise. Since the LGM, eustatic sea level rise of ∼120 m (Fleming et al., 1998; Milne et al., 2005) has dominated relative sea level rise of around 10 m (based on an average uplift rate of 0.5 mm/year over the past 20 ka (citekim1), caused by tectonic uplift. However, the long-term tectonic uplift rate does not capture cycles of glacioisostatic depression and rebound; while these cycles likely have some impact on overall uplift rates in Fiordland, a better understanding of glacioisostatic processes is required before their impact on landscape uplift can be

quantified. Due to the relatively small amount of LGM ice in Fiordland (compared to the continental land masses of Europe and North America), and the relatively buoyant crustal structure beneath northern Fiordland (Sutherland et al., 2006a), which also hosts the largest positive gravitational anomaly in New Zealand (House et al., 2002), glacioisostatic rebound is expected to be relatively minor compared to tectonic uplift.

Following the conclusions of several other workers (e.g. Barnes and Pickrill, unpublished; Pickrill et al., 1992; Putnam et al., 2010b), it seems reasonable to assume that isostatic adjustment of the Milford Sound area to recent glaciations has been minimal, and concentrated in the early LGIT. Based on observations of minimal post-LGM uplift from offshore glacial geomorphology offset by the Alpine Fault, and an estimated long-term average uplift rate of ∼0.5 mm/year for southern Fiordland, it is considered unlikely that local uplift rates are large enough to significantly effect ^{10}Be production rates over the last 20 ka; therefore exposure age calculations reported here do not include any correction for post-LGM landscape uplift. Sea level is generally presented in eustatic terms, however it should be noted that relative sea levels at the LGM were likely 10 m higher than eustatic values, due to tectonic uplift (i.e. -110 m).

3.3.3.2 Topographic shielding

Standard models for calculating cosmogenic nuclide production assume that the production takes place beneath a planar, horizontal surface (Gosse and Phillips, 2001). However, samples which are collected from sloping surfaces may have experienced enhanced shielding throughout their exposure history. Although incoming cosmic radiation is concentrated in the vertical direction, dipping surfaces can significantly enhance total topographic shielding (see Figure 3.18), especially when surfaces slope towards major topographic obstructions. In addition, foreshortening of moderately dipping surfaces to predominantly vertical incoming radiation has the effect of decreasing the radiation flux within the rock, by increasing the effective attenuation length (Gosse and Phillips, 2001).

Shielding corrections were estimated using the Cronus Earth geometric shielding calculator (Balco et al., 2008), which calculates total shielding from both topographic obstructions (i.e. the horizon), and self shielding due to sloping surfaces (see Figure 3.19).

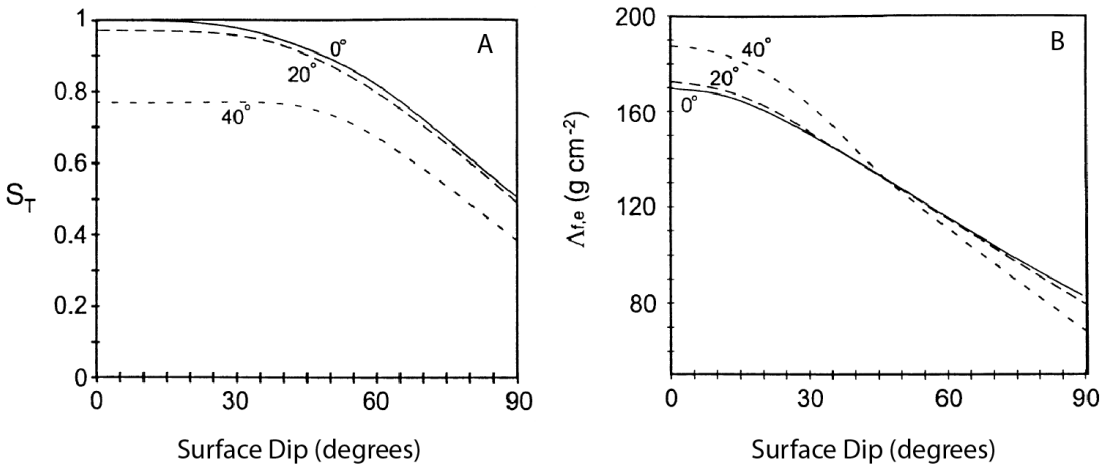

Figure 3.18: Topographic shielding. A) Total topographic scaling (S_T) as a function of surface dip angle and topographic shielding. After Gosse and Phillips (2001), fig. 15. B) Effective attenuation length ($\Delta_{f,e}$) as a function of surface dip angle and topographic shielding. After Gosse and Phillips (2001), fig. 16. Degree labels on curves refer to the angle of shielding by surrounding, axially symmetric, topographic features.

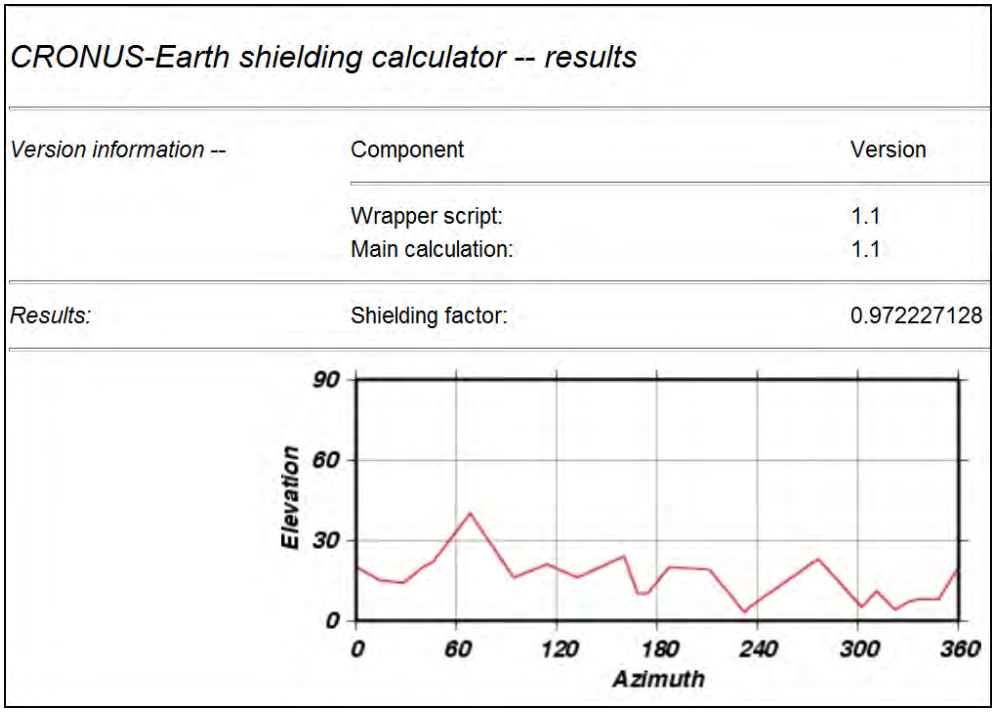

Figure 3.19: Example topographic shielding calculation from Cronus Earth online calculator, site SC8.

3.3.3.3 Evidence for negligible erosion

In general, the observed concentration of a cosmogenic nuclide in a sample is a function of both exposure age and erosion rate; in order to independently determine both, at least two nuclides must be measured. A common two-nuclide approach is the $^{26}Al/^{10}Be$ pair, which can be measured together in isolated quartz grains, have similar geochemical behaviour, and have half-lives that differ by a factor of two. The saturation level of the shorter-lived isotope can be used to determine the erosion rate; the longer-lived isotope (which has not reached saturation), can be used to calculate the actual exposure age, once the erosion rate is known (Gosse and Phillips, 2001).

However, in two specific cases, measurement of a single cosmogenic nuclide can provide a reasonably accurate estimate of exposure age: 1) where the erosion rate is negligible, as with very young exposure ages (less than ∼30 ka); and 2) where samples have been exposed to cosmogenic radiation for time periods that are long compared to the nuclide half-life, and during which erosion has been relatively incremental and steady (Gosse and Phillips, 2001 and references therein). In the latter case, cosmogenic nuclide concentrations can reasonably be inferred to be in secular equilibrium with the long term erosion rate.

For the majority of bedrock sample sites from the current study, preserved surface texture diagnostic of glacial erosion (e.g. striations and polish) allowed a reasonable inference of negligible erosion of surfaces (Gosse and Phillips, 2001 and references therein). For sample sites without obvious preservation of glacial features, negligible erosion is still considered a reasonable assumption, given the low erodibility of the bedrock in the study area, and the relatively young exposure ages of most sites. Even high rates of erosion (10 mm/ka or more) have little effect on cosmogenic nuclide concentrations until the exposure time is long enough for erosion to have removed significant amounts of surface rock; this normally takes at least 30,000 years (Gosse and Phillips, 2001), therefore, all TCND exposure ages were calculated assuming negligible erosion.

Five tree slide bedrock samples (SC10-SC14) were obtained from bedrock surfaces that are normally covered by forest (i.e. they were vegetated prior to 2008), yet they displayed clear evidence of glacial modification, where striae were preserved with only slight degradation. The preservation of glacial striae after 15-20 ka years of weathering under moss and or lichen counters conventional views of weathering (Dr. J. Shulmeister, pers. comm., 2013). However, further evidence for the exceptional preservation of the ice-scoured surface exposed by the tree slide is provided by quartz veins, which criss-cross the bedrock surface exposed by the tree slide; these quartz veins commonly have polished surfaces, and were generally not observed to protrude more than ∼3 mm

above the surrounding surface. Upstanding quartz veins have been used to measure bedrock surface lowering of glacially-modified surfaces, as the quartz is more resistant to weathering than the surrounding mineral assemblages (e.g. Dahl, 1967; Nicholson, 2008). The lack of upstanding quartz veins at Milford Sound (with the exception of the softer bedrock at St. Anne Point, site SC3) suggests that there has been minimal lowering of the pre-weathered, ice-scoured bedrock surfaces since glacial retreat, regardless of whether the sites have been covered with forest, or moss and lichen.

3.3.3.4 Attenuation of cosmic radiation by forest biomass

There are no known published New Zealand studies of the effects of indigenous temperate rainforests (which are dominated by southern beech or mixed conifer/broadleaf species, Mark, 1998) on cosmic radiation flux. However, for the tree slide sample sites, which would likely be covered by thick rainforest vegetation (biomass both in the canopy, and coarse woody debris, or litter, on the forest floor) the majority of the time, it seems appropriate to consider some correction for cosmic ray attenuation by forest biomass.

In a recent investigation of the affects of forest cover (canopy and forest floor biomass) on attenuation of cosmic ray flux, Plug et al. (2007) found that thick forest cover can alter the amount of secondary cosmic radiation that reaches the ground in three ways:

1. reducing cosmic radiation due to absorption by trees,
2. inducing spatial and temporal variability because forest biomass is heterogeneously distributed, both spatially and temporally, and
3. lengthening the apparent mean attenuation length at ground level, because nucleons are preferentially shielded by forest cover, compared to muons.

Plug et al. (2007) developed a numerical simulation of the long-term attenuation effects of Acadian/boreal forests from Nova Scotia, Canada, and temperate coastal rainforest from the Olympic Peninsula of Washington State, calibrated with known properties of existing old-growth forest plots. Their simulated forest was modelled in three dimensions; they found that cosmic radiation attenuation varied significantly (from 1 to 100% of non-forested flux) over short time periods, due to the effect of the position of large individual trees (diameter $\sim$1.5 m or larger) relative to a single sample site on the forest floor. However, over long time periods (encompassing more than 80 disturbance/regeneration cycles), the effect of forest cover had a relatively consistent effect

on cosmic radiation attenuation at the forest floor. Plug et al. (2007) estimated that over a time period of ~8,000 years, the Acadian/boreal forests and temperate coastal rainforests would attenuate cosmic radiation by $2.3 \pm 0.6\%$ and $7.3 \pm 2.3\%$ respectively.

Fiordland and Olympic Peninsula temperate rainforests are probably not directly comparable in terms of attenuation of cosmic radiation, as they are typified by unique geographic and climatic conditions, unique species composition (broadleaf versus conifer, respectively), and they experience different disturbance regimes. Over time periods of thousands of years, nearly all individual forest stands are subject to some sort of disturbance, which in turn affects the amount of cosmic radiation reaching the forest floor during regeneration. The dominant agent of forest disturbance is likely mass movement (tree slides and landslides) for Fiordland forests, and windfall for northern hemisphere temperate rainforests. However, in the absence of any locally-derived data for forest attenuation of cosmic radiation, the Plug et al. (2007) simulation of cosmic ray flux in temperate northern hemisphere rainforest is considered to the be the most applicable to Fiordland forests. Therefore, a forest attenuation correction factor of 7.3% was applied to exposure age calculations for TCND sampling sites SC10-SC14, based on observations of thick adjacent forest cover, and flat or gently sloping benches that would have supported forest growth. A correction factor for forest attenuation was not applied to TCND calculations for site SC9, which was located on the top of a substantial exposed ridge; this ridge would have been surrounded by forest, but probably would not normally have thick forest vegetation growing directly on top of it (similar, unvegetated ridges were sampled at non-treeslide sites SC1,SC7,SC8 and SC16).

A correction for attenuation by forest biomass was calculated only for tree slide sites SC10, SC11, SC12 and SC14; these four sites have clearly been covered by mature forest in the past, based on aerial photography obtained prior to the 2008 tree slide. It should be noted that this is the first known New Zealand study which has incorporated such a correction; previous studies have assumed that attenuation by forest biomass is negligible. However, most previous studies have involved TCND exposure dating of rock surfaces east of the main divide of the Southern Alps (e.g. Putnam et al., 2010b; Shulmeister et al., 2010; Winkler, 2009), where precipitation is substantially lower, and Holocene forest cover would likely have been much lighter (both in terms of density and size of mature trees) than in northwestern Fiordland. Of the four tree slide sites where the correction was applied, one site (SC11) produced an anomalously low TCND age, and was not used in the analysis presented here. ^{10}Be exposure ages for the remaining three sites are about 1-1.26 ka younger when calculated without the applied forest attenuation correction factor of 7.3%; this is about half the difference

between exposure ages calculated with the Macaulay ^{10}Be production rate, compared to the global production rate. As there is no independent age-calibration data for the tree slide sites, it cannot be confirmed at this time whether or not using a correction for attenuation by forest biomass is valid for these sites. However, results presented here incorporate the correction for the three sites described above, based on the presence of thick, mature lowland forests, which presumably would have had a similar attenuating effect as the temperate rainforests of western North America.

Figure 3.20: Typical forest cover adjacent to tree slide. Largest tree (upper left) diameter ∼80 cm. Elevation ∼150 m.a.s.l. Author photo, 2010.

3.3.3.5 Attenuation of cosmic radiation by overburden

In addition to attenuation of cosmic radiation by forest biomass in the canopy and decomposing woody debris on the forest floor, any underlying soil or regolith will also have an attenuation effect, which should be considered in any TCND exposure age calculations of underlying rock surfaces. In order to calculate the attenuation effect of overburden on tree slide TCND sample sites, the pre-slide thickness and density of soil/regolith cover was estimated. As a first step, an estimate of the average pre-slide

overburden thickness was obtained by calculating the volume of soil/regolith in the deposit (see Figure 3.21), and dividing that volume by the three-dimensional surface area that was stripped during the tree slide. The deposit, which ended up on the floodplain between the base of the slope and the Cleddau River, was measured by GPS and surveyors tape in the field. While it is possible that some of the deposit was carried out to the Cleddau River, and subsequently eroded, any lost volume is considered to relatively insignificant, as both field observations and aerial photographs suggest that most of the deposit did not reach the river. A creek which bisects the deposit has eroded a channel 2-2.5 m deep through the thickest part of the deposit. The Milford access road also crosses the middle of the deposit, roughly perpendicular to the creek, and provides further indication of the deposit thickness. Based on field observations, the deposit covered an area of ∼18,000 m^2, with an average thickness of ∼1.75 m, therefore the total deposit volume is estimated to be (18,000 x 1.75)= 31,500 m^3. Field observations indicated that ∼30% of the deposit was comprised of coarse woody debris, therefore the remaining ∼70% ($22,000$ m^3) is considered to have been comprised of overburden from the zone between bedrock and forest floor.

It is possible that some bulking of overburden material within the tree slide could have occurred during transport, but the deposit appears to be relatively well-consolidated, and comparable to undisturbed regolith, therefore a bulking factor was not included in the volume calculation. The possibility of large pieces of fractured bedrock being entrained and transported with the tree slide debris was also considered, but there was little field evidence to support this; most bedrock surfaces exposed by the tree slide exhibited features of glacially-smoothed or scoured bedrock (e.g. glacial polish, striations, p-forms), and very few freshly fractured faces were observed. However, on much of the exposed bedrock surface, impact marks and shattered shards of rock were observed, suggesting that the tree slide debris travelled downslope with high energy, and included rock debris.

The three dimensional aerial extent of the tree slide was estimated using a combination of field observations and Google Earth aerial photos that post-date the event. Based on these observations, a total forested area of approximately 125,000 m^2 contributed to the tree slide. The average pre-slide overburden thickness over that area would therefore be (22,000 $m^3 \div$ 125,000 m^2)= 0.18 m. Based on observations of overburden thickness from adjacent forested slopes, an average thickness of 18 cm certainly seems reasonable, however, the distribution is clearly not uniform. Broad benches and flatter areas were observed to have much thicker overburden cover, while steeper slopes and narrow benches had minimal, if any cover.

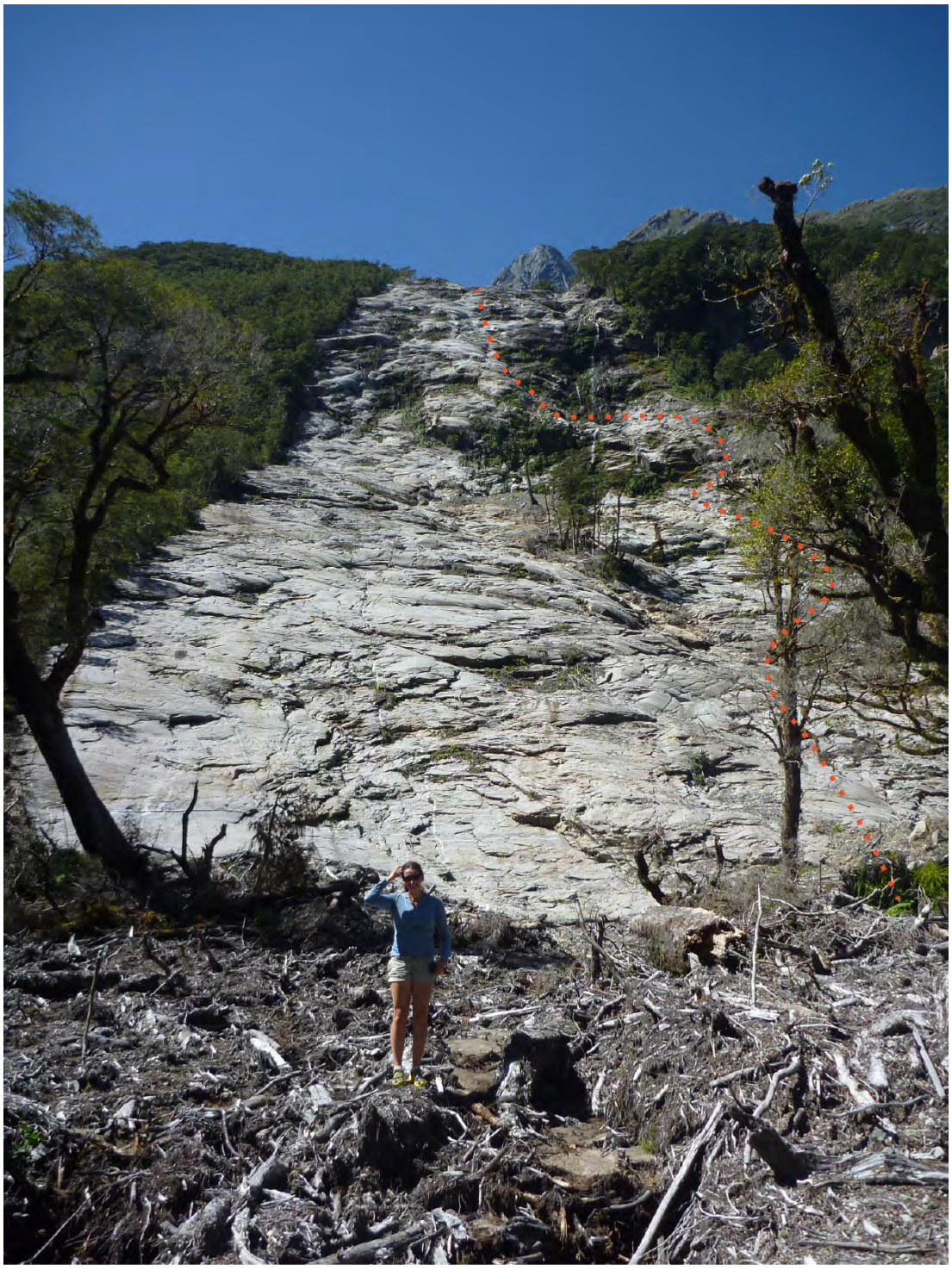

Figure 3.21: Lower tree slide and deposit area. Approximate access route to mid-bench shown as dashed red line. Author photo, 2010.

Due to the obvious heterogeneity of soil/regolith cover, site specific examination of adjacent, undisturbed slopes was considered to provide a better estimation of overburden thickness that would have existed prior to the tree slide, than using the average thickness calculated above. In general, steep forested slopes next to the tree slide appeared to support very little overburden, while broad flat benches were blanketed with a thick cover of overburden. At the nearly flat, broad bench approximately mid-way up the tree slide, a narrow swath had been eroded through the overburden to the underlying bedrock; the maximum overburden thickness observed was ∼3-4 m. This bench was not sampled, due to the thick blanket of overburden, and the fact that the relatively small elevation change across the bench meant that sufficient coverage of sample sites could be achieved without sampling where there was thick overburden. By contrast, the relatively steep lower slopes of the tree slide presented few benches large enough for sampling, and site SC10 was chosen despite apparently thick overburden cover, because of the limited number of sampling sites available at suitable elevation spacing.

Of the four previously forested TCND sites for which exposure ages were calculated (SC10, SC11, SC12 and SC14), only SC10 and SC12 are located on relatively wide, flat expanses of bedrock that could have supported significant overburden cover. SC11 is located on a narrow bench in the midst of the steepest part of the lower tree slide, while SC14 is located on a narrow bench on the steep upper tree slide; forested slopes adjacent to these sites appeared to support minimal overburden. In contrast, field observations (see Figure 3.22) of undisturbed, relatively flat ground near site SC10 suggest that the bench could have been covered by as much as ∼2 m of overburden. Similarly, site SC12 appears to have been covered by ∼0.3 m of overburden.

Based on these observations, and in addition to non-corrected ages, corrected exposure age calculations for sites SC10 and SC12 were included for 200 cm and 30 cm of overburden (respectively), assuming a uniform density of cover material (e.g. Gosse and Phillips, 2001). Corrections assume that these are average overburden thicknesses over the exposure history of the underlying bedrock (i.e. since deglaciation). The length of time required for the overburden to accumulate is therefore not considered, however the corrected ^{10}Be exposure ages compare well with calibrated SH exposure ages (regardless of whether the sites with overburden correction are used in the calibration or not), suggesting that the overburden corrections are generally reasonable (see results below). Considering the coarse granular nature of observed soil/regolith cover, bulk density of in-situ overburden was assumed to be constant at 1.6 g/cm^3 (e.g. Hillel, 1980). Non-overburden-corrected ^{10}Be-age calculations are also provided in Table 3.2 for comparison.

Figure 3.22: Overburden observations: A) ∼200 cm near site SC10. B) ∼30 cm near site SC12. C) Thick overburden eroded by tree slide, flat mid-bench, between SC12 and SC14. Photos by S. Furkert.

This is the first known New Zealand study which has incorporated an exposure-age correction for overburden; previous studies have assumed that attenuation by overburden is negligible. These studies have generally involved TCND exposure dating of boulders exposed on the highest surfaces of moraine ridges, therefore it can be reasonably inferred that significant overburden would not have developed following deposition (e.g. Putnam et al., 2010b; Shulmeister et al., 2005, 2010; Sutherland et al., 2007; Winkler, 2009). Based on field observations of adjacent slopes on the tree slide at Milford Sound, it is clear that significant overburden is present at flatter sites, therefore it was deemed appropriate to apply an attenuation correction at the three sites described above.

3.3.3.6 Radiocarbon samples

All samples were thoroughly cleaned with tap water and dried in an oven for 48 hours, at 50°C. Two samples from each deposit were then selected for radiocarbon analysis; conventional radiocarbon ages (BP) were provided by the GNS Science National Isotope Centre in Lower Hutt. Calibrated radiocarbon ages were calculated with Oxcal version 4.1 (Bronk Ramsey, 2010), using the ShCal04 (McCormac et al., 2004) calibration curve. Calibrated ages are presented relative to calendar year 2010 (see Table 3.5).

3.4 Results

3.4.1 Surface exposure dating (TCND)

3.4.1.1 Terrestrial cosmogenic nuclide (^{10}Be) exposure dates

Eleven samples from exposed bedrock surfaces around Milford Sound were processed and analysed for ^{10}Be concentrations, including five in a vertical transect on a tree slide exposed in 2008 (see Tables 3.1 and 3.2). Of these, two samples yielded unexpected results; SC11 (from midway up the steepest part of the lower treeslide) and SC20 (from exposed bedrock near sea level at Harrison Cove).

The anomalously young ^{10}Be exposure age of 5.70 ± 0.93 ka at SC11 may be due to spalling of the bedrock surface, possibly during earthquakes or tree slide events around that time. Unlike most other bedrock sites, SC11 lacks clear evidence of glacial modification (e.g. striations or grooves), but does have a smoothed appearance, suggesting that spalling is unlikely. In addition, a calibrated SH exposure age of 16.38 ± 0.65 ka indicates that the surface is older than the TCND age; thus it is considered more likely that the underlying bedrock surface was shielded from incoming cosmic radiation by some sort of obstruction, such as thick overburden, or overhanging bedrock that later spalled off. Either scenario is possible, as the site is a narrow ledge in the midst of a steep cliff, with an adjoining ridge of rock that could trap landslide debris.

A second anomalously low ^{10}Be age at site SC20 is more difficult to explain, as the site is on a flat bench that is bare and free of any overburden, and the seaward face of the bedrock surface displays clear evidence of glacial erosion (grooves and polish). The ^{10}Be exposure age of 11.57 ± 0.77 ka is considerably lower than similar nearby shoreline sample sites, which appear to be around 18 ka.

Is it possible that the ^{10}Be exposure age reflects a Younger Dryas or Antarctic Cold Reversal glacier re-advance from the Harrison valley which culminated around 12 ka? Although the Harrison valley does drain the southern aspects of the Mount Pembroke area (which supports a small modern glacier only 6 km from Harrison Cove), this scenario is considered to be unlikely for the following reasons: 1) other ^{10}Be exposure ages do not support any local re-advance of the Milford or tributary glaciers during the YD or ACR (however, these valleys have not been investigated closer to their headwaters); 2) there is no bathymetric evidence of a late-glacial terminal moraine near Harrison Cove; 3) available seismic reflection data of the Harrison delta do not clearly show any evidence of glacial deposits, although there are some strong parabolic reflectors that could be evidence of landslide or moraine material, and; 4) a calibrated SH exposure age of 17.79 ± 0.66 ka for the same surface suggests that it has been

Table 3.2: Calculated ^{10}Be and SH exposure ages[a]

Sample ID	Global[b] (kyrs)	NZ[c](kyrs)	SH Age[d] (kyrs)	Cal ^{14}C Age[e] (kyrs)
Mitre/SC1	16.73 ± 2.54	19.33 ± 2.27	$19.35 \pm 0.67(1.91)$	
St. Anne/SC3	21.22 ± 2.68	24.48 ± 1.99	NA	
Dale Pt./SC4	15.85 ± 1.74	18.29 ± 0.95	$18.32 \pm 0.66(1.99)$	
Tutoko/SC5*	3.11 ± 0.53	3.61 ± 0.51		$4.05 \pm 0.06, 4.08 \pm 0.05$
Village/SC7	15.45 ± 1.72	17.83 ± 0.99	$18.01 \pm 0.66(2.02)$	
Village/SC8			$18.25 \pm 0.66(2.00)$	
Deepwater Basin			$17.07 \pm 0.65(2.09)$	
Treeslide2/SC9	13.60 ± 2.45	15.72 ± 2.39	$15.90 \pm 0.64(2.18)$	
Treeslide3			$16.42 \pm 0.65(2.14)$	
Treeslide4/SC10	14.52 ± 1.74	16.64 ± 1.18	$16.58 \pm 0.65(2.13)$	
	(6.50 ± 0.78)	(7.50 ± 0.53)		
Treeslide5			$16.75 \pm 0.65(2.12)$	
Treeslide6/SC11	4.94 ± 0.93	5.70 ± 0.93	$16.38 \pm 0.65(2.14)$	
Treeslide7			$17.14 \pm 0.65(2.09)$	
Treeslide10/SC12	15.00 ± 2.09	17.30 ± 1.74	$17.50 \pm 0.65(2.06)$	
	(13.03 ± 1.82)	(15.08 ± 1.52)		
Treeslide11			$17.68 \pm 0.66(2.04)$	
Treeslide12/SC14	15.77 ± 1.73	18.23 ± 0.95	$18.07 \pm 0.66(2.01)$	
Treeslide13			$17.92 \pm 0.66(2.02)$	
Treeslide14			$17.56 \pm 0.66(2.05)$	
Pater Pt./SC16	15.50 ± 1.85	17.89 ± 1.24	$17.73 \pm 0.66(2.04)$	
Bridget Pt.			$17.55 \pm 0.66(2.05)$	
Cleddau/SC17*	1.82 ± 0.58	2.11 ± 0.64		
Harrison/SC20	9.97 ± 1.17	11.57 ± 0.77	$17.79 \pm 0.66(2.03)$	
Bowen/SC21*	6.78 ± 1.77	7.85 ± 1.91		$8.81 \pm 0.10, 9.14 \pm 0.05$
Lk. Ada track			$16.85 \pm 0.65(2.11)$	
Bowen track			$17.93 \pm 0.66(2.02)$	

[a] ^{10}Be exposure ages calculated using the CRONUS-earth online calculator (Balco et al., 2008, see text). External uncertainties reported as $\pm 1\sigma$. For SH age calibration curve, see Figures fig:manual 3.26. All ages referenced to calendar year before 2010.

[b] ^{10}Be production rates normalized to 07KNSTD, based on the global (default) calibration dataset, as included in Balco et al. (2008), and using the high-resolution geomagnetic framework of Lifton et al. (2005), as modified by Balco et al. (2008). Bracketed values without overburden (see text).

[c] ^{10}Be production rates as above, except based on the New Zealand (Macaulay) production rate (Putnam et al., 2010b). Bracketed values without overburden.

[d] calibrated SH exposure age for bedrock sites. Age-estimate uncertainties reported as 95% confidence limits, using the graphical regression method. Figures in brackets are the uncertainties calculated using the more conserative WTLS method (see text for Q-value-age calibration and uncertainty propagation).

[e] associated calibrated ^{14}C ages, youngest of two independent samples per site (see text for sample descriptions). Calibrated with Oxcal ver. 4.1 (Bronk Ramsey, 2010), using the ShCal04 (McCormac et al., 2004) calibration curve. Uncertainties reported as $\pm 1\sigma$.

* denotes boulder sample. All other samples are bedrock.

exposed for significantly longer than 12 ka.

Another possibility is that the surface at site SC20 was beneath sea level for some time after the LGIT (it is currently the lowest TCND sample site, at 4 m.a.s.l.), and has since been raised by a combination of isostatic rebound and tectonic uplift. However, it is expected that such a scenario would have affected the relative weathering of the surface as well, which does not seem to be the case.

An alternative, preferred explanation for the low ^{10}Be exposure age at SC20 is that the surface was buried beneath some overburden (e.g. glacial till or landslide debris) for some of its exposure history, and was later exhumed.

3.4.1.2 Schmidt hammer measurements: mean Q-values

Using SH hardness measurements to estimate the relative exposure age of bedrock surfaces is a technique that relies on the elimination, or control, of other factors that can potential influence weathering processes, such as differences in lithology, climate, overburden thickness and composition, and forest cover. For example, if weathering processes are enhanced at certain elevation ranges due to differences in forest or overburden cover, then it may be difficult to isolate the time component of weathering.

Most SH test sites for this project are located within 250 m of sea level, have similar biogeoclimatic conditions, are composed of very similar weathering-resistant lithology, and are confidently assumed to be of relatively young (post-LGM) age. However, tree slide bedrock test sites ranged from near sea level to nearly 600 m.a.s.l. Prior to field work, it was not known whether glacially-modified surfaces on the mid-bench or upper slopes of the tree slide were older than LGM age. SH analysis provided an opportunity to assess the relationship between elevation and surface hardness on a vertical transect, with the aim of eliminating the influence of non-time-related factors.

Included in the SH testing of glacially-modified surfaces (as evidenced by the presence of glacial grooves, striae or polish), sites were tested where shallow micro-channels (i.e. up to ~10 cm deep) running parallel to slope (and near-perpendicular to glacial striae/grooves) preferentially direct surface water run-off. Based on the preservation of glacial features (e.g. striae), these channels were clearly not substantially eroded into the bedrock subsequent to glacier retreat; field observations indicate that micro-channel surfaces were generally smoother relative to the adjacent bedrock, with reducing pitting, and the appearance of less weathering. Three surfaces were also tested which had clearly been damaged by impact from falling rocks from the steep slopes above; these surfaces appeared to be bruised, or freshly fractured.

Mean Q-values from all glacially-modified sites on the tree slide show a clear curvi-

linear relationship with elevation. Mean Q-values from sites within micro-channels show a similarly-shaped trend with elevation, albeit with a statistically significant offset (i.e. less weathered, or higher Q-value)) relationship (see Figure 3.23). Mean Q-values from micro-channel sites were consistently 2-3 points higher than for adjacent, non-channelled sites. This trend is remarkable in that it does not conform to conventional understanding of bedrock weathering, whereby the presence of water enhances weathering by facilitating chemical and physical processes that speed up the weakening of rock surfaces. Regardless, the data presented here show that the bedrock within micro-channels produced higher Q-values than adjacent bedrock bulges which should not be subject to significant water flow.

A possible explanation for the observed unusual trend, is that the bedrock surfaces within pre-existing micro-channels were temporarily subjected to enhanced souring or smoothing by sediment-charged meltwater, perhaps during glacial retreat or downwasting. This period of enhanced erosion within micro-channels must have be relatively brief, or striae would not have been preserved. If the micro-channels were subjected to enhanced erosion by sediment-charged meltwater during glacial retreat, this could have preferentially removed a small amount (i.e. a few mm) of the rock surface within the channels, like grit-blasting a rough surface to make it smoother. The resulting smoother surface would have had effectively the same exposure history, and been subjected to the same weathering processes as the adjacent un-scoured surface, but initially had a smoother, less pitted surface. The implication is that the scoured surfaces generate higher SH measurements (than adjacent un-scoured surfaces) because of the smoother surface texture, rather than any variations in exposure history or weathering processes. An analogous modern process is observed within steep mountain rivers in the Milford Catchment (e.g. the Bowen and Tutoko rivers), where the bare bedrock channels are being actively scoured by sediment-charged water during flood events, resulting in very low surface roughness. When tested for SH hardness, these recently scoured bedrock channel surfaces generated the highest Q-values recorded in the study, much higher even than freshly fractured bedrock or boulder surfaces (i.e. 68.2-70, compared to a maximum of 64.5 for freshly fractured surfaces); these results indicate that for samples with similar exposure histories, surface texture can significantly effect Q-value measurements.

Whatever the reasons for higher Q-value means from bedrock sites within micro-channels, the data presented here underline the importance of carefully choosing sampling sites for SH testing, to ensure that results are directly comparable. Small differences in bedrock texture, or varying exposure to surface water can result in a relatively

large difference in SH means, compared to adjacent surfaces that should have very similar exposure histories. For this study, all bedrock TCND samples and corresponding SH measurements used in the SH age model calibrations were collected from non-channelled sites, with similar bedrock textures.

Non-tree-slide SH test sites from glacially-modified sites around Milford Sound did not shown any apparent trend when compared with elevation, suggesting that the relationship so apparent at tree slide sites is due primarily to differences in exposure age of the rock surface, rather than elevation. This assumption can be confidently accepted, because the tree slide sample sites are a vertical transect, therefore elevation should be a proxy for exposure age (i.e. as the glacier retreated, it would have downwasted as well).

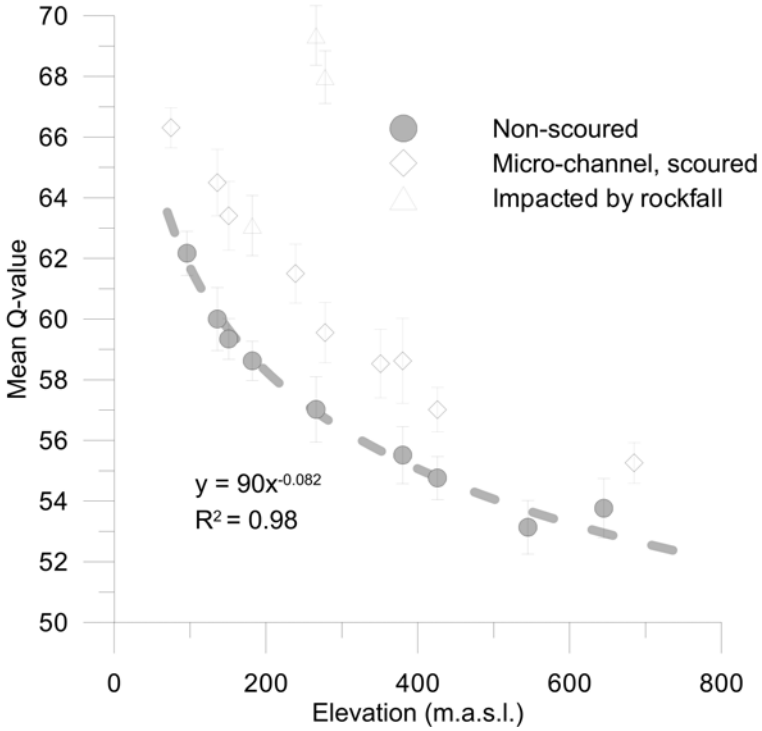

Figure 3.23: Tree slide study sites: variability of the means of Schmidt Hammer Q-values with elevation. Filled circles are measurements from glacially-modified bedrock surfaces, without micro-channels; dashed curve is best-fit power-law distribution (see equation). Diamonds are measurements from glacially-modified bedrock with micro-channels (see text). Triangles are measurements from freshly damaged surface, due to impact of falling rocks. Error bars represent $\pm 1\sigma$ uncertainty. See Tables 3.3 and 3.4 for data.

Table 3.3: Schmidt hammer results for glacially-modified bedrock and landslide boulders

Sample description (TCND sites bold)	**Elevation** (m.a.s.l.)	**Mean Q-value**[b] $\pm 1\sigma$	**No. of values** (n)	**Skewness**	**Kurtosis**	**K-S stat**[c] (K-S crit)
Mitre/SC1	238	47.80 ± 0.74	50	-0.03	-0.66	0.07 (0.17)
Dale Pt./SC4	8	52.10 ± 0.76	40	0.16	-0.69	0.07 (0.21)
Tutoko/SC5,SC6[a]	218	56.69 ± 0.55	116	-0.20	-0.67	0.07 (0.13)
Village/SC7	76	53.40 ± 0.71	54	-0.07	-0.63	0.07 (0.18)
Village/SC8	24	52.40 ± 0.81	31	-0.07	-0.57	0.10 (0.24)
Deepwater Basin	2	57.29 ± 0.90	38	0.15	-0.89	0.10 (0.22)
Treeslide2/SC9	84	62.17 ± 0.72	60	0.15	-0.78	0.08 (0.17)
Treeslide3	136	60.00 ± 1.04	20	-0.16	-0.57	0.09 (0.30)
Treeslide4/SC10	145	59.35 ± 0.69	81	-0.02	-0.43	0.06 (0.15)
Treeslide5	182	58.63 ± 0.65	40	0.39	0.22	0.07 (0.21)
Treeslide6/SC11	235	60.18 ± 0.88	41	-0.62	-0.36	0.12 (0.21)
Treeslide7	266	57.02 ± 1.08	25	-0.22	-1.26	0.15 (0.26)
Treeslide10/SC12	361	55.51 ± 0.94	44	-0.22	-0.34	0.07 (0.20)
Treeslide11	426	54.76 ± 0.71	29	-0.26	-0.80	0.09 (0.25)
Treeslide12/SC14	531	53.13 ± 0.88	60	0.12	-0.59	0.09 (0.17)
Treeslide13	645	53.76 ± 0.98	40	-0.59	0.43	0.10 (0.21)
Treeslide14	685	55.26 ± 0.67	60	-0.49	0.43	0.10 (0.17)
Sinbad Valley/SC15[a]	8	55.69 ± 0.90	40	0.38	-0.40	0.09 (0.21)
Pater Pt./SC16	34	54.56 ± 0.78	39	0.25	-0.27	0.12 (0.21)
Bridget Point	10	55.31 ± 0.60	78	0.30	-0.77	0.08 (0.15)
U. Cleddau/SC17[a]	60	52.75 ± 0.99	16	0.43	-0.80	0.17 (0.33)
Tutoko/SC18,SC19[a]	205	55.69 ± 0.83	40	-0.04	1.07	0.11 (0.21)
Tutoko Slip[a d]	215	59.14 ± 0.58	100	0.14	-0.64	0.07 (0.13)
Tutoko River[a e]	$\sim$210	69.96 ± 0.27	220	-0.13	0.05	0.05 (0.09)
Harrison/SC20	5	54.32 ± 0.65	60	0.26	-0.55	0.08 (0.17)
Bowen Falls/SC21[a]	4	53.05 ± 0.86	61	0.09	-0.41	0.05 (0.17)
Lk. Ada/SC22,SC23[a]	45	60.63 ± 0.59	78	0.13	-0.76	0.08 (0.15)
Lk. Ada track	54	58.22 ± 0.79	43	-0.03	-0.42	0.08 (0.20)
Bowen Valley/SC24[a]	255	52.96 ± 0.74	40	0.25	-0.63	0.08 (0.21)
Bowen track	158	53.74 ± 1.37	34	-0.34	-0.24	0.10 (0.23)
Bowen streambed[f]	$\sim$250	69.90 ± 0.55	100	0.001	-0.47	0.06 (0.13)
Bowen River[a e]	$\sim$250	68.21 ± 0.53	80	-0.21	0.19	0.06 (0.15)
Lake Adelaide[a]	$\sim$1,000	52.77 ± 0.37	239	-0.05	-0.59	0.04 (0.09)

[a] boulder sample, see Chapter 4 for discussion of specific deposit.
[b] statistical mean and standard error of mean.
[c] Kolmogorov-Smirnov statistic. Bracketed value is critical value for $\alpha = 0.05$.
[d] boulders from bank, recently exhumed by slip. For comparison.
[e] scoured boulders in active river bed. For comparison.
[f] scoured bedrock in active river bed. For comparison.

Table 3.4: Schmidt hammer results for bedrock micro-channel and rockfall impact sites[a]

Sample description bold => TCND	**Elevation (m.a.s.l.)**	**Mean Q-value**[b] $\pm 1\sigma$	**No. of values (n)**	**Skewness**	**Kurtosis**	**K-S stat**[c] (K-S critical)
Treeslide1[d]	84	66.31 ± 0.66	60	0.25	-0.61	0.07 (0.17)
Treeslide3[d]	136	64.50 ± 1.12	20	-0.49	-0.70	0.14 (0.29)
Treeslide4[d]	145	63.40 ± 1.16	21	0.04	-0.12	0.11 (0.29)
Treeslide5[e]	182	63.08 ± 1.03	30	-0.21	-0.51	0.10 (0.24)
Treeslide6[d]	235	61.50 ± 0.99	20	-0.20	-0.81	0.16 (0.29)
Treeslide7[e]	266	69.35 ± 1.00	27	-0.08	-0.71	0.11 (0.26)
Treeslide8[d]	278	59.55 ± 0.98	39	-0.06	-0.59	0.07 (0.21)
Treeslide8[e]	278	67.98 ± 0.86	40	-0.49	-0.27	0.10 (0.21)
Treeslide9[d]	351	58.53 ± 1.11	34	0.52	-0.26	0.15 (0.23)
Treeslide10[d]	361	58.63 ± 1.43	20	-0.51	-0.83	0.20 (0.29)
Treeslide11[d]	426	57.02 ± 0.75	57	0.02	-1.13	0.10 (0.18)
Treeslide14[d]	685	55.26 ± 0.67	60	-0.49	0.43	0.10 (0.17)

[a] see text for description.
[b] statistical mean and standard error of mean.
[c] Kolmogorov-Smirnov statistic. Bracketed value is critical value for $\alpha = 0.05$.
[d] micro-channel in glacially-modified bedrock.
[e] freshly damaged bedrock surface, due to impact of falling rocks.

Differences in weathering processes can clearly be observed in stream channel SH data, which indicate predictably less-weathered (i.e. "younger") surfaces than adjacent glacially-modified surfaces; this offset suggests that enhanced erosion in stream channels (e.g. by sediment-laden flood events, debris flows, etc.) has removed some of the weathering surface. In contrast, weathering processes at sites that likely had significant overburden cover (e.g. SC10), or less forest cover (e.g. SC14) do not appear to be significantly different than for adjacent sites with less overburden, otherwise a departure from the Q-value-elevation relationship might be expected.

Based on these results, it is considered that carefully selected sites where glacially modified bedrock is exposed below treeline are generally reliable and consistent indicators of relative surface weathering, and therefore also of exposure age.

3.4.1.3 Construction of a Q-value-age calibration curve

Weathering processes in rock produce residues that slow the movement of water to unweathered material, thereby impeding chemical transport; as a result, weathering rates tend to decrease with time. Therefore, over long time periods (i.e. many millennia), age-weathering relationships are generally curvilinear (Shakesby et al., 2011, and references therein). Previous attempts to generate R-value-age calibration curves have

commonly used only two age-control points (e.g. Matthews and Owen, 2010; Matthews and Winkler, 2011; Shakesby et al., 2006), predicated on the assumption of a linear age-weathering relationship over relatively short timescales (i.e. Holocene or slightly longer). The assumption of linearity has been justified on the basis of lithologies that are relatively resistant to weathering, and comparatively brief time periods available for weathering. In theory, under these circumstances, it should take many millennia for build-up of residues to slow the weathering process.

Recently, Shakesby et al. (2011) tested these assumptions, by examining the age-weathering relationship of 9,900 R-values obtained from 30 granite beach boulders perched on a sequence of glacio-isostatically raised shorelines in northern Sweden, which have 11 well-constrained ages that span the Holocene. They found that the best-fit R-value-age relationship was linear. Shakesby et al. (2011) used shoreline ages with reported uncertainties in the range of 0.5 ka, and were therefore able to develop an R-value-age calibration curve with relatively small potential errors, based on the weighted total least squares (WTLS) regression method, which accounts for uncertainties in both the R-value means, and estimated control ages.

3.4.1.4 Estimation of predicted-age errors

For the current project, the WTLS method was applied as a method of calculating predicted-age errors for the Q-value-age calibration curve, using ^{10}Be ages calculated with local production rates from the Macaulay valley (Putnam et al., 2010b). Due to the relatively high external uncertainties associated with some of the ^{10}Be TCND ages, the WTLS method yielded errors in the range of 2 ka. Results are shown in Figure 3.24.

Winkler (2009) investigated the relationship between R-values and ^{10}Be exposure ages from boulders on a Holocene moraine system at Strauchon Glacier, in the Southern Alps. He found that a linear function, based on a minimum of three age-calibration points, best described the R-value-age relationship, and was able to statistically separate moraines of 2.4, 1.7 and 1.1 ka, despite some overlapping TCND uncertainties. Winkler (2009) calculated a best-fit calibration curve based on ordinary least squares regression (OLS) techniques previously described in the literature (e.g. Shakesby et al., 2006, and references therein), but also described a technique for reducing the error limits associated with the R-value-age calibration curve, whereby he chose what he considered to be the most representative TCND age point from each of three moraine groups as a control point. Matthews and Owen (2010) used a similar method of calculating predicted-age error uncertainty, but conservatively estimated the uncertainty by dou-

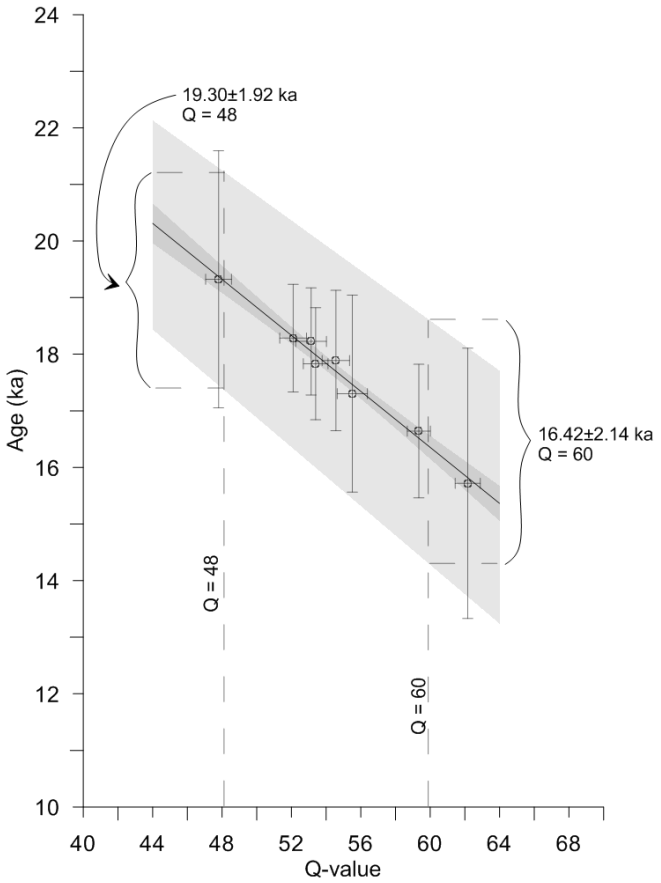

Figure 3.24: Weighted total least squares regression (WTLS) of TCND age on Q-value (solid diagonal line), with 95% confidence limits shaded in dark grey. 95% confidence limits for calculated TCND age-uncertainties shown in light grey. Error bars represent $\pm 1\sigma$ uncertainties. Estimated predicted-age errors are shown for representative Q-values of 48 and 60. See Tables 3.3 and 3.2 for data.

bling the 95% confidence interval around their calibration curve. Recently, Matthews and Winkler (2011) refined this method by combining the uncertainties associated with both the regression line for the R-value means (calculated individually at each control point), and the R-value measurement errors for each calibration point.

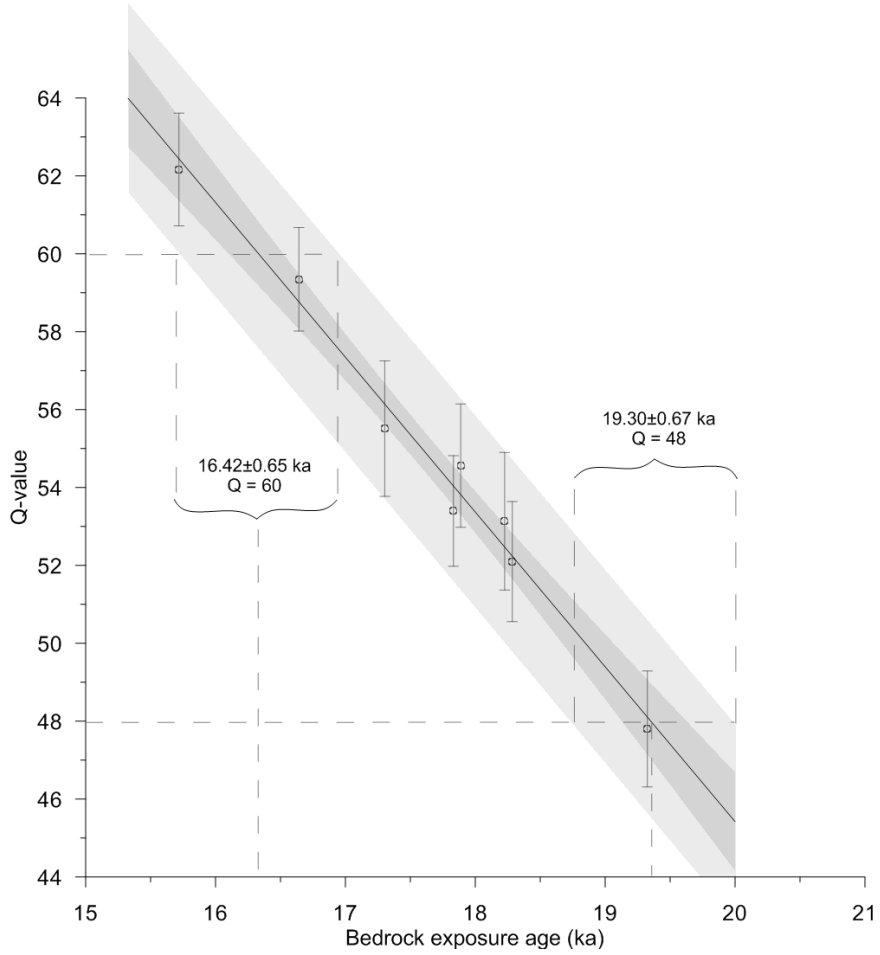

Figure 3.25: Graphical method: weighted best-fit regression on Q-value (solid diagonal line), with 95% confidence limits shaded in dark grey. Error bars represent $\pm 2\sigma$ uncertainties. Total estimated uncertainty (95% confidence limits) shown in light grey (see text). Estimated predicted-age errors are shown for representative Q-values of 48 and 60. See Tables 3.3 and 3.2 for data.

3.4.1.5 Estimation of predicted-age errors: graphical regression method

A graphical method based on the premises of Matthews and Winkler (2011) is also applied here to the problem of estimating reasonable predicted-age errors, with the following steps:

1. a simple (non-weighted) linear regression was calculated on mean Q-values, and plotted with the associated 95% confidence intervals,

2. measurement errors (at 95% confidence level) for each mean were added to the regression line uncertainty at each control point, to estimate total uncertainty at each control point,

3. best-fit maximum and minimum limits were set to encompass these total uncertainties.

The resulting limits reflect total estimated uncertainty (at 95% confidence limits) around the age-calibration curve, based on the distribution and measurement errors associated with mean Q-values (see Figure 3.25).

Following the methods of other workers (e.g. Matthews and Owen, 2010; Matthews and Winkler, 2011; Winkler, 2009), this simple regression method does not directly consider the uncertainty associated with the control exposure-age data; however, given the relatively large number of control points (8 in total), and the high confidence and obvious linear trend of Q-value means in this case, the graphical method provides a much tighter estimate of predicted age errors than the WTLS method. However, as discussed earlier in this chapter, this method may give a false sense of confidence, therefore calibrated SH exposure ages are presented with uncertainties from both the WTLS and graphical regression methods in Figure 3.34 and Table 3.2.

The Q-value-age relationship from glacially-modified bedrock surfaces represents an estimated age range of only ∼3.5 ka, so it is no surprise that the relationship is linear. Unfortunately, the ∼24.5 ka ^{10}Be age from Saint Anne Point is from a different lithology than the other sites, so a comparison of Q-values from that site is likely not valid. However, at the other end of the age spectrum, Q-value measurements from scoured bedrock surfaces and boulders in active river channels provided a convenient analogue for hardness of surfaces freshly modified by glaciers (i.e. very young, see Figure 3.26). These sites included the Tutoko and Bowen river channels, with bedrock and boulder mean Q-values of 69.96 ± 0.27 and 68.21 ± 0.53, respectively. These measurements suggest that over LGM time periods, the Q-value-age relationship for bedrock sites is likely to be best approximated by a curvilinear fit.

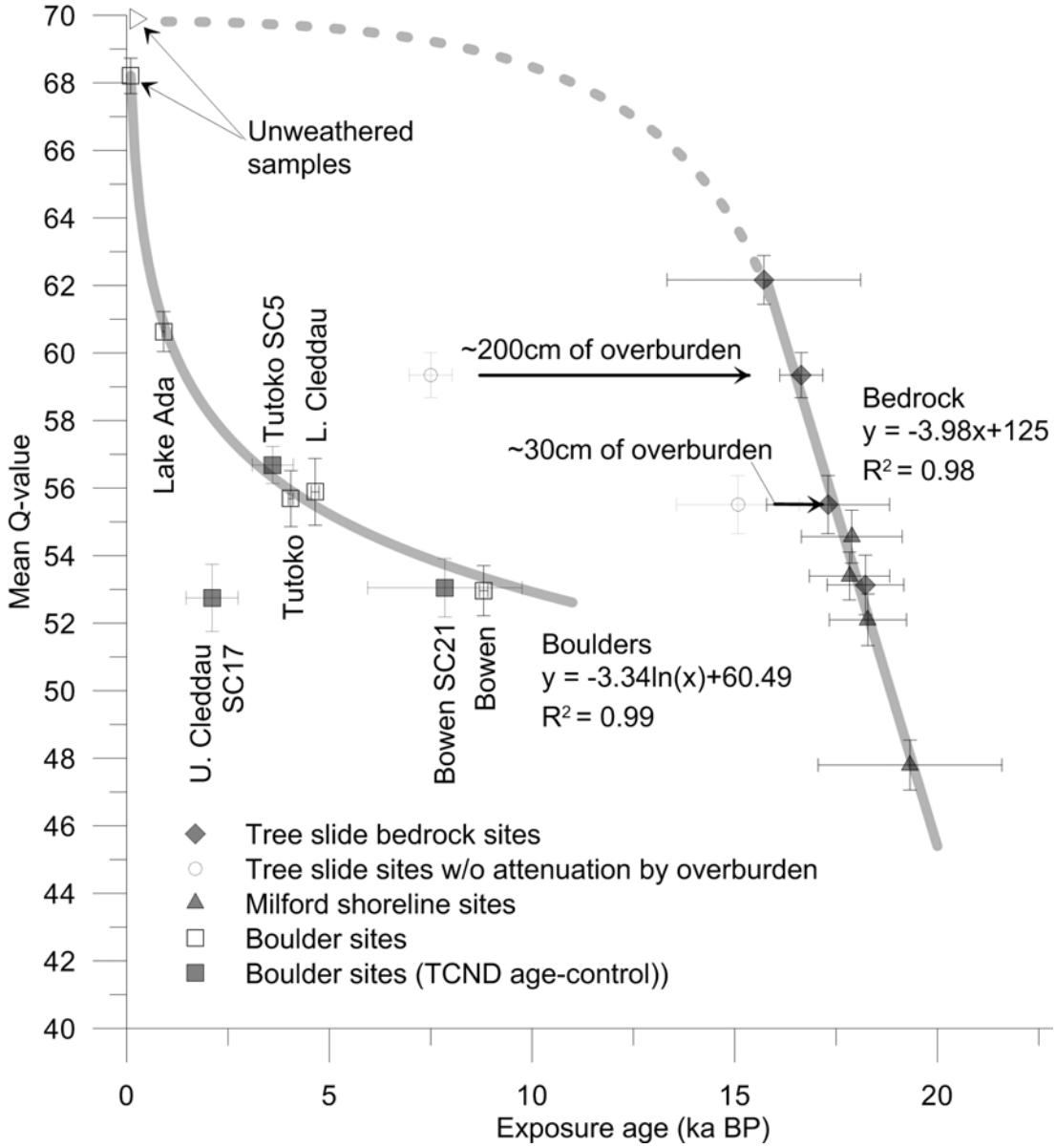

Figure 3.26: Overall Schmidt hammer Q-value-age relationship. Filled diamonds are measurements from glacially-modified bedrock surfaces on the tree slide, circles are sites SC10 and SC12 prior to exposure age (^{10}Be) correction for overburden (see text). Filled triangles are measurements from other glacially modified bedrock sites. Solid line is best-fit linear distribution for bedrock sites. Squares are measurements from boulders on the surface of landslide deposits. Filled squares are boulders with ^{10}Be ages, open squares are boulders with calibrated ^{14}C ages from landslide deposits (see text). Solid curve is best-fit curvilinear (natural-log) distribution for boulders, based on sites with ^{14}C age-control (open squares). Text describes name of landslide deposit (see Figure 4.2), and TCND sample ID, where applicable. Unweathered bedrock and boulder data from Bowen River bed samples (see Table 3.3). Arrows with text indicate correction for overburden (SC10, SC12, see text). Error bars represent $\pm 1\sigma$ uncertainty. See Tables 3.2, 3.3 and 3.5 for data.

For landslide boulder sites, the relevant Q-value-age relationship spans from ∼1 ka to 9 ka, a much longer time period than the bedrock data. Even without the inclusion of the "zero-age" (stream channel) boulder sample, it appears that over the Holocene, the Q-value-age relationship begins to trend towards a curvilinear fit. If the data point associated with the youngest boulder exposure age is removed (Lake Ada), then the resulting time period is ∼4 ka to 9 ka, over which a more linear trend is apparent.

Based on the Q-value-age relationships of Figure 3.26, a Q-value of ∼54 implies an age of ∼18 ka for bedrock sample sites, and ∼7 ka for boulder sample sites. How can this be, if both boulders and bedrock have experienced similar weathering processes? There are two factors which potentially contribute to this apparent contradiction:

1. Boulders on the surfaces of large landslide deposits have presumably interacted with other boulders and debris during their transport, so their surfaces are not directly comparable to glacially-modified bedrock, which has remained in-situ. The forces that cause fracturing and comminution during transport by landslide may have an effect on the physical (near-surface) properties of large clasts within the deposit,

2. Glacially-modified bedrock is comparatively smooth and polished when it is recently exposed; as previously discussed, Q-values of ∼70 are typical of smooth, "young" bedrock that has been eroded by sediment transport in active river beds. By contrast, the freshly fractured faces of boulders (which had fallen out of rock avalanche deposits and broken upon impact with the bedrock below) yielded much lower Q-values (maximum measured Q-value was 64.5). Lower hardness values (compared to bedrock) from landslide boulders could therefore be due to textural differences on freshly fractured faces, rather than exposure-age differences.

Together, these factors imply that baseline Q-values and progressive weathering of landslide boulders are different than for bedrock; therefore Q-value-age relationships are not directly comparable between landslide boulders and glacially-modified bedrock surfaces. Similar conclusions have been reached by other workers with respect to Little Ice Age moraine boulders in Norway (e.g. Winkler et al., 2003), although glacially-modified bedrock surfaces and moraine boulders have been found to be directly comparable for ∼9 ka glacial geomorphology in Norway (Matthews and Winkler, 2011).

Table 3.5: Radiocarbon data and age calibrations

Sample ID[a]	Location	Material dated	^{14}C Age[b] (^{14}Cyrs BP)	Cal ^{14}C Age[c] (yrs)
RC-1b	lower Cleddau	7.5 x 2 cm branch	4132 ± 20	4650 ± 96
RC-1c	lower Cleddau	19 x 1.5 cm twig	4137 ± 20	4661 ± 96
RC-2b	Lake Ada	drowned tree, outer	1009 ± 20	920 ± 36
RC-2c	Lake Ada	drowned tree, outer	985 ± 15	912 ± 34
RC-3a	Bowen valley	15 x 1.5 cm twig	8178 ± 25	9135 ± 50
RC-3b	Bowen valley	10 x 3.5 cm branch	7959 ± 35	8806 ± 104
RC-4a	Tutoko valley	25 x 8 cm branch	3741 ± 20	4084 ± 51
RC-4b	Tutoko valley	20 x 4 cm branch	3716 ± 20	4051 ± 57

[a] Paired data; two separate samples were analysed for each of four landslide deposit (lower Cleddau, Lake Ada, Bowen and Tutoko valleys).
[b] conventional radiocarbon age before present (BP). Analysis by National Isotope Centre, GNS Science, Lower Hutt. Uncertainties reported as $\pm 1\sigma$.
[c] calibrated ^{14}C ages. Calibrated with Oxcal ver. 4.1 (Bronk Ramsey, 2010), using the ShCal04 (McCormac et al., 2004) calibration curve. Ages referenced to calendar year before 2010. Uncertainties reported as $\pm 1\sigma$.

3.4.2 Independent TCND and radiocarbon dating of landslide deposits

Two of the landslides (Tutoko and Bowen valleys) were dated by TCND analysis of large boulders on the deposit surfaces. The availability of four independent ^{14}C ages for these landslide deposits provides a convenient check of the exposure age calculations for the landslide boulders. Both sets of results are included in Table 3.2. All ^{14}C ages agree with associated ^{10}Be exposure ages (within $\pm 1\sigma$ error) when calculated using the Macaulay production rate. In contrast, ^{14}C ages do not agree with exposure ages calculated using the global ^{10}Be production rate, therefore the Q-value-age calibration curves presented here use control points based on Macaulay production rates. See Chapter 4 for a detailed discussion of landslide deposits and age constraints.

3.4.3 Core analysis and seismic interpretation

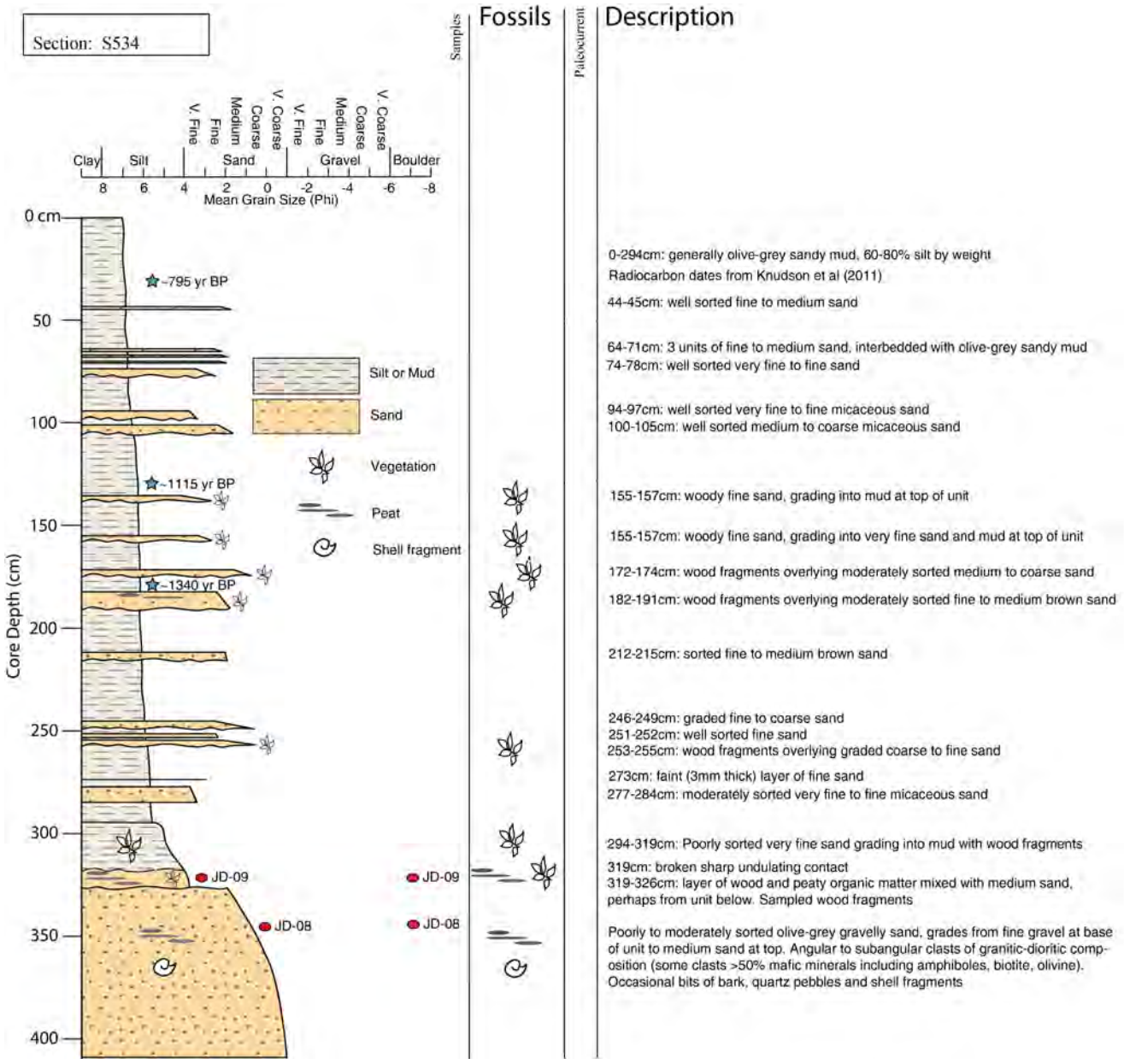

Figure 3.27: Core log section view, NIWA core S534. Blue stars represent calibrated ^{14}C ages from Knudson et al. (2011). Red ellipses are samples collected by the author for future analysis. Silt/mud units are massive gyttja (interpreted to be marine-derived, organic-rich mud), interrupted by thin graded beds of sand and gravel (interpreted to be episodic bursts of sedimentation, possibly relating to subaerial or submarine slope failures and/or tree slides).

Core S534 (see Figure 3.27, see Appendix C.5 for other core logs) is considered to be the most representative of the four Stirling Basin cores, for the following reasons: 1) it was recovered from the deepest part of the basin, from a location where sedimentation is less likely to be dominated by pulses from the large Cleddau/Arthur or Harrison deltas, therefore sand and gravel units within core S534 probably reflect either local mass-movement events originating from the steep rock walls above, or large-scale episodes of coarse deposition that affect sedimentation on a basin-wide scale; and 2) core S534 was recovered from within 4 km of the new Milford Visitors Centre, the Milford Village, and the airport, and therefore can help us understand past geomorphic processes that may have implications for future, potentially hazardous processes, and associated risk management decisions.

Milford Sound cores S542 and S534, both from Stirling Basin, confirm that the veneer of fine sediment observed in seismic reflection profiles is comprised of massive gyttja (marine-derived, organic rich mud), interrupted by thin graded beds of sand and gravel; in seismic profiles this thin veneer of opaque to parallel-bedded sediments typically overlies extensive, discontinuous parabolic reflectors and chaotic seismic facies typical of massive blocky landslide debris (see Figure 3.28). In the cores, thin (typically 0.2-2.5 cm thick, up to 8 cm thick) beds of granular sediment are interspersed with the massive gyttja; these beds are generally characterized by sharp (erosional) bottom contacts, and grade from gravel or sand at the bottom to silt or sandy silt at the top. Sandy laminae commonly contain broken shell fragments and woody debris, and may be capped with coarse plant remains where they grade into the gyttja unit above. The sedimentological characteristics of many of these units are indicative of bursts of sedimentation, followed by a quick transition to background marine sedimentation during a waning-energy regime. Some sandy laminae contain fossils from near-surface or subaerial environments, suggesting that they are the result of episodic deposition from catastrophic subaerial or near-sea-level slope failures.

Cores S535 and S536 are located on the foreslope of the Cleddau delta, and while they do not display the same episodic deposition as the deeper Stirling Basin cores, they do provide some insight into deltaic sedimentation processes (see discussion below).

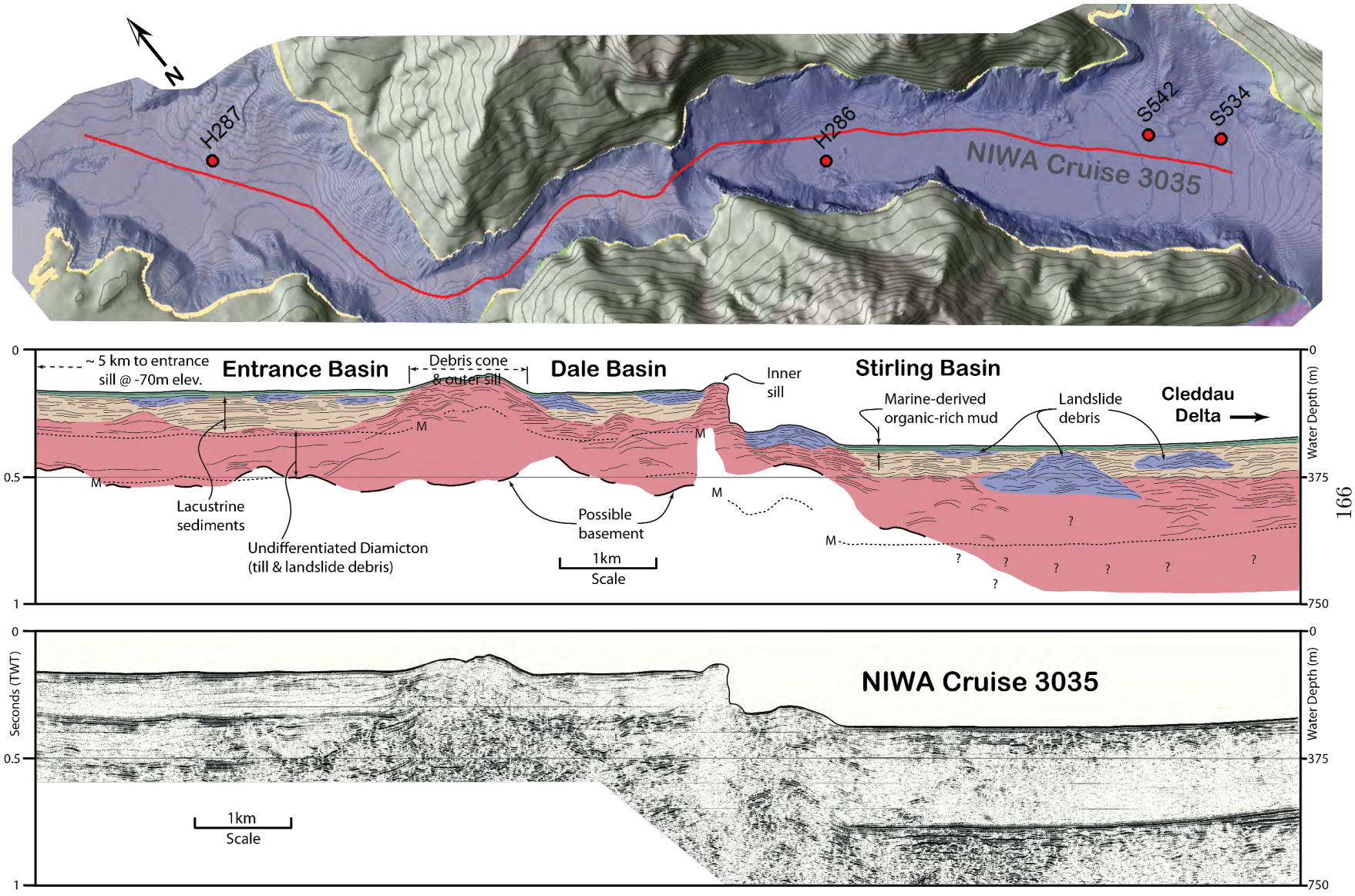

Figure 3.28: Multi-channel seismic interpretation. Plan-view hillshade model with NIWA core locations, 100 m contours and 10 m bathymetry. Red line is navigation data for seismic profile. Note thick, discontinuous, parallel-bedded unit (lacustrine, light brown) overlying poorly reflective, chaotic diamicton fill (till and landslide debris, red).

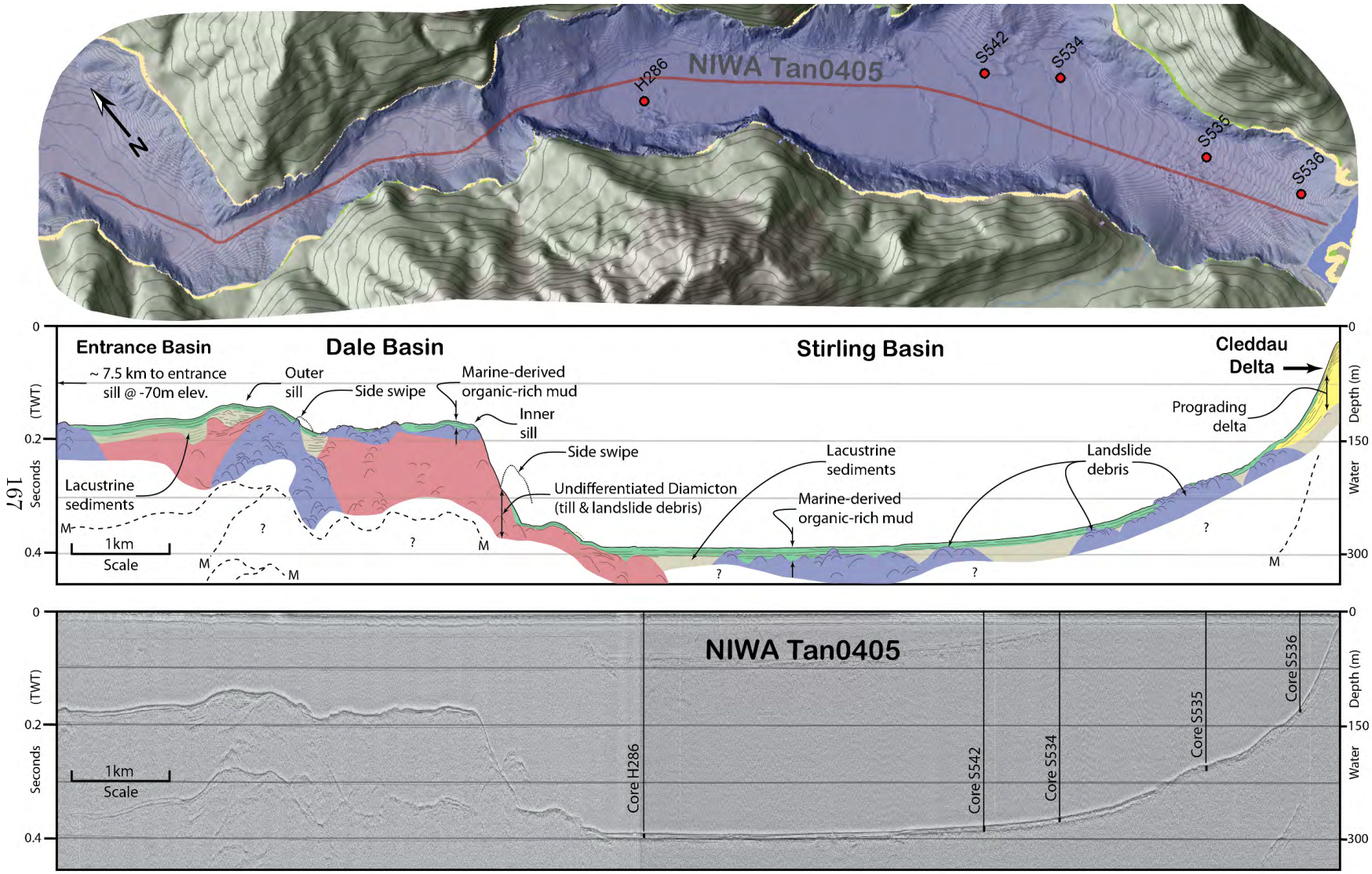

Figure 3.29: Uniboom seismic interpretation. Plan view hillshade model with NIWA core locations, 100 m contours and 10 m bathymetry. Red line is navigation data for seismic profile. Note thin veneer of gyttja (green shading) overlying landslide debris (blue) and lacustrine deposits (light brown).

3.5 Discussion

3.5.1 Timing of post-LGM glacier retreat

3.5.1.1 Terminal moraine abandonment and retreat through Entrance basin

The most seaward ^{10}Be exposure date of 24.5±2.0 ka from bedrock exposed at ∼14 m.a.s.l. at St. Anne Point (site SC3) is located just inboard of a remnant lateral moraine, which rises up to ∼120 m.a.s.l., before continuing offshore onto the continental shelf, where it is clearly visible in the bathymetry (see Figure 3.30). Site SC3 was chosen as the bedrock there was high enough above water level to be protected from most waves, and contained veins of quartz which were easily sampled. Approximately 9 km directly north, across the entrance of Milford Sound, a larger ridge (also ∼120 m.a.s.l.) forms Yates Point; the arcuate shape and orientation of the ridge suggests that it is also a moraine related to the terminal position of the Milford glacier (Sutherland et al., 2006b; Turnbull et al., 2010).

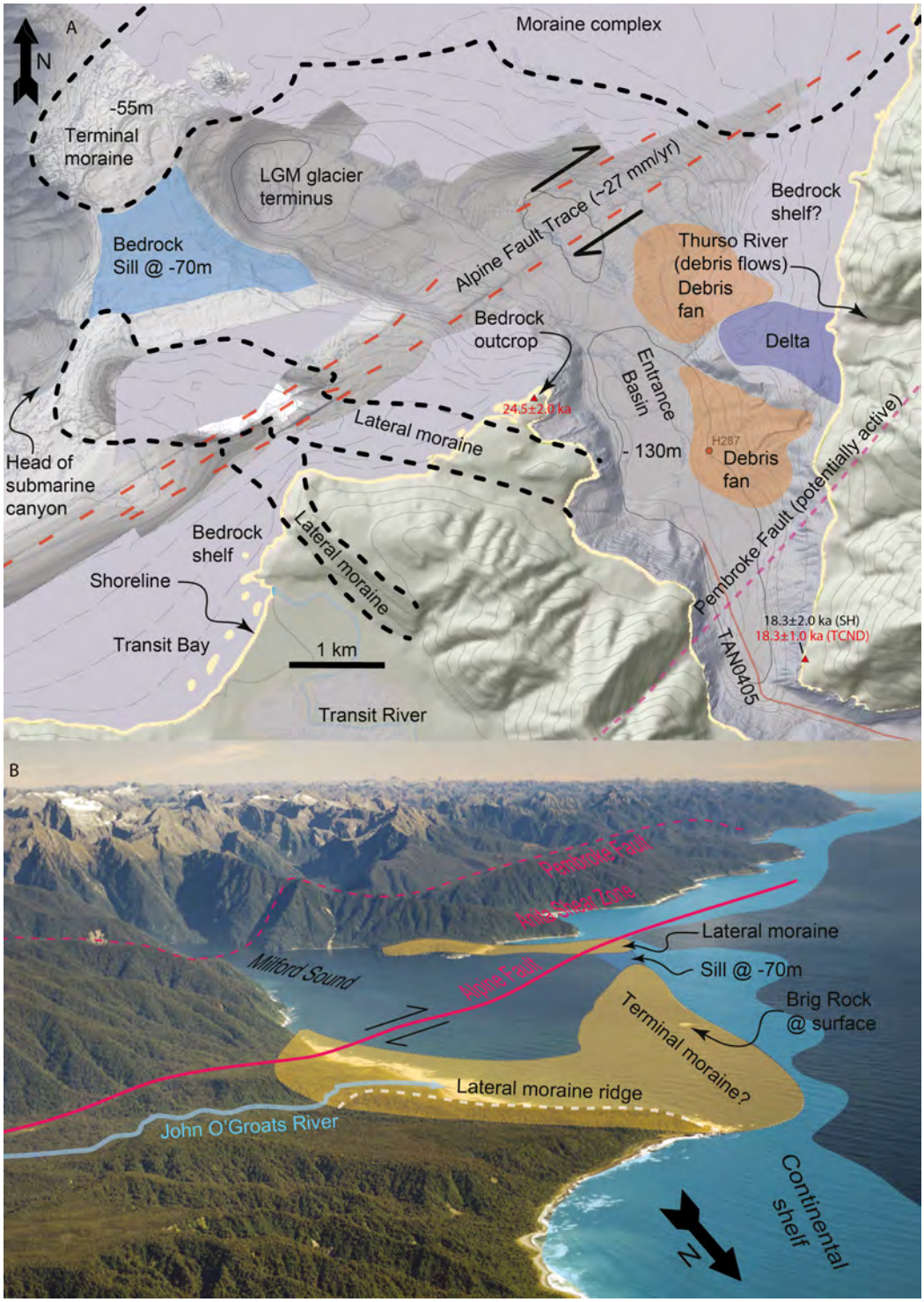

Figure 3.30: Milford Sound entrance & glacial/tectonic geomorphology. A: Hillshade geomorphology map. Contours at 100 m intervals, bathymetry at 10 m intervals. Land contours & hillshade derived from LINZ 20 m DEM, fiord bathymetry & hillshade derived from NIWA data. Alpine Fault trace inferred from bathymetry, slip rate from Barnes (2009). Pembroke Fault after Turnbull et al. (2010). B: Oblique aerial photo & schematic view of major geomorphic features. Yates Point at centre right. Photo by D.L. Homer.

The age of the Yates Point moraine is unknown, however where the John O'Groats river valley crosses the moraine, the valley wall (∼140-220 m elevation) has been offset ∼450 m by the Alpine Fault (see Figure 3.31). The valley wall is inferred to be a relict LGM glacial geomorphological feature (Sutherland et al., 2006b), therefore the amount of offset caused by faulting can provide an indication of when the Yates Point moraine was abandoned. The dextral offset in the valley wall is about 454±46 m, as calculated by Sutherland et al. (2006b), who adopted an age of 18±1 ka for the moraine and other late-glacial features (this age control is rough, as it reflects a global LGM age, and is not constrained by local data), resulting in a weighted mean displacement rate of 23.2±1.4 mm/yr (at the 95% confidence level) for the south Westland portion of the Alpine Fault.

Barnes (2009) calculated a displacement rate of 27.2 (-3.0/+1.8) mm/yr (at the 95% confidence level) for the offshore section of the Alpine Fault, between Milford and George Sounds, based on dextral displacements of glacial features (e.g. moraines) that have been offset by the fault. One of the most well-preserved offset features is at Poison Bay (just south of Milford Sound), where a lateral moraine has been offset by 465±15 m (Barnes, 2009). Radiocarbon dating of coeval surface deposits on abandoned glacial outwash fans led Barnes (2009) to infer an age of 17 ka for the offset glacial features. Similar offset features (although not as clearly defined) can be identified in the glacial geomorphology of the Milford Sound Entrance Basin, although the displacement of these features may be masked by a prograding body of long-shore drifting sediment (Barnes, personal communication, 2012).

Applying the Sutherland et al. (2006b) slip rate of 23.2±1.4 mm/yr to the 454±46 m displacement of the Yates Point moraine yields an age estimate of 22.9-16.6 ka for the Yates Point moraine. Similarly, applying the Barnes (2009) slip rate of 27.2 (-3.0/+1.8) mm/yr results in a moraine age of 20.8-14.1 ka. If the extremely well-preserved offset (465±15 m) moraine at Poison Bay is used instead of the offset valley wall at the John O'Groats river, then the age estimates for the Yates Point moraine become 19.8-15.5 ka (Barnes, 2009 slip rate) and 22.0-18.3 ka (Sutherland et al., 2006b slip rate).

Both of these estimated age-ranges for the Yates Point Moraine are younger than the ^{10}Be exposure age for Saint Anne Point (24.5±2.0 ka). TCND (18.3±1.0 ka) and calibrated SH ages (18.3±2.0 ka) for bedrock site SC4 (Dale Point, ∼10 km directly to the south of Yates Point), provide a minimum-limiting age for the moraine. Sutherland et al. (2007) documented 8-10 lateral moraine ridges at Cascade Plateau (80 km north of Milford Sound), which were deposited during the peak LGM from 22-19 ka; the moraines are preserved in a significantly more seaward position (i.e. closer to the

glacier terminus) than the on-shore moraines at Milford Sound. At actively eroding sea cliffs at Cascade Plateau, LGM moraine ridges yielded ^{10}Be exposure ages ranging from 18.6±1.7 ka to 21.1±1.8 ka (Sutherland et al., 2007). These published age estimates for the oldest LGM moraines at Cascade Plateau overlap with both the ^{10}Be exposure age for Saint Anne Point, and the estimated age ranges for the Yates Point moraine, which is based on two independently derived Alpine Fault slip rates, one from just north of Milford Sound, and one from just south of the fiord. Interestingly, if the (Sutherland et al., 2007) age estimates are revised by using the local production rate from the Macaulay valley (which was used to calculate the 24.5±2.0 ka TCND exposure age presented here for Saint Anne Point), then the oldest LGM moraine at Cascade Plateau becomes about the same age as the bedrock exposed at Saint Anne Point. Additional evidence for an early end to the LGM around comes from Shulmeister et al. (2010), who concluded that the end of peak glacial conditions in New Zealand was around 24 ka, based on ^{10}Be exposure ages of ice recessional moraines in the Rakaia valley.

A possible explanation for the relatively old bedrock exposure age at St. Anne Point is inheritance of some cosmogenic ^{10}Be that was not completely eradicated by LGM glacier erosion. St. Anne Point is the closest sample site to the glacier terminus, and it is likely that glacier ice thinned and slowed dramatically as it spilled out onto the continental shelf, being no longer confined by the steep valley walls of Milford Sound. Thin ice cover at SC3 for a relatively short period of time (i.e. at the peak of the LGM) compared to other sites, could have resulted in the sample site experiencing only light erosion by glacier ice. However, given the position of SC3 inboard and lower than the crest of the lateral moraine, and the broad agreement of the Saint Anne Point age with moraine-age estimates from Cascade Plateau, it is considered that the exposure age of 24.5±2.0 ka, is probably representative of peak-LGM conditions at Milford Sound.

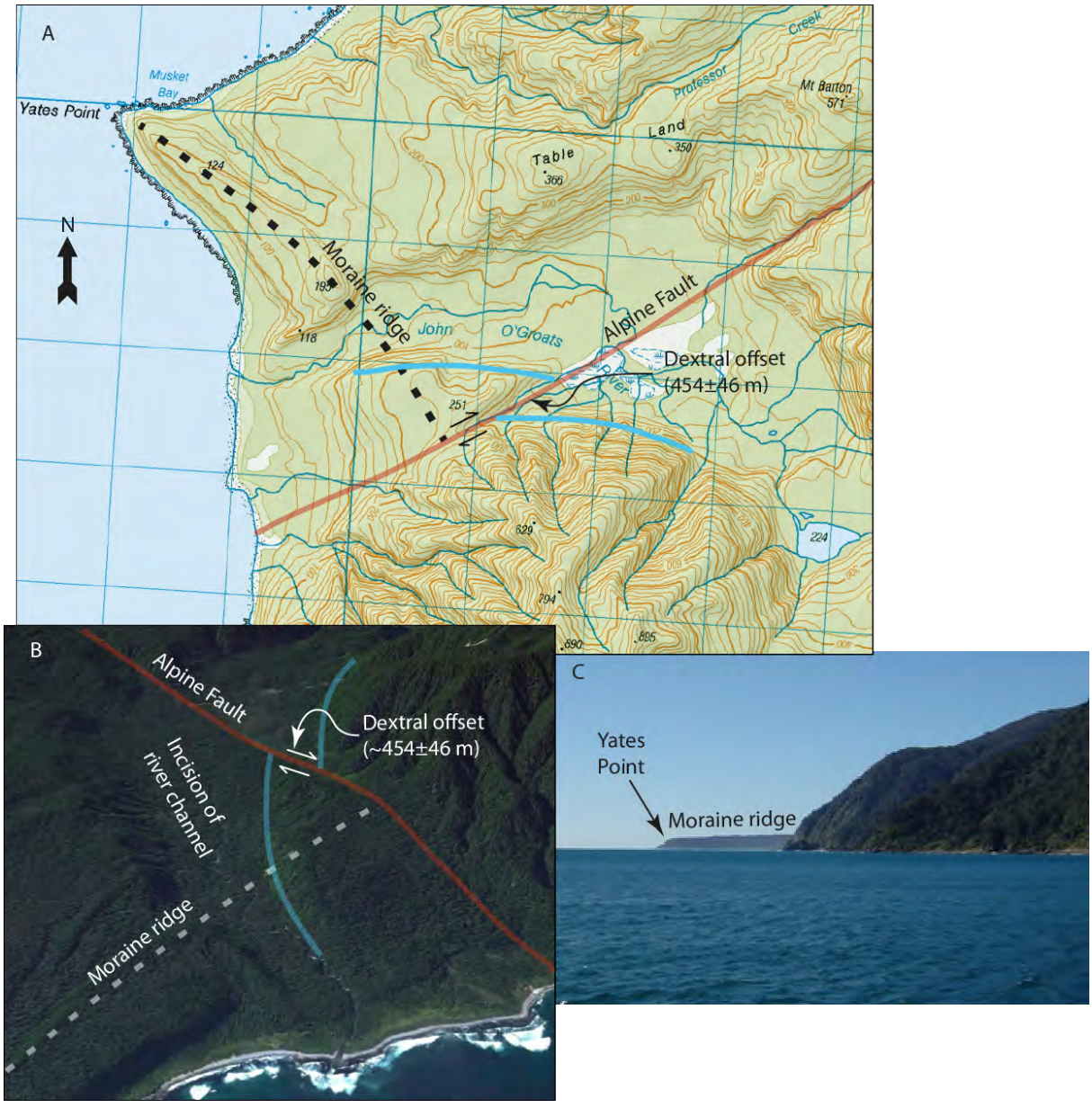

Figure 3.31: Yates Point, moraine ridge and John O'Groats river channel offset by Alpine Fault. A: Yates Point topographic map, contours at 20 m intervals (LINZ). Alpine Fault trace inferred from Turnbull et al. (2010), and topography. Offset data from Sutherland et al. (2006b). B: Oblique aerial image (Google Earth) showing offset channel, view looking east. C: Photo of Yates Point from near Saint Anne point, view looking north. Photo by MarsFKA (www.panoramio.com, accessed 5 September, 2012).

Although the bathymetry from the multi-beam sonar survey (i.e. at 4 m resolution) of the relatively shallow continental shelf offshore of Milford Sound is incomplete, available 10 m bathymetry from an earlier NIWA survey of the continental shelf and slope clearly shows the presence of a ridge which continues offshore and to the south of Yates point. This ridge includes Brig Rock, which breaks the surface between Saint Anne and Yates points (see Figure 3.30), and is probably related to the off-shore continuation of the Yates Point moraine. Together, the St. Anne and Yates Point moraines, and their offshore extensions, imply a large moraine complex overlying the bedrock of the continental shelf near the entrance to Milford Sound.

NIWA photos of the submarine terminal moraine ridge near Brig Rock (see Figure 3.32), appear to show large angular blocks, typical of rock avalanche deposits. Similar blocky material is apparent along the shoreline of Yates Point, where large angular boulders of up to 20 m long have been eroded from the moraine wall by wave action. If the extensive, hummocky moraine complex is composed primarily of very coarse angular debris, it may be that rock avalanche debris which fell onto the glacier from the outer fiord walls was subsequently transported to form the terminal moraine. This explanation is compatible with seismic reflection data and core logs which indicate that mass movement may have dominated post-LGM sedimentation in the inner basins of Milford Sound, as well as numerous submarine and terrestrial landslide deposits which show that large-scale mass movement has continued throughout the Holocene (see Chapter 4).

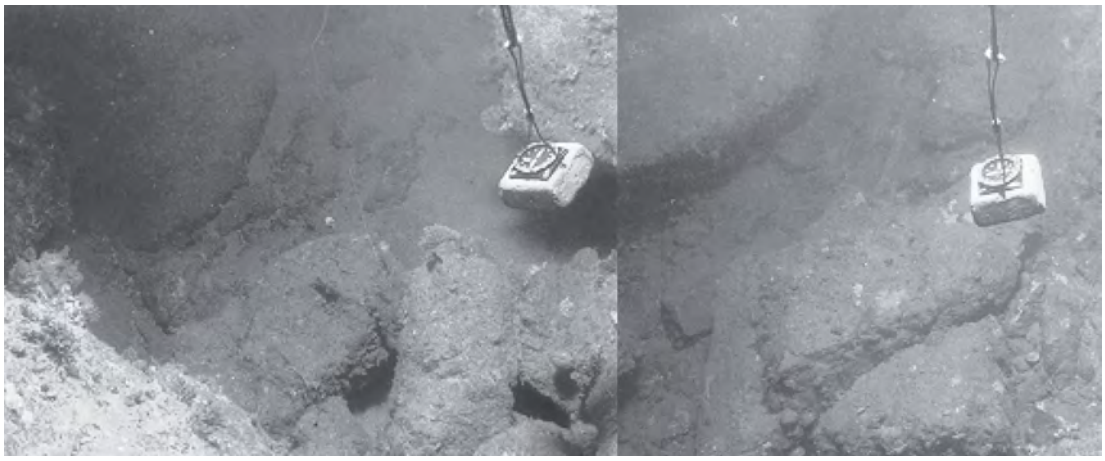

Figure 3.32: Milford Sound: photos of submarine terminal moraine complex. Note large angular blocks, partially buried in fine sediment. NIWA photos.

Landward of the terminal moraine complex is Entrance Basin, with a maximum

depth of ∼150 m, and an average basin floor depth of ∼130 m. During glacial retreat from the terminal moraine and entrance sill, a pro-glacial freshwater lake would have formed in Entrance Basin, with a maximum water level controlled by the entrance sill (-70 m), as relative sea level was ∼110 m lower at that time. Mass-movement deposits originating from upstream locations in the catchment would have been transported towards the glacier terminus, and bare rock walls, recently vacated by glacier ice, may have been more susceptible to failure, with landslides contributing to thick units of diamicton which were left to blanket the underlying bedrock. As the glacier retreated into the inner basins, proglacial lakes would have expanded, trapping sediment that was transported by rivers, and accumulating as thick lacustrine deposits.

3.5.1.2 Retreat through Dale Basin to inner sill

Although Milford Sound has a relatively simple, single-arm geometry, there is evidence for an inner sill, separating the 290 m deep inner Stirling basin from the shallower (130 m) Dale basin (see Figures 3.28 and 3.29). The sill occurs at a constriction where the fiord narrows significantly; bedrock spurs enter the fiord from either side, suggesting that the narrowing is controlled by the presence of a band of underlying bedrock geology that is even more resistant to erosion than the surrounding rock. Site SC1 is located on the south spur at an elevation of 238 m.a.s.l., at the top of the steep lower cliffs. TCND exposure (19.3±2.27 ka) and calibrated SH (19.4±1.9 ka) ages indicate that the glacier probably terminated at the sill some time after 19 ka.

The underwater extension of the bedrock spurs from either side of the fiord is apparent in bathymetry, which also shows that the central part of the sill crest has been removed by erosion; a nick point has eroded away ∼300 m of the floor of Dale basin. A bedrock sill may have existed at ∼60-100 m depth, before progressive erosion of the crest moved the nick point some 300 m back into Dale basin. However, this interpretation does not appear to be well-supported by a multi-channel seismic reflection profile, which shows some evidence of organized sub-parallel bedding and chaotic pockets of parabolic reflectors beneath the remnant sill; this is indicative of depositional facies (e.g. glacial till and/or landslide debris), rather than the seismically opaque signal expected of shallow underlying bedrock.

Based on the seismic reflection data, and the amount of erosion that appears to have occurred since glacier retreat, an alternative interpretation is preferred; the sill is likely comprised of glacial till that was deposited at the glacier terminus, burying the underlying bedrock, possibly during a temporary still-stand during overall glacier retreat. The constricting effect of the protruding bedrock spurs may have helped "ground" the

glacier at the sill, and temporarily halted overall glacier retreat by stabilizing the glacier terminus. Eventually, climate amelioration, rising lake levels in Dale Basin and associated disintegration may have destabilized the glacier terminus, resulting in retreat from the moraine/sill. Development of a deep pro-glacial lake in Stirling Basin would have accelerated calving and glacial retreat. The steep face of the moraine sill may have been debuttressed following glacier retreat, with resulting retrogressive collapse of the middle part of the sill during the development of the pro-glacial lake that occupied Stirling Basin (or during later marine transgression). Progression of the nick point occurred through deep deposits of erodible glacial material (see Figure 3.29), travelling some 300 m from the moraine sill into Dale Basin. Erosion of the sill crest may have been enhanced by marine transgression over the sill, and later by strong currents through the narrow constriction (e.g. Barnes and Pickrill, unpublished; Pickrill et al., 1992).

3.5.1.3 Retreat through Stirling Basin and the lower Cleddau valley

After the formation of a pro-glacial lake in Stirling Basin, the Milford Glacier retreated relatively quickly, due to enhanced iceberg calving driven by decoupling of the glacier base in deep water (see explanation below). Paleo-lake Stirling would have been at least 220 m deep, assuming that the lake level was controlled by the outer sill at the terminal moraine. It is also possible that the inner sill at the seaward end of Stirling basin was significantly larger prior to eroding back into Dale basin, and it could have impounded a lake in Stirling Basin at a higher level than the outer sill.

SH exposure ages of 17.6±2.0 ka and 17.1±2.1 ka from exposed, low-level bedrock near the present head of Milford Sound indicate that overall retreat through Dale and Stirling Basins occurred over ∼1,200 years. During retreat, ice-terminal deposits (diamicton, dropstones, glaciofluvial sand and gravel) would have been deposited proximal to the glacier terminus, and lacustrine sediments would have accumulated in the pro-glacial lake that occupied Stirling Basin. Large tributary rivers (e.g. Stirling, Harrison, Sinbad) would also have contributed meltwater and glaciofluvial sediment directly to Stirling Basin as their tributary glaciers retreated back from Milford Sound.

The extent of the Cleddau/Arthur river deltas that formed in paleo-lake Stirling during LGIT ice retreat is unknown, but it is likely that the modern base of Deepwater Basin (-50 m) lies on top of a large paleo delta. Deepwater Basin has nearly been closed off by Holocene growth of the modern Cleddau and Arthur deltas (see Figure 3.39).

3.5.2 Glacier retreat rate

During periods of significant climate amelioration, glaciers can retreat very quickly; estimated rates of 200 - 300 m/year have been suggested for retreat of the Cordilleran Ice Sheet following the LGM (e.g. Porter and Swanson, 1998, and references therein), and contemporary retreat rates of the Tasman glacier in the Southern Alps range from 54 to 144 m/year (Dykes et al., 2011). Tidewater glaciers or glaciers that terminate in pro-glacial lakes can retreat especially quickly, as rising water level, relative to ice thickness, can effectively decrease overburden pressure, causing buoyancy-driven iceberg calving, as is the case at Tasman Glacier (Dykes et al., 2011). Calving rates correlate closely with the depth of water at the glacier terminus, and glacier retreat can accelerate once the terminus loses contact with a grounding line. In the fiords of Glacier Bay, Alaska (which are up to 500 m deep), maximum retreat rates from maximum Little Ice Age positions probably exceeded 500 m/yr (Brown et al., 1983).

The deglaciation chronology presented here for Milford Sound indicates that retreat from the grounding line on the continental shelf (-120 m) through the Entrance Basin (∼130 m deep) to the outer sill of Dale Basin occurred by ∼18 ka. Bedrock exposure ages from St. Anne Point (SC3, 24.5±2.0 ka) and Dale Point (SC4, 18.3±1.0 ka) suggest that on average, the ∼9 km retreat from the glacier terminus through Entrance Basin was relatively slow (∼1.5 km/ka). Alternatively, considering possible inheritance of ^{10}Be at SC3, and adopting the estimated age-range for the Yates Point moraine based on the well-constrained offset (465±15) m of the Poison Bay moraine (Barnes, 2009), and the full range of published slip rates and uncertainties on the southern Alpine Fault (i.e. 22.0-15.5 ka, based on Barnes, 2009; Sutherland et al., 2006b), then the minimum retreat rate from the glacier terminus to Dale Point is ∼2.4 km/ka. It is possible that during early LGIT (i.e. 22-18 ka) recession, the Milford glacier experienced a number of smaller advance and retreat phases, although this is not evident in the geomorphology of Entrance Basin.

It appears that glacial retreat through the inner basins (Dale and Stirling) was much faster than through the outer basin. TCND and SH exposure ages of ∼17.8 ka at Pater Point (SC16) and Harrison Cove (SC20) suggest that the glacier retreated nearly 8 km from Dale Point in around 500 years (16 km/ka. A rapid retreat is corroborated by calibrated SH exposure ages of 17.6±2.0 ka and 17.1±2.1 ka at Bridget Point and Deepwater Basin, indicating an overall retreat through Dale and Stirling Basins in ∼1,200 years (average retreat rate ∼11 km/ka). TCND and SH exposure ages from ∼4 km up the Cleddau River (SC9, 15.7±2.4 ka and 15.9±2.2 ka respectively) indicate that slightly slower glacial retreat followed evacuation of ice from the fiord basins.

The estimated retreat rates proposed here for Milford Sound are generally more variable and rapid than that proposed by Shulmeister et al. (2010) for retreat from the LGM-ice position in the Rakaia Valley, in the eastern Southern Alps. Shulmeister et al. (2010) estimated a gradual and uniform retreat rate of ∼1 km/ka, based on TCND exposure ages of boulders from recessional moraines, and suggested that ice recession began in the Rakaia valley at ∼24 ka, marking the end of peak glacial conditions in New Zealand. They estimated that the Rakaia glacier had retreated 10 km by ∼15 ka. In general, the topographic relief in the central Southern Alps is significantly greater than that for Fiordland. However, comparing the drainages of the Rakaia and Milford catchments, it becomes apparent that they share similar topographic relief of around 2 km, with the higher peaks hosting small contemporary glaciers on their southern aspects.

Despite similar topographic relief, it is likely the the style of deglaciation in Fiordland was different that on the eastern slopes of the Southern Alps. The large east-flowing river valleys such as the Rakaia gain elevation gradually, reaching about 700-1,000 m.a.s.l. in their headwater reaches (at least 100 km from the east coast), while the valleys which flow into Milford Sound are much shorter, with flatter valley bottoms near sea level, and very steep headwater reaches (generally reaching 400-600 m.a.s.l. within 20 km of the fiord). This suggests that the response of Milford glaciers to climate amelioration in the LGIT could have been quite rapid, as relatively small changes in annual temperature or precipitation could have a major effect on the location of the equilibrium line altitude (ELA), due to the low gradient of the ice surface in the lower valley reaches. In addition, a more rapid and variable retreat through Milford Sound is not surprising, given that the glacier would have terminated in pro-glacial lakes of increasing depth, as it receded towards the head of the fiord; this would have facilitated buoyancy-driven iceberg calving, which would have been most enhanced in the deeper inner (Stirling) basin. Youngest exposure ages of ∼16 ka, obtained from glacially-modified bedrock near the base of the tree slide, and ∼16.9 ka from exposed bedrock near the northern shoreline of lake Ada, suggest that Milford Sound was ice-free by around 16 ka, around which time forests would have begun to re-establish in the lower valleys (e.g. Pickrill et al., 1992). There is no specific evidence for any late-glacial re-advance of the Milford glacier during either the ACR or the YD, however only records from the lower valleys are considered in the current study.

The LGIT retreat history suggested for Milford Sound is generally in agreement with a paleoclimate reconstruction for Preservation Inlet. Pickrill et al. (1992) noted that radiocarbon dates put the transition from light-coloured late-glacial silt and clay

to laminated organic-rich mud (and therefore to a forested catchment with limited headwater glaciers) between ∼14.25 and 18.45 years BP for Preservation Inlet. Between ∼14.4 and 11.9 ka the catchment was extensively re-forested, and marine transgression into the fiord occurred between ∼9.4 and 6.5 ka (Pickrill et al., 1992).

Exposure ages from sample sites on the upper slopes of the tree slide (e.g. SC14) imply an ice surface elevation of 600-700 m at the tree slide, 27 km from the terminal moraine complex. TCND and SH exposure ages (SC1, 19.3±2.3 ka and 19.4±0.7 ka respectively) from ∼240 m.a.s.l., on the bedrock bench above the inner sill of Dale Basin, indicate that the flat-topped spur there was over-ridden by LGM ice, and is therefore not simply a relict surface from an earlier glaciation. The same conclusions apply to the broad bench exposed by the tree slide (∼360-400 m.a.s.l.), and the smaller bedrock spur behind the Milford Visitors Centre (∼80 m.a.s.l.).

3.5.2.1 Theoretical LGIT ice surface profiles

Exposure ages of glacially modified terrain were calculated for sites of various elevation around Milford Sound, including up to 600 m.a.s.l. on the tree slide. These ages provide a snapshot of approximately where the glacier surface was at a known point in time, therefore not all points represent the terminus of the glacier; in some cases the control point represents the top surface of the glacier many kilometres back from it's terminus (e.g. tree slide points and SC1). But is there a simple mathematical model that can be used to represent the entire surface profile of a glacier? Such a model would be useful, given the limited number of available age-control points (see Table 3.2).

Bennett and Glasser (1996) address this problem in their book section, "The prediction of ice sheet profiles". They note that it is a reasonable approximation to consider ice to be a perfect plastic with a yield stress of 100 kPa (a value that is broadly consistent with modern glaciers). Bennett and Glasser (1996) refer to Nye (1952), who used this assumption to derive a simple equation to calculate ice surface profiles:

$$h = \sqrt{2h_o s} \tag{3.1}$$

and

$$h_o = \tau \div \rho g = \sim 11 \tag{3.2}$$

where h is ice altitude (m), τ is basal shear stress, s is the horizontal distance from the glacier margin (m), ρ is the density of ice and g is acceleration due to gravity. The constant value of $h_o = 11$ assumes an average basal shear stress of 100 kPa and an average glacier ice density of 0.9 g/cm^3 (Bennett and Glasser, 1996).

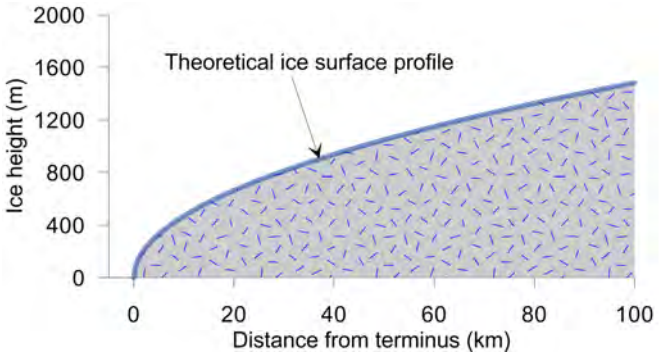

Figure 3.33: Theoretical relationship between ice surface altitude and distance from terminus, on a horizontal bed. Based on Nye (1952) (see equation 3.1).

This approximation assumes a horizontal glacier bed, which is of course not realistic, particularly for the relatively complex bottom profile of a fiord such as Milford Sound. Comparisons with real glaciers indicate that Nye's simple relationship tends to slightly overestimate the slope near the centre of an ice sheet, however the above equation has been widely used in reconstructing former ice sheets (Bennett and Glasser, 1996).

The theoretical relationship of Nye (Figure 3.33) was used here to model ice surface profiles at 500 year intervals (see Figure 3.34) between the LGM and ∼16ka, based on known surface elevations, and assuming a constant glacier bed elevation of -120 m. This is considered to be a reasonable assumption, as -120 m is roughly the elevation of the grounding line at the glacier terminus, and is close to the average bottom elevation over the entire length of the fiord. No attempt was made to extend this relationship further up the Cleddau or tributary valleys. Modelled ice-surface profiles are shown on Figure 3.34 for the time interval from 19 ka to 16.5 ka, at 0.5 ka intervals. The LGM ice surface reconstruction is an estimate based on a best-fit of available age-control points, considering the variations in basin depth and fiord width, and is meant to be a schematic representation of what the LGM ice-surface profile could have looked like.

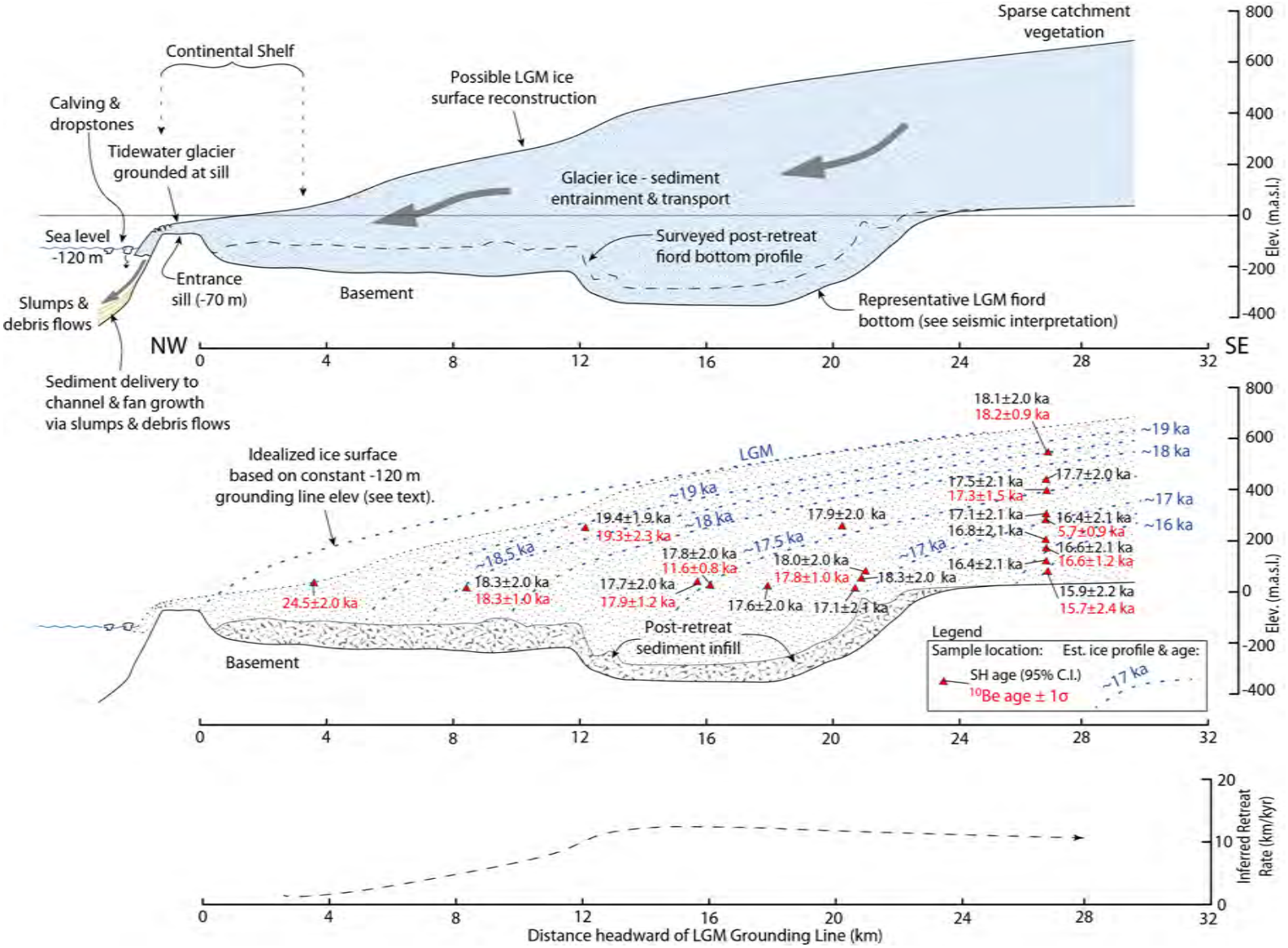

Figure 3.34: Modelled ice-surface profiles: LGM to 16 ka. TCND and calibrated SH exposure ages from Table 3.2, SH uncertainties based on WTLS. LGM ice-surface reconstruction based on a best-fit of available age-control points, considering the variations in basin depth and fiord width. Dashed blue curves represent modelled ice-surface profiles, based on Nye (1952), utilizing best-fit of available age-control points (see text).

3.5.3 Catchment size and sediment production

Milford Sound has a relatively large catchment/fiord area ratio compared to more southern New Zealand fiords (Table 2.1), and is fed by several large rivers which originate in the highest reaches of the Fiordland Mountains. Major rivers that flow into Milford Sound include the Cleddau, Tutoko, Gulliver, Donne, Arthur, Joes, Bowen, Harrison and Sinbad rivers.

3.5.3.1 Delta sedimentation

The influence of most modern New Zealand fiord-head deltas extends only up to a few 100s of metres from the river inlet (Barnes and Pickrill, unpublished), but the main Milford deltas continue to influence both proximal and distal sedimentation patterns. Relatively rapid delta sedimentation at Milford Sound has resulted in post-depositional deformation of forset slopes, based on geomorphological and sedimentalogical evidence for recent delta slumps and turbidity currents (see below). The Cleddau and Arthur river deltas at the head of the fiord, and the Harrison delta on the north shoreline, are large by Fiordland standards, and extend to the bottom of Stirling Basin (-290 m). These deltas have undergone significant progradation during the Holocene, due to ample sediment supply ($\sim$109 tonnes/km^2/yr, Pickrill, 1993) from the relatively large, mountainous catchment.

The Cleddau delta is one of the only modern Fiordland deltas that has completely buried its relict lowstand delta during Holocene progradation. Other features unique to the Cleddau delta include post-depositional deformation (Barnes and Pickrill, unpublished), due to heavy sediment accumulation at the river outlet, and resulting delta slumps and density (turbidity) currents; these are characteristics typical of fiord deltas with high sedimentation rates.

Barnes and Pickrill (unpublished) investigated the four NIWA core samples closest to the Cleddau delta, as well as seismic reflection profiles of the delta, and identified four separate types of morphology that can be identified on the prodelta slope:

1. upper delta (0-130 m) - steep sand and gravel, spilling downslope in tongues, resting at the angle of repose. Sub-parallel, undeformed bedding.

2. mid-slope (130-195 m) - undulating surface relief, broken into blocks bounded by failure planes. Gyttja foreslope sediments interbedded with turbidites, which fine upwards from sand and gravel at the base to sandy mud near the top. Sub-parallel to complex bedding.

3. lower slope (195-236 m) - complex hummocky relief, raised 5-10 m above concave exponential delta profile. Chaotic bedding apparent in seismic profile. Turbidites thin and grain size decreases downslope and onto the flat floor of Stirling Basin.

4. proximal sediment wedge - seismically transparent at the surface, but with strong parallel reflectors in the shallow subsurface, thinning rapidly downslope to merge with the parallel bedded sediments on the basin floor.

New high-resolution bathymetry adds additional geomorphic evidence to these observations. The steep slope of the upper delta is deeply incised in places, and slope failures appear to have deposited thin, elongated sediment lobes which run downhill, spanning the mid-slope (see Figure 3.35). These are interpreted to be turbidite deposits, based on their geomorphology, and sedimentary evidence from cores (described below). There is also clear geomorphic evidence of at least one large rock avalanche-type event with a subaerial origin, where a blocky, lobate deposit, with local relief of up to 10 metres, has over-ridden the mid and lower slopes of the Cleddau delta (see Chapter 4 for details). In addition, there are several steep, talus-like debris cones along the base of the steep fiord walls adjacent to the delta, suggesting that small rock falls and slides are a common and ongoing geomorphic process.

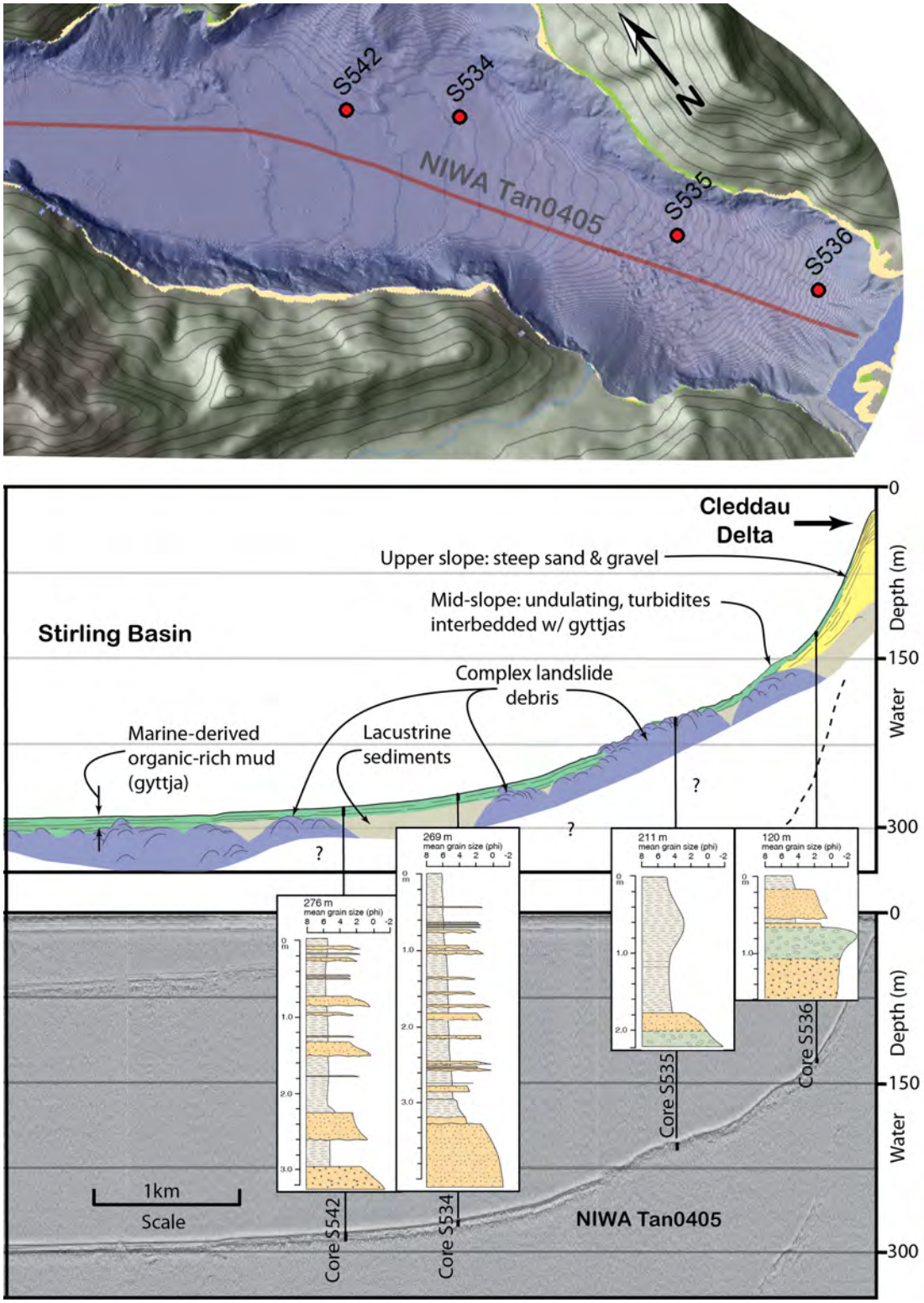

Figure 3.35: Cleddau delta: submarine geomorphology, seismic reflection and core logs. Plan view hillshade model with NIWA core locations, 100 m contours and 10 m bathymetry. In core logs, green, brown and grey-shaded units are gravel, sand and silt, respectively. See text for interpretation).

The large rivers that drain to the Cleddau/Arthur delta transport coarse sediments, depositing sand and gravel to the edge of the foreset slope. Sediment builds up at the front of the delta (where energy is waning), until eventually slope failures move sediment downslope. In this way the foreset slope gradually progrades; as it moves seaward, the steep upper slope maintains something near the angle of repose. Earthquake-shaking may be a common triggering mechanism for surficial sliding and turbidity currents which flow to the toe of the delta, where they settle as sandy graded sequences that interbed with muddy gyttjas on the mid and lower slopes. Most turbidite deposits are capped with thin layers of mud, which may have originated as foreslope gyytja that was incorporated in the flow. The bases of some of the thicker turbidite deposits contain odd outsized clasts of gravel or cobble that outran the main deposit (e.g. basal unit of core S535), or rip-up clasts of mud that were incorporated as the density current ran over underlying gyttja deposits. Beyond the toe of the delta slope and into the deepest part of Stirling Basin, the gyytja veneer appears to generally increase in depth.

3.5.4 Basin Sedimentation

In open New Zealand fiords, late-glacial sediments commonly fill less than one third of fiord basin cross sections (e.g. Thompson Sound, Figure 2.5). However, at Milford Sound, seismic reflection profiles suggest that significantly more of the fiord cross section has been filled in (Figure 3.28). Barnes and Pickrill (unpublished) suggested that this is due to higher terrigenous sediment input from the headwater rivers.

At Milford Sound, gyttjas appear as a thin, poorly reflective veneer with occasional parallel reflectors, and commonly form an unconformity against an underlying discontinuous, opaque to parallel-bedded unit; this sequence is similar to other fiords (e.g. Preservation inlet, Thompson/Bradshaw and George Sounds, Pickrill et al. (1992)), where the underlying parallel-bedded unit has been interpreted as a late glacial clay, that was deposited in a lacustrine environment during glacial retreat (see Chapter 2). However, the parallel-bedded unit at Milford Sound appears to be generally much shallower (i.e. the gyttja veneer is thinner) than in other fiords, which given relatively high sedimentation rates at Milford Sound, suggests that it could be Holocene in age, rather than related to a late-glacial transition.

Unfortunately, the core record does not extend beyond the Holocene, as evidenced by marine shell fragments in the basal units of all Stirling Basin cores. Therefore, the data are insufficient to confirm either a late-glacial or Holocene age for the underlying "lacustrine" unit. However, the thickness of the unit (up to ∼100 m) is similar to that for the equivalent unit at George Sound, suggesting that deposition must have

occurred over a relatively long period of time, even in a sediment-charged pro-glacial lacustrine environment such as that proposed for George Sound (Barnes and Pickrill, unpublished) and Preservation Inlet (Pickrill et al., 1992).

3.5.4.1 The role of landslides

Seismic reflection profiles and high-resolution multi-beam sonar data indicate that high sediment input from co-seismic landslides is likely a major contributing factor to Holocene terrestrial sediment input that is much higher than other New Zealand fiords. In seismic profiles, a thin reflective veneer of parallel-bedded sediments commonly overlies either extensive, discontinuous units characterized by parabolic reflectors (typical of massive blocky landslide debris), or parallel to sub-parallel bedded units (lacustrine silts). Cores show that the veneer is comprised of massive gyttja, interrupted by thin graded beds of sand and gravel, and indicate an overall coarsening trend and slight thinning of gyttja veneer closer to the Cleddau delta. This suggests that closer to the major river outlets, deltaic sedimentation of relatively coarse material derived from terrigenous sources dominates over fine background marine sedimentation.

There is also abundant geomorphic evidence for extensive submarine landslide activity observed from high-resolution multi-beam sonar data, indicating that the majority of the sediment infill in Milford Sound has probably been contributed by mass wasting from the steep fiord walls. The role of large landslides in shaping the geomorphic history of Milford Sound is discussed in more detail in Chapter 4.

3.5.4.2 Thickness of basin fills

Entrance basin has probably been incised into the bedrock of the underlying continental shelf by glacier erosion, but seismic reflection data indicate up to 100 m of parallel-bedded material (interpreted as lacustrine silt) overlying thick units characterized by parabolic reflectors, which are indicative of chaotic depositional facies such as glacial till and/or landslide debris. The bedrock horizon is not readily apparent in the seismic data (largely due to multiple seafloor reflections), although occasional strong reflectors at ∼250 to 300 m below the basin floor suggest that Entrance and Dale Basin have been approximately two-thirds filled in with sediment (see Figure 3.28).

Stirling Basin may have an even deeper sediment fill; the lacustrine unit is very similar in thickness to the outer basins, but the underlying diamicton appears to extend down to around 300 m below the basin floor. However, the bedrock horizon is not visible in the seismic reflection data, so the total thickness of the fill in Stirling Basin is unknown.

3.5.4.3 Tree slides

Aerial reconnaissance of the Milford area indicated that virtually all steep forested slopes show visible evidence of past tree slide activity. Evidence of tree slide events is somewhat ephemeral in Fiordland, as forest regrowth quickly fills in the slide scars. However, it is clear that at least some decades are required to erase all evidence of a substantial tree slide. Comparison of (apparently) fresh tree slides scars shown in aerial photos from 1988, with the same slide scars evident in 2010 Google Earth images, indicates that it probably takes well over 20 years for forests to fully re-establish on steep, slide-prone slopes.

Field investigations included an average-sized tree slide that occurred about 3:30 pm on 23 September, 2008 (source: Otago Daily Times, 25 September, 2008). The slide swath was nearly entirely denuded of all regolith and vegetation, providing a rare accessible vertical transect of freshly exposed bedrock from near sea level to tree line. The slide scar was extensively investigated and sampled for surface exposure dating, offering substantial insight into the processes that control tree sliding in Fiordland.

The tree slide scar extends from the tree line at ∼1,000 m on the northwest face of Mount Underwood (2,222 m), to the floor of the Cleddau valley at ∼35 m.a.s.l., where the deposit temporarily blocked the Milford road. Fortunately no vehicles were caught in the path of the slide, although two women who were walking on the Milford Road had to run for their lives, and seven workers from Milford Sound were cut off from the village by the debris. The road was blocked over a length of 150 m, and took four days to clear (www.geonet.org.nz, accessed 5 July, 2012). Based on field measurements, the slide swath had a length of ∼1,800 m, varying width from 30-160 m and a surface area of ∼125,000 m^2. Local topographic depressions and flat benches appear to have acted as sediment sinks, which were commonly observed where islands of regolith and patches of vegetation had survived the treeslide (see Figure 3.36).

As forest cover matures on steep slopes, the vegetation load progressively builds, until eventually failure occurs, and part of the vegetation mat begins to slip downslope. Heavy precipitation is an observed triggering mechanism for tree slide failure (the 2008 Mt. Underwood slide was preceded by ∼170 mm of precipitation the day before), but earthquakes are also an important triggering mechanism; hundreds of shallow landslides and tree slides were triggered by the 2003 M_w 7.2 Fiordland earthquake (Hancox et al., 2003).

The failure surface is generally along a thin soil/overburden horizon between the bedrock and thick overlying vegetation. Once initial failure occurs, the failure may quickly propagate up and/or downslope, as the supporting influence of downslope veg-

Figure 3.36: Typical island of vegetation in the midst of the Mt. Underwood tree slide scar. Photo by S. Furkert.

etation is lost, and the load increases on downhill slopes, causing the failure to sweep down the hillside. This process may explain why the majority of observed tree slide scars extend from tree line (or the top of ridge lines which are below tree line) to the valley floor (or sea/lake level). Long, narrow tree slide scars are a common feature on most slope aspects in Fiordland (see Figure 3.37); the slides usually denude a narrow swath of the rock face of all vegetation, and most soil/regolith, leaving behind obvious scars. These scars are whitish (in stark contrast to the surrounding green forest cover) when they are fresh, but within a few years they begin to blend in with the surrounding forest, as regrowth covers the bedrock. Vegetation trimlines, which differentiate areas of regrowth from mature forest, likely persist for several decades, but may not be immediately obvious to the casual observer. Regrowth gradually reclaims the vacated swath, with mosses covering the bare rock first. The moss cover thickens quickly, allowing retention of water, dust and soil, which soon provide habitat suitable for growth of pioneer species such as kamahi, lacebark and mountain ribbonwood (Holloway, 1954).

Figure 3.37: Tree slides extending from ridgeline to sea level, north face of Mitre Peak, Milford Sound. Photo by S. Furkert.

Adjacent mature forest cover likely provides a ready supply of seeds and nutrients, as well as shelter, which may encourage growth of juvenile plants. Fieldwork on the Mt. Underwood slide, completed in February, 2011 (some 2.5 years after the slide), confirmed that most of the bedrock surface had developed some moss growth, and in local pockets where regolith had accumulated during the slide, pioneer tree species had already established (see Figure 3.38).

As described earlier, tree slide paths can extend downslope to the bottom of fiord basin, denuding submarine slopes of benthic fauna, and depositing thin graded beds of granular sediment; these sandy laminae commonly contain broken shell fragments and woody debris, and are often capped with coarse plant material. Similar sandy laminae are evident in shallow cores from the deepest part of Stirling Basin, where they are interbedded with massive marine-derived mud.

Figure 3.38: Regrowth of vegetation on the scar of the 2008 Mt. Underwood tree slide scar. Photo by S. Furkert, 2011.

3.6 Summary and conclusions

3.6.1 Post-LGM evolution

Milford Sound has experienced a complex suite of geomorphic processes since the LGM. Geomorphic and sedimentary evidence of these processes include a massive and complex terminal moraine complex, up to over 200 m of basin fill dominated by thick units of diamicton (glacial till and landslide debris that were probably deposited at the front of the retreating glacier) and parallel-bedded, lacustrine sediments (representative of rapid sedimentation of glacial silt and clay in deep pro-glacial lakes) that are interrupted or overlain by hummocky deposits of landslide debris. Overlying veneers of organic-rich marine-derived mud indicate marine transgression and transition to an open-fiord environment. Following marine transgression some 13 ka ago, background basin sedimentation appears to have been predominantly marine-biased, with veneers of massive gyttja interbedded with thin sandy, organic-rich laminae that are probably related to tree slides. There is also abundant geomorphic evidence for large post-glacial landslides, observed in high-resolution bathymetry and seismic reflection data.

3.6.1.1 Terminal moraine complex

Milford Sound has a somewhat unusual entrance sill, which is formed by a system of terminal and lateral moraines deposited on the ∼1-3 km-wide continental shelf, well seaward of the fiord entrance. Most other New Zealand fiords have bedrock sills at their entrances, and comparatively narrow (or virtually non-existent) continental shelves, where they would have delivered sediment directly to offshore canyons and slopes; therefore other New Zealand fiords generally do not display significant moraine deposits (Barnes and Pickrill, unpublished; Pickrill et al., 1992). The relatively wide continental shelf off Milford Sound supported the growth of an extensive offshore terminal moraine system, where the glacier deposited abundant sediment transported from the catchment. NIWA photos of the terminal moraine appear to show large angular blocks typical of rock avalanche deposits, suggesting that mass movement may have been a major contributor to high LGM sedimentation at Milford Sound.

3.6.1.2 Episodic basin sedimentation

Although laterally extensive, the parallel-bedded (lacustrine) unit at Milford Sound is discontinuous, being interrupted by chaotic seismic facies. This is in marked contrast to other New Zealand fiords, such as George Sound, where the lacustrine unit has similar

thickness, but is generally continuous throughout the available seismic profile. Based on the evidence presented here, it is suggested that the lacustrine unit at Milford Sound is related to sedimentation in proglacial lakes during the LGIT, similar to other New Zealand Fiords, but with the following fundamental differences:

1. thick deposits of diamicton (glacial till/landslide debris) were left behind following glacier retreat, due to high rates of terrigenous sediment input from mass failures and subsequent glacial transport,

2. lacustrine sedimentation was accompanied by periodic landsliding episodes (likely relating to seismic activity, see Chapter4); these deposits are interspersed with the lacustrine unit, and generate the discontinuous parabolic reflectors and chaotic depositional facies seen in the seismic reflection profiles,

3. following the transition to a marine environment around ∼13 ka, episodic landsliding continued; the largest catastrophic events may have impacted sedimentation on a basin-wide scale, temporarily swamping background marine sedimentation, and disturbing fine-grained sediment veneers,

4. on a smaller scale, but probably much more frequently than large landslides, tree slides have regularly entered fiord basins in the Holocene, resulting in sandy, organic-rich laminae that interrupt the gyttja veneer. While it is likely that most vegetation involved in tree slides floats away after entering the water (common Fiordland beech species have a wood density of ∼600-700 kg/m^3 at 12% moisture content, Norman, 1990), it is possible that some trees end up buried in the sediment at the fiord bottom.

3.6.2 Glacial retreat history

3.6.2.1 LGM

The trunk glacier that occupied Milford Sound during the last glaciation was grounded on the continental shelf, where it deposited an extensive moraine system which supplied sediment to the head of a system of submarine canyons; relative LGM sea level was ∼110 m lower than it is today. A TCND exposure age from a bedrock bulge at St. Anne Point suggests that peak glacial conditions may have ceased some time around 24.5±2.0 ka, but a lateral moraine at Yates point, that is offset by the Alpine Fault, provides evidence that moraine deposition culminated there between 22.0-15.5 ka, based on the range of fault slip rates from near Milford Sound, on both the onshore (Sutherland et al., 2006b), and offshore (Barnes, 2009) portions of the fault.

3.6.2.2 LGIT

Retreat from the terminal moraine complex over a distance of ∼9 km to Dale point was complete by 18.3±1.0 ka, suggesting that climate amelioration had commenced by then. Freshwater proglacial lakes formed behind sills, and these lakes acted as sediment sinks, trapping thick fills of diamicton, overlain by thick lacustrine sediments, transported by glaciers and abundant meltwater from a largely barren catchment. Relatively rapid retreat over a further ∼13 km through Dale and Stirling Basins, to a position near present-day head of Milford Sound was complete by ∼17 ka, aided by buoyancy-driven iceberg calving in a deep proglacial lake (paleo Lake Stirling). Milford Sound was ice-free by ∼16 ka, around the time when reforestation of the lower valleys in the Milford catchment would have commenced.

A detailed paleoclimate reconstruction covering the period between ∼16 ka and the beginning of the Holocene (∼12 ka) is not possible given the data presented here, however, general timing of major evolutionary phases can be approximated from sedimentological and geomorphic evidence. From ∼16 ka to 13 ka, glaciers retreated back into the valley headwaters, and during catchment reforestation, outwash rivers transported abundant terrigenous sediment to prograding lake deltas. Predominantly lacustrine basin sedimentation was periodically interrupted by episodes of increased sedimentation from landslide events, either upstream in the catchment, or directly into the lakes. The Milford catchment was probably largely reforested, with reduced terrigenous sediment supply to lake basins and glaciers limited to valley headwaters, by ∼13 ka. Relative sea level was ∼100 m below present at around 15 ka, so at least one large freshwater lake would have persisted in Milford Sound at that time. At ∼13 ka, rising eustatic sea level breached the outer sill (-70 m), and marine transgression occurred, eventually transforming the lakes into an open fiord environment. Eustatic sea level rise continued, reaching present-day level by ∼7 ka (Fleming et al., 1998; Milne et al., 2005). Marine transgression between ∼13 and 7 ka drowned the river deltas that had formed in paleo Lake Stirling, and new deltas formed where rivers entered the fiord.

3.6.2.3 Holocene

During the Holocene, Milford Sound has continued to experience much higher terrigenous sediment input than other New Zealand fiords, based on the overall thickness of basin fills, clear evidence from high-resolution bathymetry and seismic reflection data of large landslide deposits overlying lacustrine sediment units, and the presence of sandy laminae which are interbedded with massive marine-mud in shallow cores. Further

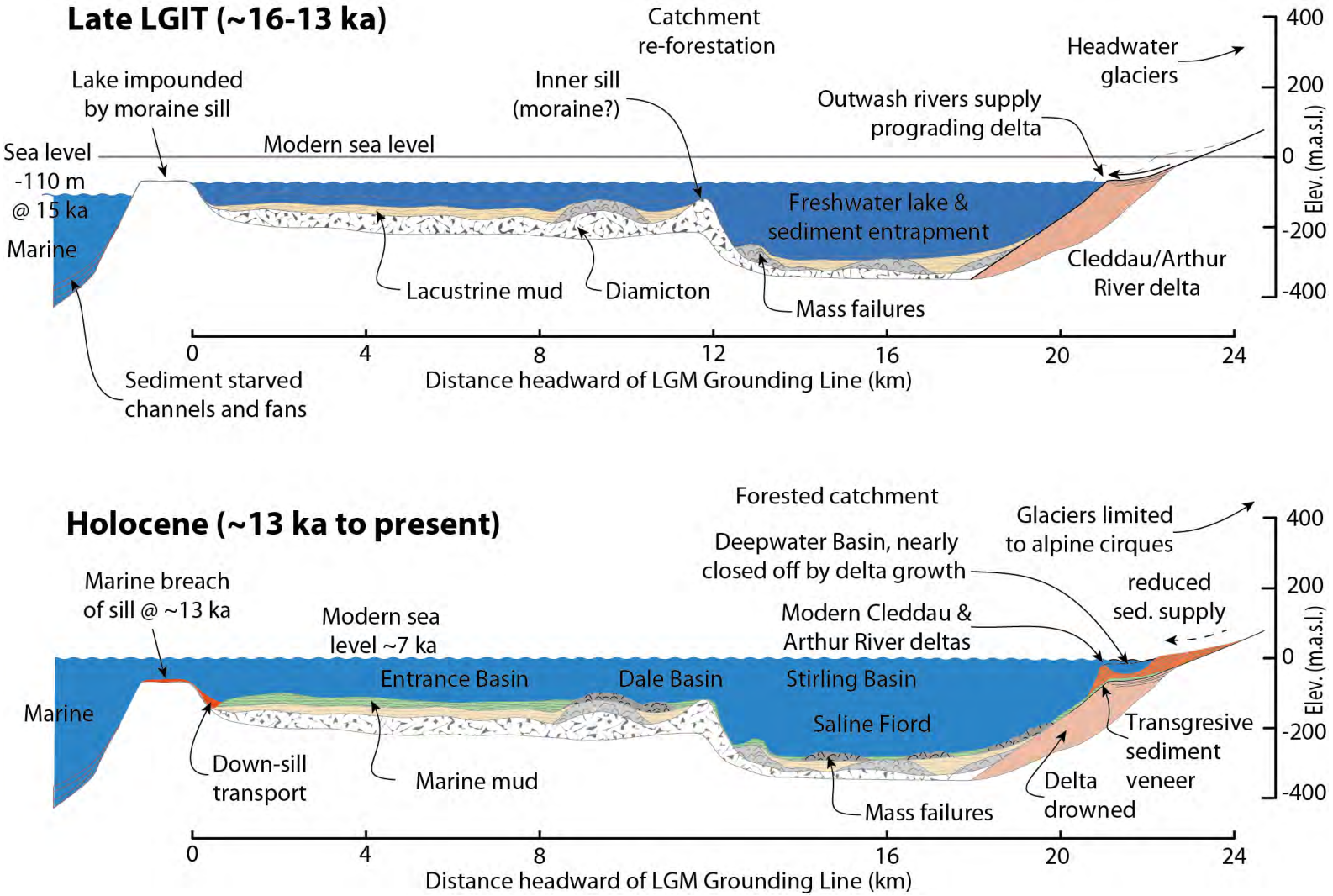

Figure 3.39: Schematic post-glacial fiord evolution. Top figure represents late-LGIT lacustrine environment(~16-13 ka). Bottom figure represents Holocene marine transgression (~13-7 ka), and transition to an open-fiord environment by 7 ka. Note growth of Holocene delta on top of paleo-Cleddau delta, and accumulation of mass failure deposits throughout the LGIT and Holocene.

evidence for relatively high Holocene sedimentation rates is the progradation of the main river deltas, which have buried their relict, low-stand deltas. The large modern deltas of Milford Sound show clear evidence of continued growth and instability, including slumping and turbidity currents. These features are typical of fiords with high sedimentation rates.

3.6.3 Milford Sound compared to other New Zealand fiords

Milford Sound stands out as different from other New Zealand fiords, for the following reasons:

- a catchment-to-fiord area ratio that is 2-4 times larger than other fiords (see Table 2.1).
- the catchment includes the highest and steepest topography of the Fiordland Mountains, which generates the highest orographic precipitation.
- the Cleddau/Arthur river deltas are fed by several large rivers, and are by far the largest and most active fiord-head deltas in Fiordland.
- the Cleddau delta is the only Fiordland example where extensive delta slumps and turbidity currents are apparent, probably due to heavy sediment accumulation. It is possibly the only modern Fiordland fiord-head delta that has completely buried it's relict, lowstand delta during Holocene sedimentation.
- basin sediment infill is dominated by mass wasting from the steep fiord walls and terrigenous input at river deltas, compared to in-situ biogenic dominated sedimentation at other fiords.
- during the LGM the glacier that occupied Milford Sound extended out onto the narrow continental shelf, where it deposited an extensive system of moraines which now overly the entrance sill (see Figure 3.30). Glaciers in other fiords south of Sutherland Sound did not deposit moraines on the continental shelf (which is much narrower at other fiord entrances), and delivered sediment directly to the continental slope.

Chapter 4

Landslide distribution at Milford Sound & implications for natural hazards and risk management

4.1 Introduction and background

Milford Sound is an iconic natural attraction with international tourist appeal. Each year nearly 600,000 visitors arrive to experience the spectacularly rugged scenery, most of whom visit the Milford Village and cruise the fiord with one of several commercial tour operators. International visitors make up ∼80% of tourists at Milford Sound. Fiordland National Park visitors (∼90% of whom travel to Milford Sound) contributed ∼$228 million to the New Zealand economy in 2005. A high concentration of large post-glacial landslide deposits preserved in the Milford Sound catchment, including many on the fiord bottom, indicate a high coseismic landslide hazard.

Landslide-generated tsunami have been responsible for the three worst natural disasters in Norway over the last century. Between 1905 and 1936, 174 people were killed by landslide-generated tsunami in the fiords of western Norway (see Table 4.1). The hazard is the highest priority for hazard management in Norway; the associated risk is quantified by identifying and monitoring potential failure areas, estimating landslide properties based on field measurements, and modelling impact velocity, wave propagation and runup with a combination of numerical simulations and laboratory models. Large landslides that fall into the fiords of Norway are generally not coseismic, so warning signs such as tension cracks, slumping or increased minor landslide activity normally precede major events; locations considered to be high-risk to local communi-

ties are monitored intensively.

Just offshore of the entrance to Milford Sound lies one of the world's most active plate-boundary faults, the Alpine Fault, which averages ~330 years between ruptures, and last ruptured in 1717 with an earthquake of around M_w 8.1. In addition, seismic activity originating from the Fiordland subduction zone commonly affects Fiordland, such as the 2009 M_w 7.8 earthquake near Dusky Sound. The potential risk associated with landslide-generated tsunami has not been previously investigated at Milford Sound, despite the exceptionally steep and seismically active setting, high concentration of post-glacial landslides, and knowledge of historical disasters in Norway.

4.1.1 Landslides in Fiordland

The narrow valleys and extremely steep, rugged mountain ranges of Fiordland contain a relatively high concentration of large landslide events, with at least 70 very large ($> 10^6$ m^3) known prehistoric landslides of post-glacial age (Hancox and Perrin, 2009, this study) including the 27 x 10^9 m^3 Green Lake Landslide. Korup (2005b) produced an inventory of 778 large post-glacial landslides in the western Southern Alps and Fiordland Mountains, and found that the highest local landslide densities occurred near Milford and George Sounds, and south of Doubtful Sound.

4.1.1.1 Precursor factors and triggering mechanisms

Possible precursor factors that can precondition slopes to failure include gravitational stresses due to post-glacial slope debuttressing and river incision, localized reduction of rock mass strength due to faulting and earthquake shaking, and slope dilation following precursory landsliding (Allen et al., 2011; Korup, 2005b,c). Key triggering mechanisms for landslides include seismic ground shaking, fluvial undercutting, groundwater and pore pressure fluctuations and high intensity rainstorms (Hancox et al., 2002; Hancox and Perrin, 1994; Korup, 2005a,c).

In Fiordland, it is likely that seismic activity serves as the primary trigger for failures that ultimately result from progressive degradation of rock mass strength, beginning with deglaciation of the valley below. Progressive reduction of rock strength by brittle fracture propagation can continue for many thousands of years after deglaciation, and is considered a primary failure mechanism for the 1991 Randa rock avalanche in the Swiss Alps (Eberhardt et al., 2004). Progressive degradation of rock strength punctuated with seismic activity may help to explain the high level of rock avalanche activity during the second half of the Holocene in Fiordland (see Figure 4.12), as well as in some of the fiords of western Norway (Blikra et al., 2002).

Based on the results of the current study, the distribution of large landslides in the study area appears be primarily influenced by episodic seismic activity (see Figure 4.12). Coseismic landslides are common in New Zealand, especially with earthquakes over magnitude 6.2; at least 22 earthquakes have triggered damaging landslides in New Zealand since 1840, with great earthquakes ($>M_w$ 8) triggering large landslides up to 300 km away from the fault rupture (Hancox et al., 2002; Hancox, 1998. Based on a suite of paleoseismic records, including evidence of widespread landslide damage (inferred from tree ring analysis near Milford Sound, Wells et al., 1999), four earthquakes of around M_w 8 have occurred along the Alpine Fault over the past one thousand years, the last two at around 1620 and 1717 A.D. Two earlier ruptures at around A.D. 1230 $\pm$ 50 and A.D. 750 $\pm$ 50 are also inferred from radiocarbon dating of offset strata in trenches excavated across the Alpine Fault between the Haast and Turnbull rivers, in South Westland (Berryman et al., 2012a). The M_w 8.1 1717 A.D. earthquake ruptured over a distance of nearly 400 km, extending from near Milford Sound to the Haupiri River (Berryman et al., 2012a; De Pascale and Langridge, 2012; Wells et al., 1999; Yetton, 1998). Recent investigation of the southern portion of the onshore Alpine fault has extended the record of fault ruptures; an ∼8,000 year record of at least 24 ponding events is recorded in river terrace sediments at Hokuri Creek (near Lake McKerrow), suggesting that the probability of the next rupture occurring within the next 50 years is ∼30% (Berryman et al., 2012b).

4.1.2 Displacement waves in fiords

4.1.2.1 Examples from Norway

During the last 100 years, entire villages have been virtually destroyed by landslide-generated tsunami in the steep-walled fiords and lakes of western Norway. The three worst natural disasters (in terms of number of lives lost) in Norway in the twentieth century were caused by tsunami that were triggered by landslides falling from steep mountainsides into fiords or lakes; 61 people were killed at Loen in 1905, 41 at Tafjord in 1934, and another 73 at Loen in 1936 (Eidsvig et al., 2011, and references therein).

At Loen in 1936, following months of smaller rockfalls, an ∼1 x 10^6 m^3 sheet of bedrock collapsed and fell off 1,500 m high Mount Ramnefjell from a height of between 400 and 800 m, and slid down a slope of ∼60° into Loenvann Lake, which had a maximum depth of ∼120 m (Jorstad, 1968; Slingerland and Voight, 1979). The impact generated a wave that surged up the opposite headland to a maximum height of 74 m, and inundated the nearby village of Loen killing 73 people, including several deaths at

the far end of the lake (∼15 km away from the impact), where maximum observed wave runup was 15 m (Jorstad, 1968). The disaster had a devastating effect on the Loen area, with over a third of the local population killed by the waves (Jorstad, 1968).

Two years earlier, a similar disaster occurred when ∼3 x 10^6 m^3 of rock detached from a height of up to 700 m on Langhammaren on the northeast wall of Tafjorden. The landslide crashed into the fjord and generating a tsunami that reached a maximum runup of 62 m at shore. Multiple displacement waves caused great destruction in the villages of Tafjord and Fjora, where the waves ran up to 16 m and 13 m respectively; at least 41 people were killed. Numerical modelling of the Tafjord event by Harbitz et al. (2006) suggested that wave energy was trapped in the inner fiord by valley geometry (a constricting bend), and that wave reflection and interference due to the steep fiord walls compounded the effects of the initial displacement wave.

A slightly smaller wave (∼40 m maximum runup height) had previously caused 61 deaths at Loen (1905), when a relatively small slab of rock (∼0.05 x 10^6 m^3 according to Jorstad (1968)) fell from 500 m height on Ramnefjell, entraining around 0.3 x 10^6 m^3 of additional scree and gravel before impacting the fjord; the villages of Bodal and Ytre Nesdal were almost entirely destroyed (Jorstad, 1968).

The Norwegian fiords are generally not subject to substantial seismic activity, and a precise triggering mechanism has not been established for the Tafjord disaster. However, residents were aware of an expanding fracture high on Langhammaren as early as the turn of the century. Accelerated movement of the rock bodies and several small precursor slides occurred during the month prior to the disaster (Blikra et al., 2002; Braathen et al., 2004; Hermanns et al., 2006).

4.1.2.2 Examples from other regions

In seismically active fiord landscapes such as those in British Columbia/Alaska, Chile and New Zealand, large rockfalls and rock avalanches may be initiated by earthquakes without prior warning from small rockfalls. A M_w 6.2 earthquake centred near Aysen Fjord in Patagonian Chile occurred on 21 April, 2007, initiating many landslides that fell into the fiord. Two rock/debris avalanches, with respective volumes of approximately 8 and 12 x 10^6 m^3 generated a tsunami in the fiord, which caused 10 fatalities and damaged several salmon farms (Sepulveda et al., 2010).

Landslide-generated tsunami have also caused significant damage and loss of life in the fiords of Alaska and western British Columbia. Perhaps the most spectacular and well-known historical example of a coseismic subaerial landslide-generated tsunami occurred in 1958 in Lituya Bay, Alaska, where strong ground motion associated with

a M_w7.7 earthquake on the Fairweather Fault caused a 30 x 10^6 m^3 landslide that fell into the bay, generating a ~100-150 m high displacement wave. The wave ran up a mountain-side opposite the slide to an elevation of 524 m, and devastated forests in a wide swath around the bay Miller (1960)). The Lituya bay tsunami is relatively well-constrained due to survivor accounts and preserved physical evidence (e.g. forest trim lines and source area scar), and the event has been successfully replicated using physical modelling (e.g. Fritz et al., 2004) and numerical simulation (e.g. Quecedo et al., 2004).

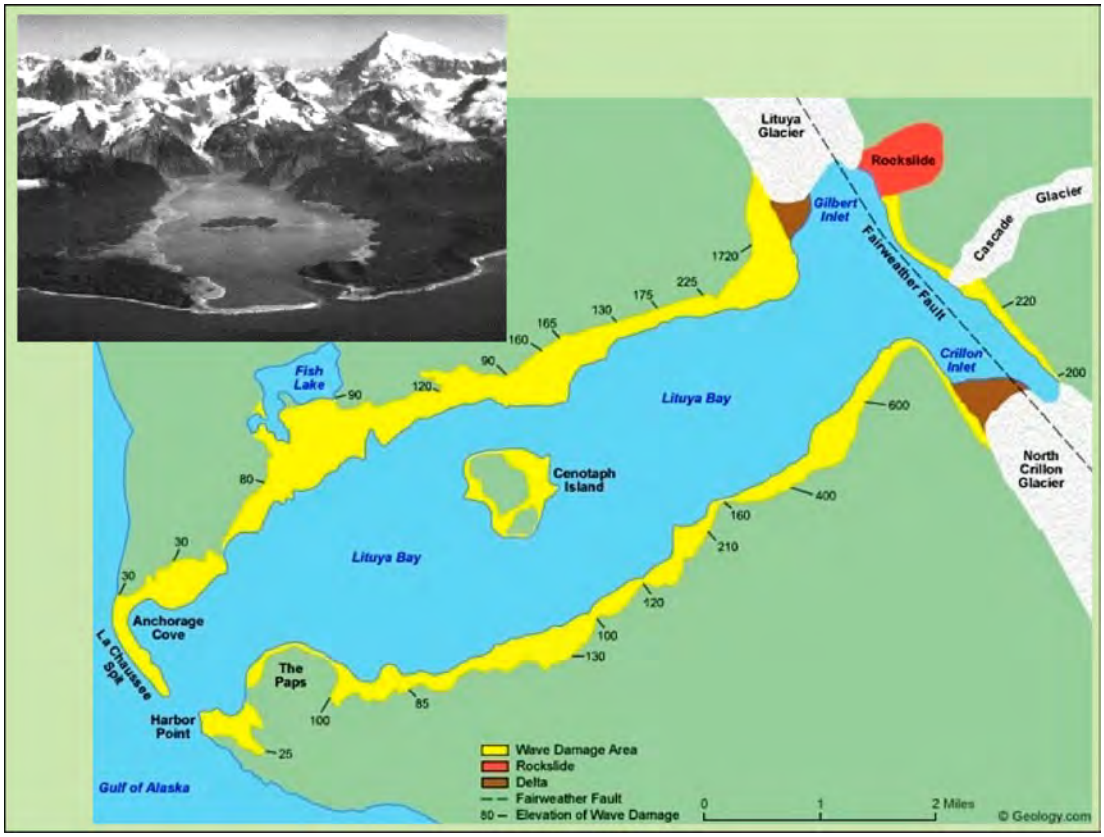

Figure 4.1: Map of Lituya Bay, Alaska, with yellow-shaded area indicating maximum wave run-up following the 1958 coseismic rockslide (shown in red) and resulting displacement waves. Maximum run-up heights are shown in feet. Inset photo shows trimline shortly after 1958 tsunami. Source: geology.com

Other historical landslide-generated tsunami in fiord landscapes include an 8 m tsunami generated by submarine landslides at Kitimat in 1975 (Johns et al., 1986), and a 9-11 m tsunami resulting from a submarine delta failure in Skagway in 1994 (Cornforth and Lowell, 1996).

Table 4.1: Selected historical tsunami disasters associated with rock-slope failures.

Year	Location	Volume of rock - slope failure (x 10^6 m^3)	Maximum scarp height (m)	Maximum wave height (m)	Number of fatalities
1905	Loen, Norway	0.35	500	40	61
1934	Tafjord, Norway	3.1	730	62	41
1936	Loen, Norway	~1.0	800	74	73
1958	Lituya Bay, AK	31	914	524	2
1963	Vajont Dam, Italy	270	450	235	1909

4.1.2.3 Have landslide-generated tsunami occurred in Fiordland?

The only confirmed historical record of a landslide-generated tsunami in Fiordland is related to the M_w 7.2 2003 Fiordland earthquake, which generated more than 400 landslides. Approximately 200,000 m^3 of rock collapsed into Gold Arm of Charles Sound, generating a displacement wave that travelled across the fiord, stripping vegetation up to 5 m above the normal high tide line (Hancox et al., 2003).

There are references to possible tsunami or seiches within Doubtful Sound, following the 1826 Fiordland earthquake (~M_w 7.6 - 7.8, Downes et al., 2005), based on eyewitness accounts from a sealing party who were anchored at Cascada Bay at the time of the earthquake (Taylor, 1855). Following the 1826 earthquake, significant landslides were visible along ~180 km of the Fiordland coast, from Doubtful Sound to Cascade Point in South Westland; Taylor (1855) compiled eyewitness accounts from the 1826 earthquake which indicated that "large masses of the mountains had fallen" into the sea.

4.2 Milford Sound landslide distribution

4.2.1 Data and methods

A wide range of data sources, field investigation and sampling methods, and laboratory techniques were utilized in order to interpret the landslide distribution documented in the current chapter. High-resolution submarine seismic reflection data and bathymetry, sediment cores from Stirling Basin, and field investigation and mapping of terrestrial landslide deposits were complemented with three dimensional geomorphic modelling. Ages for terrestrial landslide deposits were constrained by radiocarbon and TCND exposure-age dating. Maximum ages for post-LGM submarine landslide deposits were constrained by timing of glacier retreat; a deglacial chronology was developed by using

an extensive suite of SH exposure ages, calibrated with eight ^{10}Be surface exposure ages (see Chapter 3, Figure 3.2 for details).

Terrestrial landslide deposits were digitally mapped in ArcGIS, based on geomorphic evidence from mapping and photography, and field data (where available). See Figures 3.1 and 3.2 for geomorphic mapping and sample locations. Locations of individual landslide deposits in relation to the study area are shown in Figure 4.2, with the exception of the Donne and Adelaide deposits, which are farther away from Milford Sound.

4.2.1.1 Geomorphic evidence and Vulcan model

Potential subaerial landslide deposits in the study area were prioritized for field investigation based on aerial reconnaissance surveys, and interpretations of aerial photography and DEMs. Diagnostic landforms included failure scarps, asymmetrical and/or hummocky topography in otherwise symmetrical valley bottoms, and evidence of flow lobes. Uniform vegetation stands that could indicate relatively recent disturbance were generally not present, as most deposits are completely overgrown with mature forest.

Large deposits in relatively close proximity to Milford Sound were investigated in the field, and any additional physical and sedimentological characteristics were documented. These deposits are generally extensive (2-D surface area >1 km^2), and heavily forested; therefore only representative parts of the deposits were investigated in the field. Deposits that were not investigated in the field were generally remote (e.g. the $\sim$114 x 10^6 m^3 deposit in the Donne valley, and a $\sim$24 x 10^6 m^3 deposit in the upper Sinbad valley), or had difficult access (e.g. a $\sim$19 x 10^6 m^3 deposit in the lower Arthur River valley, and a $\sim$3 x 10^6 m^3 deposit in the Stirling valley, above Stirling Falls).

4.2.1.2 Other landslides in the Milford catchment

Several other large landslide deposits exist in more remote locations within the Milford catchment; these were not considered as high a priority for risk assessment as those that are closer to Milford Sound, and therefore they were not included in field work for this project. These include, but are not limited to:

- a giant deposit in the Green valley (a tributary of the Arthur), near the Dumpling hut on the Milford Track. With a volume of $\sim$700 x 10^6 m^3(Hancox and Perrin, 2009) and a maximum thickness of $\sim$450 m, the deposit is one of the largest in Fiordland.

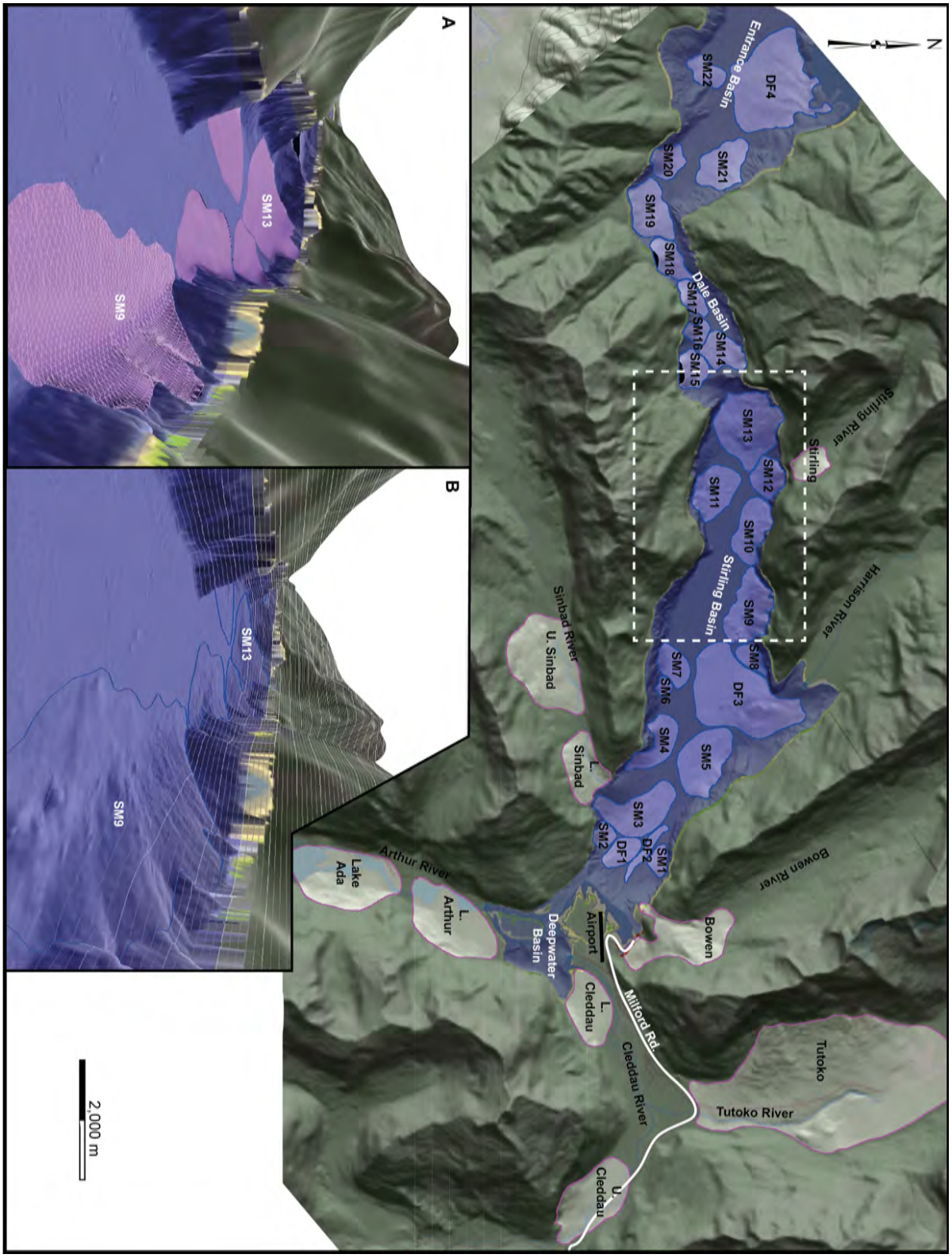

Figure 4.2: Study area landslides (Donne and Adelaide not shown). Dashed white rectangle shows location of Fig. 4.3. A) Perspective view of modelled pre-deposit bathymetry, looking west. B) Existing 20 m bathymetry, same area as B. Scale refers to plan view only.

- a very large deposit below the south face of Mount Pilans, near Sutherland falls in the upper Arthur valley.
- several large deposits in other north-western tributary valleys of the Arthur River.

These deposits were not investigated from the ground (although some were observed during reconnaissance flights), due to their remote nature. Most are readily accessible by helicopter from Milford Sound, but time and budget limitations precluded them from detailed field investigation as part of the current project.

As described in Chapter 3, a three-dimensional geomorphic model of the Milford Sound area was developed from available GIS data, using Vulcan geological modelling software. The model was used for three-dimensional landscape visualization and geomorphic interpretation, as well as measurement of slope aspect and gradient, and estimation of physical landslide characteristics, including:

- aspect and gradient of slope failure plane,
- deposit area and volume,
- fall height and runout distance,
- 3-D slide path length for approximate centre of mass,
- water depth (for submarine landslide deposits)

Landslide areas and volumes were calculated for subaerial and submarine deposits by a 3-D geometrical modelling approach. Vulcan was used to re-construct pre-deposit topography based on the bathymetry of adjacent fiord walls that are not affected by landslide deposits (see Figures 4.2 and 4.3). Estimated deposit extents were segregated with a 3-D polyline, and contours were interpolated using a visual best fit to the topography outside the deposit area. Contours were then joined vertically with third or fourth order polynomial curves to best approximate what was considered to be the most likely pre-deposit bathymetry. Boundary polylines, contours and connecting polynomial functions were then triangulated to generate a three-dimensional pre-deposit surface for each landslide. These surfaces were then compared to a second triangulation of the same extent, but based on the post-deposit bathymetry. Volume between the pre-deposit and post-deposit triangulations were calculated using Vulcan.

The resulting volumes for submarine deposits are considered to be conservative, as they are based on the existing fiord bottom profile. Interpretation of seismic reflection data indicates that some deposits are partially or completely buried beneath

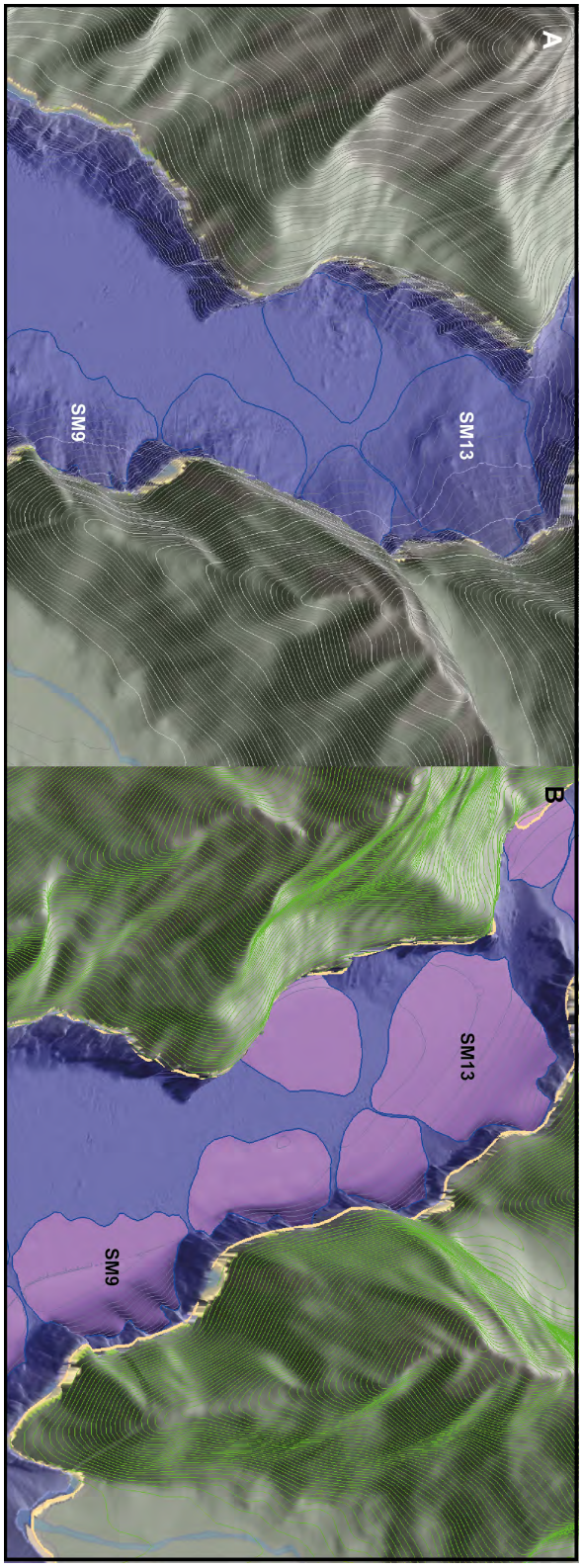

Figure 4.3: Reconstructing pre-deposit bathymetry using Vulcan; central Stirling Basin (area shown by dashed white rectangle in Fig. 4.2), oblique view looking west, 20 m bathymetry and contours. A) Submarine in blue, subaerial in green, landslide deposits outlined in dark blue. B) Pre-deposit bathymetry in pink.

fine-grained lacustrine or marine sediments, so their actual volumes may be significantly larger than calculated. An example is deposit SM10, near Stirling Falls, which appears to have a much larger source area than the visible part of the deposit suggests (see Figure 4.8); however seismic data indicate that there is a substantial thickness of sub-surface landslide material, which has penetrated into and deformed the muddy basin sediments. The failure scarp above SM10 suggests that there may have been more than one landslide initiated on the same steeply-dipping slope.

Landslide characteristics (based on the Vulcan model) are listed in Table 4.2, and specific features of representative individual landslide deposits that were investigated in the field are discussed in subsequent sections.

4.2.2 Terrestrial landslide deposits

Deposit surfaces that were investigated in the field (i.e. Tutoko, Lower and Upper Cleddau, Lake Ada, Bowen, Sinbad, Lake Adelaide) were generally covered with large angular boulders, commonly measuring over 6 m in longest dimension. Thick forest has enveloped and overgrown these boulders, so beyond the typical coarse blocky surface texture, details of the surface sediments are difficult to determine. One possible exception is the giant ($\sim$625 x 10^6 m^3) Lake Adelaide deposit in the upper Moraine creek valley, which has an elevation of around 1000 m.a.s.l., therefore the deposit is sparsely vegetated, primarily with alpine scrub and grasses. The Adelaide deposit was investigated due to its exceptionally large size, and because it's surficial geomorphic and sedimentary characteristics are easier to observe than the lower, densely forested deposits in the Milford catchment. The Adelaide deposit surface is comprised of a roughly 2 km by 2 km jumbled mass of large angular boulders (see Figure 3.6), which form several large hummocks or lobes which extend up to 2 km away from the source area, and have local relief of up to 100 m. The extremely coarse, jumbled material typically observed on the surface of the deposit is clearly clast-supported; moving around the deposit often entailed crawling between and under huge blocks, and un-suspected cavities were occasionally discovered hiding beneath thick mats of scrub. However, closer to the base of the failure slope (i.e. on the proximal part of the deposit) the texture of the surface material was much finer, with cobbles and smaller boulders dominant; it is uncertain whether this is an inherent feature of the deposit, or the result of subsequent small rock falls and snow avalanches. Rock avalanches of this size are usually pervasively fragmented below the coarse surface carapace (Davies et al., 1999).

The Adelaide deposit appears to have initiated from the ridgeline at around 1,500 m.a.s.l., and fallen some 600 m before travelling across Moraine Creek and running

Table 4.2: Landslide deposit characteristics based on Vulcan 3-D model.

Deposit ID	**3-D Area**[a] (km^2)	***V*=Volume**[b] (x 10^6 m^3)	***l*=slide-path length**[c] (m)	***d*=Water depth**[d] (m)	α=**failure plane**[e] (°)
Subaerial source and deposit (see Table 3.5 for ages)					
Adelaide	4.14	625.2	1,220	NA	44
Donne	2.67	114.1	1,330	NA	37
Tutoko	6.88	362.4	1,210	NA	65
U. Cleddau	1.10	16.4	1,500	NA	37
L. Cleddau	0.68	8.9	860	NA	55
L. Arthur	1.26	18.5	1,170	NA	59
Lake Ada	1.47	20.2	520	NA	50
Bowen	1.17	26.6	1,080	NA	68
U. Sinbad	1.56	23.5	930	NA	59
L. Sinbad	0.62	7.3	1,330	NA	56
Stirling	0.27	3.5	900	NA	56
Subaerial source with submarine deposit					
SM1	0.14	1.0	560	200	64
SM2	0.13	0.5	390	170	42
SM3	0.72	2.2	560	240	63
SM4	0.41	4.6	460	270	56
SM5	0.75	4.8	970	270	61
SM6	0.07	0.2	120	280	56
SM7	0.26	1.5	480	290	58
SM8	0.15	0.7	250	290	56
SM9	0.67	11.0	440	290	68
SM10	0.48	4.3	280	290	67
SM11	0.50	2.3	1,060	290	65
SM12	0.29	4.9	130	290	58
SM13	0.99	18.5	650	290	70
SM14	0.33	1.7	1,640	130	43
SM15	0.24	3.9	1,950	130	49
SM16	0.12	0.8	980	130	57
SM17	0.19	3.0	190	130	61
SM18	0.28	4.9	1,490	130	46
SM19	0.53	6.7	1,820	130	36
SM20	0.25	2.3	1,310	130	36
SM21	0.49	4.3	1,200	130	37
SM22	0.21	0.9	820	130	35
Submarine density flows (granular)					
DF1	0.23	0.5	1,100	190 (20)	22
DF2	0.15	0.2	1,600	220 (20)	25
DF3	1.7	14.2	2,400	290 (55)	28
DF4	1.7	13.2	1,500	130 (55)	25

[a] three-dimensional surface area of deposit, calculated on Vulcan triangulation of deposit surface.
[b] calculated from estimated pre-deposit topography (see text).
[c] distance travelled by centre of mass to valley floor, or impact with water (submarine deposit).
[d] maximum fiord depth at entry point, initial submergence depth in brackets (submarine source).
[e] dip angle of failure plane.

part way up the opposite side of the valley to an elevation of over 1,050 m. The exact amount of runup is not certain because the distal part of the deposit appears to have partially slumped back into the outlet channel. The deposit blocked off the valley for about 2 km, but a precise landslide dam length is difficult to ascertain, because the upper part of the deposit is now within Lake Adelaide. A channel eroded in the downstream end of the deposit suggests that lake levels were as much as 50 m higher before over-topping the dam; the low point of the channel matches the current lake level, although the majority of the outlet runoff appears to travel within the deposit, before reappearing at it's toe, some 150 m below lake level.

The largest boulders on the surface of the Adelaide deposit reach up to 40 m across, with one boulder even hosting it's own 10 m long tarn on top. Attempts to retrieve material for radiocarbon dating from the shallow bottom of the tarn were abandoned when rubbish was found nearby, suggesting that the sediments may have been disturbed.

Most of the landslide deposits investigated displayed common geomorphic characteristics; in plan view, most deposits are approximately fan-shaped, with the mid-line of the fan perpendicular to the failure slope, and uneven or arcuate distal edges that commonly rest against the opposite valley wall. In long section (i.e. perpendicular to valley thalweg), deposits tend to have a slightly concave top profile, with the steepest slope at the base of the fan, and occasionally run up the opposite valley wall (see Figure 4.4). In longitudinal profile (i.e. parallel to valley thalweg), deposit surfaces are generally convex. Average deposit surface-slope angles range from $\sim$10°(Lake Adelaide) to $\sim$22° (Bowen), with most under 12°. These values fit within the frequency distribution of Korup (2005b), for landslide surface-slope angles in Fiordland (he found that the majority had surface slopes that were less than $\sim$25°). Deposit thicknesses range from $\sim$5 m to over 100 m, based on reconstructions of pre-deposit topography. Field observations of three river bank exposures (in the Tutoko, Bowen and Lower Cleddau deposits) showed no evidence of buried soil horizons or unconformities that could suggest that they are composite deposits resulting from multiple events. However, subaerial deposits that were investigated in the field are large, with 3-D areas between 0.7 and 6.9 km^2, and almost entirely covered with thick forest (with the exception of the Adelaide deposit). Due to these factors, it was not practical to investigate all possible exposures or surface features, so the possibility that some deposits are the result of multiple landslide events cannot be ruled out.

The majority of deposits appear to have run across the entire width of valley bottoms; one possible exception is in the lower Cleddau valley, where a distinct bend in the Cleddau River indicates that the river channel was deflected some 300 m to the North,

Figure 4.4: Typical landslide geomorphology. A) Tutoko deposit, looking downriver towards the Cleddau Valley, source area out of frame on the upper right. B) Lower Cleddau deposit, source area directly above deposit, Milford Village and airport in foreground (in shadow). C) Bowen deposit above Bowen Falls, looking west towards Cleddau delta. The landslide probably spilled over the ∼200 m bluff that forms the falls. D) Lake Adelaide deposit, source area is upper left of frame, view looking north.Author photos

directly opposite the Milford Lodge. Here the river has been pinched between the "L. Cleddau" deposit (see Table 4.2), and a much smaller (~200 m by 500 m) fan-shaped deposit of bouldery debris. The shape and orientation of the smaller fan suggest that it is related to mass failures originating from the opposite (north) side of the Cleddau River, and is therefore probably not related to the larger deposit.

4.2.2.1 Boulder (^{10}Be) and SH exposure dates, and ^{14}C data from landslide deposits

Surface exposure dating using TCND and SH hardness measurements was completed for some of the largest boulders on the surfaces of six large landslide deposits near the head of Milford Sound. One of the landslides is located in the Tutoko valley, two in the Cleddau valley, one in the Bowen Valley, one in the Arthur valley (Lake Ada) and one in the lower Sinbad valley. Fresh near-vertical exposures within the river-gorges of three of these deposits (Tutoko, lower Cleddau, and Bowen) allowed the deposits to be independently dated using radiocarbon analysis of wood entrained within the landslide debris, and provided a visual record of the sedimentology and stratigraphy within the deposits. A fourth landslide (Lake Ada) was also independently dated using radiocarbon analysis of drowned, standing tree trunks, which would have died shortly after the landslide dam formed the lake. Surface boulders from all terrestrial landslide deposits referenced in Table 3.5 were also sampled for SH hardness.

Samples were collected for TCND from large boulders on the surfaces of the Tutoko, Bowen and Upper Cleddau landslide deposits, and analysed for ^{10}Be concentrations. The Bowen sample (SC21) was collected from a large (6m x 4m x 4m) boulder on the surface of a hummocky, angular debris deposit overlying a small delta that juts out into Milford Sound near the base of Bowen falls. The boulder exposure age was compared with the age of the main Bowen Valley deposit above the falls, in order to determine if the deposit spilled over the 200 m bluff that forms the falls (as suggested by geomorphic evidence). The maximum age of the Bowen deposit is 8.81 ± 0.10 years, based on two calibrated ^{14}C ages from twigs within the main deposit (see Table 3.5 and Figure 4.5). The boulder at the base of the falls yielded an overlapping ^{10}Be exposure age of 7.85 ± 1.91 ka, indicating that both the main valley deposit above the falls and the hummocky lobe of coarse, angular debris at the base of the falls could relate to the same event. This is particularly important when considered from a natural hazards perspective, as these data indicate not only a very large Holocene landslide deposit in the lower Bowen valley, less than 1 km from the new Milford Visitors Centre, but also that part of the deposit spilled over the bluff that forms Bowen Falls, with large blocks

entering Milford Sound itself.

The Tutoko sample (SC5) was collected from a 4 m boulder on the surface of a very large landslide deposit that partially fills the lower Tutoko valley, and yielded a ^{10}Be exposure age of 3.61 ± 0.51 ka, which agrees (within uncertainty) with two nearly identical calibrated ^{14}C ages from separate pieces of intact wood within the interior of the Tutoko deposit. The wood was exposed by a fresh landslip in the gorge (see Figure 4.5), approximately 1.5 km downstream of SC5; the radiocarbon data indicate a maximum age of $4,051 \pm 57$ years for the deposit, which falls within the uncertainty of the ^{10}Be exposure age.

The upper Cleddau sample (SC17) was collected from a 5 m, moss-covered boulder within the Cleddau river channel, across from the confluence with the Donne River. The aerial extent of the deposit is relatively small, but it appears to have run across the narrow valley and diverted the river channel to the east. The boulder yielded a ^{10}Be exposure age of 2.11 ± 0.64 ka. The deposit is overgrown with thick bush, and no locations were identified where material for independent ^{14}C dating could be sampled. However, the boulder was SH tested, with a resulting mean Q-value of 52.75 ± 0.99. This hardness value is much lower than expected given the supposed ^{10}Be age of only 2.11 ka, and falls well below the representative boulder Q-value-age relationship curve (see Figure 3.26. A possible explanation for the discrepancy between ^{10}Be concentration and hardness of the weathered surface is that the boulder was previously buried within the deposit, and was later exhumed and exposed to cosmogenic radiation by river erosion. The boulder was chosen as a sample site due to it's large size, and height relative to the present-day river, but it does lie at the edge of the modern river channel, and exhumation is therefore difficult to rule out. Alternatively, the boulder surface may have experienced accelerated weathering for some reason, possibly due to the presence of thick moss cover, or small fractures in the rock surface. However, exhumation by channel erosion is considered to be the simplest and most likely scenario, therefore an age similar to that for the Bowen deposit (i.e. $\sim$9 ka) is suggested for the Upper Cleddau deposit.

^{10}Be exposure ages were not obtained from either the Lower Cleddau or Ada deposits, however Q-values measured on large boulders on the surface of those deposits suggest exposure ages of $\sim$4.0 ka and 0.9 ka, respectively, based on the Q-value-age curve (Figure 3.26). Both of these suggested SH exposure ages are in agreement with independent radiocarbon data. The maximum age for the Cleddau deposit is $4,650 \pm 96$ years, based on two separate pieces of wood entrained within the deposit (both yielded nearly identical ages, see Table 3.5). A riverbank exposure revealed $\sim$6 m of angular

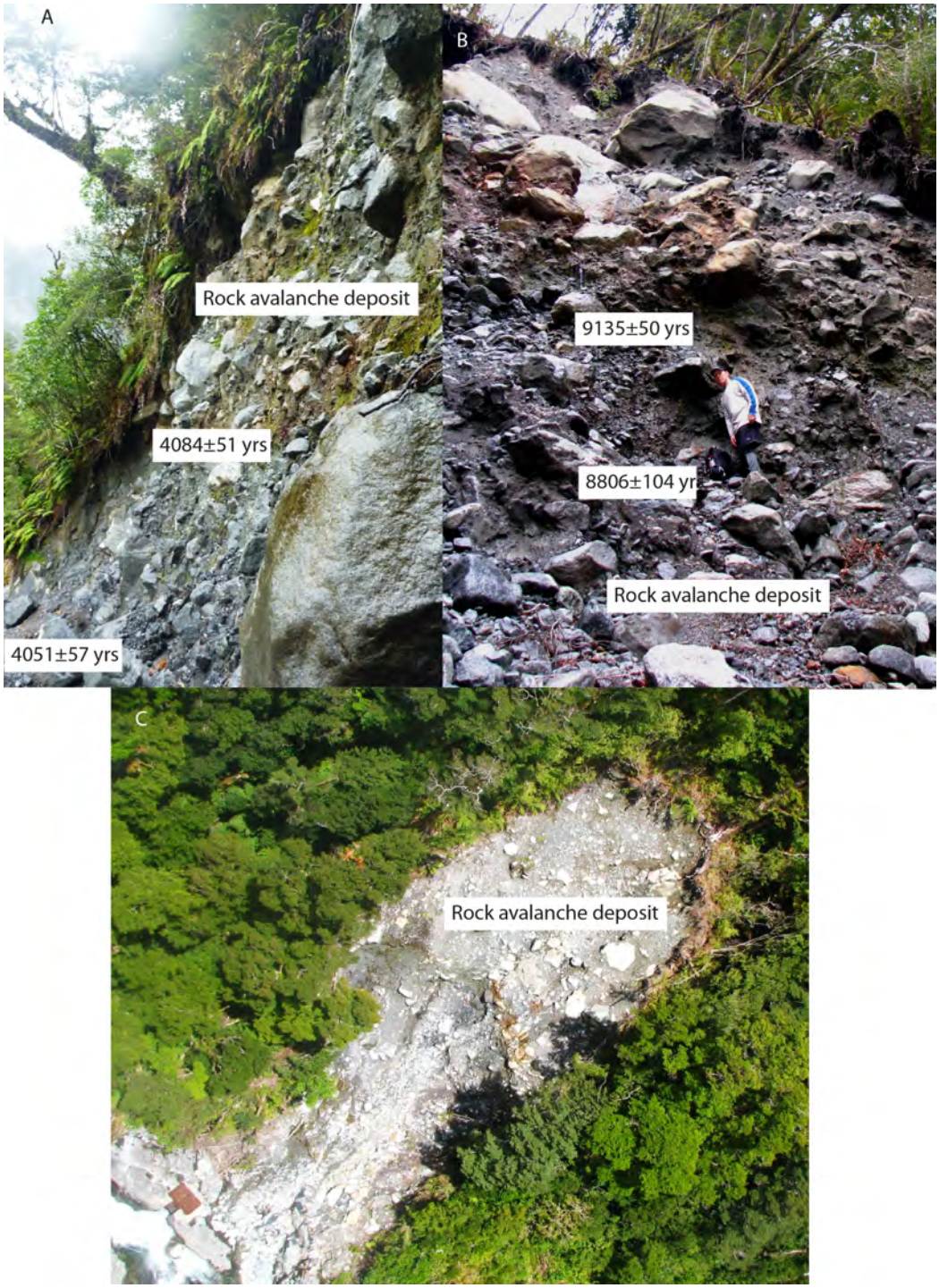

Figure 4.5: Tutoko and Bowen exposures in Holocene rock avalanche deposits. Calibrated ^{14}Cages, referenced to calendar year before 2010, shown at approximate position where entrained wood was sampled. A) Recent slip in Tutoko river gorge, near mid-point of landslide deposit. ∼20 m high exposure is massive, angular boulder diamicton. B) Recent slip in Bowen Valley, figure at mid-exposure height (lower part of exposure not shown). ∼30 m high exposure is massive, angular boulder diamicton. C) Oblique aerial view of Bowen exposure. Photos by S. Furkert.

boulder diamicton overlying rounded, moderately-to-poorly sorted cobble-gravel, which is interbedded with lenses of silty sand (see Figure 4.6). The lower unit most likely consists of river channel deposits; the age of the overlying rock avalanche deposit indicates that the underlying cobble-gravel unit is probably mid-Holocene in age, due to the position of the exposure on top of the modern, prograding Cleddau delta (eustatic sea level rise would have achieved present levels ∼7 ka, see Figure 3.39). The river channel deposits extend up to ∼3 metres above the modern river channel, and may reflect a period of channel aggradation, or a temporary ponding event (e.g. due to an earlier landslide).

At lake Ada, TCND samples were collected from two boulders (SC22 and SC23), but the samples have not been analysed, due to the availability of good radiocarbon age control. The age of the deposit is dated to 912 ± 34 years (before 2010), based on radiocarbon dates from drowned, standing tree trunks that would have died shortly after the landslide dam formed the lake. A second tree produced a radiocarbon age of 920 ± 3 years (before 2010).

Radiocarbon or TCND samples were not collected from the Lower Sinbad deposit, but a mean Q-value of 55.69 ± 0.90 from a single boulder is nearly identical to results from the Tutoko deposit, which has an age of ∼4 ka based on independent ^{10}Be exposure-age and radiocarbon data. Based on the SH results, the Sinbad deposit could be around the same age as the Tutoko deposit, and therefore and age of ∼4 ka is tentatively adopted for the Sinbad deposit.

Although the Lake Adelaide deposit has previously been described (e.g. Hancox and Perrin, 2009; Whitehouse and Griffiths, 1983), it's age has not yet been determined. Future sample processing and AMS analysis of TCND samples collected from 6 boulders on top of several lobes will help to establish the age of the event (or events) that created the giant deposit.

SH hardness measurements were recorded for the Adelaide deposit. 239 Q-value measurements from 11 boulders on the surface of as many as five separate lobes over a horizontal distance of 1.5 km are normally distributed with a mean of 52.8 ± 0.37 (standard error), standard deviation of 5.7, and a Kolmogorov-Smirnov statistic of 0.04 (compared to K-S critical value of 0.09 at α=0.05 significance level). The distribution of Q-value measurements suggests that all tested boulders have similar exposure ages. The mean Q-value of 52.8 comes from the same Darran Mountain lithology as deposits on the other side of the divide (e.g. Upper Cleddau, Tutoko), and is statistically equivalent to SH results for boulders from the Bowen and Upper Cleddau deposits. This suggests a similar age to the Bowen deposit (i.e. ∼9 ka, as confirmed by ^{10}Be exposure age and

Figure 4.6: Lower Cleddau landslide deposit, Cleddau River bank exposure. Calibrated ^{14}C ages, referenced to calendar year before 2010, shown at approximate position where entrained wood was sampled. Unit above dashed red line is ~6 m of angular to subangular boulder diamicton, interpreted to be rock avalanche debris. Below line are moderately to poorly-sorted units of rounded to well-rounded cobble-gravel, interbedded with lenses of silty sand; these are interpreted to be mid-Holocene river channel deposits. Author photo.

independent radiocarbon dating). However, this estimated age is considered to be very rough, as there are no independent age data for the Adelaide deposit, which is nearly 800 m higher elevation than the Bowen deposit; therefore the possible effects of higher elevation on weathering processes have not been considered. Recent analysis of peat material from a small tarn which has formed on the fringe of the deposit yielded an age of ∼6 ka from above the deposit, confirming that it must have occurred prior to 6 ka (G. Hancox, pers. comm.).

4.2.3 Submarine landslide distribution

4.2.3.1 Sedimentary evidence

In addition to identifying submarine landslide deposits from geomorphic evidence (i.e. bathymetry), seismic reflection data were also considered. As discussed in Chapter 3, seismic reflection profiles of Milford Sound basin sediments indicate extensive, discontinuous pockets, characteristic of massive blocky landslide debris (see Figures 3.28 and 3.29). In some locations, seismic data suggest landslide deposits that are not apparent in the bathymetry; this suggests that there are some pre-Holocene deposits that have been buried during periods of heavy Lacustrine sedimentation, such as could have existed during the period after glacier retreat, and prior to marine transgression. These buried deposits are difficult to quantify, and are therefore not considered in subsequent analysis. In addition, some deposits which are visible in the bathymetry may be composite deposits resulting from multiple events, therefore the estimated number of landslide events based on geomorphic evidence is considered to be conservative.

While most deposits in Milford Sound are related to landslides that fall into the fiord from adjacent mountainsides, there is evidence for wholly submarine slope failures in Milford Sound. The steep (∼25-28°) upper slopes of the Cleddau and Harrison delta are deeply incised in places, and slope failures appear to have deposited thin, elongated sediment lobes which span the mid-slopes. There is also clear geomorphic evidence of a large submarine slope failure originating from a drowned delta (-55 m) across the entrance of Milford Sound from Saint Anne Point (see Figure 4.2). The drowned delta is currently the site of a smaller modern delta at the mouth of the Thurso River (see Figure 3.30 for location), which drains the western slopes of Mount Pembroke. Based on evidence from aerial photographs, the delta has grown significantly over the last 30 years due to persistent debris flow activity from the catchment. The potentially active (Barth et al., submitted) Pembroke Fault crosses the Thurso valley near where debris flows are currently being generated (see Figure 4.7).

Figure 4.7: Left pane: debris flow source, Thurso Valley, view looking south (see Figure 3.30 for location). Right pane: small delta forming due to debris flow activity, view looking west. Offshore paleodelta is at -55 m (not visible). Author photos.

4.2.3.2 Deglacial chronology, basin sedimentation and implications for landslide age

Maximum ages of submarine landslide deposits in Milford Sound are constrained by the the timing of glacial retreat (as presented in Chapter 3); therefore deposits in Dale Basin must be younger than ∼18 ka, and deposits in Stirling Basin have a maximum age of ∼18-16 ka. While these are maximum ages, some deposits may be much younger, based on the excellent preservation of geomorphic evidence on the floor of Milford Sound. Pre-Holocene deposits in particular may be buried beneath thick units of lacustrine sediment. However, the risk analysis presented here assumes a conservative maximum age of 17 ka for all deposits.

Prior to glacial retreat, most landslide debris that fell onto the glaciers would have been entrained and transported by the moving ice; the lack of preserved geomorphic evidence for subaerial moraines (with the exception of the lateral moraines near Saint Anne and Yates Points) suggests that much transported material eventually ended up near the entrance to Milford Sound, where it was incorporated into the extensive terminal moraine complex. During glacial retreat, landslide debris was likely deposited at the retreating ice-margin, where it may have formed recessional moraines, although there is little evidence of this preserved in the bathymetry of Milford Sound (see Ch.

3).

4.2.4 Source areas

Source areas for most of the terrestrial landslide deposits investigated at Milford Sound are apparent from geomorphic evidence (e.g. failure scarps, dislocated ridgelines, wedge or basin-shaped depressions), either observed in the field, or from geomorphic mapping. Most landslides appear to have initiated as plane failures along steeply-dipping, deep-seated weaknesses in the rock; most extend to the ridgeline above, and some very steep failure planes extend to well below the water surface (e.g. SM10, Stirling Basin). There is also some geomorphic evidence for exfoliation of shallow slabs, and wedge failures. Slump or rotational-type failures were rarely observed, however helicopter reconnaissance of the southern aspects of Rover Peak (on the north side of Dale Basin) indicated that there are steeply dipping (∼60 - 65°), deep seated foliations in the bedrock that are roughly parallel to the existing failure plane above deposit SM13. These foliations may reach the bedrock surface near the bottom of the fiord, due to the nearly 70° slope angle of the fiord wall. Similar deep-seated structures were noted on Mitre Peak, and on western aspects above the Stirling and Harrison valleys.

While source areas for most of the large submarine deposits in Stirling Basin are obvious, source areas for smaller deposits (such as some in Dale Basin) are more difficult to pinpoint, partly because adjacent slopes are less steep, and are therefore generally covered in thick vegetation.

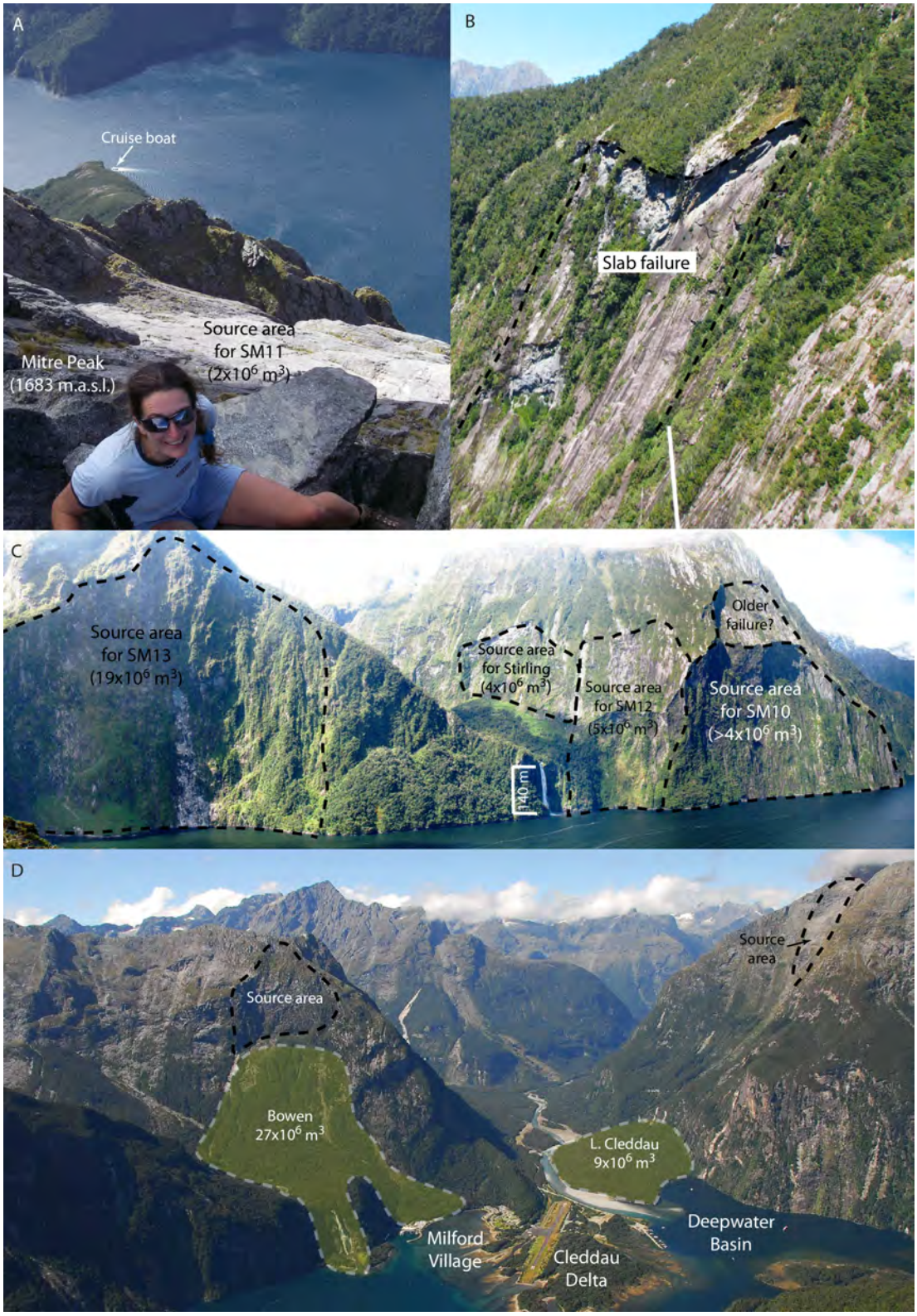

Figure 4.8: Landslide source areas, selected examples. A) Mitre Peak, above source area for SM11 looking down at Stirling Basin, 1,683 m below. B) Relatively small slab failures, Harrison valley. C) North side of Stirling Basin, Stirling Falls in middle of frame. D) Cleddau Delta, looking south. Photo A by S. Huchinson, D by GNS, C & D by Author.

4.2.4.1 Potential slope failure mechanisms

Obvious indicators of incipient large-scale failure, including tension cracks or slumping, were not noted on slopes that were inspected during the aerial survey (i.e. aspects that could contribute landslides directly into Milford Sound), however there are some indications of progressive weakening that could lead to failure in the future, especially considering that deep-seated failures may be triggered by seismic activity. Potentially unstable areas include Rover Peak (for the reasons listed above), and the north face of Mitre Peak, where there are some precarious-looking rock spires, and deep erosional gullies that follow steeply-dipping sheeting joints (see Figure 4.9). Also of particular note is The Lion, where drainage is exploiting sheeting joints that are nearly parallel to the steep rock face. Based on multiple failure scarps and the presence of at least one large landslide deposit on the fiord bottom below, it appears that weakness along steeply-dipping foliations has resulted in past slab failures from the southwest face of The Lion.

In addition, the steep slopes of Sheerdown Peak above Deepwater Basin are the source area for a number of slab failures, including "Lower Cleddau". Augustinus (1995) noted that slab failures on Sheerdown Peak are associated with steeply-dipping sheeting joints that are nearly parallel to the slopes above Deepwater Basin. The potential for catastrophic displacement waves resulting from a future slab failure falling into the relatively shallow waters of Deepwater Basin is considered later in this Chapter.

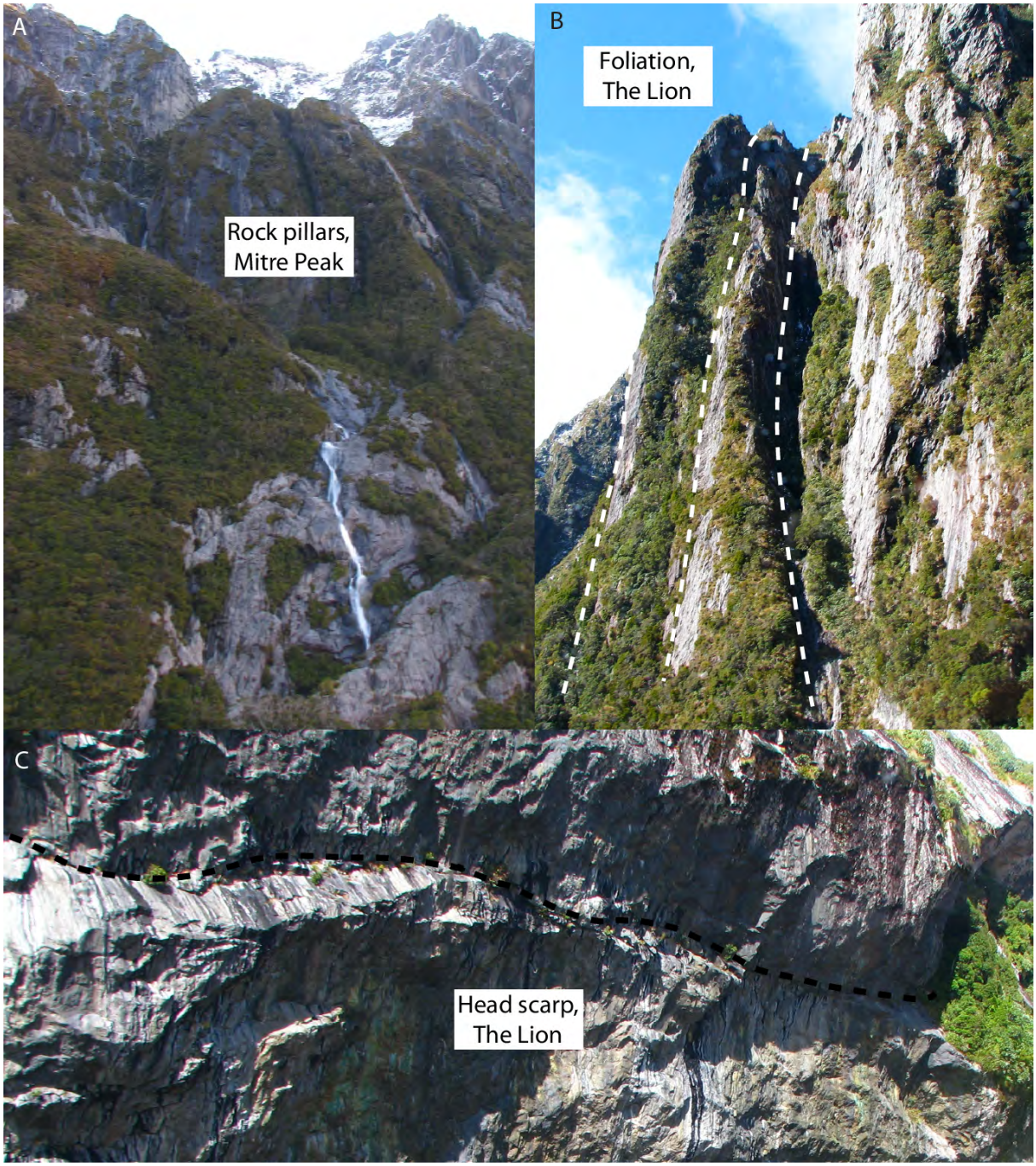

Figure 4.9: Potential rock-slope failure mechanisms. A) Mitre Peak, rock pillars and deep erosional gullies, probably related to folliated bedrock structure. B) The Lion, dashed white lines indicate foliation and preferential gully erosion, view looking north. C) The Lion, top of uppermost landslide failure scarp, above SM10. Dashed black line denotes a smooth failure plane, inclined at ∼67°. Note dark streaks of water exiting the rock at, or just above, the foliation, indicating that water is piping from above. Upper slab thickness (above the dashed line) is on the order of 10 m. Beneath the failure scarp is over 1,000 m of near-vertical to overhanging cliff face, including ∼200 m below sea level. Author photos.

4.2.5 Landslide distribution trends

4.2.5.1 Source area slope aspect, and relationship to deposit volume

In his inventory of Fiordland landslides, Korup (2005b) found that there is no preferential slope aspect for failure, compared to the Southern Alps, where significantly more landslides occur on southwest-facing slopes. Korup (2005b) also noted that around two-thirds of large landslides in southwest New Zealand (including Fiordland) extend from ridge crest to valley floor, resulting in dislocated ridge crests and interfluves; these features were also observed for many of the landslide source areas investigated near Milford Sound.

In the study area, a much higher proportion (43%) of landslides occured on northeast facing slopes, with northwest and southwest slopes each making up 24% of landslide source slopes, and the remainder (∼9%) on southeast facing slopes. These results are not unexpected, as the sample size is small compared to Korup (2005b), and the majority of the deposits (26 of 37) fell off the slopes above Milford Sound, which generally face either northeast or southwest. However, the azimuth of the Alpine Fault is ∼54° NE, which roughly parallels the dip direction of about half of the observed failure slopes, suggesting that dextral slip on the fault may preferentially cause failures on northeast and southwest facing slopes. Failure slope direction was also plotted against deposit volume; interestingly, the three largest deposits (i.e. Adelaide, Tutoko and Donne) all originated from southeast facing slopes.

4.2.5.2 Magnitude-frequency relationship

Hungr et al. (1999) compared the relative magnitude (M) and frequency (F) of approximately 700 historical rockfalls and rockslides along the main transportation corridors of British Columbia, and developed empirical formulae based on the power-law distribution to represent the M-F relationship. They found that the type of bedrock, and the frequency of jointing were critical, and established the formula,

$$logF = a + blogM \tag{4.1}$$

where F is the cumulative frequency per year, M is the magnitude (m^3), a is an empirically determined constant which depends on the exposure of the region to landslides, and b is the slope of the power-law relationship, which depends on the specific distribution of landslide frequencies within the area of interest. Hungr et al. (1999) empirically determined a and b with values of 0.773 and -0.434 respectively, for the hard plutonic

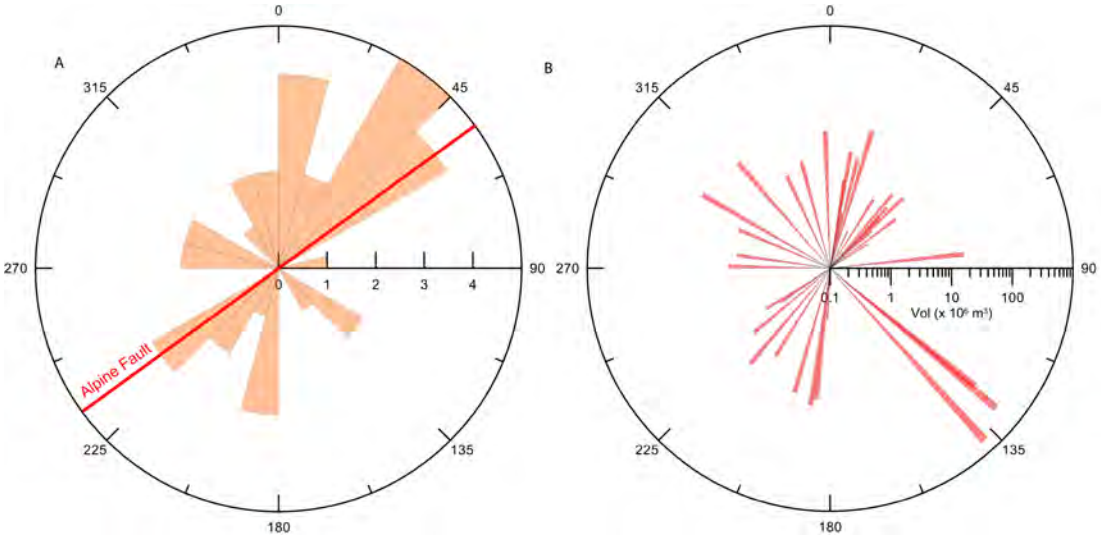

Figure 4.10: A) Rose diagram of landslide dip direction for Milford Sound study area, including subaerial and submarine deposits, and submarine density flows. Horizontal axis is frequency. B) Log-scale deposit volume and failure plane dip direction.

rocks of the west coast ranges.

Following the empirical method of Hungr et al. (1999), the cumulative frequency (per 1,000 years) of known landslide events at Milford Sound (see Table 4.2) was calculated as function of deposit volume, using an assumed maximum age for all deposits of 17 ka. The two smallest submarine landslide deposits (between 0.1 and 0.2 x 10^6 m^3) were ignored in calculations, as they enhanced the "roll-over" effect (Hovius et al., 1997) that is commonly observed at the small-magnitude end of landslide M-F relationships (e.g. Blikra et al., 2005; Hungr et al., 1999 The resulting power-law relationship is shown in Figure 4.11.

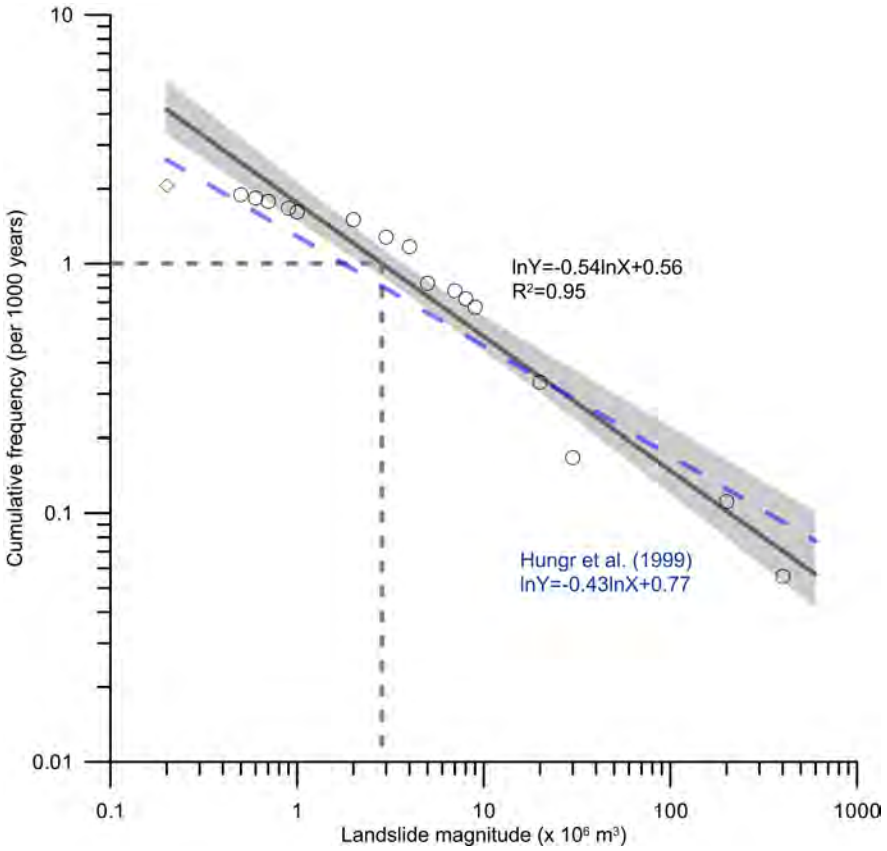

Figure 4.11: Landslide magnitude-frequency relationship for Milford Sound area. Hollow circles are empirical data points from the Milford Sound landslide inventory (Table 4.2); each point represents the number of landslides of a given magnitude range that occur every 1,000 years. Magnitude ranges (bins) were set to match each division of the log-scale axis. Diamond represents the two smallest landslide deposits (one bin), which are not included in regression, in order to reduce the impact of the "roll-over" effect (see text). Grey solid line is the best-fit power-law distribution to the data (circles). Shaded grey area is the 95% confidence interval on the regression line. Dashed blue line represents the Hungr et al. (1999) power-law relationship for western British Columbia, for comparison.

Based on the best-fit power-law curve, constants a and b are 0.56 and -0.54, respectively. The Hungr et al. (1999) relationship for hard plutonic rocks of British Columbia coast ranges is also shown for comparison, and generally agrees with the Milford Sound curve (within 95% confidence limits); this provides additional evidence that the M-F curve proposed for Milford Sound is reasonable, despite the relatively conservative methods used here to establish landslide distribution. The methods employed in the current study are very similar to the methods employed by Blikra et al. (2005) to estimate deposit volume, total number of deposits, and maximum deposit ages at Tafjord in Norway.

4.2.6 Evidence for co-seismic landslides

One of the main objectives of the current study is to better understand the relationship between large landslides in the Milford catchment, and strong earthquake shaking, either from Alpine Fault rupture or Fiordland Subduction Zone earthquakes. Resolving the role of earthquakes as a landslide triggering mechanism is crucial to future hazard assessment and risk management efforts; if large landslides and associated displacement waves are generally triggered by earthquakes (rather than by extreme weather events, for example), the ability to monitor potential source areas, and develop prior warning and prediction capabilities, are severely limited. Large earthquakes occur without warning, leaving very little time for vulnerable communities to react.

Are large landslides near Milford Sound normally generated by earthquakes? Maximum ages of submarine landslide deposits in Milford Sound are constrained only by glacial retreat chronology, to ∼18-16 ka (see Chapter 3), so it is not yet possible to determine which of those events were triggered by paleo-earthquakes. However, the ages of several large subaerial landslide deposits near Milford Sound have been constrained by a combination of radiocarbon dating and TCND and SH exposure ages.

Inferred ages of subaerial landslide deposits in the Milford catchment are presented with the most recent rupture chronology for the southern onshore section of the Alpine Fault (based on Berryman et al., 2012b), and evidence for pulses of terrigenous sediment input (based on grain-size analysis and Carbon/Nitrogen ratio analysis by Knudson et al. (2011) from Stirling Basin, Core S534). The radiocarbon ages of Knudson et al. (2011) were used to produce the chronology for core S534, however it should be cautioned that this wiggle-match was based on just three ages in the range of ∼1,350-800 years BP, therefore additional radiocarbon age-control from deeper in the core is desirable. Results are summarized in Figure 4.12.

Barnes et al. (2012) investigated turbidites from George, Looking Glass and Sec-

retary Basins, which are offshore sedimentary basins within 10 km of the Fiordland coast, located approximately 40 km, 65 km and 100 km southwest of Milford Sound, respectively. Cores from within the basins provided a 2,300 year record of large magnitude paleo-earthquakes associated with the Alpine Fault and the Fiordland subduction zone, including two recent interplate thrust earthquakes (in 1993 and 2003), the 1826 AD Fiordland earthquake, and the 1717 AD Alpine Fault earthquake. Barnes et al. (2012) interpreted stacked proximal sand-silt turbidites as deposits resulting from coseismic density flows, and determined mean recurrence intervals of 191 years in George Basin, 156 years in Looking Glass Basin, and 145 years in Secretary Basin. Barnes et al. (2012) analysis of sediment transport during extreme (160 year) storm events indicates turbidites were likely triggered by strong ground shaking associated with large magnitude earthquakes, rather than storm-driven build-up of sediment. The turbidite record from offshore Fiordland has a mean recurrence interval of 161±36 years, which is roughly half the 330 year recurrence interval inferred from southern on-shore Alpine Fault records (Berryman et al., 2012b), and probably reflects mixed Alpine Fault and subduction earthquake records.

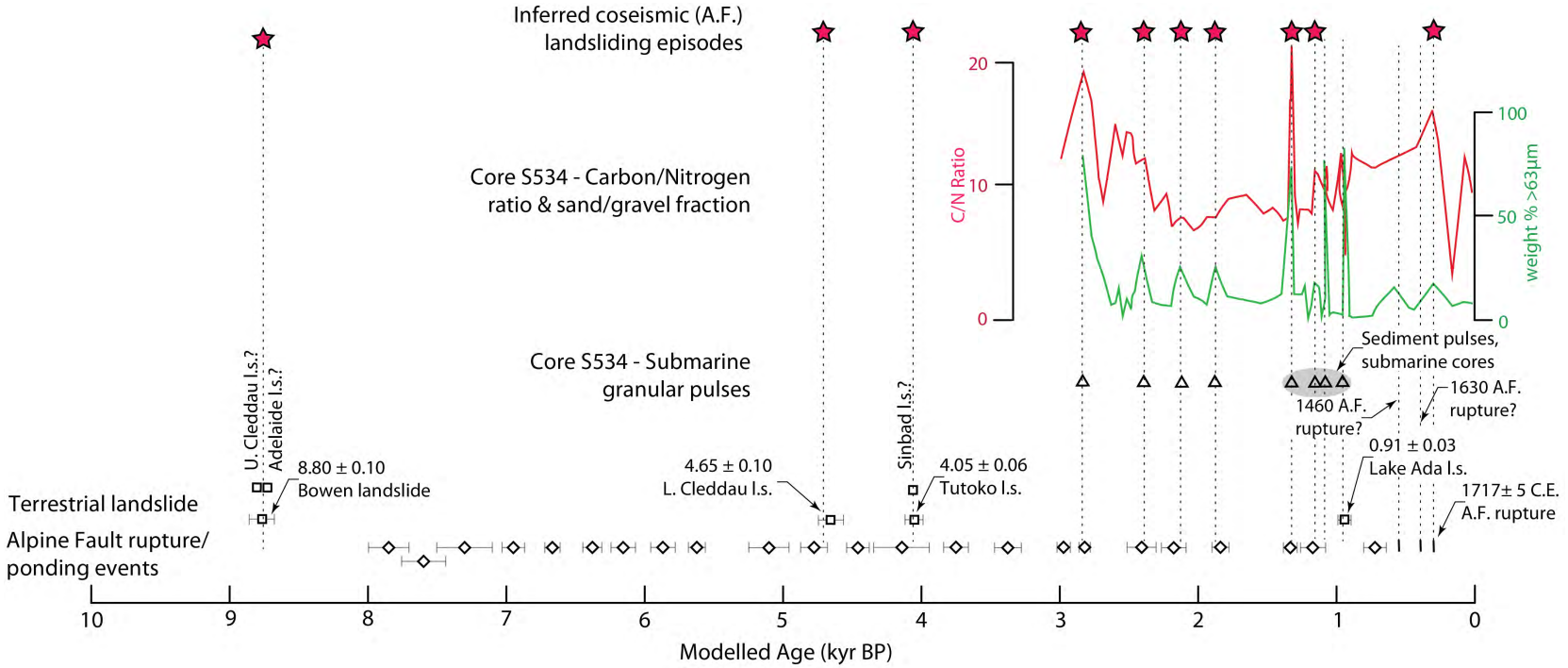

Figure 4.12: Reconciling the Alpine Fault earthquake record with the terrestrial landslide record at Milford Sound. Alpine Fault record after Berryman et al. (2012b). Terrestrial landslide record from current study (Tables 3.2 and 3.5); landslides with tentative age-control from SH measurements are listed vertically, with "?" at the end of their name. Core S534 data after Knudson et al. (2011), wiggle-matched according to radiocarbon dates presented in Knudson et al. (2011). Inferred coseismic landsliding episodes based on matching Hokuri Creek Alpine Fault (A.F.) record (Berryman et al., 2012b) with landslide ages, or submarine granular pulses from Core S534. Radiocarbon dates from Table 3.5). Grey-shaded ellipse represents approximate period of enhanced sediment input, based on cores from Milford, Nancy and Bradshaw Sounds, which may be related to a large subduction zone earthquake, as well as Alpine Fault rupture (see text).

These results indicate a possible correlation between the ages of subaerial landslides at Milford Sound, and inferred rupture dates from the southern onshore portion of the Alpine Fault. Of the four landslide deposits which have been radiocarbon dated (i.e. Bowen, L. Cleddau, Tutoko, Lake Ada), the ages of the Bowen, L. Cleddau and Tutoko deposits match Alpine Fault rupture events inferred from ponded sediments at Hokuri Creek, just north of Milford Sound (Berryman et al., 2012b); however, the deposit which formed Lake Ada ∼900 years ago does not match any earthquake recorded in Hokuri Creek sediments. However, there is no reason to suspect that the Hokuri Creek record includes all large earthquakes that have affected Milford Sound; for example, subduction zone earthquakes may cause landsliding at Milford Sound, but may not be recorded by ponding events on the Alpine Fault at Hokuri Creek. The age of the Lake Ada deposit does appear to correspond with pulses of sandy sediment between ∼1,115 and 795 calendar years BP (see Figure 3.27 for core S534 analysis), suggesting that Milford Sound was experiencing high terrigenous sediment input around the time that Lake Ada was formed, so it is possible that the landslide that dammed the lake was triggered by an earthquake which is not evident in the Hokuri Creek record. The offshore basin turbidite record of Barnes et al. (2012) indicates a mean recurrence interval for strong earthquake shaking, related to both Alpine Fault and subduction zone earthquakes, of 161±36 years; this suggests that the Hokuri Creek record records about half of all large earthquakes that affect Fiordland.

Three terrestrial landslide deposits do not have particularly reliable age-control; the Upper Cleddau deposit produced conflicting ^{10}Be and SH exposure-age results, and is tentatively estimated to be about the same age as the Bowen deposit (∼8.7 ka), based on matching SH Q-values. Numerous large boulders spread around the surface of the giant Adelaide deposit showed excellent internal agreement of SH measurements, producing a mean Q-value that is also statistically the same as the Bowen deposit. Therefore, the relatively well-constrained ∼8.7ka age of the Bowen deposit is adopted for the Adelaide deposit as well. This is somewhat speculative, as potential effects of the 800 m higher elevation at Lake Adelaide (compared to the Bowen valley) on weathering processes, and therefore Q-value-age relationships, have not been resolved. However, it is considered plausible that the Bowen, Upper Cleddau and Lake Adelaide deposits were triggered by an earthquake at around 8.7 ka.

The age of the Sinbad deposit is also not well-constrained; however the mean Q-value from a single large boulder on the surface of the deposit matches the mean Q-value for boulders on the surface of the ∼4 ka old Tutoko deposit, suggesting that the Sinbad deposit could be approximately the same age. Two radiocarbon ages from the giant

Tutoko deposit indicate a maximum age of $4,051 \pm 57$, which overlaps an inferred earthquake record from Hokuri Creek (Berryman et al., 2012b). It should be noted that the uncertainties surrounding the age of that particular Hokuri Creek record are relatively large, so the inferred Alpine Fault rupture may not actually be the same age as the Tutoko landslide. However, an earthquake trigger for the Sinbad and Tutoko landslides is certainly possible. Based on the data presented in Figure 4.12, several broad assertions can be made:

- earthquakes on the southern portion of the Alpine Fault can cause increased input of terrigenous sediment to Stirling Basin. Pulses of granular sediment recorded in core S534 are probably related to periods of increased landslide activity in the catchment, and seem to match up well with the Hokuri Creek Alpine Fault rupture record (Berryman et al., 2012b), although additional age-control on the sediment pulses is required to confirm this relationship.

- of seven landslide deposits with age-constraints, three can confidently be related to Alpine Fault rupture events (Berryman et al., 2012b), and three can be tentatively correlated with the same earthquake ruptures, based on matching SH hardness measurements. Therefore, if our study landslides are representative of the entire Milford catchment, then the majority of large ($>10^6$ m^3) landslides in the catchment are probably triggered by earthquakes.

- a period of enhanced sediment input between ~1,350 and 800 calendar years BP is evident in core S534. At least two Alpine Fault ruptures during this period are captured by the Hokuri Creek record (Berryman et al., 2012b), but they post-date the age of the Lake Ada landslide. One possible explanation is that an earthquake originating further south (e.g. on the Fiordland Subduction Zone) could have triggered landslides early in this period, causing increased sediment input at Nancy, Bradshaw, and Milford Sounds. This is supported by the offshore basin turbidite record of Barnes et al. (2012), which probably reflects mixed Alpine Fault and subduction earthquake records, and indicates a mean recurrence interval of 161±36 years.

4.3 Quantifying the landslide-generated tsunami hazard at Milford Sound

Analytical solutions for estimating impact speed, initial wave amplitude, and runup height for landslide-generated tsunami at Milford Sound are considered in subsequent

sections.

4.3.1 Displacement wave prediction

Numerous researchers have attempted to describe impulse waves generated by landslides, using numerical simulations based on theoretical mathematical relationships, and empirical data based on physical model experiments (e.g. Abadie et al., 2008; Ataie-Ashtiani and Shobeyri, 2008; Enet and Grilli, 2007; Fritz, 2002; Fritz et al., 2004; Huber and Hager, 1997; Kamphuis and Bowering, 1972; Najafi-Jilani and Ataie-Ashtiani, 2008; Noda, 1970; Panizzo et al., 2005a; Quecedo et al., 2004; Slingerland and Voight, 1979; Walder et al., 2003; Watts, 1997; Wieczorek et al., 2007). While a detailed review of these methods is beyond the scope of the current study, the reader is directed to useful reviews on the subject by Gisler (2008) and Di Risio and Sammarco (2008).

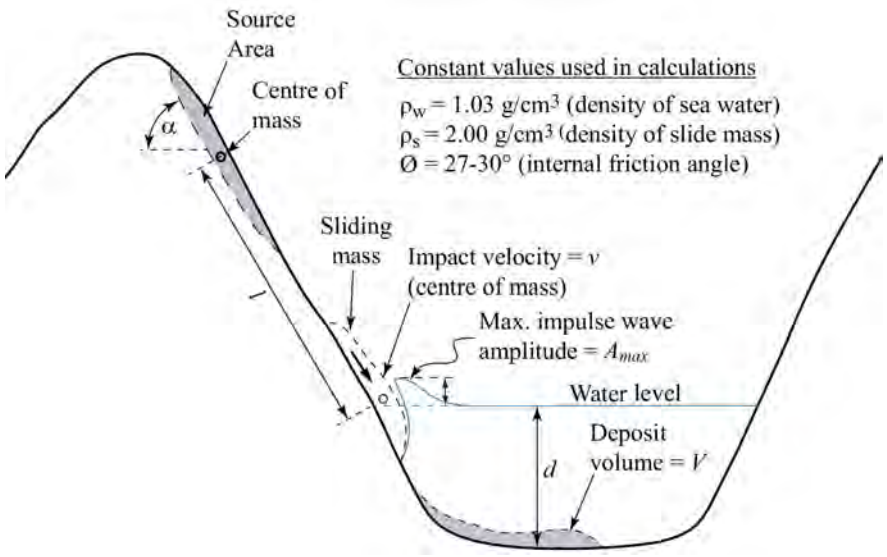

Figure 4.13: Subaerial landslide and displacement wave attributes and values used in calculations (see text for definitions).

4.3.1.1 Subaerial landslides: estimating impact velocity

It is generally accepted that the impact speed of a landslide of given mass at the air-water boundary is directly related to the amplitude of the initial wave field, for a given water depth. The closer the landslide speed is to the shallow-water celerity (phase velocity of a tsunami in water of a certain depth), given by $c = \sqrt{gd}$, where

g is gravitational acceleration and d is water depth, the higher the wave amplitude (Sorensen, 1993, and references therein). The ratio of the the landslide velocity (v) and tsunami phase velocity is the Froude number, given by $F = v/\sqrt{gd}$.

A common approach to modelling subaerial landslide-generated displacement waves is to first assume a slide impact velocity, which can be based on theoretical analysis of a rigid block sliding on a plane (e.g. Slingerland and Voight, 1979) or in freefall (e.g. Noda, 1970). Other predictive models are based on granular mass movement, where internal resistance due to the interactions of the granular material are considered (e.g. Fritz, 2002; Walder et al., 2003). These approaches require some prior knowledge of slide geometry (e.g. failure slope angle, slide distance, dynamic bed friction angle) and bulk material properties (e.g. density, effective internal friction angle).

Slingerland and Voight (1979) found that the downslope movement of bedrock landslides originating on steep slopes could be approximated by the sliding of a rigid block on a plane. They modelled this behaviour with the simple equation of gravity motion, modified to allow for frictional resistance of the sliding block:

$$v = \sqrt{2gl(sin(\alpha) - tan(\theta)cos(\alpha))} \tag{4.2}$$

where g is gravitational acceleration, l is slide path length, α is the failure plane angle, and θ is the angle of dynamic bed friction. Slingerland and Voight (1979) noted that this mathematical relationship tends to overestimate (by as much as 100%) the maximum velocity of a block traveling over multiple planar segments of significantly differing slope angle. However, Equation 4.2 provides a reasonable estimate of maximum impact velocity for steep landslides on relatively simple, planar failure planes.

Slingerland and Voight (1979) calculated an impact velocity of 55 m/s for the 1958 Lituya Bay landslide, based on field observations by Miller (1960) of slide path length of 356 m, failure plane angle of 40°, and dynamic bed friction angle of 14° (it is noted that this assumed dynamic bed friction angle is relatively low compared to the 27-30° used in our calculations for Milford Sound landslides - see below). By comparison, Quecedo et al. (2004) reported a velocity range of 80 to 87 m/s for landslide impact at Lituya Bay, based on numerical analyses performed under slip boundary conditions. Fritz (2002) used a three-dimensional physical model to replicate the Lituya Bay landslide, and found that an impact velocity of 110 m/s was required to reproduce the observed wave amplitude and runup. However, Fritz (2002) used a model-equivalent slide path length of 610 m, based on observations of the likely pre-slide location of the centre of mass at Lituya Bay. If 610 m is used in Equation 4.1 (Slingerland and Voight, 1979), then their velocity estimate increases to ∼75 m/s. Recently, Fritz et al. (2009) refined their

physical granular slide model of Gilbert Inlet, and confirmed that an impact velocity of around 110 m/s was required to generate the observed wave height and near-field wave runup observed at Lituya Bay.

Most subaerial landslides documented in the current study appear to have travelled over a relatively short horizontal distance, compared to vertical fall height, along a planar surface (see Table 4.2), and have commonly ended up as blocky deposits on the valley floor. Some, presumably more recent, deposits show evidence of cratering from high impact velocities; similar features have also been identified in Norwegian fjords (Hermanns et al., 2006), and have been replicated by high-velocity landslide-generated impulse waves in physical laboratory experiments (Fritz et al., 2003). At Milford Sound, high impact velocities are expected, as most landslide deposits fall down near-vertical slopes (60° inclination or steeper), from heights of at least 500 m (some as high as 1,650 m) before hitting the water.

Based on evidence presented in the current study, and after Slingerland and Voight (1979), it is considered that most landslides that fall into Milford Sound could be approximated as semi-intact, rigid blocks travelling on a plane, with frictional resistance governed by the dynamic bed friction angle; therefore, maximum impact velocities used in wave amplitude calculations are estimated using Equation 4.1. The angle of dynamic bed friction (θ) was conservatively varied between 27 and 30°, after a dynamic fragmentation model of the Falling Mountain rock avalanche in New Zealand (Davies and McSaveney, 2002), and observations that typical angles-of-repose for scree slopes in the study area were between ∼25 and 35°. In addition, an analyses of rock slope stability from similar geology in the fiord landscape of western Norway (Bhasin et al., 2004), indicated an ∼30 degree static friction angle. At the lowest observed failure slope angles (∼35°), varying dynamic bed friction substantially influences velocity calculations; increasing the bed friction angle from 27 to 30° reduces impact velocity by ∼20 - 25%, and reduces corresponding wave amplitudes by ∼30 - 35%, depending on slide path length. For steeper slope angles (∼65 - 70°), the frictional braking effect is small compared to gravitational acceleration, and the effect of increasing the bed friction angle from 27 to 30° was relatively minor; impact velocity and wave amplitude were both decreased by ∼2 - 3%. Analytical results presented in Table 4.3 are based on a bed friction angle of 27°.

4.3.1.2 Estimated maximum displacement wave amplitudes

Once an estimate of impact velocity at the water boundary has been obtained, the subsequent interactions between slide material and water must be considered in order

Table 4.3: Estimated maximum wave amplitude near-shore runup and inundation at Cleddau Delta.

Deposit ID	***V*=Vol.** (x 10^6 m^3)	***d*=Water depth** (m)	***v*=impact velocity**[a] (m/s)	**Distance**[b] (km)	A_{max}**=Amp.**[c] (m)	**Runup**[d,e] (m)	
Subaerial source with submarine deposit						R_{max}	R_{inn}
SM1	1.0	200	86	1.2	6.2	27	27
SM2	0.5	170	47	1.2	2.4	8	10
SM3	2.2	240	85	1.7	8.0	41	38
SM4	4.6	270	70	2.7	8.2	42	39
SM5	4.8	270	109	2.8	15.8	93	82
SM6	0.2	280	36	3.8	0.3	1	1
SM7	1.5	290	74	4.2	3.5	15	15
SM8	0.7	290	52	4.8	1.2	4	5
SM9	11.0	290	81	5.3	16.4	97	85
SM10	4.3	290	72	6.6	7.2	37	35
SM11	2.3	290	120	7.1	9.5	49	46
SM12	4.9	290	38	7.5	3.2	14	14
SM13	18.5	290	99	8.3	31.5	186	164
SM14	1.7	130	100	9.3	25.7	152	26
SM15	3.9	130	127	8.9	65.1	456	65
SM16	0.8	130	104	9.5	16.3	96	16
SM17	3.0	130	49	10.3	14.0	71	14
SM18	4.9	130	103	10.9	56.9	398	57
SM19	6.7	130	79	11.6	49.0	343	49
SM20	2.3	130	67	12.5	17.9	105	18
SM21	4.3	130	68	13.5	28.3	198	28
SM22	0.9	130	50	14.2	6.0	26	6
Tafjord[f]	3.0	200	69	NA	**10**	**61**(62)	NA
Lituya[g]	30.6	140	74	NA	**96**(∼100)	**540**(542)	NA
DW1[h]	*1.0*	*50*	86	*1.0*	*82*	*460*	*460*
Submarine density flows (granular)							
DF1	0.5	190 (20)	NA	1.2	1.3	4	4
DF2	0.2	220 (20)	NA	1.0	1.4	5	5
DF3	14.2	290 (55)	NA	4.2	1.2	4	4
DF4	13.2	130 (55)	NA	15.1	0.3	1	0.3

[a] estimated impact velocity assuming dynamic bed friction angle θ=27°(see text).
[b] distance from impact site to Cleddau delta.
[c] estimated maximum first-wave amplitude, assuming slide density ρ=2.0 g/cm^3 (see text).
[d] R_{max} = estimated max. near-field runup, 45°shoreline amplification, see text and Fig. 4.16.
[e] R_{inn} = inundation; maximum runup at Cleddau delta, 10°shoreline amplification. Grey highlighted values are waves originating from the outer basins (Dale or Entrance), which are not scaled for shoreline amplification, due to expected attenuation by Stirling Basin (see text).
[f] Tafjord, 1934 simulation, parameters: ρ=2.0 g/cm^3, θ=27°, slope failure angle α=60°(Hermanns et al., 2006; Jorstad, 1968). Values in brackets are observational data.
[g] Lituya Bay, 1958 simulation, parameters as per Fritz (2002); Miller (1960): ρ=1.6 g/cm^3, θ=14°, slope failure angle α=40°, 610 m slide path. Values in brackets are observational data.
[h] Hypothetical landslide into Deepwater Basin, and displacement wave (see text).

to quantify the waves that result from water displacement. In addition to impact speed, wave height depends on water depth and geometry of the bottom, material density and porosity (assumed to be zero for solid block models) and to a lesser extent, the ability of the material to deform (e.g. Ataie-Ashtiani and Shobeyri, 2008). The complexities of these interactions are not easily quantified; many authors have attempted a variety of approaches to modelling this behaviour (see Di Risio and Sammarco, 2008; Gisler, 2008), including experimental observations and empirical relationships based on two dimensional flume models (e.g. Kamphuis and Bowering, 1972; Noda, 1970) and three dimensional scale models (e.g.Fritz, 2002; Fritz et al., 2009; Huber and Hager, 1997). Recently, efforts have also focussed on numerical methods, as increased computing capacity has enabled intensive numerical simulations which incorporate equations of fluid motion and interactions between water, land and air, allowing the prediction of wave propagation and runup, despite complex basin and shoreline geometry (e.g. Gisler, 2008; Harbitz et al., 1993; Walters et al., 2006).

The simplest qualitative description of solitary, impact-driven wave generation is as follows; as a landslide enters the water, it pushes the fluid ahead, generating a positive seaward wave which radiates outwards from the impact site (Di Risio and Sammarco, 2008). For an intact or semi-intact mass of sliding blocks, landslide shape, as well as volume, may influence wave height; Panizzo et al. (2005b) determined through experimental methods and empirical data that wave height increases as the landslide Froude number and area of the front of the solid landslide increase. However, using numerical simulations confirmed by empirical data from their own similar physical model experiments using rigid blocks of various sizes and shapes, Ataie-Ashtiani and Shobeyri (2008) concluded that landslide shape does not significantly affect wave height.

Notwithstanding the inherent complexities noted above, near-field wave behaviour has been reasonably approximated by simple mathematical relationships; it is possible to calculate initial maximum wave amplitude from a subaerial landslide impact, given only the landslide volume and density, impact velocity and water depth. For example Noda (1970) presented a method for maximum wave amplitude estimation as a function of the basal dimension of a box dropped vertically into water of depth d, and the Froude number, given by $F = v/\sqrt{gd}$), where g is acceleration due to gravity, and d is water depth. Noda's method tends to result in slightly more conservative initial wave amplitudes than the Slingerland and Voight (1979) method described below.

Slingerland and Voight (1979) developed a regression equation for maximum first wave amplitude, based on empirical relationships derived from a physical three-dimensional laboratory model of Lake Koocanus (British Columbia and Montana), combined with

field observations of wave-generating slides during the filling of the Mica Reservoir (British Columbia):

$$log(\frac{A_{max}}{d}) = a+b[log(KE)] \tag{4.3}$$

where $a = -1.25$ and $b = 0.71$ (empirically determined), V is slide volume (in m^3) and KE is the dimensionless kinetic energy:

$$KE = 0.5(\frac{V}{d^3})(\frac{\rho_s}{\rho_w})(\frac{v^2}{gd}) \tag{4.4}$$

where ρ_s and ρ_w are the density of the slide material and water, respectively.

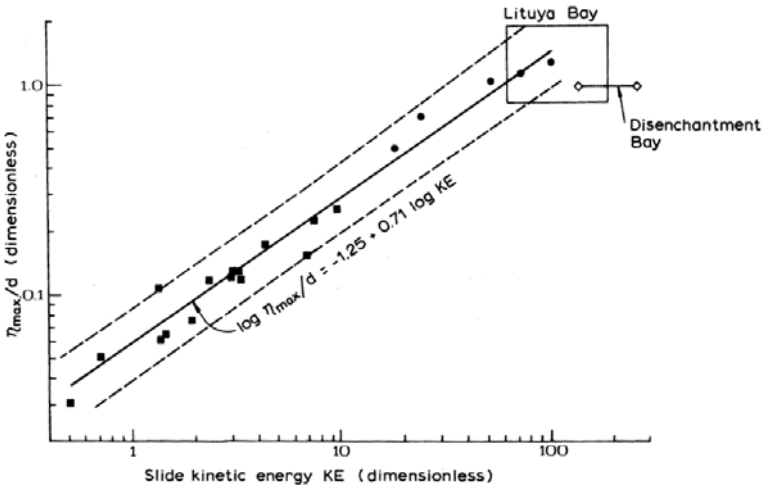

Figure 4.14: Maximum wave amplitude as a function of landslide dimensionless kinetic energy (KE): log-scale empirical relationship of Slingerland and Voight (1979), from Lake Koocanus physical model(squares), and field observations of wave generated slides during the filling of Mica Reservoir (circles), with best estimates for Lituya Bay (box) and Disenchantment Bay (line connecting open diamonds) historical events.

A major objective of the current study is to provide an estimate of risk associated with future landslide-generated tsunami at Milford Sound, based on reasonable approximations of wave amplitude and near-shore runup from past events that are recorded in the geological record. Many discrete landslide events must be considered in the risk analysis, therefore physical laboratory models and complex numerical simulations are beyond the resources available for the current project. As a relatively simple and practical alternative, the analytical solution of Slingerland and Voight (1979) was used to generate a range of estimated values for maximum displacement wave amplitude; these results are presented in Table 4.3.

A bulk slide debris density of 1.6 g/cm^3 was inferred by Miller (1960) for the land-

slide that caused the 1958 Lituya Bay tsunami, and verified by Fritz et al. (2009) in their physical laboratory model of Gilbert Inlet. However, as described above, it is expected that landslides that fall into Milford Sound are better approximated by nearly-intact blocks of material (which has an in-situ density of ∼2.7 - 2.9 g/cm^3), therefore a conservative slide density of 2.0 g/cm^3 was used in all calculations. For comparison, calculations using bulk slide debris densities of 1.6 or 2.5 g/cm^3 results in maximum wave amplitudes that are typically 20 - 25% lower/higher (respectively), depending upon water depth and landslide velocity.

4.3.1.3 Waves caused by submarine landslides

Submarine mass failures can also generate large displacement waves, as on 17 July, 1998, when a M_w 7 earthquake offshore of Sandaun Province, Papua New Guinea triggered a 4-8 x 10^6 m^3 submarine landslide that generated waves with a maximum run-up of 15 m, affecting ∼30 km of coastline, and killing over 2,100 people (Imamura and Hashi, 2003; Okal et al., 2002). Suleimani et al. (2011) investigated the combined impacts of landslide-generated waves and tectonically-generated tsunami that killed over 100 people following the 1964 mega thrust earthquake(M_w 9.2) in Prince William Sound, Alaska. They found that the devastating tsunami run-up that severely damaged the port town of Seward was caused first by local submarine landslide-generated waves, and followed approximately 20-30 minutes later by tectonic tsunami of a similar magnitude. The initial landslide-generated displacement waves reached 10 m high at Seward, destroying and setting alight a fuel tank depot. The 12 m high tectonic tsunami reached Seward 20-30 minutes later, spreading a wall of flaming oil into Seward, causing further fires.

Predicting wave amplitude from submarine landslides is perhaps even more difficult than for subaerial impact-driven displacement waves (Grilli and Watts, 2005). Nonetheless, Watts et al. (2005) developed a mathematical approximation of the kinematics of submarine slides and slumps, based on a dynamic balance of inertia, gravity, buoyancy, friction and hydrodynamic forces for the centre of mass; this allowed them to define characteristic travel distance and time of motion as a function of slide geometry, specifically the initial submergence depth (d), relative to the slide travel distance (l) and slope angle (θ).

$$A_{max} = (1.74 \times 10^{-5})(b)(1 - 0.75sin\theta)(\frac{bsin\theta}{d})^{1.75} \tag{4.5}$$

The mathematical relationship described above relates the vertical extent of the slide to

the local water depth, similar to the empirical relationship found by Watts (1997) from laboratory experiments, and is used in the current study to provide a first-order approximation of wave amplitude from submarine mass failures inferred from bathymetry (i.e. DF1-DF4, see Table 4.3).

4.3.2 Wave propagation and runup

When displacement waves are directed nearly perpendicular to shore, refraction and wave entrapment can occur (Di Risio and Sammarco, 2008); numerical simulations have indicated that this phenomenon can result in secondary edge waves with larger runup than the initial wave (Harbitz et al., 2006; Lynett and Liu, 2005). Wave reflection and entrapment was also observed experimentally by Di Risio and Sammarco (2008), in a three dimensional wave tank with a beach plane positioned opposite the landslide impact site.

Madsen and Schaffer (2010) confirmed analytically the complex wave interactions due to shoreline reflection of large waves, and demonstrated that their analytical solution was in close agreement with numerical model results. Nonetheless, most wave-runup experiments have considered only solitary breaking or non-breaking waves (Di Risio and Sammarco, 2008). Pedersen and Gjevik (1983) developed a Lagrangian-based numerical simulation for the runup behaviour of a single impulse wave, governed by the Boussinesq equations. Using a combination of empirical data and results from their numerical simulation, Pedersen and Gjevik (1983) established a wave amplification factor for large waves, which allowed the calculation of runup height, based on the initial wave amplitude and angle of the slope. This relationship is shown in Figure 4.16.

Recently, numerical models have been employed to simulate impact wave generation and propagation in the fjords of western Norway, specifically with the aim of assessing the risk from a future catastrophic collapse of the Åknes slide, and resulting displacement wave and inundation of communities. Eidsvig et al. (2011) used a refined version of the linear long-wave model of Harbitz et al. (2006), which incorporates the shoreline wave amplification factors of Pedersen and Gjevik (1983); the model has been verified by successfully simulating the observed wave amplitude and runup resulting from the 1934 Tafjord tsunami. The numerical model also compares well with experimental observations from a 1:500 scale three-dimensional physical scale-model of the Synnylvsfjord and Geirangerfjord fjords and mountainsides, which has been used to simulate displacement waves from a future rockfall of $\sim$54 x $10^6 m^3$ at Åknes.

In order to estimate maximum wave runup at Milford, the wave amplification factors of Pedersen and Gjevik (1983) were applied to estimated maximum displacement

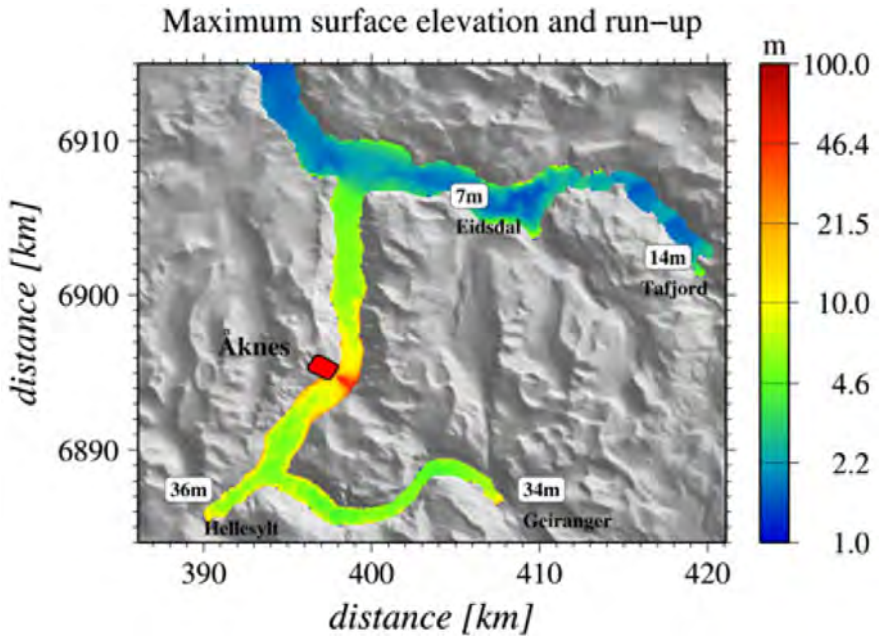

Figure 4.15: Model results from Eidsvig et al. (2011) (Fig. 7), showing maximum fiord surface elevation as a result of a hypothetical 35 x $10^6 m^3$ rock-slope failure at Åknes, Norway. Maximum runup of ∼20 m is simulated for Hellesylt, which is about 6 km away from the Åknes slide.

wave amplitudes (see Table 4.3). Two separate runup heights were calculated for each landslide:

1. R_{max}, based on runup at the nearest shoreline, assuming near-perpendicular runup, a 45° slope, and no wave attenuation during fiord crossing.

2. R_{inn}, inundation of the Cleddau delta, assuming near-perpendicular runup and 10° slope.

All calculations are based on a solitary wave, and do not take into account reflection and/or entrapment along the steep shorelines. These complex phenomena are captured by the numerical and physical models referred to in Eidsvig et al. (2011). Simulations indicate that a maximum wave runup of ∼30 m can be expected at Hellesylt, at the head of Synnylvsfjord (some 13 km south of the Åknes slide), following an initial wave height of more than 50 m. At Tafjord, historical observations following the 1934 tsunami suggest that the maximum runup (62 m) was attenuated by a factor of 4 over just 5 km.

Based on evidence from Norwegian fjords, it is considered that the estimated maximum wave inundation heights (R_{inn}) calculated here for the Cleddau delta may over-

estimate the runup by as much as a factor of 2 to 4 for waves that are initiated in the outer (Dale or Entrance) basins. The outer basins are relatively shallow (∼130 m) compared to Stirling basin (290 m), so while it is possible that very large displacement waves may be generated in the outer fiord, the complex geometry and transition to much deeper water at Stirling Basin is likely to have a significant attenuation effect. However, this ignores potential wave amplification due to fiord geometry or reflections by the fiord wall; resulting wave amplification and standing wave oscillations lasting for up to hours after the initial impact as have been observed and modelled for Lituya Bay and and Tafjord (e.g. Harbitz et al. (1993)). Unfortunately, the complexities of geometric amplification can not be simulated by the simple analytical models used in the current project, therefore the non-scaled maximum amplitudes (i.e. A_{max} instead of R_{inn}) are presented in Table 4.3 for runup at the Cleddau delta from waves originating in Dale or Entrance basins.

4.3.3 Interaction between tsunami and vessels

Within a fiord environment, large tsunami waves can transport vessels distances of up to several km; as seen in Lituya Bay in 1958, where boats were transported at speeds of over 150 km/hr (Miller, 1960); at Milford Sound, the most likely scenario is that initial displacement wave energy will be directed across the fiord, towards the opposite shoreline. During daylight hours on most days, there are a minimum of several cruise boats and smaller vessels operating within Milford Sound; during peak tourist season, the number of boats is much higher. If vessels on the open fiord were to be transported by large displacement waves, they would likely capsize, and/or be dashed against the steep rocky shorelines that surround most of Milford Sound.

In addition to the risks posed by displacement waves to ships operating on the open fiord, there are also risks to vessels which are moored (e.g. in Deepwater Basin or Harrison Cove), or berthed at a port (e.g. the docks at Deepwater Basin or the cruise boat port at the Milford Visitors Centre). Even relatively small tsunamis of 2 to 3 m in height can cause damage to mooring ropes, fenders and docks, as smaller vessels are tossed about (PIANIC, 2009). Boats which break free from their moorings can be carried into other vessels, or drift into areas where they collide with buildings and people. With larger tsunami, boats can be carried well inland by incoming tsunami waves, until they eventually ground; the receding tsunami may then overturn the grounded boat. Most vessels operating at Milford Sound are relatively small-displacement craft, such as fishing boats and tour boats up to ∼40 m in length, so it is likely that even small tsunami will affect these vessels. When tsunami heights approach 7 m, even the largest

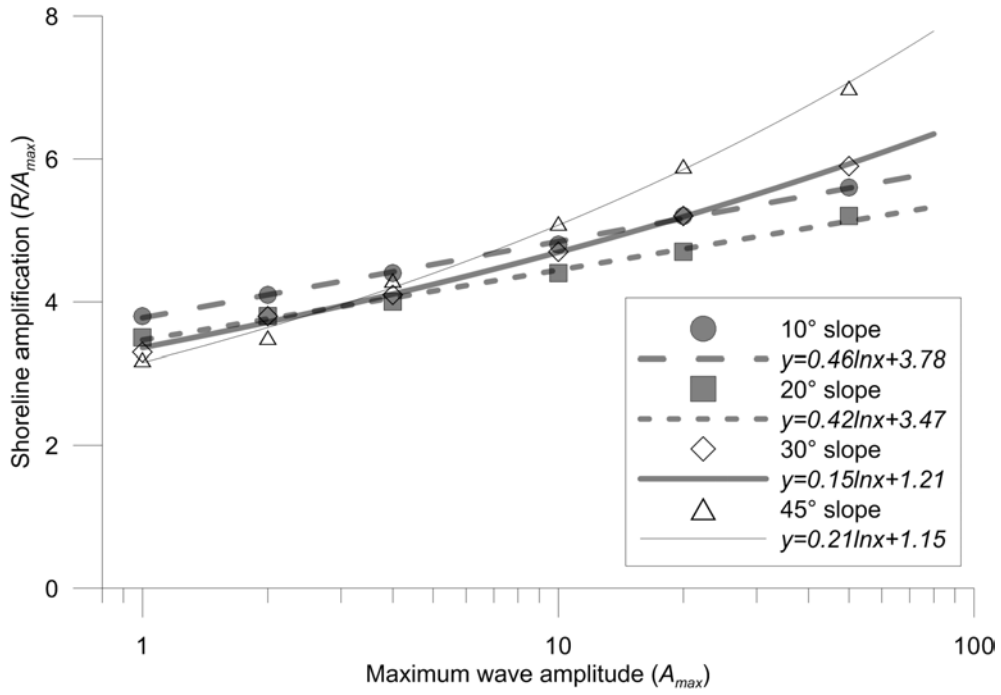

Figure 4.16: Amplification of wave height at shorelines of differing slope. Y-axis is ratio of near-shore runup (R) to maximum initial wave amplitude (A_{max}). Symbols do not represent empirical data points, but are estimations based on empirical relationships from Pedersen and Gjevik (1983) (Fig. 7). Curves represent best fit to relevant points. The general trend is for greater shoreline amplification as waves get larger. Interestingly, steeper shorelines cause less amplification of smaller waves than nearly flat shorelines, but this trend is reversed as waves get larger. The curve for 10° slope (long-dashed line) is used to estimate maximum inundation at the Cleddau Delta, 45° curve (solid thin line) is used to estimate maximum near-shore runup (see text).

cargo ships and cruise liners can be washed ashore, with catastrophic damage to vessels, and any infrastructure that they collides with (PIANIC, 2009). The devastation caused by large tsunami waves interacting with large vessels was clearly seen in Japan following the April 2011 earthquake and tsunami.

4.3.4 Analytical model results and validation against historical analogues

4.3.4.1 Deepwater basin simulation

In addition to simulating wave amplitudes and maximum potential runups based on prehistoric landslides that have fallen into Milford Sound, a potential landslide-generated displacement wave originating in Deepwater Basin was simulated. Although there is not any evidence of submarine landslide deposits preserved in the relatively small and shallow (50 m) Deepwater Basin, a displacement wave from a future landslide could present a very significant risk to the nearby Milford Village and airport. An ∼9 x 10^6 m^3 subaerial landslide fell off the northern slopes of Sheerdown Peak around 4,600 years BP; the deposit probably closed off part of Deepwater Basin and deflected the Cleddau River ∼300 m to the north. The deposit now forms the head of Deepwater Basin (see Table 4.2, "L. Cleddau"). The Arthur River end of Deepwater Basin is also constrained by a landslide deposit (∼18 x 10^6 m^3) of unknown age. Another landslide of ∼20 x 10^6 m^3 blocked off the Arthur River about 850 years ago (creating Lake Ada), and comes to within 2 km of Deepwater Basin.

Given that the relatively shallow Deepwater Basin is located at the base of a steep mountainside with known instability, and within 1 km of the Milford airport and village, a potential tsunami-inducing wave was investigated. Applying the analytical methods described above, a landslide of 1 x 10^6 m^3, released from a height of 700 m on a 50° slope would impact the water with a velocity of ∼86 m/s, generating a displacement wave with an initial amplitude of over 80 m (see Table 4.3, "*DW1*"). Despite the relatively small simulated volume (compared to existing submarine deposits and the adjacent subaerial deposits), high impact velocity and shallow water combine to generate a scenario that is almost too horrifying to contemplate.

However, there are historical precedents for such an event, from Norway (e.g. Loen; 1905 and 1936, Tafjord; 1934), and Lituya Bay, Alaska (1954) (see Table 4.1). The 1936 Loen disaster is perhaps most analogous to Deepwater Basin; therefore, as a test of the validity of the analytical results for a potential Deepwater Basin displacement wave, the Loen event was simulated using a slide volume of 1 x 10^6 m^3, slope of 60°,

centre of mass slide path length of 600 m, and an assumed water depth of 100 m. The same rock-mass parameters used for Milford Sound landslides (i.e. density ρ=2.0g/cm^3, dynamic bed friction angle θ=27°) were used. The calculations indicate a maximum wave amplitude of 23 m, and a runup of 116 m (based on a 45° shoreline slope). The shoreline wave amplitude is not known for the Loen event, but the simulation does significantly over-estimate the observed maximum runup of 74 m. This suggests that for shallow-water, high-impact-velocity scenarios, the analytical method presented here may overestimate maximum amplitude runup by around 50%; this may be because the analystical model can not account for the complicated fluid dynamics and bottom interaction of a large wave in shallow water. However, the analytical method is validated for historical displacement waves in deeper water (see Lituya Bay and Tafjord below).

4.3.5 Testing the analytical model

4.3.5.1 The 1934 Tafjord disaster

The 1934 Tafjord displacement wave is probably a good analogue for a potential Milford Sound tsunami resulting from a landslide falling into Stirling, Dale or Entrance Basins, as the overall geometry of Tafjord is similar; both fiords have similar length (∼20 km and 15 km respectively), width (varying from 1-3 km) and maximum basin depth (220 m and 290 m respectively), as well as steep (∼50 - 70°) rock walls that rise at least 1 km from water level. The 1934 Tafjord event involved an ∼3 x 10^6 m^3 sheet of gneiss spalling off between sea level and 800 m above the fjord (Hermanns et al., 2006), into ∼200 m of water, and generated a wave that ran up to 62 m directly opposite the source area. The waves propagated towards the head of the fjord, causing destruction in the villages of Tafjord and Fjora, where inundation reached heights of 16 m and 13 m respectively, killing 41 people (Jorstad, 1968). Tafjord is located at the fiord head, ∼5 km away from the slide scar, suggesting that wave runup was significantly attenuated by fiord geometry over that distance.

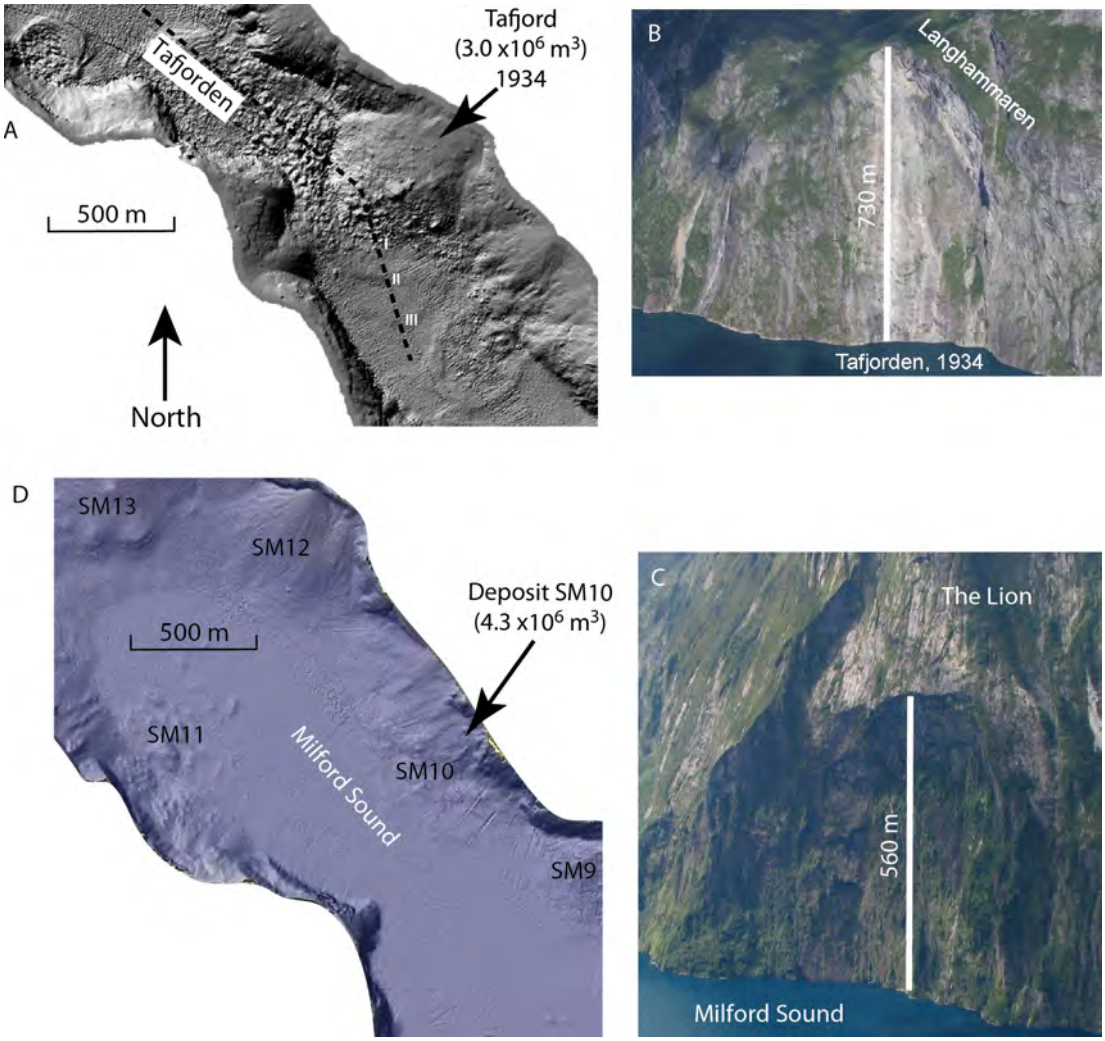

Figure 4.17: The 1934 Tafjord landslide, compared to Stirling Basin, Milford Sound. A) Tafjorden bathymetry. Dashed line represents seismic profile (not shown), position I is the edge of 1934 deposit, II and III are inferred older rock avalanche deposits. After Blikra et al. (2005). B) Source of the 1934 landslide on Langhammaren, maximum scarp height shown. C) Source of deposit SM10, on The Lion, maximum scarp height shown. D) Stirling Basin bathymetry and locations of landslide deposits SM9 through SM13. Arrow shows approximate impact site of SM10.

4.3.5.2 Model validation with the Tafjord and Lituya Bay historical events

The simple analytical model presented here for estimating maximum initial wave displacement and shoreline amplification (runup) was tested against observational data from two relatively well-constrained historical events in fiord-like environments; Tafjord (1934) and Lituya Bay (1958). Maximum wave amplitude and near-shore runup for Tafjord were calculated with the same rock-mass parameters used for the Milford cases (i.e. density $\rho = 2.0$ g/cm^3, dynamic bed friction angle $\theta = 27°$) and the slope angle $\alpha = 60°$of Jorstad (1968). Calculations for Lituya Bay used $\rho = 1.6$, $\theta = 14°$and a slope angle $\alpha = 40°$(based on Miller, 1960), and a centre of mass slide path length of 610 m (Fritz, 2002). Results are presented in Table 4.3, and confirm that the analytical method employed here can reproduce observed maximum wave height and runup in fiord environments to a level of accuracy that is useful for hazard assessment and risk analysis.

Historical observations of landslide-generated displacement waves from Norwegian fiords, along with a growing base of physical and numerical model results, indicate that fiord environments can be subject to very large landslide-triggered displacement waves. Events of similarly destructive potential should also be expected in the geographically and geologically similar, but seismically active terrain of Fiordland.

4.4 Risk assessment

4.4.1 Tsunami magnitude-frequency relationship

Tsunami amplitude/runup magnitude-frequency relationships were developed for Milford Sound, based on the estimated cumulative frequency (per 1,000 years) of simulated maximum wave heights and runups, derived from the analytical method described above (see Table 4.3), and assuming a maximum age for wave-generating landslides of 17 ka. The method is identical to that described for the landslide M-F relationship described earlier. The resulting log-normal distributions are shown in Figure 4.18, and can be used to quickly estimate maximum expected tsunami amplitude and runup heights for long return periods. For example, the estimated 1-in-1000 year tsunami amplitude at Milford Sound is ∼4 m, with an estimated runup at the Cleddau Delta of ∼17 m.

The M-F curves presented for tsunami amplitude and wave runup (inundation) on the Cleddau Delta are best-fit regressions on a range of values, which are determined by the analytical methods described above. The proposed tsunami amplitude and wave runup magnitude-frequency curves have not been validated with any empirical data from Milford Sound; therefore these curves are intended to be used for first-order approximations only.

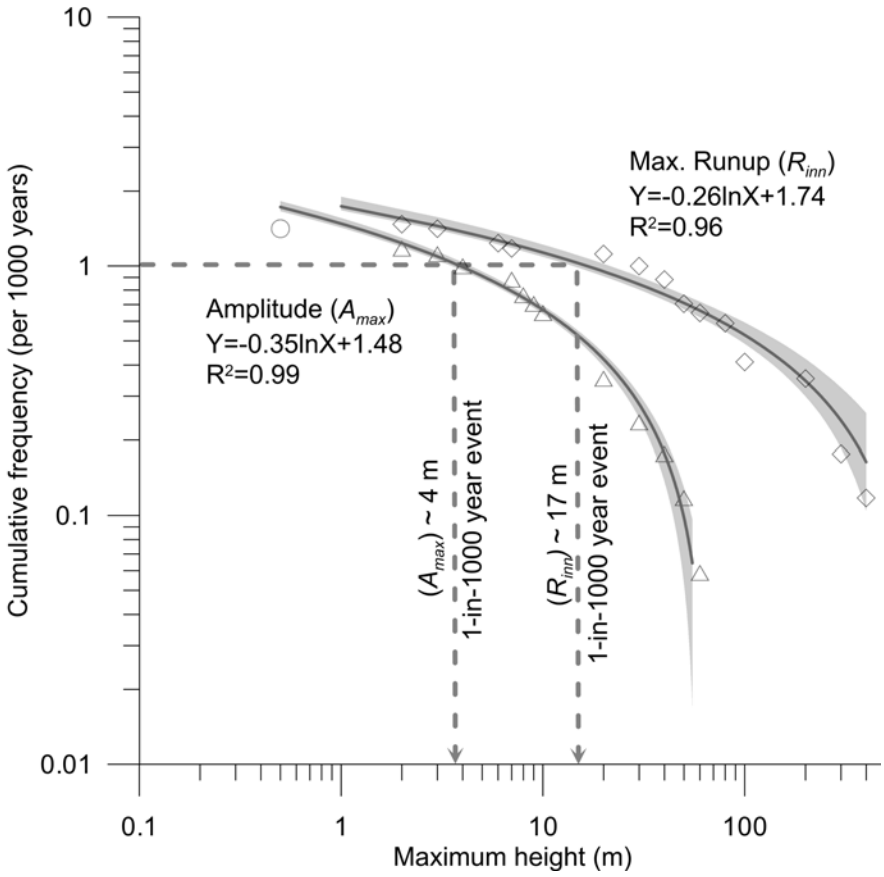

Figure 4.18: Simulated tsunami magnitude-frequency relationship for Milford Sound area. Diamonds are simulated maximum runups and triangles are simulated maximum amplitude from Table 4.3; each point represents the number of simulated waves of a given runup/amplitude range that occur every 1,000 years. Maximum runup/amplitude ranges (bins) were set to match each division of the log-scale axis. Circle represents the two smallest simulated wave amplitudes (one bin), which are not included in regression, in order to reduce the impact of the "roll-over" effect. Grey solid curves are the best-fit log-normal regression curves to the simulated points. Shaded grey areas are the 95% confidence intervals on the regression curves.

4.4.2 Vulnerability

4.4.2.1 Tsunami risk assessment for Norwegian fjords

Eidsvig et al. (2011) assessed the risk associated with a future landslide-generated tsunami at Åknes, where an ∼30 - 40 x 10^6 m^3 unstable rock mass may fall into Storfjorden (Blikra et al., 2005). Eidsvig et al. (2011) established a practical, empirically-based method to quantify the hazard, and vulnerability of elements at risk. First, they estimated the probability of a tsunamigenic landslide at Åknes from the spatial and temporal pattern of existing post-glacial landslide deposits in Storfjorden (Blikra et al., 2005) (i.e. the frequency of landslides, over the last ∼10,000 years, of similar size to the predicted Åknes slide). Second, they simulated wave runup at populated areas using a numerical tsunami propagation and runup model, based on Harbitz et al. (1993)), and calibrated with empirical data from a physical model, and historical observations. Third, they assessed vulnerability of residents and tourists in those populated areas, by developing a vulnerability function which describes the empirical relationship between wave runup (inundation) and the proportion of exposed people who died as a result of historical landslide-generated tsunami in Norway. Eidsvig et al. (2011) calculated the risk from an Åknes slide-generated tsunami at each population centre, by multiplying the hazard (probability of the slide occurring in any given year) by the vulnerability function (proportion of deaths compared to people exposed to the predicted wave) and the estimated number of people exposed.

4.4.3 Vulnerability function for Milford Sound

For the current project, vulnerability is defined as the proportion of people at Milford Sound who would likely lose their lives as the results of a landslide-generated tsunami with a given runup height (R_{inn}), or wave amplitude (A_{max}). Vulnerability can be quantitatively defined, based on data from historical tsunami disasters. By plotting the proportion of exposed people who have lost their lives in historical events, compared to observed wave inundation, a theoretical curve can be fit to the data, and used to estimate vulnerability for future events at Milford Sound.

Theoretical wave speed can be estimated from the shallow water celerity described earlier: $c = \sqrt{gd}$, where g is acceleration due to gravity, and d is the water depth. Therefore, a 10 m high impulse wave will travel through Stirling Basin (290 m deep) at around 190-200 km/hr (or ∼3.3 km/min). The vulnerability function is based on there being no prior warning, as the time between landslide impact with the water and the first waves reaching either exposed boats in the fiord, or the Cleddau delta, is likely

to be in the order of seconds (for nearby boats), to about 5 minutes for a landslide originating in the outer fiord. Waves caused by landslides from either Mitre Peak or The Lion will reach the Cleddau Delta in ∼2 minutes.

Only the inundation height is considered in the vulnerability assessment. Other factors such as flow velocity, or ground surface roughness and slope are not directly considered, although the empirical data that the vulnerability function is based on must encompass these factors. More specific and detailed future analysis will be required to incorporate these factors directly into risk analysis. The potential effects of the built environment are also not directly considered (e.g. certain buildings may provide some level of protection, or alternatively, their damage or destruction may increase vulnerability). As above, some of the effects of this factor must be included in the empirical data (i.e. exposed people in historical disasters are assumed to have been located in a variety of environments, including inside buildings).

4.4.3.1 Historical data

Norway has the most historical records of damage and loss of life due to landslide-generated tsunami in fiord environments, therefore after Eidsvig et al. (2011), a vulnerability function was developed based on historical data from the fjords of western Norway (these data are provided in Table 4.4). Material damage is not considered in the vulnerability assessment; only the vulnerability of people (i.e. proportion of lives lost) is assessed. The historical data pre-date the implementation of monitoring and early-warning systems in Norway, and therefore should reflect a similar situation as would exist for a coseismic landslide-generated tsunami at Milford Sound (i.e. no-prior-warning).

Table 4.4: Empirical data from historical landslide-generated tsunami disasters in fiord environments.

Location of fatalities	Local runup height$_b$ (m)	Number of fatalities	Number exposed	Vulnerability index$_c$
Norwegian fjords$_a$				
Rammerfjell, Stranda (1731)	<30	17	?	?
Langfjord, Tjelle (1756)	<15 (15)	32	60	0.53
Loen, Ytre Nesdal (1905)	40	34	34	1.00
Loen, Bodal/Indre Nesdal (1905)	>6 (12)	27	87	0.31
Tafjord, Fjora (1934)	12-14 (12)	17	98	0.17
Tafjord, Tafjord (1934)	4-16 (10)	23	200	0.12
Loen (1936)	2-23 (15)	73	200	0.37
Other locations				
Disenchantment Bay, AK (1845)	35	∼100	?	?
Lituya Bay, AK (1958)	40	2	4	0.50
Vajont Res., Italy (1963)	>20	1,909	?	?
Lake Chungar, Peru (1971)	20	∼600	∼1,000	0.60

[a] these data based on historical observations from Eidsvig et al. (2011, and references therein), Table 4.

[b] Local runup height, where fatalities occurred. Number in brackets is assumed runup height used in vulnerability function: 12 m assumed for Loen (1905), and 15 m for Loen 1936, based on observations of max. 15 m runup at the lake delta resulting from the slightly larger 1936 waves (Jorstad, 1968). Other values in brackets are averages of observed runup ranges. Lituya Bay runup based on forest trim-line, approximately adjacent to location (Miller, 1960. Vajont runup based on approximate observed inundation depth at Longarone, below the dam (Panizzo et al., 2005a). Lake Chungar inundation depth assumed to be 20 m, based on observations of maximum 30 m runup, and the location of the mining camp nearly directly across from the impact location (Evans and DeGraff, 2002).

[c] Ratio of fatalities to number exposed. Data from Norwegian fiords used to develop vulnerability function (see text).

The shape of the vulnerability curve must satisfy the following two general conditions (e.g. Eidsvig et al., 2011):

1. below a certain inundation height, tsunami do not normally cause deaths,

2. above a certain inundation height, nearly every exposed person dies,

These conditions are satisfied by a vulnerability function with an S-shaped curve:

$$S = \frac{1}{1 + ke^{-\lambda R}} \tag{4.6}$$

where S is vulnerability, k and λ are constants, e is the natural logarithm base (2.718), and R is the inundation height. The resulting continuous function approaches (but never equals) zero for small inundation heights, therefore vulnerability at small inundation heights should not be calculated; an example is for very large populations that are exposed to relatively small waves (i.e. less than ∼1 m inundation). Plotting the historical data from Norwegian fjords yields the following graph (see Figure 4.19), and a resulting empirically-determined vulnerability function with $k = 55$ and $\lambda = 0.25$.

The vulnerability function suggested in Figure 4.19 should be used with caution for large inundation heights, as there are few historical data for such events. However, the function approaches a value of 1 for inundations heights greater than 25-30 m, which is intuitive, as it is expected that inundation of that magnitude will cause massive devastation and loss of life. This conclusion is also supported by data from the Boxing Day tsunami of 2004, which indicate that inundation of ∼14 m caused the deaths of ∼50% of exposed people (Eidsvig et al., 2011).

4.4.4 Assigning vulnerability based on location

For the current project, vulnerability was weighted, depending on the location of people at risk. People on the shoreline were assumed to be at or near the Milford Visitors Centre, Milford Village, or the airport, all of which are within ∼5 m of normal high tide level. Therefore, exposed people onshore near the Cleddau Delta were assumed to be located at an average elevation of 5 m.a.s.l. (which was subtracted from the inundation height when assigning vulnerability).

Estimating vulnerability for people on boats out in the fiord is less straight-forward, due to additional variables that are unique to each craft; these variables include distance from impact location, depth of water beneath the boat, proximity to shorelines, and size and seaworthiness of each craft. While consideration of such specific variables is beyond the scope of the current project, it is considered that boats that are within the

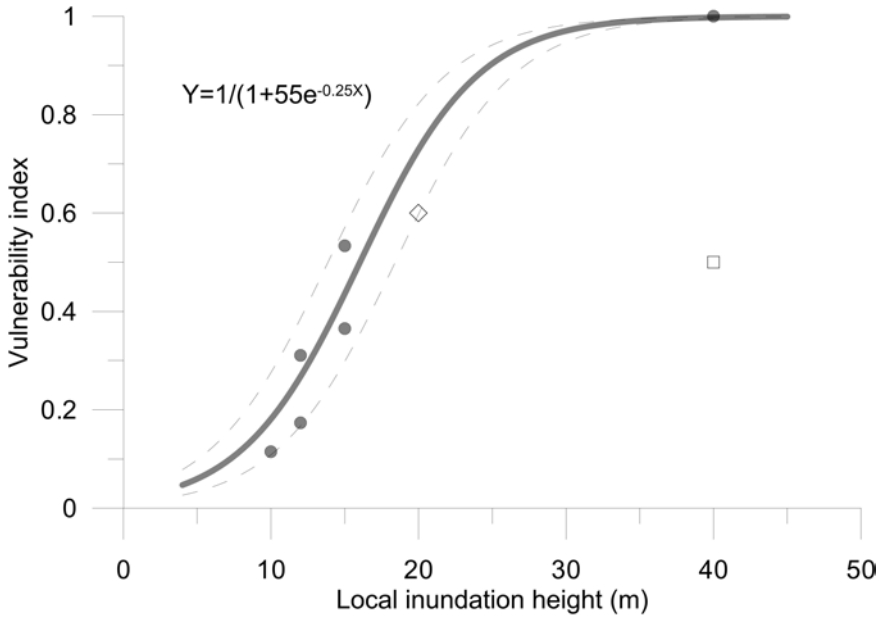

Figure 4.19: Empirically-determined vulnerability function, based on historical data from landslide-generated displacement waves in Norwegian fiords (see Table 4.4). Filled circles are empirical data from Norway. Open diamond is Lake Chungar, Peru, open square is Lituya Bay, AK (note that just two boats were exposed in Lituya Bay, incredibly one managed to ride out the giant wave). Solid curve is the best-fit function (equation) based on the Norway data only. Dashed curves are the upper and lower bounds of the vulnerability function, which together encompass the Norway data.

fiord during large landslide events may be exposed to large-amplitude impulse waves that could damage or capsize craft. Survivor accounts from Lituya Bay indicate that very large displacement waves can transport boats great distances at speeds of over 150 km/hr (Miller, 1960); clearly if a boat capsized or was dashed into rocky shorelines by such transport, the results could be catastrophic.

People exposed to impulse waves in boats were assigned a vulnerability based on wave amplitude, rather than inundation height at shore; this is predicated on the assumptions that only boats docked at the shore (i.e. not carrying people) would be affected by wave runup, and that exposed boats in open water in the fiord would not be affected by interactions of waves with the shoreline (e.g. reflection due to steep rock walls). Future assessment based on more complex numerical models will be required to test out the validity of these assumptions.

4.4.4.1 Number of people exposed

Milford Sound is a year-round tourist destination, although summer is the busiest time, especially for boat tours. Based on a vehicle census commissioned by the Department of Conservation (D.O.C., 2006), there were 605,000 to 640,000 visitors to Milford Sound in 2004, of which ∼90% went on motorized cruises on the fiord. The remaining 10% included kayakers, trampers, and casual shoreline observers who did not go on the water. About 80% of visitors to Milford Sound were from overseas.

For the current project, it is assumed that all visitors to Milford Sound go within 5 vertical metres of sea level; this may ignore some visitors who go tramping on nearby forest tracks, however such visitors represent a very small minority overall (D.O.C., 2006). In addition to visitors, there are also ∼100-200 people working at Milford Sound each day (D.O.C., 2006). Averaging the 640,000 total annual visits per year over 365 days, equates to ∼1,750 visitors each day at Milford Sound. Most people arrive by bus from Queenstown or Te Anau, and spend part of the day at Milford Sound, as overnight accommodation is limited. In general, organized tours to Milford Sound arrive no earlier than 11:00 am, and depart by 4:00 pm, so most tourists are only exposed to the tsunami hazard for ∼4 hours. Therefore, the average number of people exposed to the tsunami hazard over a 24 hour period at Milford Sound is:

$$n = \frac{4}{24}(1,750) + 200 = 492 \tag{4.7}$$

Therefore, a conservative number of 500 (exposed) people per day is adopted for subsequent calculations. Of these, it is estimated that ∼50% will be on shore, and the

Table 4.5: Example vulnerability assessment assuming a maximum wave amplitude (A_{max}) of 6.2 m and a maximum runup (R_{inn}) of 27 m (see "SM1" Table 4.3). 50% of exposed people are assumed to be near shoreline (5 m.a.s.l.) and 50% on boats.

Variable	**Cleddau Delta** ($E = 5m$) (m)	**Boats** ($E = 0m$)
Fraction of people at location	0.5	0.5
Inundation/Wave height (R_{inn}/A_{max})	$27 - 5m = 22m$	6.2 m
Contribution to vulnerability	$0.5 * S^a(22m)$	$0.5 * S(6.2m)$
Resulting vulnerability (S)	$0.5 * S(22m) + 0.5 * S(6.2m) = 0.41 + 0.04 =$ **0.45**	

[a] S is the vulnerability function.

remainder in boats on the fiord, at any given time.

Based on the calculated population of exposed people, and the vulnerability function developed above, it is possible to estimate the risk associated with an impulse wave of any given size. An example vulnerability assessment calculation is provided in Table 4.5; for an impulse wave with a maximum amplitude of 6.2 m and a maximum runup of 27m at the Cleddau delta, $S = 0.45$, or ∼45% of exposed people are expected to suffer fatal injuries.

4.4.5 Calculating aggregate risk

For the current project, risk can be defined as the expected number of fatalities per year due to landslide-generated tsunami, averaged over several thousand years. This total risk is the sum of risk contributions from each displacement wave magnitude interval.

For a single displacement wave magnitude interval A, the contribution to total risk can be defined as:

$$Risk_A = H_A * S_A * n \tag{4.8}$$

where H is the hazard (probability of the event occurring), S is the vulnerability, and n is the number of people exposed to the risk.

Total risk for each wave size interval was assessed as follows:

- separate hazard probabilities were calculated for inundation of the Cleddau delta, and maximum wave amplitude on the open fiord, based on the M-F relationships described above,

- vulnerability was calculated separately for people on the shoreline near the Cleddau delta (50% of exposed population, assuming an elevation of 5 m), and people on boats in the fiord (remaining 50% of exposed population),

- vulnerability was calculated from the vulnerability function, based on the largest inundation/amplitude in the range,
- the number of people exposed to the hazard at any given time was assumed to be *n=500*,
- the risk contribution from all wave size intervals was added together to estimate aggregate risk.

Table 4.6 shows the risk contribution from each wave amplitude or inundation height interval. The total contribution to risk from people exposed to inundation near the shoreline at the Cleddau Delta is estimated to be 0.22 deaths/year, while the total contribution to risk from people exposed to waves in the open fiord (i.e. in boats) is estimated to be 0.16 deaths/year, for a total (aggregated) risk of 0.38 deaths/year.

Table 4.6: Contribution to risk from each wave amplitude/runup range and total aggregate risk assuming no prior warning.

People near shore (Cleddau Delta):					People on boats:				
Inundation[a] (m)	**Annual probability**[b]	**Vul.**[c]	**Number exposed**[d]	**Risk** (deaths/yr)	**Amplitude**[e] (m)	**Annual probability**[f]	**Vul.**[g]	**Number exposed**[h]	**Risk** (deaths/yr)
2-8	0.00036	0.037	250	0.00334	0.5-2	0.00049	0.029	250	0.00353
8-16	0.00018	0.221	250	0.00997	2-4	0.00024	0.047	250	0.00286
16-30	0.00016	0.904	250	0.03694	4-7	0.00020	0.095	250	0.00464
30-50	0.00013	0.999	250	0.03318	7-12	0.00019	0.267	250	0.01261
50-90	0.00015	1.000	250	0.03821	12-20	0.00018	0.730	250	0.03261
90-160	0.00015	1.000	250	0.03740	20-35	0.00020	0.99	250	0.04854
>160	0.00024	1.000	250	0.05956	>35	0.00023	1.00	250	0.05811
Total				0.21859	Total				0.16290
Total aggregate risk[i]									**0.38149**

[a] Maximum wave runup at the Cleddau delta (range).
[b] Annual probability of inundation within the specified range. Calculated from the probability function for maximum runup (Figure 4.18).
[c] Vulnerability. Calculated from the vulnerability function for the highest inundation in the range (minus 5 m for average elevation of individuals prior to wave runup) (Figure 4.19).
[d] Number of people exposed near shoreline at the Cleddau Delta, based on an average equivalent daily population of 500 at Milford Sound (see text), 50% of whom are assumed to be on shore.
[e] Maximum wave amplitude which boats are exposed to on the open fiord (range).
[f] Annual probability of wave amplitude within the specified range. Calculated from the probability function for amplitude (Figure 4.18).
[g] Vulnerability. Calculated from the vulnerability function, assuming that for boats, inundation is equal to the highest amplitude in the range (Figure 4.19).
[h] Number of people who are in boats, on the open water. Based on an average equivalent daily population of 500 at Milford Sound (see text), 50% of whom are assumed to be on boats.
[i] Aggregate total risk from all people, both on land (near shore) or in boats.

4.5 Summary and conclusions

Extensive field and laboratory work, combined with analyses of existing and new data from a wide variety of sources, has enabled the documentation of the spatial and temporal landslide distribution around Milford Sound. In addition, risk associated with future landslide-generated tsunami at Milford Sound has been quantified. Key results are summarized in the following list:

1. Over 30 large post-glacial landslide deposits have been documented within ∼15 km of the Milford Village and airport, including:
   - 11 terrestrial deposits >1 x 10^6 m^3,
   - 22 submarine deposits with subaerial sources (incl. 18 >1 x 10^6 m^3),
   - 4 submarine density flows originating from delta slopes (incl. 2 >1 x 10^7 m^3),
2. The three largest deposits originated from southeast-facing slopes,
3. Source area scars commonly extend to ridgelines; most landslides fall from ∼500-1,500 m, many into Milford Sound itself,
4. Failure slopes are as steep as 70°, and commonly exceed 50°, indicating that landslide impact velocities at water level are typically high,
5. Geomorphic features indicative of progressive weakening have been identified at several locations, including Rover Peak, The Lion, the north-facing aspects of Mitre Peak, and Sheerdown Peak,
6. A magnitude-frequency relationship was developed for 35 large post-glacial landslides deposits preserved in the study area, based on an assumed maximum age of 17 ka,
7. Based on the observed magnitude-frequency relationship for post-glacial deposits, landslides of ∼3 x 10^6 m^3 have fallen off the slopes surrounding Milford Sound once every thousand years. Landslides of ∼1 x 10^6 m^3 and 0.4 x 10^6 m^3 have occurred about every 500 and 330 years, respectively (330 years is the estimated rupture interval for the southern Alpine Fault).
8. Comparing the ages of terrestrial landslide deposits near the head of Milford Sound with evidence for earthquake activity indicates that most large landslides are coseismic,

9. Landslide impact speed, initial displacement wave amplitude and maximum wave runup at the Cleddau delta were estimated for each observed submarine landslide deposit. The resulting tsunami magnitude-frequency relationship indicates that waves with amplitude 4 m and maximum local runup of up to 17 m have occurred about once every thousand years at Milford Sound. Waves with amplitude 20 m and maximum localized runup up to 100 m have occurred about once every two-thousand years at Milford Sound.

10. Even a relatively small landslide falling into the shallow waters of Deepwater Basin (e.g. from Sheerdown Peak) could generate a large displacement wave, which would be directed towards the Milford airport and village. Such an event is analogous to the landslide and displacement waves that caused the 1934 Loen disaster in Norway.

11. A vulnerability function was defined for people exposed to landslide-generated tsunami hazard at Milford Sound, based on empirical data from historical disasters in the fiords of Norway,

12. Coseismic landslides will likely occur without prior warning at Milford Sound; displacement waves will travel the length of the fiord in less than 5 minutes, with tsunami caused by landslides falling from The Lion or Mitre Peak reaching the Cleddau Delta in $\sim$2 minutes,

13. The aggregate risk due to landslide-generated tsunami at Milford Sound (both to people on shore near the Cleddau Delta, and to people in boats on the open fiord) is estimated at 0.38 deaths/year, averaged over thousands of years. This result is of the same order as risk assessments for Norwegian fiords (assuming no prior warning).

It should be noted that these results are based on the assumption that large landslides such as those described in previous sections occurred individually; in other words, it is unlikely for more than one large landslide to occur at one time, even with an earthquake trigger. Normally, earthquakes cause many smaller landslides within a catchment (e.g. Hancox et al., 2003), but large, deep-seated landslides are much more rare, and generally occur as single, isolated events (Dr. T. Davies, pers. comm.). In the unlikely event that the landslide record at Milford Sound reflects events in which more than one large landslide occurred at the same time, the risk assessment presented above may slightly overestimate the risk associated with landslide-generated tsunami.

4. LANDSLIDE DISTRIBUTION AT MILFORD SOUND & IMPLICATIONS FOR NATURAL HAZARDS AND RISK MANAGEMENT

Chapter 5

Discussion and recommendations

5.1 Discussion

The best analogue that we currently have for the future evolution of Milford Sound is recorded in the geomorphic and sedimentary changes that have occurred there since the LGIT. This project has investigated some of those records with the aim of improving our understanding of past and future fiord landscape evolution and related geomorphic hazards in New Zealand.

5.1.1 Geomorphic evolution

Milford Sound has evolved in an active tectonic setting, which continues to influence geomorphic processes within the catchment. Coseismic landslides have likely been a major contributor to a thick post-LGM sediment infill at Milford Sound, with large terrestrial landslides occurring in the catchment throughout much of the Holocene.

5.1.2 Landslide distribution: implications for natural hazards and risk management

New high-resolution bathymetric and seismic reflection data reveal the presence of at least 18 very large (10^6 - 10^7 m^3) post-glacial rock avalanche deposits which blanket ∼40% of the bottom of Milford Sound. The presence of at least ten additional very large to giant (10^6 - 10^8 m^3) terrestrial landslide deposits in the lower Milford catchment has been confirmed by geomorphic mapping and field investigation. Approximately 11% of the ∼25 km^2 study area (including the bottom of the fiord) is covered by post-glacial landslide debris. This is much higher than the overall ∼2% coverage of southwest New Zealand by subaerial landslide deposits observed from geomorphic evidence (Korup,

2005b). It appears that a higher proportion of landslide deposits in Milford Sound are preserved, compared to subaerial deposits, suggesting that the actual concentration of landslide deposits in southwest New Zealand may be significantly higher than previously thought. Investigating the landslide record from other fiords and lakes may establish whether the discrepancy between submarine and subaerial preservation of landslide deposits documented at Milford Sound is a local or region phenomenon.

Radiocarbon dating and surface exposure dating (TCND and SH) indicate that the large subaerial landslides preserved in the Milford catchment occurred during the Holocene, between ∼9-1 ka. Radiocarbon and surface exposure dating indicate that the ages of six of these deposits coincide with published rupture dates on the southern on-shore portion of the Alpine Fault. Earthquakes on the southern portion of the Alpine Fault or the Fiordland subduction zone likely cause widespread landslide activity and increased input of terrigenous sediment to Milford Sound, resulting in the pulses of granular sediment that are recorded in cores from Stirling Basin.

5.2 Risk assessment summary

The southern on-shore portion of the Alpine Fault has not ruptured for 295 years and is relatively late in its recurrence cycle (∼330 years), with an estimated rupture probability over the next 50 years of ∼30%; the next rupture will most likely generate a great earthquake (M_w8). The current probability of an Alpine Fault earthquake is much higher than the long-term average; coupled with evidence from the gemorphic record at Milford Sound which indicates that most large landslides are triggered by earthquakes, this suggests a higher-than-average risk of landslide-generated tsunami at present. The longer strain continues to build up on the Alpine Fault, the larger the resulting earthquake is likely to be.

Most large landslides at Milford Sound are probably triggered by earthquakes. The current probability of an Alpine Fault earthquake is much higher than the long-term average, therefore the risk of landslide-generated tsunami at Milford Sound is correspondingly higher. Fiordland subduction zone earthquakes may also trigger large landslides at Milford Sound; turbidite records from offshore basins suggest a mean recurrence interval of ∼160 years for large earthquakes that affect Fiordland.

The long-term average aggregate risk (0.38 deaths/year) at Milford Sound is somewhat higher than an assessed risk of 0.05 deaths/year (best-case scenario) to 0.24 deaths/year (worst-case scenario) at Tafjord, for impulse waves resulting from a future catastrophic failure of the Åknes rockslope (Eidsvig et al., 2011). It is important

to note that the Tafjord risk assessment only considers a single hypothetical event at Åknes, and would be substantially higher if repetitions of past events that are recorded in the geological record were also included (e.g. Blikra et al., 2005). In addition, the assumed number of exposed people (averaged over an entire year) at Tafjord is 100 (Eidsvig et al., 2011), which is 20% of the 500 people estimated for Milford Sound. Compared to the described risk analysis for a single hypothetical event in Tafjord, the risk assessment presented for Milford Sound considers all potential landslide-generated tsunami events recorded in the geological record, as well as the greater number of people exposed to the hazard, and therefore is expected to be significantly higher than the risk at Tafjord. At Milford Sound, the temporal distribution of large terrestrial landslide deposits is spread across the Holocene; there is no evidence that large landslide events occurred more often during the LGIT, but there is substantial evidence that several large terrestrial landslides have occurred at Milford Sound over the past 4-5 ka, suggesting that similar large events should be expected in the future.

The long-term average aggregate risk (0.38 deaths/year) equates to an annual personal risk of $\sim$0.8 x 10^{-6} deaths/capita, assuming that 500,000 individuals visit the fiord each year. This is about the same as the *acceptable* personal risk threshold commonly cited for western societies (i.e. 10^{-6}), for activities that are perceived to bring some benefit (e.g. Executive and Safety, 1992). However, this assumes that individuals are only exposed for a single 4-hour period each year. People who live and work at Milford Sound throughout the year are exposed to a much higher level of risk; for example, someone who is at Milford Sound 80% of the time over an entire year will be exposed to $\sim$1,750 times greater risk than the tourist who only stays for a single 4 hour period; this equates to a personal risk of $\sim$1 x 10^{-3} deaths/capita. While the average long-term risk to one-time visitors may be considered to be societally *acceptable* (i.e. $<10^{-6}$, Executive and Safety, 1992), the risk to seasonal or full-time workers at Milford Sound is likely to exceed the maximum risk threshold considered *tolerable* by workers (i.e. 10^{-3} - 10^{-6}) in most modern societies (Executive and Safety, 1992).

5.2.1 A conservative risk analysis

The risk analysis presented in Chapter 4, and discussed above, is considered to be conservative (i.e. it may underestimate the actual risk), for the following reasons:

1. it is based solely on landslide deposits which are preserved in the geological record, and almost certainly underestimates the actual number of post-glacial landslide events, as the analysis does not consider possible additional deposits that may have been removed from the catchment by erosion, or are buried beneath other

sediments (this may possibly be partially offset by events which involve several large landslides concurrently),

2. the current probability of an Alpine Fault earthquake is much higher than the long-term average, therefore the current risk of landslide-generated tsunami at Milford Sound is correspondingly higher,

3. the risk analysis does not consider potential wave amplifications due to fiord geometry or reflections by the fiord walls. Simulations which have accurately reproduced the Lituya Bay and and Tafjord waves indicate wave energy trapping, resulting in wave amplification and standing wave oscillations (sloshing effect) that lasted for up to hours after the initial impact (e.g. Harbitz et al., 1993).

Consequently, the present risk from landslide-generated tsunami at Milford Sound may be significantly higher than the long-term average risk estimated here.

In addition, future growth in tourist numbers, or changes in the style of tourist visits has not been considered; for example, at least four proposals have been presented for improving access to Milford Sound, including a road tunnel beneath the Routeburn Pass, a boat-road-monorail link between Lake Wakatipu and Lake Te Anau, a gondola route between the Caples and Hollyford Valleys and a coastal road link from Haast to the lower Hollyford Valley. The first three proposals have the potential to substantially reduce travel times from Queenstown, which could increase both visitor numbers at Milford Sound, and the amount of time that visitors spend there. Both these factors could significantly increase the exposure to risk from landslide-generated tsunami for visitors.

5.3 Managing the risk

Conversations with tourists, local residents and workers, and government officials indicates a low awareness of the risk of landslide-generated tsunami at Milford Sound, compared to other natural hazards such as earthquakes and flooding. This purely qualitative assessment is based on correspondence with a relatively small number of people, therefore it is recommended that a survey be circulated to quantitatively assess the awareness of risk from landslide-generated tsunami, amongst local commercial operators, as well as visitors.

5.3.1 Risk management recommendations

Potential options for mitigating the risk associated with landslide-related hazards at Milford Sound are severely limited, because most future large landslide events will probably occur co-seismically, without prior warning such as geomorphic evidence of incipient failure, gradually accelerating movement of the rock bodies, or smaller precursor rockfall events. Consequently, the risk management strategy currently adopted in Norwegian fjords (based on identifying, quantifying and monitoring locations of future, potentially catastrophic landslides) may not be effective for New Zealand fiords.

Most landslides large enough to generate tsunami at Milford Sound will probably be triggered by earthquakes, so opportunities for advanced warning will likely be limited. However, there are some management strategies that could help mitigate the risk:

- educate workers and visitors about the risk, so that they can make informed decisions,
  - workers and residents at Milford Sound should be informed of the risk that they could be exposed to,
  - tourist operators should be educated sufficiently to explain the risk to potential customers,
  - posters or other signage which explain the risk should be made available around the most popular visitor areas at Milford Sound (e.g. the Milford Village, Visitors Centre, car parking areas, etc.), and at DOC offices in Queenstown and Te Anau,
  - ensure that workers and visitors are aware that earthquake shaking is likely to trigger landslides and tsunami,
- regularly monitor potential source areas for signs of instability and/or incipient failure. Reconnaissance flights after major rainfall events or earthquakes should be a high priority,
- provide tsunami shelters for the busiest places near the head of Milford Sound; potential shelter locations must be accessible within 2 minutes of either the Visitors Centre or the Village, and could include elevated walkways and viewing decks constructed on bedrock directly behind the Visitors Centre, and on the existing walkway which ascends the bedrock spur behind the Village. Although some additional infrastructure would be required, these locations would allow elevation to be quickly gained by taking advantage of the existing steep gradients, and could

be constructed on solid bedrock. These shelters would normally serve as viewing decks and/or nature walks, and could be constructed at an elevation of ∼20 m to avoid the estimated 1-in-1000 year runup,

- consider raising existing infrastructure, and construct future critical infrastructure at a higher elevation,
- limit the number of people who permanently live and/or work at Milford Sound; these residents are exposed to much higher risk than transients.

Landslide-related hazards (particularly landslide-generated tsunami), will almost certainly affect Milford Sound in the foreseeable future, therefore local and regional authorities should consider the associated risks when planning future development there.

5.4 Recommendations for future work

The results of the current project provide strong evidence that coseismic landslide-generated tsunami are likely to represent a significant risk at Milford Sound in the future. This knowledge should establish Milford Sound as a priority for more detailed risk analysis in the future, and should also encourage future research into the risks associated with landslide-generated tsunami at other mountainous, seismically active locations in New Zealand, such as Te Anau, Queenstown, Glenorchy, Wanaka, Hawea, and others. See Appendix B for a more detailed discussion of preliminary work completed at Lake Wakatipu, and implications for the Queenstown area.

5.4.1 Numerical and/or physical modelling

The results presented in the current project provide an initial estimate of the risk associated with future landslide-generated tsunami at Milford Sound, assuming that tourist and resident numbers stay approximately the same. Wave generation, propagation and runup can be challenging to predict in fiord environments, especially where waves interact with complex bathymetry and shoreline geometry. These complexities can not be simulated by the simple analytical models used in the current project, and require the development of numerical or physical models, which can replicate the effects of wave non-linearity and complex basin geometry, and simulate wave refraction and convergence.

High-resolution bathymetry is currently available for Milford Sound, therefore it is possible to develop detailed numerical and/or physical models, such as those that

are being used for risk assessment in the fiords of Western Norway. Once developed, such models will allow the simulation of a wide range of potential future events, which can be varied by landslide size, source area location and slope angle, and impact site. Model results should provide a more accurate assessment of the potential impacts of landslide-generated tsunami on people and infrastructure at Milford Sound, allowing more informed risk management and land development decisions.

There are advantages associated with both physical and numerical models:

- numerical models run on a computer, and therefore do not have large physical space requirements,
- numerical models are somewhat transferable - for example, once set up for Milford Sound, a numerical model could be developed for other New Zealand sites with significantly less effort,
- numerical models are customisable - parameters can be adjusted to taylor the model to different requirements.
- a physical model is intended to be a scaled-down version of the real thing; experimental observations are therefore directly analogous to real-world events, and can be used to calibrate or validate other types of models,
- a detailed physical model can fully incorporate the complex bathymetry and shoreline geometry of the fiord (limited only by the level of detail constructed by the model builder), without the limitations of computing power,
- physical models can engage the combined senses of sight, sound, and touch, and may therefore be more effective as an educational tool than computer-based simulations.

There are also disadvantages associated with each type of model:

- numerical models tend to require large resources of computing-power, especially if high-resolution DEMs are incorporated in the model,
- numerical models benefit greatly from calibration/comparison with empirical data. Without such data, it may be difficult to fine-tune model parameters and verify results.
- physical models can be labour-intensive to build accurately, and take up a lot of space (e.g. a 1:500 scale model of Milford Sound would be over 30 m long).

- physical models are not easily transferable.

The risk analysis presented here is based on a simple, conservative analytical model that ignores wave amplification effects due to complex fiord geometry and steep walls, and therefore may significantly underestimate the risk at Milford Sound. For Storfjorden in Norway, a 1:500 scale physical model has been constructed so that a range of landslides and resulting displacement waves can be simulated. Resulting empirical data are compared against results from a sophisticated numerical model. Together, these data provide a scientific framework for risk assessment and management decisions, as well as educational material for residents and visitors (e.g. www.ngi.no/en/...Monitoring-and-modelling-of-the-Aknes/, accessed 25 October, 2012).

It is strongly recommended that authorities consider similar strategies for Milford Sound. As a first step, more sophisticated and detailed risk analysis should be undertaken, underpinned by a physical laboratory model and/or numerical hydrographic modelling (both of which will benefit from currently-available high-resolution bathymetry). Once developed, such models will provide a robust foundation, which future risk management decisions can be based upon.

5.4.2 Other areas potentially at risk

Milford Sound is not the only place in New Zealand where landslide-generated tsunami hazards warrant further investigation. For example, Doubtful Sound is a much larger, but similarly rugged fiord that has a growing tourist presence. The extensive fiord-lakes of seismically-active eastern Fiordland, including Te Anau, Manapouri, Monowai, Hauroko and Poteriteri are largely surrounded by steep mountains, which are a potential source for large landslides. Approximately 4,000 residents currently live on the shores of Lakes Te Anau and Manapouri, with the population of the region swelling to ∼10,000 during the peak summer season (Otago Daily Time, 18 October, 2012).

The large glacial lakes of Central Otago (lakes Wakatipu, Wanaka and Hawea) are surrounded by steep mountainous topography, and located in a seismically active region which continues to be shaped by active geomorphic and tectonic processes. The relatively high regional population (2011 census 28,440, Q.L.D.C., 2012) is concentrated along or near the shores of Lake Wakatipu, although there are also significant and growing populations in the lakeside communities of Wanaka, Hawea and Lake Hayes. The regional residential population is expected to grow to around 36,000 over the next 10 years. The region enjoys iconic status as a year-round adventure playground and tourist destination, currently hosting over 2.8 million visitor-days per year, many from overseas visitors. According to the Queenstown Lakes District Council, the population

of the region swells by over 300% during peak tourist days, with an expected peak day population of 110,000 by the year 2021 (Q.L.D.C., 2012).

Figure 5.1: Queenstown town centre and Lake Wakatipu panorama. View looking due south from the top of the Skyline gondola. Remarkables Range on the left skyline (max. 2,319 m), Cecil Peak (1,974 m) and Walter Peak (~1,800 m) on the right skyline. Queenstown Bay and town centre at bottom left, with Frankton Arm extending to the left edge of frame. Author photo.

The growing resident population of the Central Otago Lakes region combined with its popularity as a domestic and international tourist destination suggest that local and regional governments should consider landslides and landslide-generated tsunami as a priority for future hazard assessment and risk analysis. Such work could include collection of high resolution bathymetric and seismic reflection data, supplemented with sediment core samples and boat-based investigation of shorelines in areas likely to trap tsunami deposits, and tsunami modelling. Field investigation, mapping, and dating of terrestrial landslide deposits should supplement any submarine investigation. Together, this information should improve the understanding of the potential hazards related to landslides and landslide-generated tsunami in the region, and provide a sound foundation for future risk management decisions.

5.5 Implications for future evolution and geomorphic processes at Milford Sound

What will the future evolution of Milford Sound entail? As a relatively large and deep fiord that is open to the ocean, Milford Sound will likely persist in something akin to its present state for several millennia. Global-mean sea level has risen by ~17cm over the past 100 years, and is projected to rise as much as 1.4 m by AD 2100 (e.g. Engineers, 2011; Meehl et al., 2012; Zecca and Chiari, 2012), potentially reaching

3 m above present-day levels over the next 200 years (Zecca and Chiari, 2012, and references therein), even if societies adopt aggressive measures to counter anthropogenic exacerbation (Meehl et al., 2012). These projected rates for global sea level rise are at least an order-of-magnitude higher than local uplift rates, therefore it is anticipated that low-elevation infrastructure on the Cleddau delta (e.g. the Deepwater Basin wharf and public boat ramp, the airport, and the waste-water treatment plant) could be affected be sea-level rise within the next 200 years.

Current flood protection measures on the Cleddau delta consist of a stop-bank along the north side of the Cleddau River (set at an elevation of ∼5 m.a.s.l.), effectively confining future delta growth to Deepwater Basin, which will eventually become entirely filled with sediment. While the Cleddau Delta could become at least partially inundated due to global sea level rise, the Harrison delta will likely be less affected, due to a steeper slope angle to the existing shoreline. The deeper outer basins of Milford Sound will continue to gradually accumulate sediment, until the valley is re-glaciated during the next glacial period. The timing of the next glacial period will be difficult to predict, as it will be dependent upon a suite of factors (some of which are not fully understood), including anthropogenic global warming, and orbital climate forcing (e.g. Milankovitch cyles).

This background of gradual geomorphic evolution will likely be punctuated by more episodic, catastrophic geomorphic processes, including severe earthquakes and large landslides. The steep mountains and close proximity to the plate boundary mean that the Milford catchment will continue to experience large landslides in the future, some of which may fall into the fiord itself, generating displacement waves that could present a significant risk to people and infrastructure.

Bibliography

A. R. Aa, J. Sjastad, E. Sonstegaard, and L. H. Blikra. Chronology of holocene rock-avalanche deposits based on schmidt-hammer relative dating and dust stratigraphy in nearby bog deposits, vora, inner nordfjord, norway. *Holocene*, 17(7):955–64, 2007. 42, 120

S. Abadie, D. Morichon, S. Grilli, and S. Glockner. Vof/navier-stokes numerical modeling of surface waves generated by subaerial landslides. *Houille Blanche*, (1):21–26, 2008. 230

R. P. Ackert Jr, R. A. Becker, B. S. Singer, M. D. Kurz, M. W. Caffee, and D. M. Mickelson. Patagonian glacier response during the late glacial-holocene transition. *Science*, 321(5887):392–95, 2008. 98

D. J. Alexander, T. R. Davies, and J. Shulmeister. A steady-state mass-balance model for the franz josef glacier, new zealand: Testing and application. *Geografiska Annaler, Series A: Physical Geography*, 93(1):41–54, 2011. 24, 64, 69

S. K. Allen, S. C. Cox, and I. F. Owens. Rock avalanches and other landslides in the central southern alps of new zealand: A regional study considering possible climate change impacts. *Landslides*, 8(1):33–48, 2011. 4, 12, 23, 33, 45, 48, 49, 198

R. B. Alley. The younger dryas cold interval as viewed from central greenland. *Quaternary Science Reviews*, 19(1-5):213–26, 2000. 62

B. V. Alloway, D. J. Lowe, D. J. A. Barrell, R. M. Newnham, P. C. Almond, P. C. Augustinus, N. A. N. Bertler, L. Carter, N. J. Litchfield, M. S. McGlone, J. Shulmeister, M. J. Vandergoes, P. W. Williams, B. Anderson, H. Brackley, P. Burge, J. Carter, U. Cochran, P. Cooke, J. Crampton, E. Crouch, M. Crundwell, Y. Deng, F. Drost, I. Graham, M. Harper, B. Hayward, C. Hendy, C. Hollis, M. Hughes, D. Kennedy, L. Kennedy, D. King, A. Mackintosh, B. Manighetti, M. Marra, D. Mildenhall, U. Morgenstern, T. Naish, H. Neil, D. Nobes, M. Page, A. Palmer, C. Prior, U. Rieser, H. Rother, P. Shane, P. Strong, P. Suggate, J. Thomson, P. Tonkin, N. Trustrum, R. Van Dissen, C. Vucetich, J. Wilmshurst, C. Woodward, and A. Zondervan. Towards a climate event stratigraphy for new zealand over the past 30 000 years (nz-intimate project). *Journal of Quaternary Science*, 22(1):9–35, 2007. 24, 62, 63, 64, 66, 76

P. J. Applegate, T. V. Lowell, and R. B. Alley. Comment on "absence of cooling in new zealand and the adjacent ocean during the younger dryas chronozone". *Science*, 320(5877), 2008. 69

B. Ataie-Ashtiani and G. Shobeyri. Numerical simulation of landslide impulsive waves by incompressible smoothed particle hydrodynamics. *International Journal for Numerical Methods in Fluids*, 56(2):209–32, 2008. 230, 234

P. C. Augustinus. The influence of rock mass strength on glacial valley cross-profile morphometry: a case study from the southern alps, new zealand. *Earth Surface Processes and Landforms*, 17(1):39–51, 1992. 12

P. C. Augustinus. Glacial valley cross-profile development: the influence of in situ rock stress and rock mass strength, with examples from the southern alps, new zealand. *Geomorphology*, 14(2):87–97, 1995. 4, 33, 220

A. Aydin. Isrm suggested method for determination of the schmidt hammer rebound hardness: Revised version. *International Journal of Rock Mechanics and Mining Sciences*, 46(3):627–34, 2009. 118

G. Balco, J. O. Stone, N. A. Lifton, and T. J. Dunai. A complete and easily accessible means of calculating surface exposure ages or erosion rates from 10be and 26al measurements. *Quaternary Geochronology*, 3(3):174–95, 2008. 98, 136, 139, 151

C. K. Ballantyne, D. McCarroll, A. Nesje, and S. O. Dahl. Periglacial trimlines, former nunataks and the altitude of the last ice sheet in wester ross,

northwest scotland. *Journal of Quaternary Science*, 12(3):225–38, 1997. 33

J. L. Bamber, R. E. M. Riva, B. L. A. Vermeersen, and A. M. Lebrocq. Reassessment of the potential sea-level rise from a collapse of the west antarctic ice sheet. *Science*, 324(5929):901–03, 2009. 63

P. Barnes and R. A. Pickrill. The new zealand fiords: environmental changes since the last glacial maximum, December, 2003 2003. 61, 82

P. Barnes and R. A. Pickrill. New zealand fiords: Environmental changes since the last glacial maximum, unpublished. 61, 62, 72, 75, 76, 77, 78, 80, 81, 82, 83, 84, 85, 86, 87, 88, 89, 90, 91, 92, 94, 139, 175, 181, 184, 185, 191

P. M. Barnes. Postglacial (after 20 ka) dextral slip rate of the offshore alpine fault, new zealand. *Geology*, 37(1):3–6, 2009. 4, 20, 24, 26, 49, 61, 64, 66, 71, 75, 76, 83, 88, 90, 92, 138, 169, 170, 176, 192

P. M. Barnes, R. Sutherland, B. Davy, and J. Delteil. Rapid creation and destruction of sedimentary basins on mature strike-slip faults: An example from the offshore alpine fault, new zealand. *Journal of Structural Geology*, 23(11):1727–39, 2001. 4

P.M. Barnes, R. Sutherland, and J. Delteil. Strike-slip structure and sedimentary basins of the southern alpine fault, fiordland, new zealand. *Bulletin of the Geological Society of America*, 117(3-4):411–35, 2005. 4, 17, 20

P.M. Barnes, H. Bostock, H. Neil, L. Strachan, and M. Gosling. A 2300-year paleoearthquake record of the southern alpine fault and fiordland subduction zone, new zealand, based on stacked turbidites. *Bulletin of the Geological Society of America*, submitted, 2012. 225, 226, 228, 229

D. J. A. Barrell. Quaternary glaciers of new zealand. In J. Ehlers, P.L. Gibbard, and P.D. Hughes, editors, *Developments in Quaternary Science*, volume 15 of *Quaternary Glaciations - extent and chronology*, pages 1047–64. Elsevier, Amsterdam, 2011. 24, 25, 61, 67, 68, 70, 75, 76

T. T. Barrows, S. J. Lehman, L. K. Fifield, and P. De Deckker. Absence of cooling in new zealand and the adjacent ocean during the younger dryas chronozone. *Science*, 318(5847):86–89, 2007. 69, 98

N.C. Barth, C. J. Boulton, B.M. Carpenter, G.E. Batt, and V.G. Toy. Nature and timing of slip localization on the southern alpine fault, new zealand. *Tectonics*, submitted. 216

M.R. Bennett and N. F. Glasser. *Glacial Geology - Ice Sheets and Landforms*. John Wiley and Sons Ltd., Chichester, England, 1996. 26, 178, 179

K. Berryman. Review of tsunami hazard and risk in new zealand. Technical report, Institute of Geological and Nuclear Sciences Ltd., 2005. 54, 56, 57

K. Berryman, A. Cooper, R. Norris, P. Villamor, R. Sutherland, T. Wright, E. Schermer, R. Langridge, and G. Biasi. Late holocene rupture history of the alpine fault in south westland, new zealand. *Bulletin of the Seismological Society of America*, 102(2):620–38, 2012a. 20, 199

K. R. Berryman, S. Beanland, A. F. Cooper, H. N. Cutten, R. J. Norris, and P. R. Wood. The alpine fault, new zealand: variation in quaternary structural style and geomorphic expression. *Annales Tectonicae*, 6(Suppl.):126–63, 1992. 17

K. R. Berryman, U. A. Cochran, K. J. Clark, G. P. Biasi, R. M. Langridge, and P. Villamor. Major earthquakes occur regularly on an isolated plate boundary fault. *Science*, 336(6089):1690–93, 2012b. 4, 23, 138, 199, 225, 226, 227, 228, 229

R. Bhasin, A. Kaynia, L.H. Blikra, A. Braathen, and E. Anda. Insights into the deformation mechanisms of a jointed rock slope subjected to dynamic loading. *International Journal of Rock Mechanics and Mining Sciences*, 41(SUPPL. 1), 2004. 232

L. H. Blikra, O. Longva, C. B. Harbitz, and F. Lovholt. Quantification of rock-avalanche and tsunami hazard in storfjorden, western norway. In K. Senneset, K. Flaate, and J.O. Larsen, editors, *Landslides and avalanches, ICFL 2005, Norway*, pages 57–64. Taylor and Francis Group, London, 2005. 223, 225, 243, 247, 261

L.H. Blikra, A. Braathen, E. Anda, K. Stalsberg, and O. Longva. Rock avalanches, gravitational bedrock fractures and neotectonic faults, onshore northern west norway: Examples, regional distribution and triggering mechanisms, 2002. 6, 198, 200

T. Blunier, J. Schwander, B. Stauffer, T. Stocker, A. Dllenbach, A. Indermhle, J. Tschumi, J. Chappellaz, D. Raynaud, and J. M. Barnola. Timing of the antarctic cold reversal and the atmospheric co2 increase with respect to the younger dryas event. *Geophysical Research Letters*, 24(21):2683–86, 1997. 63, 64

B.D. Bornhold, R.E. Thomson, A.B. Rabinovich, E.A. Kulikov, and I.V. Fine. Risk of lanslide-generated tsunamis for the coast of british columbia and alaska. *2001 An Earth Odyssey*, 2001. 54

A. Braathen, L.H. Blikra, S.S. Berg, and F. Karlsen. Rock-slope failures in norway; type, geometry, deformation mechanisms and stability. *Norsk Geologisk Tidsskrift*, 84(1):67–88, 2004. 57, 200

J. W. Brodie and J. Irwin. Morphology and sedimentation in lake wakatipu, new zealand. *N.Z. Journal of Marine and Freshwater Research*, 4(4):479–96, 1970. 54

J.W. Brodie. The fiordland shelf and milford sound. In T. M. Skerman, editor, *Studies of a Southern Fiord*, volume Res. 157 Mem. N.Z. Oceanogr. Inst. 17. Dep. scient. industr., 1964. 54

C. S. Brown, M. F. Meier, and A. Post. Calving speed of alaska tidewater glaciers, with application to columbia glacier. *US Geological Survey Professional Paper*, 1258 C, 1983. 176

T. E. Bunch, R. E. Hermes, A. M. T. Moore, D. J. Kennett, J. C. Weaver, J. H. Wittke, P. S. DeCarli, J. L. Bischoff, G. C. Hillman, G. A. Howard, D. R. Kimbel, G. Kletetschka, C. P. Lipo, S. Sakai, Z. Revay, A. West, R. B. Firestone, and J. P. Kennett. Very high-temperature impact melt products as evidence for cosmic airbursts and impacts 12,900 years ago. *Proceedings of the National Academy of Sciences of the United States of America*, 109(28):E1903–E12, 2012. 64

G. Chevalier, T. Davies, and M. McSaveney. The prehistoric mt wilberg rock avalanche, westland, new zealand. *Landslides*, 6(3):253–62, 2009. 40

J. J. Clague. Glacio-isostatic effects of the cordilleran ice-sheet, british columbia, canada. In D.E. Smith and A.G. Dawson, editors, *Shorelines and Isostasy*, pages 321–43. Academic Press, London, 1983. 74

J. J. Clague and S. G. Evans. Formation and failure of natural dams in the canadian cordillera. *Bulletin - Geological Survey of Canada*, 464, 1994. 40

P. U. Clark, A. S. Dyke, J. D. Shakun, A. E. Carlson, J. Clark, B. Wohlfarth, J. X. Mitrovica, S. W. Hostetler, and A. M. McCabe. The last glacial maximum. *Science*, 325(5941):710–14, 2009. 24, 62, 63, 64

A.L. Claypool, K.A. Klepeis, B. Dockrill, G.L. Clarke, H. Zwingmann, and A. Tulloch. Structure and kinematics of oblique continental convergence in northern fiordland, new zealand. *Tectonophysics*, 359(3-4):329–58, 2002. 15, 17, 49

G. S. Collins and H. J. MeLosh. Acoustic fluidization and the extraordinary mobility of sturzstroms. *Journal of Geophysical Research B: Solid Earth*, 108(10):EPM 4–1 – EPM 4–14, 2003. 35, 36, 37, 42

J. Columbus, P. Sirguey, and R. Tenzer. A free fully assessed 15 metre digital elevation model for new zealand. *Survey Quarterly*, (66):16–19, 2011. 101

D.H. Cornforth and J.A. Lowell. The 1994 submarine slope failure at skagway, alaska. In Balkema and Rotterdam, editors, *Landslides*, pages 527–32. 1996. 201

C. H. Costa and E. F. G. Daz. Age constraints and paleoseismic implication of rock avalanches in the northern patagonian andes, argentina. *Journal of South American Earth Sciences*, 24(1):48–57, 2007. 40

S. C. Cox and R. H. Findlay. The main divide fault zone and its role in formation of the southern alps, new zealand. *New Zealand Journal of Geology and Geophysics*, 38(4):489–99, 1995. 49

M.J. Crozier. Landslides - people and landslides, 2009. 45

D. M. Cruden. Major rock slides in the rockies. *Canadian Geotechnical Journal*, 13(1):8–20, 1976. 34

D. M. Cruden and D.J Varnes. Landslide types and processes. In A.K. Turner Schuster and R.L., editors, *Landslides: Investigation and Mitigation*, pages 36–75. Natl. Acad. Press, Washington, D.C., 1996. 28, 29, 38

BIBLIOGRAPHY

R. Dahl. Post-glacial micro-weathering of bedrock surfaces in the narvik district of norway. *Geografiska Annaler, Series A: Physical Geography*, 49A(2-4):155–66, 1967. 142

M. C. R. Davies, O. Hamza, and C. Harris. The effect of rise in mean annual temperature on the stability of rock slopes containing ice-filled discontinuities. *Permafrost and Periglacial Processes*, 12(1):137–44, 2001. 33

T. Davies, M. McSaveney, and K. Kelfoun. Runout of the socompa volcanic debris avalanche, chile: A mechanical explanation for low basal shear resistance. *Bulletin of Volcanology*, 72(8):933–44, 2010. 29, 37

T. R. Davies and M. J. McSaveney. The role of rock fragmentation in the motion of large landslides. *Engineering Geology*, 109(1-2):67–79, 2009. 29, 42, 43

T. R. Davies, M. J. McSaveney, and K. A. Hodgson. A fragmentation-spreading model for long-runout rock avalanches. *Canadian Geotechnical Journal*, 36(6):1096–110, 1999. 207

T. R. Davies, M. J. McSaveney, and A. M. Deganutti. Dynamic rock fragmentation causes low rock-on-rock friction. In *Proceedings of the 1st Canada-US Rock Mechanics Symposium - Rock Mechanics Meeting Society's Challenges and Demands*, volume 2, pages 959–66, 2007. 37

T.R. Davies and M.J. McSaveney. Dynamic simulation of the motion of fragmenting rock avalanches. *Canadian Geotechnical Journal*, 39(4):789–98, 2002. 29, 36, 37, 42, 43, 232

T.R. Davies, M.J. McSaveney, and R.D. Beetham. Rapid block glides: Slide-surface fragmentation in new zealand's waikaremoana landslide. *Quarterly Journal of Engineering Geology and Hydrogeology*, 39(2):115–29, 2006. 37, 40

G.P. De Pascale and R.M. Langridge. New on-fault evidence for a great earthquake in a.d. 1717, central alpine fault, new zealand, 2012. 4, 20, 23, 199

A. L. Densmore, R. S. Anderson, B. G. McAdoo, and M. A. Ellis. Hillslope evolution by bedrock landslides. *Science*, 275(5298):369–72, 1997. 29

G. H. Denton and C. H. Hendy. Younger dryas age advance of franz josef glacier in the southern alps of new zealand. *Science*, 264(5164):1434–37, 1994. 64, 67

M. Di Risio and P. Sammarco. Analytical modeling of landslide-generated waves. *Journal of Waterway, Port, Coastal and Ocean Engineering*, 134 (1):53–60, 2008. 57, 230, 234, 237

R.G. Ditchburn and W.J. McCabe. Sedimentation rates of lake pukaki. Technical Report INS-R-238, Institute of Nuclear Sciences, 1977. 79

D.O.C. Regional economic impacts of fiordland national park, 2006. 58, 252

G. Downes, U. Cochran, L. Wallace, M. Reyners, K. Berryman, R. Walters, F. Callaghan, P. Barnes, and R. Bell. Understanding local tsunami sources: 1820s southland tsunami. Technical Report EQC04201, GNS Science, 2005. 55, 56, 57, 202

A. Dufresne and T. R. Davies. Longitudinal ridges in mass movement deposits. *Geomorphology*, 105 (3-4):171–81, 2009. 39, 40

A. Dufresne, T. R. Davies, and M. J. McSaveney. Influence of runout-path material on emplacement of the round top rock avalanche, new zealand. *Earth Surface Processes and Landforms*, 35(2):190–201, 2010. 29

Tibor Dunai. *Cosmogenic Nuclides*, volume 1 of *Principals, Concepts and Applications in the Earth Surface Sciences*. Cambridge University Press, 2010. 99

S. A. Dunning. The morphologies and sedimentology of valley confined rock-avalanche deposits and their effect on potential dam hazardq. In O. Hungr, R. Fell, R. Couture, and E. Eberhardt, editors, *Landslide Risk Management*, pages 691–704. A.T. Balkema, Amsterdam, 2005. 38

S. A. Dunning, N. J. Rosser, D. N. Petley, and C. R. Massey. Formation and failure of the tsatichhu landslide dam, bhutan. *Landslides*, 3(2):107–13, 2006. 40, 41

R. Dykes, M. Brook, C. Robertson, and I. Fuller. Twenty-first century calving retreat of tasman glacier, southern alps, new zealand. *Arctic,*

Antarctic, and Alpine Research, 43(1):1–10, 2011. 176

E. Eberhardt, D. Stead, and J.S. Coggan. Numerical analysis of initiation and progressive failure in natural rock slopes-the 1991 randa rockslide. *International Journal of Rock Mechanics and Mining Sciences*, 41(1):69–87, 2004. 198

D. Eberhart-Phillips, P. J. Haeussler, J. T. Freymueller, A. D. Frankel, C. M. Rubin, P. Craw, N. A. Ratchkovski, G. Anderson, G. A. Carver, A. J. Crone, T. E. Dawson, H. Fletcher, R. Hansen, E. L. Harp, R. A. Harris, D. P. Hill, S. Hreinsdttir, R. W. Jibson, L. M. Jones, R. Kayen, D. K. Keefer, C. F. Larsen, S. C. Moran, S. F. Personius, G. Plafker, B. Sherrod, K. Sieh, N. Sitar, and W. K. Wallace. The 2002 denali fault earthquake, alaska: A large magnitude, slip-partitioned event. *Science*, 300(5622):1113–18, 2003. 33

U. M. Eidsvig, Z. Medina-Cetina, V. Kveldsvik, S. Glimsdal, C. B. Harbitz, and F. Sandersen. Risk assessment of a tsunamigenic rockslide at knes. *Natural Hazards*, 56(2):529–45, 2011. 6, 199, 237, 238, 247, 248, 249, 250, 260, 261

F. Enet and T. Grilli. Experimental study of tsunami generation by three-dimensional rigid underwater landslides. *Journal of Waterway, Port, Coastal and Ocean Engineering*, 133(6):442–54, 2007. 230

U.S. Army Corps of Engineers. Sea-level change considerations for civil works programs, 2011. 267

S. G. Evans and J. J. Clague. Catastrophic rock avalanches in glacial environments. In C Bonnard, editor, *5th International Symposium on Landslides*, volume 2, pages 1153–58, Lausanne, Switzerland, 1988. 27, 33, 34

S. G. Evans and J. J. Clague. Recent climatic change and catastrophic geomorphic processes in mountain environments. *Geomorphology*, 10(1-4):107–28, 1994. 33

S. G. Evans, J. J. Clague, G. J. Woodsworth, and O. Hungr. The pandemonium creek rock avalanche, british columbia. *Canadian Geotechnical Journal*, 26(3):427–46, 1989. 34, 44

S. G. Evans, O. Hungr, and E. G. Enegren. The avalanche lake rock avalanche, mackenzie mountains, northwest territories, canada: description, dating, and dynamics. *Canadian Geotechnical Journal*, 31(5):749–68, 1994. 40

S. G. Evans, O. Hungr, and J. J. Clague. Dynamics of the 1984 rock avalanche and associated distal debris flow on mount cayley, british columbia, canada; implications for landslide hazard assessment on dissected volcanoes. *Engineering Geology*, 61(1):29–51, 2001. 43, 44

S. G. Evans, N. F. Bishop, L. Fidel Smoll, P. Valderrama Murillo, K. B. Delaney, and A. Oliver-Smith. A re-examination of the mechanism and human impact of catastrophic mass flows originating on nevado huascarn, cordillera blanca, peru in 1962 and 1970. *Engineering Geology*, 108(1-2):96–118, 2009a. 32

S. G. Evans, N. J. Roberts, A. Ischuk, K. B. Delaney, G. S. Morozova, and O. Tutubalina. Landslides triggered by the 1949 khait earthquake, tajikistan, and associated loss of life. *Engineering Geology*, 109(3-4):195–212, 2009b. 33

S.G. Evans and J.V DeGraff. *Catastrophic landslides: effects, occurrence, and mechanisms.*, volume XV. Geological Society of America Reviews in Engineering Geology, Boulder, Colorado, 2002. 28, 32, 249

U.K. Health Executive and Safety. The tolerability of risk from nuclear power stations, 1992. 261

R. G. Fairbanks. A 17,000-year glacio-eustatic sea level record: Influence of glacial melting rates on the younger dryas event and deep-ocean circulation. *Nature*, 342(6250):637–42, 1989. 71, 74, 75

D. L. Farber, A. S. Mriaux, and R. C. Finkel. Attenuation length for fast nucleon production of 10be derived from near-surface production profiles. *Earth and Planetary Science Letters*, 274(3-4):295–300, 2008. 136

C. Fauth, G. Kaye, M. Hollis, D. Richter, and T Wilson. Kaikoura district tsunami hazard: Transport corridor, warning and evacuation, economic risk, submarine dredging, and public risk awareness/eduction. Technical report, University of Canterbury, 2005. 54

R. B. Firestone, A. West, J. P. Kennett, L. Becker, T. E. Bunch, Z. S. Revay, P. H. Schultz, T. Belgya, D. J. Kennett, J. M. Erlandson, O. J. Dickenson, A. C. Goodyear, R. S. Harris, G. A. Howard, J. B.

BIBLIOGRAPHY

Kloosterman, P. Lechler, P. A. Mayewski, J. Montgomery, R. Poreda, T. Darrah, S. S. Que Hee, A. R. Smitha, A. Stich, W. Topping, J. H. Wittke, and W. S. Wolbach. Evidence for an extraterrestrial impact 12,900 years ago that contributed to the megafaunal extinctions and the younger dryas cooling. *Proceedings of the National Academy of Sciences of the United States of America*, 104(41): 16016–21, 2007. 64

S.J. Fitzsimons and H. Veit. Geology and geomorphology of the european alps and the southern alps of new zealand: A comparison. *Mountain Research and Development*, 21(4):340–49, 2001. 12, 13, 15

K. Fleming, P. Johnston, D. Zwartz, Y. Yokoyama, K. Lambeck, and J. Chappell. Refining the eustatic sea-level curve since the last glacial maximum using far- and intermediate-field sites. *Earth and Planetary Science Letters*, 163(1-4):327–42, 1998. 71, 75, 138, 193

H. M. Fritz. Initial phase of landslide generated impulse waves. *Mitteilungen der Versuchsanstalt fur Wasserbau, Hydrologie und Glaziologie an der Eidgenossischen Technischen Hochschule Zurich*, (178):1–253, 2002. 230, 231, 233, 234, 244

H. M. Fritz, W. H. Hager, and H. E. Minor. Landslide generated impulse waves. 2. hydrodynamic impact craters. *Experiments in Fluids*, 35(6):520–32, 2003. 232

H. M. Fritz, F. Mohammed, and J. Yoo. Lituya bay landslide impact generated mega-tsunami 50th anniversary. *Pure and Applied Geophysics*, 166(1-2): 153–75, 2009. 57, 231, 234, 236

H.M. Fritz, W.H. Hager, and H.E. Minor. Near field characteristics of landslide generated impulse waves. *Journal of Waterway, Port, Coastal and Ocean Engineering*, 130(6):287–302, 2004. 57, 201, 230

M. Geertsema, J. J. Clague, J. W. Schwab, and S. G. Evans. An overview of recent large catastrophic landslides in northern british columbia, canada. *Engineering Geology*, 83(1-3):120–43, 2006. 27, 34

G. R. Gisler. Tsunami simulations, 2008. 230, 234

G.P. Glasby. Fiord studies: Caswell and nancy sounds, new zealand. *Memoirs, NZ Oceanographic Institute*, 79:94, 1978. 78, 80, 87

N. F. Glasser and M. C. Ghiglione. Structural, tectonic and glaciological controls on the evolution of fjord landscapes. *Geomorphology*, 105(3-4):291–302, 2009. 72

H. Glicken. The rockslide-debris avalanche of the may 18, 1980, eruption of mount st. helens - 10th anniversary perspectives. *Geoscience Canada*, 17(3): 150–53, 1990. 28

G.N.S. Historic earthquakes, 26 April, 2012 . 20

J. Goguel. Scale-dependent rockslide mechanisms, with amphasis on the role of pore fluid vaporization. In B. Voight, editor, *Developments in Geotechnical Engineering*, volume 14a of *Rockslides and Avalanches, 1, Natural Phenomena*, pages 693–705. Elsevier, 1978. 42

N. R. Golledge, A. N. Mackintosh, B. M. Anderson, K. M. Buckley, A. M. Doughty, D. J. A. Barrell, G. H. Denton, M. J. Vandergoes, B. G. Andersen, and J. M. Schaefer. Last glacial maximum climate in new zealand inferred from a modelled southern alps icefield. *Quaternary Science Reviews*, 46:30–45, 2012. 67

N. Gomez, J. X. Mitrovica, M. E. Tamisiea, and P. U. Clark. A new projection of sea level change in response to collapse of marine sectors of the antarctic ice sheet. *Geophysical Journal International*, 180 (2):623–34, 2010. 63

J. C. Gosse and F. M. Phillips. Terrestrial in situ cosmogenic nuclides: Theory and application. *Quaternary Science Reviews*, 20(14):1475–560, 2001. 95, 98, 99, 134, 139, 140, 141, 147

K.R. Grange and R.J. Singleton. Population structure of black coral, antipathes aperta, in the southern fiords of new zealand. *N.Z. Journal of Zoology*, 15: 481–89, 1988. 87

G.A. Griffiths and M.J. McSaveney. Distribution of mean annual precipitation across some steepland regions of new zealand (southern alps). *New Zealand Journal of Science*, 26(2):197–209, 1983. 10

S. T. Grilli and P. Watts. Tsunami generation by submarine mass failure. i: Modeling, experimental validation and sensitivity analyses. *Journal of Waterway, Port, Coastal and Ocean Engineering*, 131(6):283–97, 2005. 236

J. Grindley, A. Pepper, P. Woodmansey, and G. Webby. Cleddau village development natural hazards risk assessment. prepared for the department of conservation. Technical report, Opus International Consultants Ltd., 2007. 56

J. E. Gutsell, J. J. Clague, M. E. Best, P. T. Bobrowsky, and I. Hutchinson. Architecture and evolution of a fjord-head delta, western vancouver island, british columbia. *Journal of Quaternary Science*, 19(5):497–511, 2004. 74

G. T. Hancox and N. D. Perrin. Green lake landslide and other giant and very large postglacial landslides in fiordland, new zealand. *Quaternary Science Reviews*, 28(11-12):1020–36, 2009. 7, 48, 49, 51, 52, 94, 198, 203, 214

G. T. Hancox, N. D. Perrin, and G. D. Dellow. Recent studies of historical earthquake-induced landsliding, ground damage, and mm intensity in new zealand. *Bulletin of the New Zealand Society for Earthquake Engineering*, 35(2):59–95, 2002. 20, 45, 198, 199

G.T. Hancox. Landslide and ground damage caused by earthquakes. *Tephra*, June, 1998:15–20, 1998. 199

G.T. Hancox and N.D. Perrin. Green lake landslide: a very large ancient rock slide in fiordland, new zealand. In R. Oliveira, L.F. Rodrigues, A.G. Ceolho, and A.P. Cunha, editors, *Proceedings of the seventh international congress of International Association of Engineering Geology*, pages 1677–89. Lisboa, 1994. 48, 198

G.T. Hancox, S.C. Cox, I.M. Turnbull, and M.J. Crozier. Reconnaissance studies of landslides and other ground damage caused by the mw 7.2 fiordland earthquake of 22 august 2003, 2003. 20, 34, 45, 48, 49, 54, 55, 186, 202, 257

G.T. Hancox, M.J. McSaveney, V.R. Manville, and T.R. Davies. The october 1999 mt adams rock avalanche and subsequent landslide dam-break flood and effects in poerua river, westland, new zealand. *New Zealand Journal of Geology and Geophysics*, 48(4):683–705, 2005. 34, 41, 42

C. B. Harbitz, G. Pedersen, and B. Gjevic. Numerical simulation of large water waves due to landslides. *Journal of Hydraulic Engineering*, 119(12):1325–42, 1993. 234, 239, 247, 262

C. B. Harbitz, F. Lvholt, G. Pedersen, and D. G. Masson. Mechanisms of tsunami generation by submarine landslides: A short review. *Norsk Geologisk Tidsskrift*, 86(3):255–64, 2006. 57, 200, 237

C. Harris, L. U. Arenson, H. H. Christiansen, B. Etzelmller, R. Frauenfelder, S. Gruber, W. Haeberli, C. Hauck, M. Hlzle, O. Humlum, K. Isaksen, A. Kb, M. A. Kern-Ltschg, M. Lehning, N. Matsuoka, J. B. Murton, J. Ntzli, M. Phillips, N. Ross, M. Seppl, S. M. Springman, and D. Vonder Mhll. Permafrost and climate in europe: Monitoring and modelling thermal, geomorphological and geotechnical responses. *Earth-Science Reviews*, 92(3-4): 117–71, 2009. 33

A. Heim. *Bergsturz und Menschenleben.* Fretz und Wasmuth Verlag, Zurich, 1932. 29, 35, 40

R.L. Hermanns, L.H. Blikra, M. Naumann, B. Nilsen, K.K. Panthi, D. Stromeyer, and O. Longva. Examples of multiple rock-slope collapses from kfels (tz valley, austria) and western norway. *Engineering Geology*, 83(1-3):94–108, 2006. 200, 232, 233, 242

K. Hewitt, J. J. Clague, and J. F. Orwin. Legacies of catastrophic rock slope failures in mountain landscapes. *Earth-Science Reviews*, 87(1-2):1–38, 2008. 4, 27, 29, 30, 32, 33, 34, 37, 38, 40, 41, 42, 44, 48

K. Hewitt, J. Gosse, and J. J. Clague. Rock avalanches and the pace of late quaternary development of river valleys in the karakoram himalaya. *Bulletin of the Geological Society of America*, 123 (9-10):1836–50, 2011. 30, 38

D. M. Hicks, J. Hill, and U. Shankar. Variation of suspended sediment yields around new zealand: The relative importance of rainfall and geology. *IAHS-AISH Publication*, 236:149–56, 1996. 12, 13

M Hicks, U Shankar, and A McKerchar. Sediment yield estimates: a gis tool. *NIWA Water and Atmosphere*, 11(4), 2003. 12

D. Hillel. *Fundamentals of Soil Physics.* Academic Press, New York, 1980. 147

J.A. Hollis, G.L. Clarke, K.A. Klepeis, N.R. Daczko, and T.R. Ireland. Geochronology and geochemistry of high-pressure granulites of the arthur river

complex, fiordland, new zealand: Cretaceous magmatism and metamorphism on the palaeo-pacific margin. *Journal of Metamorphic Geology*, 21(3): 299–313, 2003. 15, 17, 19

J.T. Holloway. Forests and climates in the south island of new zealand, 1954. 14, 87, 188

M. A. House, M. Gurnis, P. J. J. Kamp, and R. Sutherland. Uplift in the fiordland region, new zealand: Implications for incipient subduction. *Science*, 297(5589):2038–41, 2002. 139

N. Hovius, C. P. Stark, and P. A. Allen. Sediment flux from a mountain belt derived by landslide mapping. *Geology*, 25(3):231–34, 1997. 45, 48, 49, 223

K.J. Hsu. Albert heim: observations on landslides and relevance to modern interpretations. In B. Voight, editor, *Rockslides and Avalanches; 1, Natural Phenomena*, pages 70–93. Elsevier, Amsterdam, 1978. 29

A. Huber and W. K. Hager. Forecasting impulse waves in reservoirs. Technical Report Rep. XIX, 1997. 230, 234

C. Huggel, J. J. Clague, and O. Korup. Is climate change responsible for changing landslide activity in high mountains? *Earth Surface Processes and Landforms*, 37(1):77–91, 2012. 33

O. Hungr, S.G. Evans, and J. Hazzard. Magnitude and frequency of rock falls and rock slides along the main transportation corridors of southwestern british columbia. *Canadian Geotechnical Journal*, 36(2):224–38, 1999. 29, 222, 223, 224, 225

O. Hungr, S. G. Evans, M. J. Bovis, and J. N. Hutchinson. A review of the classification of landslides of the flow type. *Environmental and Engineering Geoscience*, 7(3):221–38, 2001. 28, 29

J. N. Hutchinson. Mass movement. In R.W. Fairbridge, editor, *Encylopedia of Geomorphology*, pages 688–95. Reinhold Publishers, New York, 1968. 28

F. Imamura and K. Hashi. Re-examination of the source mechanism of the 1998 papua new guinea earthquake and tsunami. *Pure and Applied Geophysics*, 160(10-11):2071–86, 2003. 53, 236

S. Ivy-Ochs, C. Schlchter, P. W. Kubik, and G. H. Denton. Moraine exposure dates imply synchronous younger dryas glacier advances in the european alps and in the southern alps of new zealand. *Geografiska Annaler, Series A: Physical Geography*, 81(2):313–23, 1999. 70

T. James, E. J. Gowan, I. Hutchinson, J. J. Clague, J. V. Barrie, and K. W. Conway. Sea-level change and paleogeographic reconstructions, southern vancouver island, british columbia, canada. *Quaternary Science Reviews*, 28(13-14):1200–16, 2009. 74, 75

R. W. Jibson, E. L. Harp, W. Schulz, and D. K. Keefer. Large rock avalanches triggered by the m 7.9 denali fault, alaska, earthquake of 3 november 2002. *Engineering Geology*, 83(1-3):144–60, 2006. 33

M.W. Johns, D.B. Prior, B.D. Bornhold, J.M. Coleman, and W.R. Bryant. Geotechnical aspects of a submarine slope failure, kitimat fjord, british columbia (canada). *Marine Geotechnology*, 6(3): 243–79, 1986. 201

F. Jorstad. Waves generated by landslides in norwegian fjords and lakes. *Norwegian Geotechnical Institute Publication*, 79:13–32, 1968. 6, 57, 199, 200, 233, 242, 244, 249

P.J.J. Kamp, P.F. Green, and S.H. White. Fission track analysis reveals character of collisional tectonics in new zealand. *Tectonics*, 8(2):169–95, 1989. 15

J.W. Kamphuis and J. Bowering. Impulse waves generated by landslides. *Proceedings of the 12th Coastal Engineering Conference, ASCE: New York.*, 1:575–88, 1972. 230, 234

M. R. Kaplan, J. A. Strelin, J. M. Schaefer, G. H. Denton, R. C. Finkel, R. Schwartz, A. E. Putnam, M. J. Vandergoes, B. M. Goehring, and S. G. Travis. In-situ cosmogenic 10be production rate at lago argentino, patagonia: Implications for late-glacial climate chronology. *Earth and Planetary Science Letters*, 309(1-2):21–32, 2011. 98

D. K. Keefer. Landslides caused by earthquakes. *Geological Society of America Bulletin*, 95(4):406–21, 1984. 33

K. Kelfoun and T. H. Druitt. Numerical modeling of the emplacement of socompa rock avalanche, chile. *Journal of Geophysical Research B: Solid Earth*, 110(12):1–13, 2005. 36

K. Kelfoun, T. Druitt, B. van Wyk de Vries, and M. N. Guilbaud. Topographic reflection of the socompa debris avalanche, chile. *Bulletin of Volcanology*, 70(10):1169–87, 2008. 37

K. J. Kim and R. Sutherland. Uplift rate and landscape development in southwest fiordland, new zealand, determined using ¡sup¿10¡/sup¿be and ¡sup¿26¡/sup¿al exposure dating of marine terraces. *Geochimica et Cosmochimica Acta*, 68(10): 2313–19, 2004. 12, 17, 23, 49, 138

K. A. Klepeis, N. R. Daczko, and G. L. Clarke. Kinematic vorticity and tectonic significance of superposed mylonites in a major lower crustal shear zone, northern fiordland, new zealand. *Journal of Structural Geology*, 21(10):1385–405, 1999. 15

K. P. Knudson, I. L. Hendy, and H. L. Neil. Reexamining southern hemisphere westerly wind behavior: Insights from a late holocene precipitation reconstruction using new zealand fjord sediments. *Quaternary Science Reviews*, 30(21-22):3124–38, 2011. 10, 12, 61, 71, 76, 78, 92, 94, 100, 164, 225, 227, 308

O. Korup. Recent research on landslide dams - a literature review with special attention to new zealand. *Progress in Physical Geography*, 26(2): 206–35, 2002. 40

O. Korup. Geomorphic implications of fault zone weakening: Slope instability along the alpine fault, south westland to fiordland. *New Zealand Journal of Geology and Geophysics*, 47(2):257–67, 2004. 45

O. Korup. Geomorphic imprint of landslides on alpine river systems, southwest new zealand. *Earth Surface Processes and Landforms*, 30(7):783–800, 2005a. 12, 41, 198

O. Korup. Distribution of landslides in southwest new zealand. *Landslides*, 2(1):43–51, 2005b. 4, 7, 23, 26, 48, 49, 94, 198, 209, 222, 259

O. Korup. Large landslides and their effect on sediment flux in south westland, new zealand. *Earth Surface Processes and Landforms*, 30(3):305–23, 2005c. 41, 48, 198

O. Korup and J. J. Clague. Natural hazards, extreme events, and mountain topography. *Quaternary Science Reviews*, 28(11-12):977–90, 2009. 48

O. Korup, M.J. McSaveney, and T. R. Davies. Sediment generation and delivery from large historic landslides in the southern alps, new zealand. *Geomorphology*, 61(1-2):189–207, 2004. 12, 15, 48

O. Korup, A.L. Strom, and J.T. Weidinger. Fluvial response to large rock-slope failures: Examples from the himalayas, the tien shan, and the southern alps in new zealand. *Geomorphology*, 78 (1-2):3–21, 2006. 40

O. Korup, D. R. Montgomery, and K. Hewitt. Glacier and landslide feedbacks to topographic relief in the himalayan syntaxes. *Proceedings of the National Academy of Sciences of the United States of America*, 107(12):5317–22, 2010. 44

N. Le Corvec. *Socompa Volcano destabilisation (Chile) and debris avalanches*. PhD thesis, Blaise Pascal University, 2005. 37

J. Lee, T. Davies, and D. Bell. Successive holocene rock avalanches at lake coleridge, canterbury, new zealand. *Landslides*, 6(4):287–97, 2009. 33

T. Lee, W. R. Hobbs, J. K. Willis, D. Halkides, I. Fukumori, E. M. Armstrong, A. K. Hayashi, W. T. Liu, W. Patzert, and O. Wang. Record warming in the south pacific and western antarctica associated with the strong central-pacific el nio in 2009-10. *Geophysical Research Letters*, 37 (19), 2010. 10

F. Legros. The mobility of long-runout landslides. *Engineering Geology*, 63(3-4):301–31, 2002. 42

R. A. B. Leschen, T. R. Buckley, H. M. Harman, and J. Shulmeister. Determining the origin and age of the westland beech (nothofagus) gap, new zealand, using fungus beetle genetics. *Molecular Ecology*, 17 (5):1256–76, 2008. 14

Y. Li and F. Raichlen. Solitary wave runup on plane slopes. *Journal of Waterway, Port, Coastal and Ocean Engineering*, 127(1):33–44, 2001. 56

N. A. Lifton, J. W. Bieber, J. M. Clem, M. L. Duldig, P. Evenson, J. E. Humble, and R. Pyle. Addressing solar modulation and long-term uncertainties

in scaling secondary cosmic rays for in situ cosmogenic nuclide applications. *Earth and Planetary Science Letters*, 239(1-2):140–61, 2005. 136, 151

J. G. Liu, P. J. Mason, E. Yu, M. C. Wu, C. Tang, R. Huang, and H. Liu. Gis modelling of earthquake damage zones using satellite remote sensing and dem data. *Geomorphology*, 139-140:518–35, 2012. 33

P. Lynett and P. L. F. Liu. A numerical study of the run-up generated by three-dimensional landslides. *Journal of Geophysical Research C: Oceans*, 110 (3):1–16, 2005. 57, 237

M. Mabin and C. Tipler. Milford village tsunami hazard: a review. prepared for the department of conservation. Technical report, URS New Zealand Ltd., 2008. 56, 57

P. A. Madsen and H. A. Schaffer. Analytical solutions for tsunami runup on a plane beach: Single waves, n-waves and transient waves. *Journal of Fluid Mechanics*, 645:27–57, 2010. 237

A.F. Mark. Te waahipounamu: South-west new zealand world heritage area. ecological research and conservation history. *Journal of the Royal Society of New Zealand*, 28(4):657–84, 1998. 12, 142

W.H. Mathews. Profiles of late pleistocence glaciers in new zealand. *New Zealand Journal of Geology and Geophysics*, 10:146–63, 1967. 75

J. A. Matthews and G. Owen. Schmidt hammer exposure-age dating: Developing linear age-calibration curves using holocene bedrock surfaces from the jotunheimen-jostedalsbreen regions of southern norway. *Boreas*, 39(1):105–15, 2010. 120, 121, 157, 160

J. A. Matthews and S. Winkler. Schmidt-hammer exposure-age dating (shd): Application to early holocene moraines and a reappraisal of the reliability of terrestrial cosmogenic-nuclide dating (tcnd) at austanbotnbreen, jotunheimen, norway. *Boreas*, 40(2):256–70, 2011. 120, 157, 159, 160, 162

D. McCarroll. Potential and limitations of the schmidt hammer for relative-age dating: field tests on neoglacial moraines, jotunheimen, southern norway. *Arctic and Alpine Research*, 21(3): 268–75, 1989. 119

D. McCarroll. The schmidt hammer, weathering and rock surface roughness. *Earth Surface Processes and Landforms*, 16(5):477–80, 1991. 119

S. T. McColl and T. R. Davies. Evidence for a rock-avalanche origin for 'the hillocks' "moraine", otago, new zealand. *Geomorphology*, 127(3-4):216–24, 2011. 30, 48

S. T. McColl, T.R.H. Davies, and M.J. McSaveney. Glacier retreat and rock-slope stability: debunking debuttressing., 5-10 September, 2010 2010. 27, 34

F. G. McCormac, A. G. Hogg, P. G. Blackwell, C. E. Buck, T. F. G. Higham, and P. J. Reimer. Shcal04 southern hemisphere calibration, 0-11.0 cal kyr bp. *Radiocarbon*, 46(3):1087–92, 2004. 149, 151, 163

B.G. McFadgen, F.B. Knox, and T.R.L. Cole. Radiocarbon calibration curve variations and their implications for the interpretation of new zealand prehistory. *Radiocarbon*, 36:221–36, 1994. 308

M. S. McGlone. Plant biogeography and the late cenozoic history of new zealand. *New Zealand Journal of Botany*, 23(4):723–49, 1985. 14

M. S. McGlone, J.M. Salinger, and N.T. Moar. Paleovegetation studies of new zealand's climate since the last glacial maximum. In H.E. Wright, T-III Webb, W.F. Ruddiman, F.A. Street-Perrott, and P.J. Bartlein, editors, *Global Climates since the Last Glacial Maximum*, pages 294–317. University of Minnesota Press, Minneapolis, 1993. 61, 76

M. McSaveney. Sherman glacier rock avalanche, alaska, usa. In B Voight, editor, *Rockslides and Avalanches*, pages 197–258. Elsevier, New York, 1978. 33, 40

M. McSaveney. Recent rockfalls and rock avalanches in mount cook national park, new zealand. In S. G. Evans and J.V Degraff, editors, *Catastrophic landslides: Effects, occurrence, and mechanisms*, volume XV, pages 35–70. Geological Society of America Reviews in Engineering Geology, Boulder, Colorado, 2002. 34, 37, 45, 46, 49

M. McSaveney, T.R. Davies, and G.L. Ashby. The fatal ramsay glacier rockfall of 9 november 2002. Technical report, GNS Science, 2003/2 2003. 48

M. J. McSaveney, I. J. Graham, J. G. Begg, A. G. Beu, A. G. Hull, K. Kim, and A. Zondervan. Late holocence uplift of beach ridges at turakirae head, south wellington coast, new zealand. *New Zealand Journal of Geology and Geophysics*, 49(3):337–58, 2006. 308

G. A. Meehl, A. Hu, C. Tebaldi, J. M. Arblaster, W. M. Washington, H. Teng, B. M. Sanderson, T. Ault, W. G. Strand, and J. B. White. Relative outcomes of climate change mitigation related to global temperature versus sea-level rise. *Nature Climate Change*, 2(8):576–80, 2012. 267, 268

L. Menviel, A. Timmermann, O. E. Timm, and A. Mouchet. Climate and biogeochemical response to a rapid melting of the west antarctic ice sheet during interglacials and implications for future climate. *Paleoceanography*, 25(4), 2010. 63

D.J. Miller. Giant waves in lituya bay, alaska, 1960. 6, 31, 57, 201, 231, 233, 235, 239, 244, 249, 252

G. A. Milne, A. J. Long, and S. E. Bassett. Modelling holocene relative sea-level observations from the caribbean and south america. *Quaternary Science Reviews*, 24(10-11):1183–202, 2005. 71, 75, 138, 193

J. X. Mitrovica, N. Gomez, and P. U. Clark. The sea-level fingerprint of west antarctic collapse. *Science*, 323(5915):753, 2009. 63

M.R. Mudge. Rock avalanche and rockslide avalanche deposits at sawtooth range, montana. *Geol. Soc. Amer. Bull.*, 76:1003–14, 1965. 29

A. Najafi-Jilani and B. Ataie-Ashtiani. Estimation of near-field characteristics of tsunami generation by submarine landslide. *Ocean Engineering*, 35(5-6): 545–57, 2008. 230

D. T. Nicholson. Rock control on microweathering of bedrock surfaces in a periglacial environment. *Geomorphology*, 101(4):655–65, 2008. 142

N.I.W.A. The national climate database, 26 April, 2012 . 12

E. Noda. Water waves generated by landslides. *journal of Waterway, Port, Coastal and Ocean Engineering*, 96(4):835–55, 1970. 230, 231, 234

C. Norman. *New Zealand Timbers. Exotic and Indigenous. The complete guide.* Wright and Carman Ltd., Upper Hutt, 1990. 192

R.J. Norris and I.M. Turnbull. Cenozoic basins adjacent to an evolving transform plate boundary, southwest new zealand. In P. F. Ballance, editor, *South Pacific Sedimentary Basins*, pages 251–70. Elsevier, New York, 1993. 15, 17, 20, 49

J.F. Nye. A method of calculating the thickness of ice sheets. *Nature*, 169:529–30, 1952. 178, 179, 180

E. A. Okal, J. C. Borrero, and C. E. Synolakis. Solving the puzzle of the 1998 papua new guinea tsunami: The case for a slump. In *Solutions to Coastal Disasters 2002*, pages 863–77, 2002. 53, 236

J. F. Orwin. The application and implications of rock weathering-rind dating to a large rock avalanche, craigieburn range, canterbury, new zealand. *New Zealand Journal of Geology and Geophysics*, 41(3): 219–23, 1998. 48

G. Owen, J. A. Matthews, and P. G. Albert. Rates of holocene chemical weathering, 'little ice age' glacial erosion and implications for schmidt-hammer dating at a glacier-foreland boundary, fbergstlsbreen, southern norway. *Holocene*, 17(6): 829–34, 2007. 120

M. Paetzel and T. Dale. Climate proxies for recent fjord sediments in the inner sognefjord region, western norway, 2010. 78

A. Panizzo, P. De Girolamo, M. Di Risio, A. Maistri, and A. Petaccia. Great landslide events in italian artificial reservoirs. *Natural Hazards and Earth System Science*, 5(5):733–40, 2005a. 53, 230, 249

A. Panizzo, P. De Girolamo, and A. Petaccia. Forecasting impulse waves generated by subaerial landslides. *Journal of Geophysical Research C: Oceans*, 110(12):1–23, 2005b. 234

H.M. Pantin. Sedimentation in milford sound: Studies of a southern fiord. *Memoirs N.Z. Oceanographic Institute*, 17:35–47, 1964. 78

G. Pedersen and B. Gjevik. Run-up of solitary waves. *Journal of Fluid Mechanics*, 135:283–99, 1983. 57, 237, 240

BIBLIOGRAPHY

F. Petchey, A. Anderson, A. Hogg, and A. Zondervan. The marine reservoir effect in the southern ocean: An evaluation of extant and new r values and their application to archaeological chronologies. *Journal of the Royal Society of New Zealand*, 38(4):243–62, 2008. 307

Working Group PIANIC. Mitigation of tsunami disasters in ports. Technical Report Draft version III-4, 2009. 239, 241

R.A. Pickrill. Circulation and sedimentation of suspended particulate matter in new zealand fjords. *Marine Geology*, 74(1-2):21–39, 1987. 79, 308

R.A. Pickrill. Sediment yields in fiordland. *Journal of Hydrology (New Zealand)*, 31(1):39–55, 1993. 12, 78, 80, 87, 94, 181

R.A. Pickrill, J.M. Fenner, and M.S. McGlone. Late quaternary evolution of a fjord environment in preservation inlet, new zealand. *Quaternary Research*, 38(3):331–46, 1992. 61, 71, 75, 76, 77, 78, 80, 81, 83, 87, 88, 90, 91, 92, 139, 175, 177, 178, 184, 185, 191

N. Pinter, A. C. Scott, T. L. Daulton, A. Podoll, C. Koeberl, R. S. Anderson, and S. E. Ishman. The younger dryas impact hypothesis: A requiem. *Earth-Science Reviews*, 106(3-4):247–64, 2011. 64

G. Plafker and G.E. Ericksen. Nevados huascaran avalanches. In B Voight, editor, *Rockslides and avalanches*, volume 1. Natural phenomena, pages 277–314. Elsevier Scientific Publishing Company, New York, 1978. 31, 32

L. J. Plug, J. C. Gosse, J. J. McIntosh, and R. Bigley. Attenuation of cosmic ray flux temperate forest. *Journal of Geophysical Research F: Earth Surface*, 112(2), 2007. 142, 143

S. C. Porter and T. W. Swanson. Radiocarbon age constraints on rates of advance and retreat of the puget lobe of the cordilleran ice sheet during the last glaciation. *Quaternary Research*, 50(3):205–13, 1998. 176

A. E. Putnam, G. H. Denton, J. M. Schaefer, D. J. A. Barrell, B. G. Andersen, R. C. Finkel, R. Schwartz, A. M. Doughty, M. R. Kaplan, and C. Schlchter. Glacier advance in southern middle-latitudes during the antarctic cold reversal. *Nature Geoscience*, 3(10):700–04, 2010a. 65, 70, 98, 136

A. E. Putnam, J. M. Schaefer, D. J. A. Barrell, M. Vandergoes, G. H. Denton, M. R. Kaplan, R. C. Finkel, R. Schwartz, B. M. Goehring, and S. E. Kelley. In situ cosmogenic 10be production-rate calibration from the southern alps, new zealand. *Quaternary Geochronology*, 5(4):392–409, 2010b. 24, 69, 70, 75, 98, 134, 136, 138, 139, 143, 149, 151, 157

S. Qi, Q. Xu, B. Zhang, Y. Zhou, H. Lan, and L. Li. Source characteristics of long runout rock avalanches triggered by the 2008 wenchuan earthquake, china. *Journal of Asian Earth Sciences*, 40 (4):896–906, 2011. 29, 33

Q.L.D.C. 2012-2022: The 10 year plan, 2012. 266, 267, 289, 291

M. Quecedo, M. Pastor, and M.I. Herreros. Numerical modelling of impulse wave generated by fast landslides. *International Journal for Numerical Methods in Engineering*, 59(12):1633–56, 2004. 201, 230, 231

P. J. Reimer, M. G. L. Baillie, E. Bard, A. Bayliss, J. W. Beck, P. G. Blackwell, C. B. Ramsey, C. E. Buck, G. S. Burr, R. L. Edwards, M. Friedrich, P. M. Grootes, T. P. Guilderson, I. Hajdas, T. J Heaton, A. G. Hogg, K. A. Hughen, K. F. Kaiser, B. Kromer, F. G. McCormac, S. W. Manning, R. W. Reimer, D. A. Richards, J. R. Southon, S. Talamo, C. S. M. Turney, J. van der Plicht, and C. E. Weyhenmeyer. Intcal09 and marine09 radiocarbon age calibration curves, 050,000 years cal bp, 2009. 307

M. Reyners, R. Robinson, A. Pancha, and P. McGinty. Stresses and strains in a twisted subduction zone - fiordland, new zealand. *Geophysical Journal International*, 148(3):637–48, 2002. 17, 20

N. V. Reznichenko, T. R. H. Davies, and D. J. Alexander. Effects of rock avalanches on glacier behaviour and moraine formation. *Geomorphology*, 132(3-4): 327–38, 2011. 24, 44

K. Rostami, W. R. Peltier, and A. Mangini. Quaternary marine terraces, sea-level changes and uplift history of patagonia, argentina: Comparisons with predictions of the ice-4g (vm2) model of the global process of glacial isostatic adjustment. *Quaternary Science Reviews*, 19(14-15):1495–525, 2000. 74

J. M. Schaefer, G. H. Danton, D. J. A. Barrell, S. Ivy-Ochs, P. W. Kubik, B. G. Andersen, F. M. Phillips, T. V. Lowell, and C. Schlchter. Near-synchronous interhemispheric termination of the last glacial maximum in mid-latitudes. *Science*, 312(5779): 1510–13, 2006. 24, 63, 64, 70, 98, 134

M. Scherwath, T. Stern, F. Davey, and R. Davies. Three-dimensional lithospheric deformation and gravity anomalies associated with oblique continental collision in south island, new zealand. *Geophysical Journal International*, 167(2):906–16, 2006. 75

R.L. Schuster and R.J. Krizek. *Landslides; Analysis and Control.* Nat. Acad. Sci., Trans. Res. Bd. Spec. Rep., 1978. 29

M.J. Selby. *Hillslope Materials and Processes*. Oxford University Press, Oxford, 2 edition, 1993. 29

S. A. Sepulveda, A. Serey, M. Lara, A. Pavez, and S. Rebolledo. Landslides induced by the april 2007 aysn fjord earthquake, chilean patagonia. *Landslides*, 7(4):483–92, 2010. 200

R. A. Shakesby, J. A. Matthews, and G. Owen. The schmidt hammer as a relative-age dating tool and its potential for calibrated-age dating in holocene glaciated environments. *Quaternary Science Reviews*, 25(21-22):2846–67, 2006. 118, 119, 120, 121, 157

R. A. Shakesby, J. A. Matthews, W. Karln, and S. O. Los. The schmidt hammer as a holocene calibrated-age dating technique: Testing the form of the r-value-age relationship and defining the predicted-age errors. *Holocene*, 21(4):615–28, 2011. 119, 120, 156, 157

R.L. Shreve. The black hawk landslide. *Geological society of America Special Paper*, 108:47, 1968. 42

D. H. Shugar and J. J. Clague. The sedimentology and geomorphology of rock avalanche deposits on glaciers. *Sedimentology*, 58(7):1762–83, 2011. 29, 34, 37, 39, 40

J. Shulmeister, D. Fink, and P. C. Augustinus. A cosmogenic nuclide chronology of the last glacial transition in north-west nelson, new zealand - new insights in southern hemisphere climate forcing during the last deglaciation. *Earth and Planetary Science Letters*, 233(3-4):455–66, 2005. 26, 70, 149

J. Shulmeister, T. R. Davies, D. J. A. Evans, O. M. Hyatt, and D. S. Tovar. Catastrophic landslides, glacier behaviour and moraine formation - a view from an active plate margin. *Quaternary Science Reviews*, 28(11-12):1085–96, 2009. 30

J. Shulmeister, D. Fink, O. M. Hyatt, G. D. Thackray, and H. Rother. Cosmogenic 10be and 26al exposure ages of moraines in the rakaia valley, new zealand and the nature of the last termination in new zealand glacial systems. *Earth and Planetary Science Letters*, 297(3-4):558–66, 2010. 66, 67, 70, 88, 98, 130, 134, 136, 137, 143, 149, 171, 177

D. L. Shuster, K. M. Cuffey, J. W. Sanders, and G. Balco. Thermochronometry reveals headward propagation of erosion in an alpine landscape. *Science*, 332(6025):84–88, 2011. 17, 23

C. Singer, J. Shulmeister, and B. McLea. Evidence against a significant younger dryas cooling event in new zealand. *Science*, 281(5378):812–14, 1998. 69

R.L. Slingerland and B. Voight. Occurrences, properties, and predictive models of landslide-generated water waves. In B Voight, editor, *Developments in Geotechnical Engineering 14B: Rockslides and Avalanches*, pages 317–97. Elsevier Scientific Publishing Company, 1979. 57, 199, 230, 231, 232, 234, 235

R.M. Sorensen. *Basic Wave Mechanics for Coastal and Ocean Engineers*. John Wiley and Sons Inc., New York, 1993. 231

D. Sornette and A. Sornette. Acoustic fluidization for earthquakes? *Bulletin of the Seismological Society of America*, 90(3):781–85, 2000. 43

A.L. Strom and O. Korup. Extremely large rockslides and rock avalanches in the tien shan mountains, kyrgyzstan. *Landslides*, 3(2):125–36, 2006. 33

R. P. Suggate. Late pliocene and quaternary glaciations of new zealand. *Quaternary Science Reviews*, 9(2-3):175–97, 1990. 25, 67

R. P. Suggate and P. C. Almond. The last glacial maximum (lgm) in western south island, new zealand: Implications for the global lgm and mis 2. *Quaternary Science Reviews*, 24(16-17):1923–40, 2005. 24, 64, 66

BIBLIOGRAPHY

E. Suleimani, D. J. Nicolsky, P. J. Haeussler, and R. Hansen. Combined effects of tectonic and landslide-generated tsunami runup at seward, alaska during the mw 9.2 1964 earthquake. *Pure and Applied Geophysics*, 168(6-7):1053–74, 2011. 236

R. Sutherland, P. Barnes, and C. Uruski. Miocene-recent deformation, surface elevation, and volcanic intrusion of the overriding plate during subduction initiation, offshore southern fiordland, puysegur margin, southwest new zealand. *New Zealand Journal of Geology and Geophysics*, 49(1):131–49, 2006a. 17, 75, 139

R. Sutherland, K. Berryman, and R. Norris. Quaternary slip rate and geomorphology of the alpine fault: Implications for kinematics and seismic hazard in southwest new zealand. *Bulletin of the Geological Society of America*, 118(3-4):464–74, 2006b. 20, 23, 26, 168, 170, 172, 176, 192

R. Sutherland, K. Kim, A. Zondervan, and M. McSaveney. Orbital forcing of mid-latitude southern hemisphere glaciation since 100 ka inferred from cosmogenic nuclide ages of moraine boulders from the cascade plateau, southwest new zealand. *Bulletin of the Geological Society of America*, 119(3-4):443–51, 2007. 24, 64, 66, 70, 71, 88, 98, 149, 170, 171

J. P. M. Syvitski, K. W. Asprey, D. A. Clattenburg, and G. D. Hodge. The prodelta environment of a fjord: suspended particle dynamics. *Sedimentology*, 32(1):83–107, 1985. 78, 79

R. Taylor. *Te Ika a Maui, or New Zealand and its inhabitants*. Wertheim and MacIntosh, London, 1855. 202

J. R. Toggweiler, J. L. Russell, and S. R. Carson. Midlatitude westerlies, atmospheric co2, and climate change during the ice ages. *Paleoceanography*, 21 (2), 2006. 10

D. S. Tovar, J. Shulmeister, and T. R. Davies. Evidence for a landslide origin of new zealand's waiho loop moraine. *Nature Geoscience*, 1(8):524–26, 2008. 64, 67, 69

I.M. Turnbull and S. Beanland. Te anau earthquake inspection., 1988. 54

I.M. Turnbull, A.H. Allibone, and R. Jongens. Geology of the fiordland area, 2010. 11, 16, 17, 18, 20, 21, 22, 25, 26, 52, 70, 101, 168, 169, 172

C. S. M. Turney, R. G. Roberts, N. de Jonge, C. Prior, J. M. Wilmshurst, M. S. McGlone, and J. Cooper. Redating the advance of the new zealand franz josef glacier during the last termination: evidence for asynchronous climate change. *Quaternary Science Reviews*, 26(25-28):3037–42, 2007. 67

C.S.M. Turney, A.P. Kershaw, J.J. Lowe, S. van der Kaars, R. Johnston, S. Rule, P. Moss, L. Radke, J. Tibby, M.S. McGlone, J.M. Wilmshurst, M.J. Vandergoes, S.J. Fitzsimons, C. Bryant, S. James, N.P. Branch, J. Cowley, R.M. Kalin, N. Ogle, G. Jacobsen, and L.K. Fifield. Climatic variability in the southwest pacific during the last termination (20-10 kyr bp). *Quaternary Science Reviews*, 25(9-10):886–903, 2006. 24, 64, 66

B. Van Wyk De Vries, S. Self, P. W. Francis, and L. Keszthelyi. A gravitational spreading origin for the socompa debris avalanche. *Journal of Volcanology and Geothermal Research*, 105(3):225–47, 2001. 36

M. J. Vandergoes, R. M. Newnham, F. Preusser, C. H. Hendy, T. V. Lowell, S. J. Fitzsimons, A. G. Hogg, H. U. Kasper, and C. Schlu?chter. Regional insolation forcing of late quaternary climate change in the southern hemisphere. *Nature*, 436(7048):242–45, 2005. 24, 64, 66

M. J. Vandergoes, A. C. Dieffenbacher-Krall, R. M. Newnham, G. H. Denton, and M. Blaauw. Cooling and changing seasonality in the southern alps, new zealand during the antarctic cold reversal. *Quaternary Science Reviews*, 27(5-6):589–601, 2008. 66, 69, 98

D. J. Varnes. Slope movement type and processes. Technical report, Transportation Research Board, National Academy of Sciences, 1978. 28

R. I. Walcott. Modes of oblique compression: Late cenozoic tectonics of the south island of new zealand. *Reviews of Geophysics*, 36(1):1–26, 1998. 15

S.J. Walder, P. Watts, O.E. Sorensen, and K. Janssen. Tsunamis generated by subaerial mass flows. *Journal of Geophysical Research B: Solid Earth*, 108 (5), 2003. 230, 231

R. Walters, P. Barnes, K. Lewis, J.R. Goff, and J. Fleming. Locally generated tsunami along the kaikoura coastal margin: Part 2. submarine landslides. *New Zealand Journal of Marine and Freshwater Research*, 40(1):17–28, 2006. 54, 234

R. A. Walters and J. Goff. Assessing tsunami hazard along the new zealand coast. *Science of Tsunami Hazards*, 21(3), 2003. 55

A. M. Wandres, S. D. Weaver, D. Shelley, and J. D. Bradshaw. Change from calc-alkaline to adakitic magmatism recorded in the early cretaceous darran complex, fiordland, new zealand. *New Zealand Journal of Geology and Geophysics*, 41(1):1–14, 1998. 15

P. Watts. *Water waves generated by underwater landslides*. PhD thesis, University of Caltech, 1997. 230, 237

P. Watts, S. T. Grilli, D. R. Tappin, and G. J. Fryer. Tsunami generation by submarine mass failure. ii: Predictive equations and case studies. *Journal of Waterway, Port, Coastal and Ocean Engineering*, 131(6):298–310, 2005. 236

J. T. Weidinger and O. Korup. Frictionite as evidence for a large late quaternary rockslide near kanchenjunga, sikkim himalayas, india - implications for extreme events in mountain relief destruction. *Geomorphology*, 103(1):57–65, 2009. 30

A. Wells and J. Goff. Coastal dunes in westland, new zealand, provide a record of paleoseismic activity on the alpine fault. *Geology*, 35(8):731–34, 2007. 20

A. Wells, M. D. Yetton, R. P. Duncan, and G. H. Stewart. Prehistoric dates of the most recent alpine fault earthquakes, new zealand. *Geology*, 27(11):995–98, 1999. 20, 199

I. E. Whitehouse and G. A. Griffiths. Frequency and hazard of large rock avalanches in the central southern alps, new zealand. *Geology*, 11(6): 331–34, 1983. 45, 48, 49, 214

G. F. Wieczorek, E. L. Geist, R. J. Motyka, and M. Jakob. Hazard assessment of the tidal inlet landslide and potential subsequent tsunami, glacier bay national park, alaska. *Landslides*, 4 (3):205–15, 2007. 230

P. Wilson. Storurdi: A late holocene rock-slope failure (sturzstrom) in the jotunheimen, southern norway. *Geografiska Annaler, Series A: Physical Geography*, 91(1):47–58, 2009. 34

S. Winkler. The schmidt hammer as a relative-age dating technique: Potential and limitations of its application on holocene moraines in mt cook national park, southern alps, new zealand. *New Zealand Journal of Geology and Geophysics*, 48 (1):105–16, 2005. 119

S. Winkler. First attempt to combine terrestrial cosmogenic nuclide (10be) and schmidt hammer relative-age dating: Strauchon glacier, southern alps, new zealand. *Central European Journal of Geosciences*, 1(3):274–90, 2009. 119, 120, 137, 143, 149, 157, 160

S. Winkler, J. A. Matthews, R. A. Shakesby, and P. Q. Dresser. Glacier variations in breheimen, southern norway: Dating little ice age moraine sequences at seven low-altitude glaciers. *Journal of Quaternary Science*, 18(5):395–413, 2003. 162

S. Winkler, T. Chinn, I. Grtner-Roer, S. U. Nussbaumer, M. Zemp, and H. J. Zumbhl. An introduction to mountain glaciers as climate indicators with spatial and temporal diversity. *Erdkunde*, 64 (2):97–118, 2010. 30

M. Yetton. The alpine fault. *Tephra*, June, 1998: 30–32, 1998. 20, 199

A. Zecca and L. Chiari. Lower bounds to future sea-level rise. *Global and Planetary Change*, 98:1–5, 2012. 267, 268

J. Zhao, C. Liu, T. Lv, and L. Dai. Identification of landslide spatial distribution and their types along the riviere frorse drainage basin triggered by the earthquake in haiti on 12 january 2010. *Disaster Advances*, 5(1):5–13, 2012. 33

Appendix A

Figure enlargements

A.1 Study area Map

Submarine environment in blue, terrestrial landslide deposits shaded in purple, submarine landslide deposits shaded in orange.

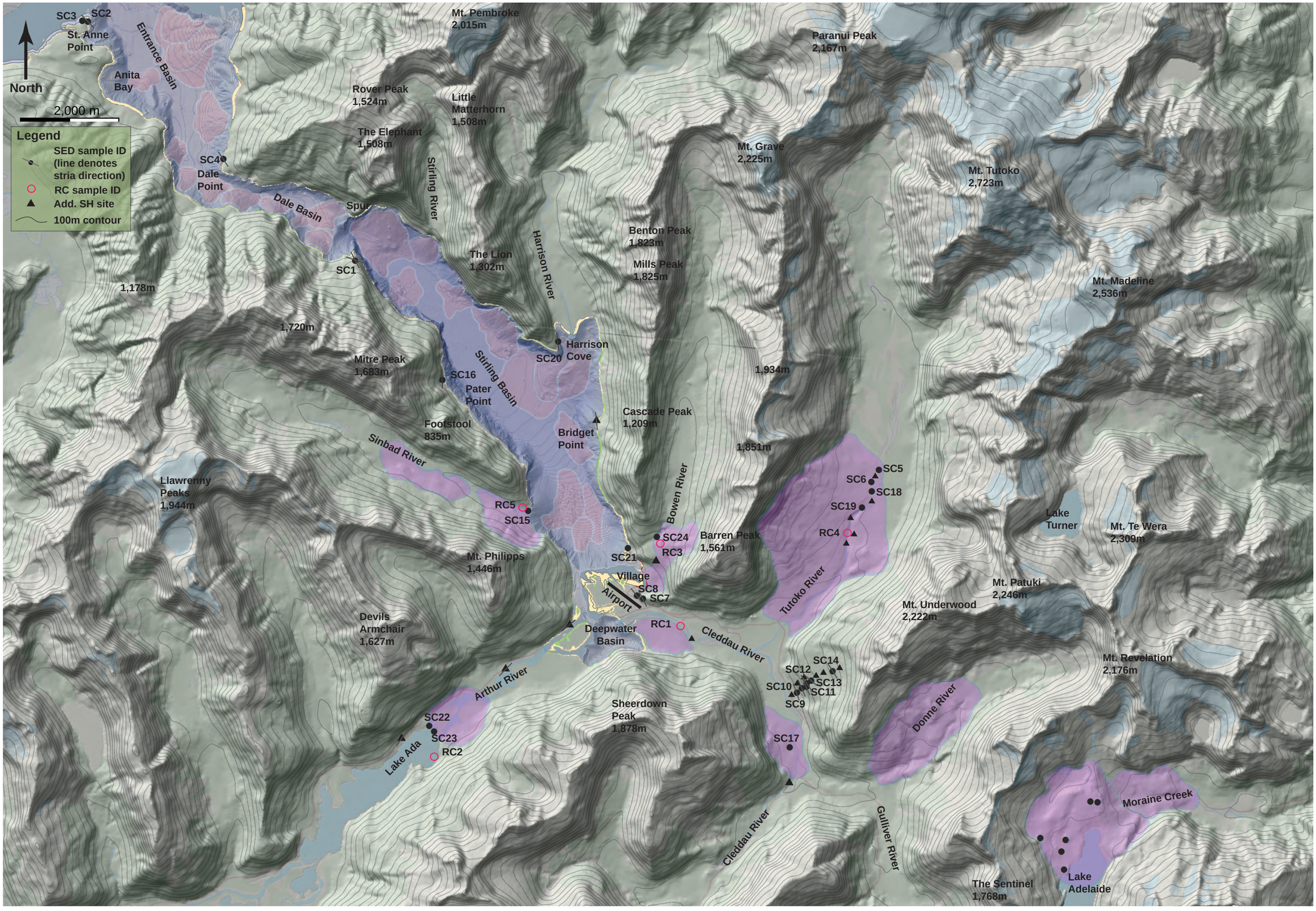
North
2,000 m
Legend
SED sample ID (line denotes stria direction)
RC sample ID
Add. SH site
100m contour
SC3
SC2
St. Anne Point
Entrance Basin
Anita Bay
Mt. Pembroke 2,015m
Paranui Peak 2,167m
Rover Peak 1,524m
Little Matterhorn 1,508m
The Elephant 1,508m
Mt. Grave 2,225m
Mt. Tutoko 2,723m
SC4
Dale Point
Dale Basin
Spur
Stirling River
Benton Peak 1,823m
Mills Peak 1,825m
Harrison River
The Lion 1,302m
SC1
1,178m
Mt. Madeline 2,536m
1,720m
Harrison Cove
SC20
Mitre Peak 1,683m
SC16
Pater Point
Stirling Basin
1,934m
Cascade Peak 1,209m
Footstool 835m
Bridget Point
1,851m
Sinbad River
SC5
SC6
SC18
SC19
RC4
Lake Turner
Mt. Te Wera 2,309m
Llawrenny Peaks 1,944m
RC5
SC15
Bowen River
SC24
RC3
Barren Peak 1,561m
Mt. Philipps 1,446m
SC21
Village
Airport
SC8
SC7
Tutoko River
Mt. Patuki 2,246m
Mt. Underwood 2,222m
Devils Armchair 1,627m
Deepwater Basin
RC1
Cleddau River
SC14
SC12
SC13
SC10
SC11
SC9
Mt. Revelation 2,176m
Arthur River
Sheerdown Peak 1,878m
Donne River
SC22
SC23
RC2
Lake Ada
SC17
Moraine Creek
Cleddau River
Gulliver River
Lake Adelaide
The Sentinel 1,768m

Appendix B

Lake Wakatipu Work

B.1 Introduction

Originally, the scope of the project was to include Lake Wakatipu, a large glacially-carved lake in south-western Otago, and the third largest lake in New Zealand. The popular tourist destination and adventure playground of Queenstown, as well as various smaller centres, is situated along the shores of Lake Wakatipu. Due to the relatively high population of the Queenstown Lakes area (est. 28,440 Q.L.D.C., 2012) and the importance of the region to the New Zealand tourism industry, I believe that it is essential to establish the risk of landslide-generated tsunami at Lake Wakatipu. As part of this project I spent several weeks reviewing and processing the available Land Information New Zealand (LINZ) bathymetric data, as well as investigating the shoreline of the lake for evidence of past tsunami.

B.2 Approaching the Otago Regional Council

After looking into the potential costs and logistical challenges associated with collecting new sonar data for Lake Wakatipu, I met with Richard Woods at the Otago Regional Council (ORC) to discuss the potential project and data requirements. That meeting confirmed that the ORC had an interest in investigating the potential hazards related to landslide-generated tsunami at Lake Wakatipu, but due to limited funding available for such investigation, the council could not contribute financially to the cost of data collection. As a result, I decided to investigate the potential for using existing LINZ bathymetric data for Lake Wakatipu.

B.2.1 Data processing and availability

I used ArcGIS to process several million data points from the LINZ dataset for Lake Wakatipu, generating a bathymetric model to test the areas with the highest density of available points (ie. Queenstown Bay, Frankton Arm, and the adjacent reach of Lake Wakatipu). Unfortunately, the density of that data was insufficient to generate a sub-10 m resolution grid, and the resulting bathymetric model proved to be inadequate for reliably identifying submarine landslide deposits.

I also investigated the likely costs associated with collecting new high resolution multi-beam sonar data for Lake Wakatipu, which could have been achieved either by bringing NIWA's research vessel the RV Tangaroa from Wellington, or by mounting a multi-beam sonar scanning unit (such as the Simrad EM300 multibeam echo sounder used by NIWA) on a smaller vessel. The first option would have required expensive transport, as well as significant costs for the necessary personnel to pilot the vessel, and run the equipment. Without external financial support, this option would have been prohibitively expensive (over $100,000). The second option would have been slightly less expensive, but required the remounting and calibration of the multibeam echo sounder on a smaller vessel, and a minimum of two weeks of technician time to run the instruments, and process the large amounts of data.

B.3 Field Investigation of Lake Wakatipu shoreline

Around the same time I undertook a preliminary field investigation of the north and eastern shorelines of Lake Wakatipu, including the Rees-Dart delta at the northern end of the lake. While not exhaustive, these investigations did not reveal any sites that were both undisturbed by human activity, and likely to preserve post-glacial evidence of landslide-generated tsunami. Most low-gradient areas along Lake Wakatipu are either developed, or host active debris fans or river deltas. The western shoreline of the lake (from Kingston to the mouth of the Caples River) was not investigated due to the lack of road access or boat transport.

After discussing the options with Tim Davies and Phil Barnes at NIWA, we decided to keep the project focused on areas where good data was already available, in particular the Milford Sound Area.

B.4 Lake Wakatipu: Future research priorities

Despite being unable to include Lake Wakatipu in this project, I believe that a risk assessment of hazards related to landslides and landslide-generated tsunami in the region should be undertaken in the near future. The spectacular Central Otago Lakes region continues to be shaped by active geomorphic and tectonic processes. The relatively high regional population (2011 census 28,440, Q.L.D.C., 2012) is concentrated along or near the shores of Lake Wakatipu, although there are also significant and growing populations in the lakeside communities of Wanaka, Hawea and Lake Hayes. The regional residential population is expected to grow to around 36,000 over the next 10 years. The region enjoys iconic status as a year-round adventure playground and tourist destination, currently hosting over 2.8 million visitor-days per year, many from overseas visitors. According to the Queenstown Lakes District Council, the population of the region swells by over 300% during peak tourist days, with an expected peak day population of 110,000 by the year 2021 (Q.L.D.C., 2012).

The growing resident population of the region combined with its popularity as a domestic and international tourist destination suggest that local and regional governments may want to consider landslides and landslide-generated tsunami in the Lake Wakatipu region as a priority for future hazard assessment. Such work could include collection of high resolution bathymetric and seismic reflection data, combined with boat-based investigation of shorelines in areas likely to trap tsunami deposits, and tsunami modelling. Field investigation, mapping, and dating of terrestrial landslide deposits should supplement any submarine investigation. Together, this information should improve the understanding of the potential hazards related to landslides and landslide-generated tsunami around Lake Wakatipu.

Appendix C

Additional field data and calculations

C.1 TCND sample site details

TCND sample site details

Sample Number	Location	Elev. (m a.s.l.)	Boulder (B) or Bedrock (R)	Estimated Density (g/cm^3)	Primary Bedrock Structure		Glacial Striations & Features	Surface Dip (°)	Dip Azimuth (°)	Average Sample Depth (cm)	Average Pitting Depth (mm)	Overburden Depth (cm)	Debris-equivalent rock depth	Equivalent (total) Sample Depth	Forest Attenuation Correction	Topographic Shielding Correction	Boulder Size (LxWxH) (m)
					Strike	Dip	Bearing					cm	cm	cm			
SC-1	Bedrock Spur	238	R	2.9	NA	NA	288	0	0	5	3.5	0	0.00	5.00	1	0.944	NA
SC-2	St. Anne Pt.	5	R	2.6	30	70nw	316	0	0	2	3	0	0.00	2.00	1	0.996	NA
SC-3	St. Anne Pt.	14	R	2.6	258	70nw	NA	0	0	1	3	0	0.00	1.00	1	0.998	NA
SC-4	North of Dale Pt.	8	R	2.9	10	90	326	35	125	5	5	0	0.00	5.00	1	0.933	NA
SC-5	Tutoko Deposit	218	B	2.9	NA	NA	NA	30	85	5	2	0	0.00	5.00	1	0.920	4x4x4
SC-6	Tutoko Deposit	212	B	2.9	NA	NA	NA	0	80	2	2	0	0.00	2.00	1	0.935	15x4.5x4.5
SC-7	VC Bedrock Spur	76	R	2.9	NA	NA	334	15	110	2	2	0	0.00	2.00	1	0.938	NA
SC-8	VC Bedrock Spur	24	R	2.9	NA	NA	320	0	0	1.5	2.5	0	0.00	1.50	1	0.972	NA
SC-9	Tree Slide	84	R	2.9	310	32n	340	0	0	2	2	0	0.00	2.00	1	0.971	NA
SC-10	Tree Slide	145	R	2.9	347	20ne	336	15	145	2	2	200	111.03	113.03	0.927	0.896	NA
SC-11	Tree Slide	235	R	2.9	340	20sw	335	20	140	2	1.5	0	0.00	2.00	0.927	0.829	NA
SC-12	Tree Slide	361	R	2.9	NA	NA	310	45	140	2	1.5	30	16.66	18.66	0.927	0.927	NA
SC-13	Tree Slide	289	R	2.9	NA	NA	325	20	145	2	1.5	0	0.00	2.00	0.927	0.889	NA
SC-14	Tree Slide	531	R	2.9	NA	NA	327	10	150	2	1	0	0.00	2.00	0.927	0.943	NA
SC-15	Sinbad Deposit	8	B	2.9	NA	NA	NA	0	0	1.5	1.5	0	0.00	1.50	1	0.943	4x3x4
SC-16	Pater Point	34	R	2.9	315	65ne	359	0	0	2	2	0	0.00	2.00	1	0.930	NA
SC-17	Upper Cleddau	60	B	2.9	NA	NA	NA	0	0	3	1	0	0.00	3.00	1	0.935	5x4x4
SC-18	Tutoko Deposit	207	B	2.9	NA	NA	NA	0	0	1.5	1	0	0.00	1.50	1	0.944	10x5x8
SC-19	Tutoko Deposit	201	B	2.9	NA	NA	NA	0	0	1.5	1	0	0.00	1.50	1	0.953	12x4x9
SC-20	Harrison Cove	5	R	2.9	NA	NA	354	0	0	2	1.5	0	0.00	2.00	1	0.863	NA
SC-21	Base of Bowen	4	B	2.9	NA	NA	NA	25	320	7	1	0	0.00	7.00	1	0.889	4x4x6
SC-22	Lake Ada	45	B	2.9	NA	NA	NA	0	0	2	1	0	0.00	2.00	1	0.945	6x3x5
SC-23	Lake Ada	45	B	2.9	NA	NA	NA	0	0	1.5	0.5	0	0.00	1.50	1	0.954	4x3x4
SC-24	Bowen Deposit	255	B	2.9	NA	NA	NA	0	0	2	1.5	0	0.00	2.00	1	0.914	9x8x9
SC-50	Lake Adelaide	962	B	2.9	NA	NA	NA	0	0	1.5	6	0	0.00	1.50	1	0.973	5x3x4
SC-51	Lake Adelaide	977	B	2.9	NA	NA	NA	0	0	2	5	0	0.00	2.00	1	0.981	5x4x4
SC-52	Lake Adelaide	983	B	2.9	NA	NA	NA	0	0	2	6	0	0.00	2.00	1	0.985	8x5x8
SC-53	Lake Adelaide	1048	B	2.9	NA	NA	NA	0	0	2	7	0	0.00	2.00	1	0.983	5x4x5
SC-54	Lake Adelaide	1049	B	2.9	NA	NA	NA	0	0	2	4	0	0.00	2.00	1	0.981	20x10x>15
SC-55	Lake Adelaide	1047	B	2.9	NA	NA	NA	0	0	2.5	5	0	0.00	2.50	1	0.987	9x7x10

C.2 Topographic shielding calculations

Cronus shielding calculations

Cosmo Site	Strike	Dip	Declination (adj. = 20° E)	Inclination (°)	Shielding Factor
SC-1	0	0	0 20 30 88 92 126 138 190 255 300 308	28 30 18 22 10 8 5 38 32 0 0	0.943873408
SC-2	0	0	330 18 45 60 80 110 128 134 161 163 207 242 300	0 0 3 8 8 17 5 14 14 11 15 10 12	0.995837
SC-3	0	0	246 17 48 72 80 90 108 140 148 218	0 0 4 10 9 14 12 6 12 10	0.998185747
SC-4	125	35	356 64 162 164 218 242 252 290 309 317	0 30 26 28 23 18 20 6 6 0	0.933333281
SC-5	85	30	332 355 6 48 60 66 68 81 94 108 130 142 168 174 180 189 196 198 199 200 201 232 255 292 306	16 8 8 20 25 28 28 31 30 34 36 37 32 26 19 10 8 7 6 6 8 16 24 32 22	0.9200929
SC-6	80		15 20 31 50 56 64 113 136 157 212 230 232 266 296 348 5	17 20 17 21 26 30 32 26 32 10 15 18 30 35 15 10	0.935075282
SC-7	110	15	0 14 28 40 46 68 94 114 132 160 168 174 187 211 232 235 276 302 311 322 330 336 348	20 15 14 20 23 44 18 21 16 24 10 10 20 19 3 5 23 5 11 4 7 8 8	0.937580061
SC-8	0	0	0 14 28 40 46 68 94 114 132 160 168 174 187 211 232 235 276 302 311 322 330 336 348	20 15 14 20 22 40 16 21 16 24 10 10 20 19 3 5 23 5 11 4 7 8 8	0.972227128
SC-9	0	0	157 174 190 195 200 204 238 247 265 295 298 328 330 336 10 133	10 18 17 13 9 17 29 30 26 6 5 17 22 18 13 27	0.971
SC-10	145	15	164 178 192 200 241 260 282 294 297 304 308 311 328 340 350 60 97	15 21 16 10 31 27 6 9 4 4 6 5 17 17 16 48 46	0.896325912
SC-11	140	20	326 334 130 152 168 176 194 200 207 240 257 277 284 294 296 303 306 308	19 28 60 32 13 17 12 7 10 29 22 7 6 7 3 3 6 4	0.828835933
SC-12	140	15	240 274 290 296 306 308 312 320 40 56 69 72 80 150 167 170 173 184 194 204 223	22 8 7 7 4 3 8 17 13 21 38 40 42 26 10 12 11 15 13 8 9	0.927414779
SC-13	145	20	112 159 156 172 177 192 195 201 242 272 288 290 300 305 318 320 336 0	40 10 13 13 17 13 5 8 23 5 6 2 2 5 15 17 18 45	0.8890339
SC-14	150	10	180 190 198 208 226 245 272 279 289 300 308 316 336 34 69 75 84	9 10 10 5 7 19 3 4 5 2 5 13 11 29 41 40 42	0.943425208
SC-15	0	0	225 270 280 294 322 12 24 37 44 68 83 102 119 135 146	44 18 16 15 33 10 18 15 20 21 16 17 7 10 12	0.942652258
SC-16	0	0	72 77 120 128 137 164 262 326 0 8 10 36 40	20 15 9 9 7 19 46 16 6 10 21 13 20	0.929857073
SC-17	0	0	14 48 80 95 128 137 170 195 206 246 280 316	7 30 39 20 12 10 30 20 14 40 32 18	0.935067427
SC-18	0	0	20 37 44 54 61 129 140 177 183 241 286 315 345 4	18 15 22 21 28 24 38 22 18 19 34 28 10 9	0.943791131
SC-19	0	0	60 118 127 171 182 205 220 229 239 248 297 333 32	24 29 34 21 11 9 15 14 7 16 32 21 16	0.952965039
SC-20	0	0	358 32 152 162 171 238 278 324	20 30 17 9 42 50 44	0.863342826
SC-21	320	25	147 170 206 217 225 235 254 274 288 290 303 306 320 338 344 3 36 100	30 22 14 4 4 9 21 10 9 13 15 12 2 7 8 36 46 38	0.889101115
SC-22	0	0	166 203 211 219 228 250 265 296 348 20 25 40 74 90 105 122 139 158 164	29 7 9 8 2 13 28 32 36 19 20 7 6 18 24 21 28 26 23	0.944918204
SC-23	0	0	18 24 42 68 100 119 138 154 162 164 166 207 214 223 228 264 270 344 12 14	15 19 5 5 25 22 33 30 26 26 32 9 10 10 4 14 25 32 16 14	0.954358077
SC-24	0	0	95 181 190 198 202 216 224 228 234 248 259 266 275 290 314 325 10 26 37 50 54	39 15 16 14 15 5 8 3 4 13 15 13 10 12 25 32 46 18 28 25 32	0.91413418
SC-50	0	0	302 333 340 349 4 12 55 58 76 84 98 112 124 126 150 160 164 168 194 210 237 260 305	16 17 14 17 10 14 8 4 10 14 18 25 20 24 18 19 14 16 14 17 28 30 20	0.972927463
SC-51	0	0	114 125 128 140 147 156 161 165 189 238 240 255 273 295 296 332 340 348 0 10 58 60 70 80 86 100	24 16 19 18 12 14 10 14 10 25 26 21 25 21 17 19 16 19 10 15 6 2 2 5 10 14	0.981218147
SC-52	0	0	282 288 324 334 343 0 10 55 61 79 110 123 130 132 142 148 158 160 164 188 228 235 245 262	26 15 18 16 19 9 15 5 1 1 20 22 15 16 15 10 14 10 14 9 21 22 18 21	0.985228506
SC-53	0	0	85 108 115 124 126 136 142 152 158 160 176 290 284 340 347 0 10 17 66	1 13 16 10 13 12 9 12 9 12 10 29 21 22 15 20 9 12 1	0.982812581
SC-54	0	0	266 272 301 307 321 334 340 0 2 20 30 64 68 97 102 132 168 171 175 178 205	28 21 22 19 25 22 14 16 19 21 14 7 2 2 8 20 10 12 10 11 9	0.981193519
SC-55	0	0	344 356 0 18 30 64 88 123 158 163 200 218 254 258 297 306 324 334	14 16 19 20 11 3 3 19 11 12 10 15 17 13 22 19 22 18	0.987304127

C.3 Lithology

Sample lithology identification

Sample Number	Location	Grainsize (mm)	Colour	Mafic Colour Index (%)	Mineral & Proportion	Notes	General Rock Name
SC-1	Bedrock Spur	coarse (1-10)	l-m grey	35-45	Quartz (~5%) Plagioclas (45-50%) Muscovite (1%) Amph (30-40% Garnet (~2%) Olivine (<1%)	Moderate folliation, Granitic in composition. Quartz/feldspar & Amphibole xtals interlocking. Amphiboles/Garnet "frosted" w Quartz. Quartz smokey-milky-pinkish-clear	Harrison Gneiss
SC-2	St. Anne Pt.	sm-med (0.5-2)	l-m grey w/ pinkish orange patches	20-30	Qtz/Plag (70-80%) Biotite (10%) Amph (<1%) Garnet (10-15%)	High grade, folded Gneiss, Garnet "frosted" w Quartz	Intensly deformed Gneiss of the Tuhua Sequence (Thurso Gneiss?)
SC-3	St. Anne Pt.	sm-med (0.5-2)	l-m grey w/ pinkish orange patches	30-40	Qtz/Plag (60-65%) Biotite (10%) Amph (<1%) Garnet (20-30%)	High grade, folded Gneiss, Garnet "frosted" w Quartz. Sampled Quartz-rich vein	Intensly deformed Gneiss of the Tuhua Sequence (Thurso Gneiss?)
SC-4	North of Dale Pt.	med (1-5)	m-d grey w/ white Quartz veins	50-60	Quartz (40-50%) Plag/Orthoclase (3%) Biotite (10%) Amph (40-50%) Garnet (<1%) Olivine (<1%)	High grade, folded Gneiss. Elongated Amphibole xtals "frosted" w Quartz. Sampled Quartz-rich vein	Garnet Gneiss (Milford Gneiss)
SC-5	Tutoko Deposit	m-l (2-20)	m-d grey w/ white Quartz veins	40-50	Qtz/Plag (50-60%) Biotite (<1%) Amph (40-50%) Garnet (<1%)	Amphibole xtals "frosted" w Quartz and streaked out in places. Occasional biotite/garnet. Quartz interlocking milky/glassy xtals (could be plag?). Sampled Qtz-rich area	Metadiorite = Folliated Horneblende Diorite
SC-6	Tutoko Deposit	m-l (2-20)	m-d grey w/ white Quartz veins	40-50	Qtz/Plag (50-60%) Biotite (<1%) Amph (40-50%) Garnet (<1%)	Amphibole xtals "frosted" w Quartz and streaked out in places. Occasional biotite/garnet. Quartz interlocking milky/glassy xtals (could be plag?). Sampled Qtz-rich area	Metadiorite = Folliated Horneblende Diorite
SC-7	VC Bedrock Spur	m-l (1-5)	m-d grey w/ lighter inclusions and Quartz veins	45-55	Qtz/Plag (45-50%) Biotite (<1%) Amph (45-50%) Garnet (<1%)	Amphibole xtals "frosted" w Quartz and streaked out in places. Occasional biotite/garnet. Quartz interlocking milky/glassy xtals (could be plag?) + smokey qtz	Metadiorite = Folliated Horneblende Diorite
SC-8	VC Bedrock Spur	m-l (1-10)	m-d grey w/ lighter inclusions and Quartz veins	45-55	Qtz/Plag (45-50%) Biotite (<1%) Amph (45-50%) Garnet (<1%)	Amphibole xtals "frosted" w Quartz and streaked out in places. Occasional biotite/garnet. Quartz interlocking milky/glassy xtals (could be plag?) + smokey qtz	Metadiorite = Folliated Horneblende Diorite
SC-9	Tree Slide	m-l (2-20)	m-d grey w/ lighter inclusions and Quartz veins	50-60	Qtz/Plag (40-45%) Biotite (<1%) Amph (55-60%) Garnet (<1%)	Amphibole xtals "frosted" w Quartz and streaked out in places. Occasional biotite/garnet. Quartz interlocking milky/glassy xtals (could be plag?)	Metadiorite = Folliated Horneblende Diorite
SC-10	Tree Slide	m-l (2-20)	m grey w/ lighter inclusions and Quartz veins	35-40	Qtz/Plag (50-60%) Amph (35-40%) Garnet (5-10%)	Amphibole xtals "frosted" w Quartz and streaked out in places. High conc Garnet. Quartz interlocking milky/glassy xtals (could be plag?) + smokey qtz	Metadiorite = Folliated Horneblende Diorite
SC-11	Tree Slide	m-l (1-10)	m-d grey w/ lighter inclusions and Quartz veins	45-50	Qtz/Plag (45-55%) Amph (40-50%) Garnet (~5%)	Amphibole xtals "frosted" w Quartz and streaked out in places. High conc Garnet. Quartz interlocking milky/glassy xtals (could be plag?) + smokey qtz	Metadiorite = Folliated Horneblende Diorite
SC-12	Tree Slide	m-l (3-20)	m-d grey w/ lighter inclusions and Quartz veins	40-45	Qtz/Plag (50-55%) Amph (40-45%) Garnet (<1%) Apatite? (<1%)	Amphibole xtals "frosted" w Quartz and streaked out in places. Occasional garnet & green/blue glassy mineral (Apatite?). Quartz interlocking milky/glassy xtals (could be plag?) + smokey qtz	Metadiorite = Folliated Horneblende Diorite
SC-13	Tree Slide	m-l (3-20)	m-d grey w/ lighter inclusions and Quartz veins	35-45	Qtz/Plag (50-60%) Amph (35-40%) Biotite (<1%) Garnet (trace)	Amphibole xtals "frosted" w Quartz and streaked out in places. Quartz interlocking milky/glassy xtals (could be plag?) + smokey qtz	Metadiorite = Folliated Horneblende Diorite

SC-14	Tree Slide	m-l (3-20)	m-d grey w/ lighter inclusions and Quartz veins	35-45	Qtz/Plag (50-60%) Amph (35-40%) Garnet (<1%) Biottie (<1%) Apatite? (<1%)	Amphibole xtals "frosted" w Quartz and streaked out in places. Occasional garnet & green/blue glassy mineral (Apatite?). Quartz interlocking milky/glassy xtals (could be plag?) + smokey qtz	Metadiorite = Folliated Horneblende Diorite
SC-15	Sinbad Deposit	s-m (1-10)	m-d grey	60-65	Qtz/Plag (35-40%) Amph (60-65%) Garnet (trace)	Amphibole xtals "frosted" w Quartz and streaked out in places. Quartz interlocking milky/glassy/pinkish xtals (could be plag?)	Metadiorite = Folliated Horneblende Diorite (almost Gabbroic)
SC-16	Pater Point	s-l (1-30)	l-m grey	25-30	Qtz/Plag (50-60%) Orthoclas (10-15%) Amph (20-30%) Biotite (~3%) Muscovite (<1%) Garnet (trace)	Mild Foliation, Granitic composition. Fine elongated Horneblende xtals, frosted w Qtz/Plag, streaked out in places. Qtz milky-glassy-smokey. Pink Orthoclase.	Harrison Gneiss? Metagranite?
SC-17	Upper Cleddau	s-m (1-10)	l-m grey	30-40	Qtz/Plag (70-75%) Amph (20-25%) Biotite (2-3%)	Mild Foliation, Granitic composition. Fine elongated Horneblende xtals, frosted w Qtz/Plag, streaked out in places. Qtz milky-glassy-smokey.	Harrison Gneiss? Metagranite?
SC-18	Tutoko Deposit	s-m (1-20)	m-d grey w/ white Quartz veins	40-50	Qtz/Plag (50-60%) Amph (40-50%) Garnet (trace)	Amphibole xtals "frosted" w Quartz and streaked out in places. Occasional garnet. Quartz interlocking milky/glassy/pinkish xtals (could be plag?)	Metadiorite = Folliated Horneblende Diorite
SC-19	Tutoko Deposit	s-m (1-10)	m-d grey w/ white Quartz veins	30-40	Qtz/Plag (60-70%) Amph (30-40%) Biotite (~2%) Garnet (trace)	Amphibole xtals "frosted" w Quartz and streaked out in places. Occasional biotite/garnet. Quartz interlocking milky/glassy/pinkish xtals (could be plag?)	Metadiorite = Folliated Horneblende Diorite
SC-20	Harrison Cove	s-m (1-20)	l-m grey w/ veins of Qtz and pink Orthoclase	20-25	Quartz (30-40%) Orthoclas (25-35%) Biotite (20-25%) Amph (<1%) Garnet (trace)	Moderate folliation, Granitic in composition. Quartz & Amphibole xtals interlocking. Amphiboles/Garnet "frosted" w Quartz. Quartz smokey-milky-pinkish-clear	Harrison Gneiss
SC-21	Base of Bowen	s-m (1-15)	l-m grey w/ veins of Qtz and pink Orthoclase	25-30	Quartz (35-45%) Orthoclas (30-40%) Biotite (<1%) Augite? (20-25%) Garnet (trace)	Moderate folliation, Granitic in composition. Quartz & Augite xtals interlocking. Augite/Garnet "frosted" w Quartz. Quartz smokey-milky-pinkish-clear	Metadiorite = Folliated Horneblende Diorite
SC-22	Lake Ada	s-m (1-10)	l-m grey	40-50	Qtz/Plag (50-60%) Amph (40-50%)	Amphibole xtals "frosted" w Quartz and streaked out in places. Quartz interlocking milky/glassy xtals (could be plag?)	Metadiorite = Folliated Horneblende Diorite
SC-23	Lake Ada	s-m (1-10)	l-m grey	50-60	Qtz/Plag (40-50%) Amph (50-60%) Garnet (1-2%)	Amphibole xtals "frosted" w Quartz and streaked out in places. Occasional garnet. Quartz interlocking milky/glassy xtals (could be plag?)	Metadiorite = Folliated Horneblende Diorite
SC-24	Bowen Deposit	s (<1-10)	l-m grey w/ veins of Qtz and pink Orthoclase	25-30	Qtz/Plag (45-50%) Orthoclas (20-25%) Biotite (<1%) Amph (25-30%) Garnet (trace)	Moderate folliation, Granitic in composition. Quartz & Amphibole xtals interlocking. Amphiboles/Garnet "frosted" w Quartz. Quartz smokey-milky-pinkish-clear	Metadiorite = Folliated Horneblende Diorite
SC-50	Lake Adelaide	m-l (2-20)	m-d grey	40-60	Quartz (25-30%) Plag/Orthoclase (15-25%) Biotite (<2%) Amph (40-50%) Garnet (<1%) Olivine (<1%)	Amphibole xtals "frosted" w Quartz and streaked out in places. Occasional biotite/olivine. Quartz interlocking w Plag xtals. Some carlsbad twins => orthoclase. Some metamorphism apparent.	Metadiorite = Folliated Horneblende Diorite
SC-51	Lake Adelaide	m-l (2-20)	m-d grey	40-60	Quartz (25-30%) Plag/Orthoclase (15-25%) Biotite (<2%) Amph (40-50%) Garnet (<1%) Olivine (<1%)	Amphibole xtals "frosted" w Quartz and streaked out in places. Occasional biotite/olivine. Quartz interlocking w Plag xtals. Some carlsbad twins => orthoclase. Some metamorphism apparent.	Metadiorite = Folliated Horneblende Diorite
SC-52	Lake Adelaide	m-l (2-20)	m-d grey	40-60	Quartz (25-30%) Plag/Orthoclase (15-25%) Biotite (<2%) Amph (40-50%) Garnet (<1%) Olivine (<1%)	Amphibole xtals "frosted" w Quartz and streaked out in places. Occasional biotite/olivine. Quartz interlocking w Plag xtals. Some carlsbad twins => orthoclase. Some metamorphism apparent.	Metadiorite = Folliated Horneblende Diorite

SC-53	Lake Adelaide	m-l (2-20)	m-d grey	40-60	Quartz (25-30%) Plag/Orthoclase (15-25%) Biotite (<2%) Amph (40-50%) Garnet (<1%) Olivine (<1%)	Amphibole xtals "frosted" w Quartz and streaked out in places. Occasional biotite/olivine. Quartz interlocking w Plag xtals. Some carlsbad twins => orthoclase. Some metamorphism apparent.	Metadiorite = Folliated Horneblende Diorite
SC-54	Lake Adelaide	m-l (2-20)	m-d grey	40-60	Quartz (25-30%) Plag/Orthoclase (15-25%) Biotite (<2%) Amph (40-50%) Garnet (<1%) Olivine (<1%)	Amphibole xtals "frosted" w Quartz and streaked out in places. Occasional biotite/olivine. Quartz interlocking w Plag xtals. Some carlsbad twins => orthoclase. Some metamorphism apparent.	Metadiorite = Folliated Horneblende Diorite
SC-55	Lake Adelaide	m-l (2-20)	m-d grey	40-60	Quartz (25-30%) Plag/Orthoclase (15-25%) Biotite (<2%) Amph (40-50%) Garnet (<1%) Olivine (<1%)	Amphibole xtals "frosted" w Quartz and streaked out in places. Occasional biotite/olivine. Quartz interlocking w Plag xtals. Some carlsbad twins => orthoclase. Some metamorphism apparent.	Metadiorite = Folliated Horneblende Diorite

C.4 ^{10}Be Concentration calculations

10Be Concentration Calculations

GNS ID	Field ID	10Be/9Be ABS Ratio (1E-15)	Absolute Error (1-sigma) (1E-15)	Percentage Error	Sample Mass (g)	Mass of 9Be in carrier (mg)	10Be Conc (atoms/g-Q)	10Be Conc Err (atoms/g-Q)
NZ0637	SC-1	13.89548	1.59592	11.49	7.32	0.6555	8.3162E+04	9.5513E+03
NZ0638	SC-3	116.66190	9.08589	7.79	56.86	0.6878	9.4313E+04	7.3453E+03
NZ0639	SC-4	116.39421	5.51977	4.74	80.57	0.6536	6.3102E+04	2.9925E+03
NZ0640	SC-5	15.74856	2.15288	13.67	47.82	0.6773	1.4908E+04	2.0379E+03
NZ0641	SC-7	64.01715	3.28285	5.13	39.01	0.6158	6.7534E+04	3.4632E+03
NZ0642	SC-9	22.76046	3.41245	14.99	17.12	0.6963	6.1872E+04	9.2764E+03
NZ0643	SC-10	41.61559	2.80569	6.74	69.29	0.6816	2.7359E+04	1.8445E+03
NZ0644	SC-11	7.10214	1.14053	16.06	15.15	0.6627	2.0762E+04	3.3342E+03
NZ0645	SC-12	18.91658	1.85381	9.80	13.07	0.7008	6.7785E+04	6.6428E+03
NZ0646	SC-14	73.85005	3.49481	4.73	34.11	0.6714	9.7145E+04	4.5972E+03
NZ0647	SC-16	74.41972	4.91090	6.60	51.69	0.6719	6.4653E+04	4.2664E+03
NZ0648	SC-17	5.01946	1.52033	30.29	29.26	0.6860	7.8650E+03	2.3822E+03
NZ0649	SC-20	34.76420	2.20263	6.34	42.86	0.6990	3.7891E+04	2.4007E+03
NZ0650	SC-21	9.78969	2.36398	24.15	17.36	0.6808	2.5657E+04	6.1955E+03

C.5 Stirling Basin core logs

C.5.1 Cores S535, S536 and S542

In addition to Core S534 (described in Chapter 3), NIWA cores S535, S536 and S542 were logged:

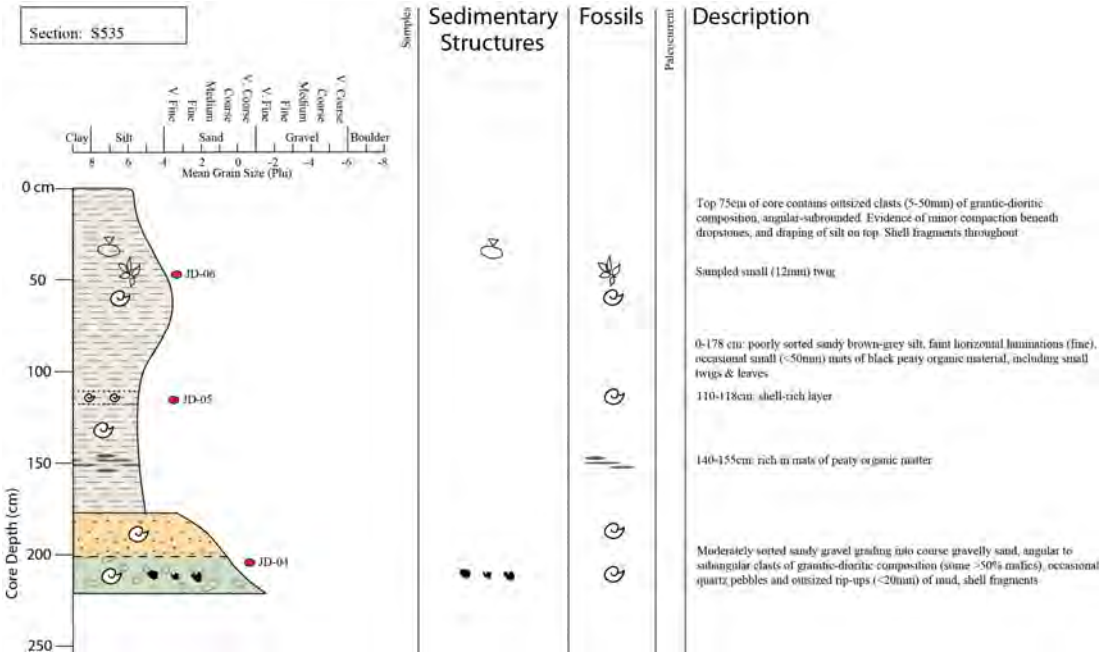

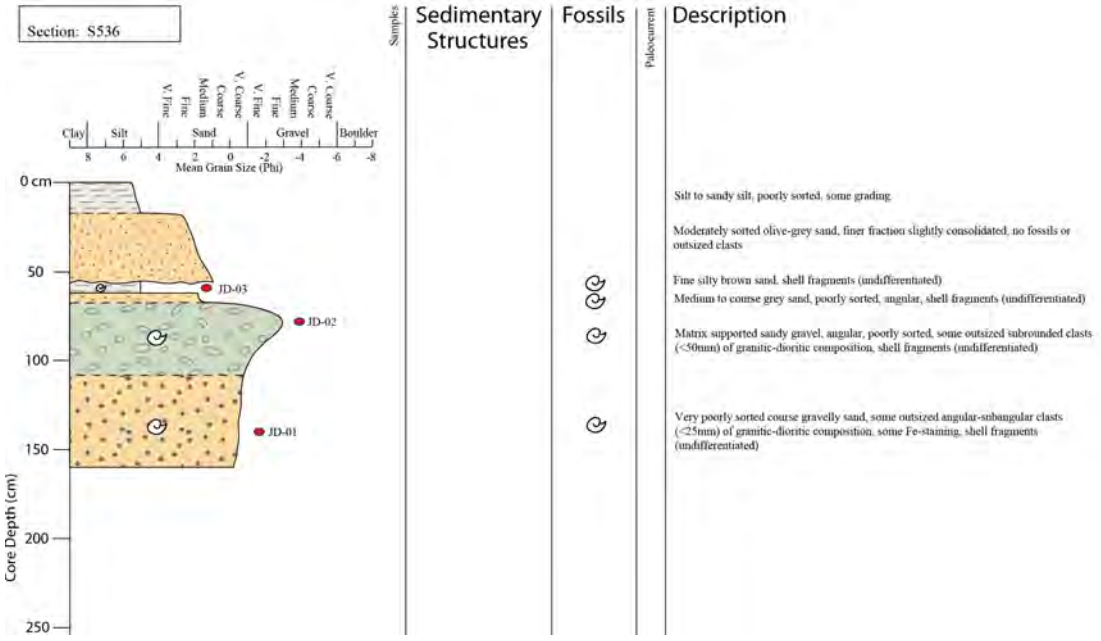
Section: S536
Samples
Sedimentary Structures
Fossils
Paleocurrent
Description
Clay
Silt
Sand
Gravel
Boulder
V. Fine
Fine
Medium
Coarse
V. Coarse
Mean Grain Size (Phi)
0 cm
50
100
150
200
250
Core Depth (cm)
JD-03
JD-02
JD-01
Silt to sandy silt, poorly sorted, some grading
Moderately sorted olive-grey sand, finer fraction slightly consolidated, no fossils or outsized clasts
Fine silty brown sand, shell fragments (undifferentiated)
Medium to course grey sand, poorly sorted, angular, shell fragments (undifferentiated)
Matrix supported sandy gravel, angular, poorly sorted, some outsized subrounded clasts (<50mm) of granitic-dioritic composition, shell fragments (undifferentiated)
Very poorly sorted course gravelly sand, some outsized angular-subangular clasts (<25mm) of granitic-dioritic composition, some Fe-staining, shell fragments (undifferentiated)

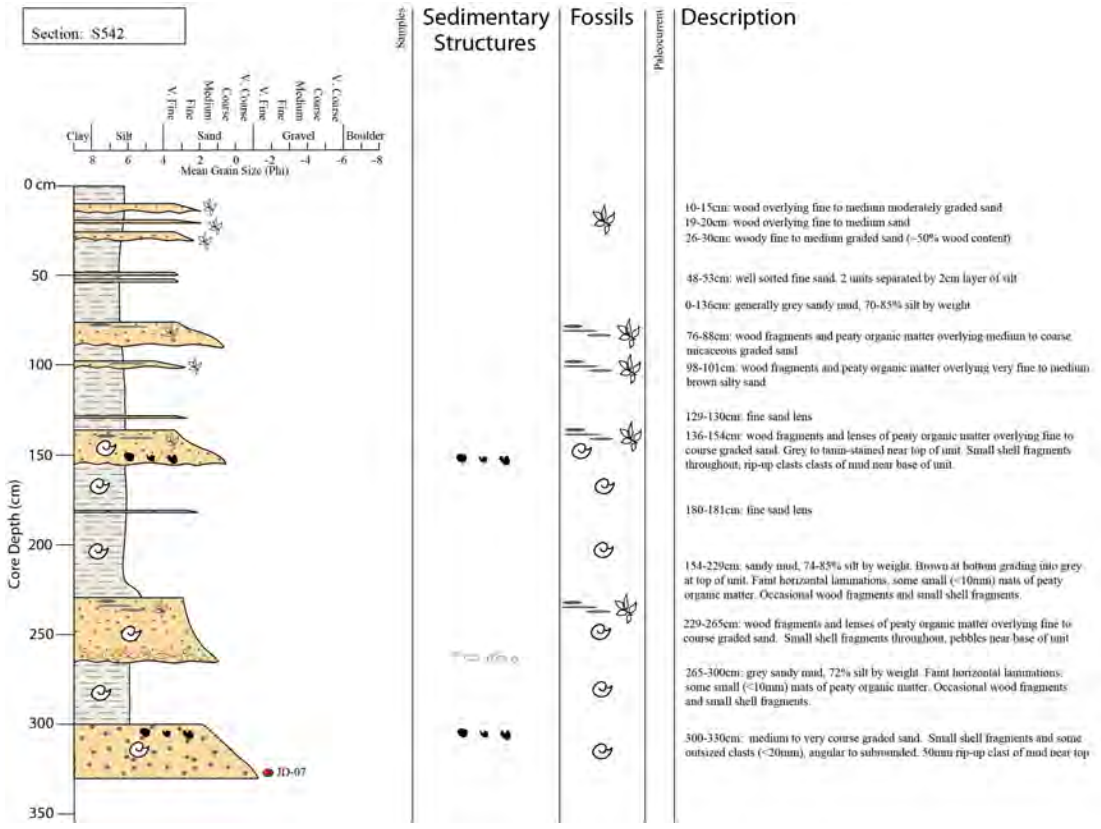
Section: S542
Samples
Sedimentary Structures
Fossils
Paleocurrent
Description
Clay
Silt
Sand
Gravel
Boulder
V. Fine
Fine
Medium
Coarse
V. Coarse
Mean Grain Size (Phi)
0 cm
50
100
150
200
250
300
350
Core Depth (cm)
JD-07
10-15cm: wood overlying fine to medium moderately graded sand
19-20cm: wood overlying fine to medium sand
26-30cm: woody fine to medium graded sand (~50% wood content)
48-53cm: well sorted fine sand. 2 units separated by 2cm layer of silt
0-136cm: generally grey sandy mud, 70-85% silt by weight
76-88cm: wood fragments and peaty organic matter overlying medium to coarse micaceous graded sand
98-101cm: wood fragments and peaty organic matter overlying very fine to medium brown silty sand
129-130cm: fine sand lens
136-154cm: wood fragments and lenses of peaty organic matter overlying fine to course graded sand. Grey to tann-stained near top of unit. Small shell fragments throughout, rip-up clasts clasts of mud near base of unit.
180-181cm: fine sand lens
154-229cm: sandy mud, 74-85% silt by weight. Brown at bottom grading into grey at top of unit. Faint horizontal laminations, some small (<10mm) mats of peaty organic matter. Occasional wood fragments and small shell fragments.
229-265cm: wood fragments and lenses of peaty organic matter overlying fine to course graded sand. Small shell fragments throughout, pebbles near base of unit
265-300cm: grey sandy mud, 72% silt by weight. Faint horizontal laminations, some small (<10mm) mats of peaty organic matter. Occasional wood fragments and small shell fragments.
300-330cm: medium to very course graded sand. Small shell fragments and some outsized clasts (<20mm), angular to subrounded. 50mm rip-up clast of mud near top

C.5.1.1 Core data from NIWA repository

Stn	Depth (cm)	Means			Std Dev		Sorting Coef	Skewness				Kurtosis			Percentages					
		Arith	Folk	Inman	Inc Gr	Phi. Quart	Trask	Moment	Phi. Quart	Graph	Inc Gr	Moment	Graph	Trans Gr	Grav	Sand	Silt	Clay	S+G	CaCo3	Organic
S534A	36	5.758	5.848	6.017	1.856	1.472	2.774	0.076	0.303	0.249	0.203	−0.482	0.764	0.433	0.000	17.070	66.020	16.910	17.070	5.5	4.83
S534B	98	3.635	3.569	3.600	0.965	0.524	1.438	0.750	−0.002	0.105	0.166	2.436	1.345	0.574	0.000	74.680	23.980	1.340	74.680	3.5	1.53
S534C	101	2.273	2.293	2.257	1.020	0.598	1.514	−0.303	−0.071	−0.118	−0.090	0.739	1.257	0.557	1.460	93.110	5.440	0.000	94.570	3.0	nil
S534D	104	1.659	1.623	1.574	1.377	0.907	1.876	0.001	−0.089	−0.111	−0.052	−0.137	1.061	0.515	2.560	92.050	5.400	0.000	94.610	2.0	nil
S534E	144	6.197	6.228	6.316	1.660	1.304	2.469	0.036	0.206	0.143	0.112	−0.565	0.772	0.436	0.000	6.980	74.460	18.560	6.980	5.0	4.48
S534F	221	6.044	6.114	6.185	1.648	1.209	2.312	−0.176	0.144	0.121	0.091	0.104	0.856	0.461	0.000	8.470	76.530	14.990	8.470	6.5	5.25
S534G	261	5.750	5.806	5.980	1.692	1.236	2.356	0.207	0.226	0.280	0.272	−0.454	0.831	0.454	0.000	13.210	72.680	14.110	13.210	3.5	nil
S534H	331	1.597	1.545	1.555	0.674	0.416	1.334	0.633	−0.010	0.046	0.118	1.569	1.137	0.532	0.010	98.100	1.900	0.000	98.110	2.0	nil
S534I	366	−0.183	−0.212	−0.160	1.589	1.190	2.282	0.174	0.083	0.093	0.106	−0.177	0.849	0.459	34.920	64.050	1.030	0.000	98.970	2.0	nil
S534J	404	−1.000	−1.046	−1.085	2.192	1.887	3.698	0.064	−0.159	−0.047	0.001	−0.505	0.685	0.406	49.520	49.850	0.640	0.000	99.370	2.0	nil
S535A	11	5.491	5.592	5.742	1.961	1.377	2.598	0.051	0.221	0.214	0.165	−0.378	0.891	0.471	0.000	22.260	63.540	14.200	22.260	5.5	4.50
S535B	61	3.462	3.769	3.654	3.185	1.724	3.304	−0.417	-0.137	−0.124	−0.211	0.095	1.401	0.583	12.060	38.170	44.020	5.740	50.230	4.8	3.80
S535C	101	5.279	5.302	5.440	1.754	1.177	2.261	0.133	0.223	0.233	0.220	−0.204	0.989	0.497	0.000	23.470	67.200	9.340	23.470	3.9	3.60
S535D	166	5.326	5.350	5.485	1.670	1.135	2.196	0.099	0.210	0.237	0.237	−0.062	0.979	0.495	0.000	20.990	70.030	8.980	20.990	3.8	3.40
S535E	179	2.673	2.625	2.631	0.558	0.328	1.255	0.540	−0.016	0.038	0.146	1.050	1.273	0.560	0.000	95.760	4.240	0.000	95.760	3.5	nil
S535F	189	1.474	1.426	1.446	0.775	0.522	1.436	0.513	0.003	0.077	0.132	0.970	1.017	0.504	0.000	98.160	1.840	0.000	98.160		nil
S535G	205	0.223	0.203	0.243	1.417	1.026	2.037	0.186	0.052	0.083	0.088	0.001	0.915	0.478	20.760	77.870	1.380	0.000	98.630	2.5	nil
S535H	220	−1.588	−1.709	−1.678	1.150	0.682	1.604	0.748	0.024	0.087	0.189	1.823	1.225	0.550	77.100	22.400	0.510	0.000	99.500	3.7	nil
S536A	2	5.290	5.271	5.434	1.553	1.040	2.056	0.199	0.286	0.317	0.320	−0.010	1.019	0.505	0.000	19.080	73.040	7.880	19.080	3.8	3.60
S536B	21	2.410	2.380	2.387	0.523	0.352	1.276	0.382	0.033	0.039	0.082	0.721	1.018	0.504	0.000	99.110	0.890	0.000	99.110	2.9	0.70
S536C	36	1.943	1.909	1.930	0.668	0.423	1.341	0.426	0.056	0.092	0.106	0.844	1.069	0.517	0.000	98.380	1.620	0.000	98.380	1.7	nil
S536D	54	1.088	1.059	1.072	1.156	0.838	1.787	0.027	0.037	0.033	0.038	0.238	0.893	0.472	1.860	96.720	1.420	0.000	98.580	1.3	nil
S536E	67	−0.144	−0.198	−0.078	1.863	1.475	2.780	0.191	0.324	0.178	0.175	−0.337	0.783	0.439	37.680	60.520	1.810	0.000	98.200	2.6	nil
S536F	108	−0.716	−0.797	−0.930	2.446	2.221	4.661	−0.023	−0.356	−0.144	−0.106	−0.610	0.641	0.391	44.440	54.630	0.930	0.000	99.070	2.2	nil
S542A	4	6.156	6.248	6.253	1.803	1.401	2.641	−0.281	0.050	0.008	−0.047	0.063	0.809	0.447	0.000	11.100	69.440	19.460	11.100	7.0	5.68
S542B	41	6.471	6.495	6.489	1.676	1.418	2.672	−0.095	0.077	−0.009	−0.044	−0.589	0.712	0.416	0.000	6.440	68.940	24.620	6.440	6.0	4.60
S542C	115	6.082	6.177	6.241	1.740	1.108	2.155	0.045	-0.041	0.103	0.061	−0.479	0.966	0.491	0.000	10.640	70.950	18.410	10.640	5.5	4.84
S542D	161	6.098	6.086	6.091	1.241	0.748	1.680	0.012	-0.065	0.014	0.065	0.340	1.214	0.548	0.000	3.630	84.920	11.450	3.630	6.0	5.00
S542E	191	6.159	6.222	6.241	1.694	1.281	2.430	−0.169	0.050	0.032	0.001	−0.103	0.825	0.452	0.000	9.260	73.810	16.930	9.260	6.0	5.53
S542F	219	6.239	6.267	6.351	1.513	1.127	2.184	0.079	0.155	0.153	0.138	−0.504	0.829	0.453	0.000	3.330	81.010	15.660	3.330	5.0	7.51
S542G	229	4.286	4.159	4.334	1.526	0.731	1.660	0.610	0.190	0.423	0.481	0.618	1.672	0.626	0.000	57.950	33.670	8.380	57.950	2.0	3.21
S542H	239	2.604	2.582	2.594	0.686	0.396	1.316	0.234	-0.019	0.057	0.133	0.744	1.293	0.564	0.000	94.670	5.330	0.000	94.670	1.5	nil
S542I	251	2.226	2.183	2.210	0.800	0.523	1.437	0.366	0.049	0.114	0.179	0.369	1.122	0.529	0.000	95.530	4.460	0.000	95.530	1.5	nil
S542J	261	1.264	1.279	1.148	1.776	1.144	2.210	-0.236	-0.192	-0.230	-0.218	-0.076	1.086	0.521	12.250	83.100	4.650	0.000	95.350	1.0	nil
S542K	281	5.796	5.910	5.971	1.823	1.293	2.450	-0.206	0.080	0.098	0.032	0.031	0.929	0.482	0.000	14.360	71.990	13.650	14.360	3.0	5.32

Appendix D

The reservoir effect

D.1 Considerations for radiocarbon dating in New Zealand fiords

Ocean surface waters (down to about 200 m depth) are depleted in ^{14}C compared to the atmosphere, so radiocarbon ages of marine samples that were formed in the ocean (e.g. shells, fish bones) are commonly around 400 years older than their terrestrial counterparts. This Marine Reservoir Effect (MRE) is the result of dilution caused by the mixing of surface waters with upwelling deep waters, combined with a delay in exchange rates between atmospheric CO_2 and marine bicarbonate (HCO_3) (Petchey et al., 2008). Due to the MRE, an age-model correction is generally applied when calibrating marine-based radiocarbon ages; this correction is an integral part of marine ^{14}C calibration curves, such as the Marine 09 curve (Reimer et al., 2009) used in the Oxcal version 4.1 (Bronk Ramsey, 2010) calibration software. In addition, local and regional deviations from the global average MRE correction are compensated for by using a local correction factor (δR), which varies depending on terrestrial carbon input (e.g. from peat of calcareous bedrock) and local variations in marine ^{14}C circulation.

In coastal waters off of New Zealand, various (δR) values have been reported; Petchey et al. (2008) investigated marine shells of known calendar age from Norfolk Island, the Kermadec Islands, and the Chatham Islands. They reported average δR values of -19 ± 13 ^{14}C for the Kermadecs, and -49 ± 10 ^{14}C for Norfolk Island, and attributed these values to heightened absorption of atmospheric CO_2 in the region south of the South Pacific Convergence Zone. In contrast, Petchey et al. (2008) found that δR values for the Chatham Islands are much higher, and more variable; they reported average δR values of 134 ± 83 ^{14}C for the Chathams, which they attributed to upwelling

and mixing of ^{14}C-depleted water along the Chatham rise. Within New Zealand, McFadgen et al. (1994) analysed 11 shells from various locations around the coast that were alive from 1923-1957, and calculated a ^{14}C open-ocean reservoir correction (δR) of -31 ± 13 years. However, in a study of raised beach ridges at Turakirae Head, resulting from the 1855 Waiarapa earthquake, McSaveney et al. (2006) calculated an average open-ocean reservoir correction of 3 ± 14 years, from 11 shell samples that were stranded following catastrophic shoreline uplift.

There are few published records of local reservoir corrections from the west coast coast of the South Island, including Fiordland. Perhaps the only reference to a MRE correction for Fiordland comes from a recent Fiordland paleoclimate study; Knudson et al. (2011) dated marine bivalve shells, formaminiferal calcite, and bulk organic carbon from various fiords (including Milford Sound). They determined that uncorrected radiocarbon ages for shell fragments from marine cores within George Sound were only $\sim$50 years older than (corrected) ^{14}C ages determined for foraminfera and bulk organic carbon samples from the same depth. Knudson et al. (2011) attributed this apparent absence of a MRE within George Sound to the presence of a low salinity (brackish) layer moving seaward over more saline marine replacement waters; this restricted circulation environment is common in many New Zealand fiords, due to precipitation-driven haloclines and flow restrictions caused by shallow entrance sills (Knudson et al., 2011; Pickrill, 1987). The presence of shell fragments from primarily benthic species (e.g. *Mytilus edulis aoteanus*, which lives on the upper 5m of fiord rock-walls), within the deep basins of George and Milford Sounds indicates that those shell fragments were transported there from shallower water, where they would have lived in a low-salinity marine environment. As a result of their findings, Knudson et al. (2011) applied a reservoir effect correction of 50 years to their calibrated radiocarbon ages.

Appendix E

Supplementary information

E.1 New Zealand geological time scale

New Zealand geological time scale (after Cooper 2004).

E.2 Fiordland geological events (from Fiordland Qmap)

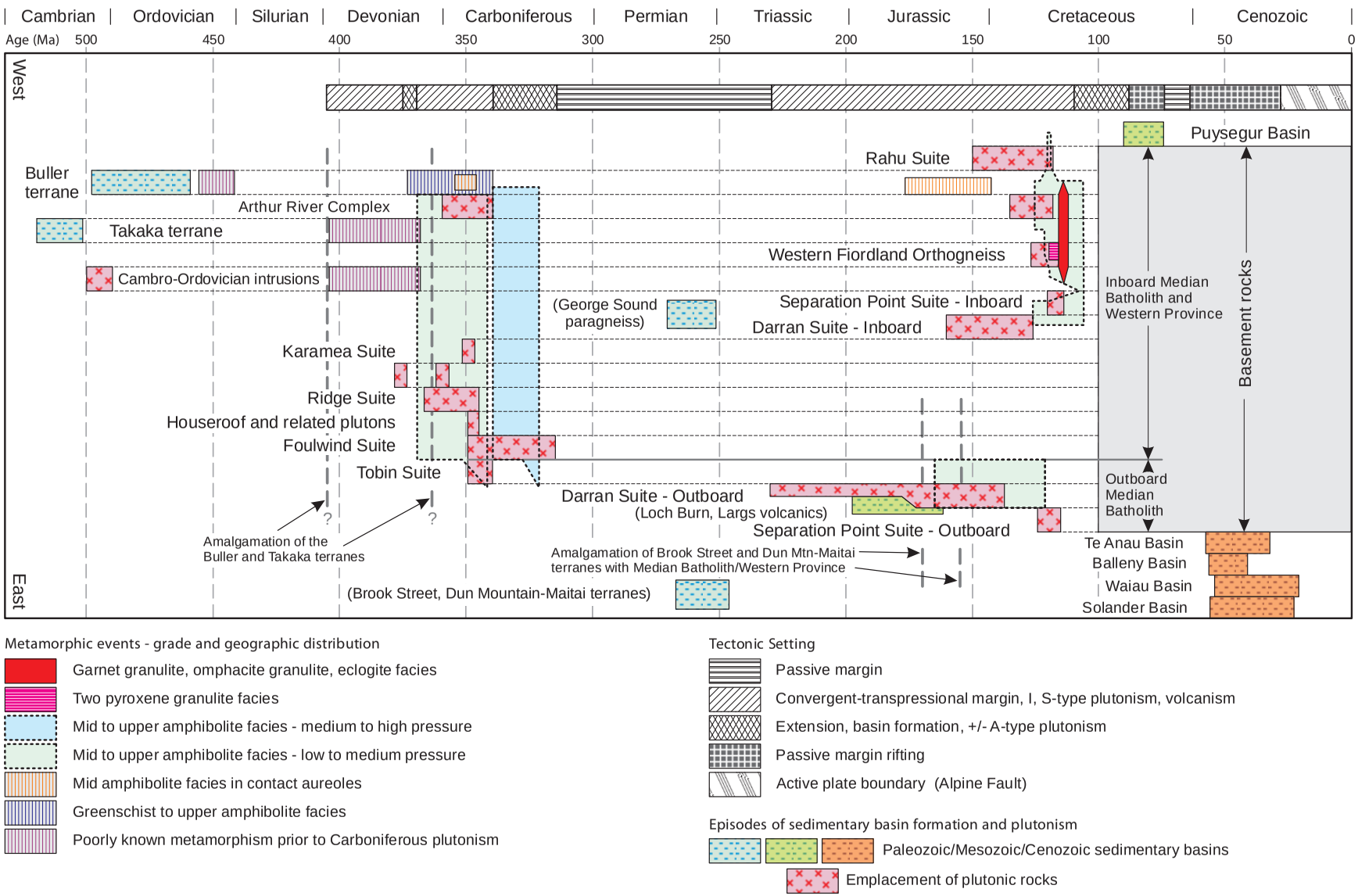

Figure 64 Time-space diagram showing major geological events in Fiordland, related to their tectonic setting.

E.3 The Modified Mercalli intensity scale (MM)

The Modified Mercalli intensity scale (MM)

The Modified Mercalli intensity scale (summarised from Downes (1995), Dowrick (1996) and Hancox et al. *(2002)) is a descriptive scale used to rank the intensity of an earthquake at a particular location. The intensity of any earthquake will vary from place to place, because of factors such as distance from the epicentre and localised differences in ground conditions (for example, shaking will be much greater on swampy ground than on solid rock).*

MM 2 *Felt by people at rest, on upper floors or favourably placed.*

MM 3 *Felt indoors; hanging objects may swing, vibration similar to passing of light trucks.*

MM 4 *Generally noticed indoors but not outside. Light sleepers may be awakened. Vibration like passing of heavy traffic. Doors and windows rattle. Walls and frames of buildings may be heard to creak.*

MM 5 *Generally felt outside, and by almost everyone indoors. Most sleepers awakened. A few people alarmed. Some glassware and crockery may be broken. Open doors may swing.*

MM 6 *Felt by all. People and animals alarmed. Many run outside. Furniture or objects may move on smooth surfaces. Objects fall from shelves. Glassware and crockery broken. Slight damage to some types of buildings. A few cases of chimney damage. Loose material may be dislodged from sloping ground. A few very small (e.g. <1000 m^3) shallow landslides and rockfalls occur.*

MM 7 *General alarm. Furniture and appliances may be shifted and unstable items overturned. Unreinforced stone and brick walls cracked. Some pre-earthquake code buildings damaged. Roof tiles may be dislodged. Many domestic chimneys broken. Small falls of sand and gravel banks. Some fine cracks appear in sloping ground and ridge crests. Rockfalls from steep slopes and cuttings are common. A few small to moderate landslides (e.g. 1 000 to 10 000 m^3) occur on steeper slopes. Some instances of liquefaction at susceptible sites.*

MM 8 *Alarm may approach panic. Steering of cars greatly affected. Some serious damage to pre-earthquake code masonry buildings. Most reinforced domestic chimneys damaged, many brought down. Monuments and elevated tanks twisted or brought down. Some post-1980 brick veneer dwellings damaged. Houses not secured to foundations may move. Cracks may appear on slopes and in wet ground. On slopes in steep or weak ground, numerous small to moderate landslides and some large landslides (e.g. 100 000 m^3). Collapse of roadside cuttings and unsupported excavations. Small sand fountains and other instances of liquefaction.*

MM 9 *Very poor quality unreinforced masonry destroyed. Pre-earthquake code masonry buildings heavily damaged or collapse. Damage or distortion to some pre-1980 buildings and bridges. Houses not secured to foundations shifted off. Brick veneers fall and expose framing. Conspicuous cracking of flat and sloping ground. On steep slopes, many small to large landslides and some very large (>1 000 000 m^3) landslides and rock avalanches that may block narrow valleys and form lakes. Liquefaction effects intensified, with large sand fountains and extensive cracking or settlement of weak ground.*

MM 10 *Most unreinforced masonry structures destroyed. Many pre-earthquake code buildings destroyed. Many pre-1980 buildings and bridges seriously damaged. Many post-1980 buildings and bridges moderately damaged or permanently distorted. Widespread cracking of flat and sloping ground. Widespread and severe landsliding on sloping ground. Very large landslides (>$10^6 m^3$) from steep mountain faces and coastal cliffs. Widespread and severe liquefaction.*